# UMTIK 2026

— İSTANBUL —

# 21. INTERNATIONAL CONFERENCE ON MACHINE DESIGN AND PRODUCTION

## AUGUST 19-21, 2026

## İSTANBUL TECHNICAL UNIVERSITY, TÜRKİYE

## CONFERENCE PROCEEDINGS

İTÜ

MATIMAREN
Makina Mühendisliği Bölümü
Orta Doğu Teknik Üniversitesi
Ankara-Türkiye

# 21st INTERNATIONAL CONFERENCE ON MACHINE DESIGN AND PRODUCTION

## CONFERENCE PROCEEDINGS

**Editorial Board**

Mustafa BAKKAL
Mustafa Cemal ÇAKIR
Barış ÇETİN
Ender CİĞEROĞLU
Hakan KALKAN
Sadık Engin KILIÇ
Erhan İlhan KONUKSEVEN
Bahram LOTFİ
Ramazan Hakkı NAMLU
Ali ORAL
Semih PİLATİN
İbrahim Etem SAKLAKOĞLU
Ulvi ŞEKER
Hakkı Özgür ÜNVER
Ulaş YAMAN
Tanfer YANDAYAN

umtik 2026

19–21 August 2026

Istanbul–TÜRKİYE

**MATIMAREN**
**DEPARTMENT OF MECHANICAL ENGINEERING**
**MIDDLE EAST TECHNICAL UNIVERSITY**
**ANKARA-TURKEY**

Dedicated to the memory of

**Prof. Dr. Turgut Tümer**

and of all other IPC members we have lost in previous years.

All rights of this book are reserved by the
Middle East Technical University.
None of the papers printed in this book may be
reproduced without the prior permission, in
writing, from the Author(s) of the paper(s)
and the editors of the book. The papers can
however be cited by giving
the source.

This book can be obtained from the following
addresses:

**UMTIK**
**Mechanical Engineering Department**
**Middle East Technical University**
**06800 Ankara- Turkey**

**Cover Print:**
METU- Ankara

**Printing and Binding:**
METU- Ankara

**Printed by:**
METU- Ankara

**ISBN**

## Organizing Committee

| | | |
|---|---|---|
| **Mustafa BAKKAL** | ITU | bakkalmu@itu.edu.tr |
| **Mustafa Cemal ÇAKIR** | Uludağ University | cemal@uludag.edu.tr |
| **Barış ÇETİN** | FNSS | cetin.baris@fnss.com.tr |
| **Ender CİĞEROĞLU** | METU | ender@metu.edu.tr |
| **Hakan KALKAN** | Atılım University | hakan.kalkan@atilim.edu.tr |
| **Sadık Engin KILIÇ** | METU (Professor Emeritus) | senginkilic@gmail.com |
| **Erhan İlhan KONUKSEVEN** | METU | konuk@metu.edu.tr |
| **Bahram LOTFİ** | TOBB ETU | blotfi@etu.edu.tr |
| **Ramazan Hakkı NAMLU** | Atılım University | ramazan.namlu@atilim.edu.tr |
| **Ali ORAL** | Balıkesir University | a.oral@balikesir.edu.tr |
| **Semih PİLATİN** | Kale Pratt & Whitney | pilatin.semih@gmail.com |
| **İbrahim Etem SAKLAKOĞLU** | Ege University | i.e.saklakoglu@ege.edu.tr |
| **Ulvi ŞEKER** | Gazi University | useker@gazi.edu.tr |
| **Hakkı Özgür ÜNVER** | TOBB ETU | hounver@etu.edu.tr |
| **Ulaş YAMAN** | METU | uyaman@metu.edu.tr |
| **Tanfer YANDAYAN** | TÜBİTAK | tanfer.yandayan@tubitak.gov.tr |

## International Program Committee

| | | | |
|---|---|---|---|
| **Erdem ACAR** | TÜRKİYE | **Jui-Pin HUNG** | TAIWAN R.O.C. |
| **Serpil ACAR** | UNITED KINGDOM | **Wen-Yuh JYWE** | TAIWAN R.O.C. |
| **Edwin Gerardo ACUÑA ACUÑA** | COSTA RICA | **Bilgin KAFTANOĞU** | TÜRKİYE |
| **Samet AKAR** | TÜRKİYE | **Mete KALYONCU** | TÜRKİYE |
| **Mustafa ALKAN** | TÜRKİYE | **Fatma KARA** | TÜRKİYE |
| **Yusuf ALTINTAŞ** | CANADA | **Yiğit KARPAT** | TÜRKİYE |
| **Saleh AMAITIK** | LIBYA | **Şükran KATMER** | TÜRKİYE |
| **Carla ANFLOR** | BRASIL | **Takeo KATO** | JAPAN |
| **Ömer ANLAĞAN** | TÜRKİYE | **Yağız KAYALI** | TÜRKİYE |
| **Ahmet Hakan ARGEŞO** | TÜRKİYE | **Yusuf KAYNAK** | TÜRKİYE |
| **Özgür ASLAN** | UNITED KINGDOM | **Zafer KAZANCI** | UNITED KINGDOM |
| **Hediye ATİK** | TÜRKİYE | **Uğur KEMİKLİOĞLU** | TÜRKİYE |
| **Besim BARANOĞLU** | TÜRKİYE | **Behzat Bahadır KENTEL** | TÜRKİYE |
| **Sedat BAYSEÇ** | TÜRKİYE | **Zekai Murat KILIÇ** | UNITED KINGDOM |
| **Bekir BEDİZ** | TÜRKİYE | **Bahattin KOÇ** | TÜRKİYE |
| **Erhan BUDAK** | TÜRKİYE | **Gökhan KÜÇÜKTÜRK** | TÜRKİYE |
| **Orhan ÇAKIR** | TÜRKİYE | **İsmail LAZOĞLU** | TÜRKİYE |
| **Mehmet ÇELİK** | TÜRKİYE | **Kuan-Ming LI** | TAIWAN R.O.C. |
| **Dursun ÇİÇEK** | TÜRKİYE | **Yangmin LI** | HONG KONG |
| **Leo COURTY** | FRANCE | **Raphael LORAIN** | FRANCE |
| **Samad DADVANDIPOUR** | HUNGARY | **Ming-Chyuan LU** | TAIWAN R.O.C. |
| **Pınar DEMİRCİOĞLU** | TÜRKİYE | **Tzuo Liang LUO** | TAIWAN R.O.C. |
| **Laszlo DUDAS** | HUNGARY | **Kei MATSUOKA** | JAPAN |
| **Volkan ESAT** | UNITED KINGDOM | **Yoshiyuki MATSUOKA** | JAPAN |
| **Mümtaz Afşin ESİ** | TÜRKİYE | **Pınar MENGÜÇ** | TÜRKİYE |
| **Tahir FİDAN** | TÜRKİYE | **Tomoyuki MIYASHITA** | JAPAN |
| **Yang GAO** | HONG KONG | **Tetsuro OGI** | JAPAN |
| **Necdet GEREN** | TÜRKİYE | **Ahmet Murat ÖZBAYOĞLU** | TÜRKİYE |
| **Greg GIBBONS** | UNITED KINGDOM | **Gökhan ÖZGEN** | TÜRKİYE |
| **Akinari HIRAO** | JAPAN | **Emre ÖZLÜ** | TÜRKİYE |

| | | | |
|---|---|---|---|
| **Fahrettin ÖZTÜRK** | TÜRKİYE | **Oğuzhan TÜYSÜZ** | CANADA |
| **Ravipudi Venkata RAO** | INDIA | **Ali ÜNÜVAR** | TÜRKİYE |
| **Ferit SAİT** | TÜRKİYE | **Min WAN** | P.R.C. |
| **Durmuş Tayyar ŞEN** | TÜRKİYE | **Charlie C.L. Wang** | UNITED KINGDOM |
| **Mert ŞENER** | TÜRKİYE | **Hakan YAVAŞ** | GERMANY |
| **Vadim S. SILBERSCHMIDT** | UNITED KINGDOM | **Wong Kuan YEW** | MALAYSIA |
| **Uğur ŞİMŞİR** | TÜRKİYE | **Çağrı Vakkas YILDIRIM** | TÜRKİYE |
| **Ekaterina SMOTROVA KAYALI** | UNITED KINGDOM | **Ali Rıza YILDIZ** | TÜRKİYE |
| **Hamit SOLMAZ** | TÜRKİYE | **Bülent YILMAZ** | TÜRKİYE |
| **Emel TABAN** | TÜRKİYE | **Oğuzhan YILMAZ** | TÜRKİYE |
| **Fuat TİNİŞ** | TÜRKİYE | **Hüseyin Serdar YÜCESU** | TÜRKİYE |
| **Meng-Shiun TSAI** | TAIWAN R.O.C. | **Michael ZAEH** | GERMANY |
| **Cihan TURHAN** | TÜRKİYE | | |

**SUPPORTING ORGANIZATIONS, ASSOCIATIONS and UNIVERSITIES**

**Istanbul Technical University (ITU)**

**Middle East Technical University (METU)**

MATIMAREN
Makina Mühendisliği Bölümü
Orta Doğu Teknik Üniversitesi
Ankara-Türkiye

**MATIMAREN**

## SILVER SPONSORS

ONPLUS

RENISHAW

MEGA DANIŞMANLIK

KAE SYSTEMS

BELGİN OIL

KALE

## BRONZE SPONSORS

YEMTAR

TEKNİKEL

GESBEY

USEL

KROHNE

PAKSAN

PROMEC

**Conference Secretariat**

**ORIGIN Event Management Company**

Çamlık, Muyar Plaza, Dinç Sokak No:4/25
Ümraniye/İstanbul,
Türkiye

TEL: +90 216 372 23 30

www.originemc.com.tr
info@originemc.com.tr

Contact Address

http://www.umtik.com
info@umtik.com

## PREFACE

It is a great pleasure to welcome you to the 21st UMTIK – International Conference on Machine Design and Production. UMTIK is an international scientific event held biennially since 1984. Covering a wide range of contemporary topics—most notably mechanical engineering, but also manufacturing technologies, machine design, artificial intelligence applications, aerospace simulations, and industrial developments—the congress brings together academics, researchers, and industry representatives from around the world.

The theme of UMTIK 2026 is selected as "From Industry 4.0 to Industry 5.0 and Beyond: Building a More Sustainable World" for the following reasons.

The primary reason for the transition from Industry 4.0 to 5.0 is that production in Industry 4.0 focused entirely on machinery and digitalization and overlooked the human factor, environmental sustainability, and personalized production. Furthermore, production issues and supply chain problems experienced during the pandemic—along with the shortcomings of "dark factories" (a key focus of Industry 4.0)—are encouraging manufacturers to adopt resilient, human-centric, and sustainable production methods, which are the core tenets of Industry 5.0. The goal of this transition is to make systems smarter and greener by having technology work in collaboration with humans.

Taking all these factors into account, this topic was selected for UMTIK 2026 with the aim of bringing together organizations operating in the fields of machine design and manufacturing processes to facilitate knowledge sharing regarding the 2026 scope areas.

The Honorary Chairpersons of the Conference, the presidents of the universities, Prof. Dr. Hasan MANDAL of Istanbul Technical University and Prof. Dr. Ahmet YOZGATLIGİL of Middle East Technical University, will make significant contributions to UMTIK 2026 by participating in the panel session on "Building Human Capability for Collaborative Augmented Intelligence Ecosystems."

ROKETSAN will arrange a special session on Lifecycle Analysis of Modern Defense Systems, which will bring industry and academia together on the subject of defense systems that have started to receive more support due to the current geopolitical situation.

Additionally, UMTIK 2026 will include world-renowned keynote speakers who are experts in their fields, such as Prof. Dr. Alessandro BALSAMO, Prof. Dr. Yusuf ALTINTAŞ, Dr. Hakan YAVAŞ, Prof. Dr. Tamotsu MURAKAMİ, Prof. Dr. Feza KORKUSUZ, Dr. Andy GLEADALL, and Dr. Emel MAHMUTYAZICIOĞLU. It will also include a special session in memory of the late Professor Dr. S. Turgut Tümer, an esteemed scholar, educator, and researcher who made outstanding contributions to mechanical engineering education.

On August 18, 2026, the day before the UMTIK 2026 conference begins, a tutorial entitled "Metrology: Its Role in Production and Applications on Machine Tools" is arranged in consideration of the particular need for high-precision, high-value-added machine tools capable of precision manufacturing, especially within the defense and aerospace sectors.

The first-day program will start with the Opening Ceremony, including welcoming and opening speeches by the Conference Chair, Prof. Dr. S. Engin KILIÇ; the Rector of the host university (ITU), Prof. Dr. S. Hasan MANDAL; and the Rector of METU, Prof. Dr. Ahmet YOZGATLIGİL. It will be followed by the panel session "Building Human Capability for Collaborative Augmented Intelligence Ecosystems – Engineering Human-AI Collaboration for Industry 5.0 and Beyond," with panelists Prof. Dr. Hasan MANDAL, Prof. Dr. Ahmet YOZGATLIGİL, Donald H. TAYLOR, and Suat BAYSAN, moderated by Assoc. Prof. Tarkan GÜRBÜZ.

The first-day program in the afternoon starts with a plenary session featuring two keynote presentations. The first will be the keynote speech by Prof. Dr. Alessandro BALSAMO (the current President of CIRP) on "Coordinate Metrology in Manufacturing," chaired by Assoc. Prof. Dr. Tanfer YANDAYAN. The second is the keynote speech by Prof. Dr. Yusuf ALTINTAŞ (The University of British Columbia) on "Digital Machining of Blades," chaired by Prof. Dr. İbrahim Etem SAKLAKOĞLU.

There will be sponsor presentations by KALE PRATT & WHITNEY and RENISHAW between the sessions.

Later, there will be four parallel sessions with papers on Manufacturing Process Quality, Surface Engineering and Environmental Control; Structural Mechanics, Constitutive Modeling and Fracture Analysis; Mechanisms, Machine Components and Mechanical Performance; and a tutorial on "Digital Machining Principles and Industrial Practice,"

given by Prof. Dr. Yusuf ALTINTAŞ from The University of British Columbia.

The first-day program will be completed by the keynote presentation of Dr. Hakan YAVAŞ (FluxionSystem GmbH) on "Toward a Physics Foundation Model in Manufacturing: From Language Intelligence to Physics Intelligence," chaired by Assoc. Prof. Dr. Zekai Murat KILIÇ.

The second-day program starts with a panel entitled "Information Security in the Machinery Manufacturing Industry," in line with the previously mentioned topics. Our panelists are academics specializing in cybersecurity and information security: Prof. Prof. Dr. Şefik BAHTİYAR, Prof. Dr. Kemal BIÇAKÇI, Prof. Dr. İbrahim ÖZÇELİK, Prof. Dr. Alptekin KÜPÇÜ, and Prof. Dr. Mustafa ALKAN. We are addressing this subject because, in today's world, information assets, critical infrastructures, digital and smart manufacturing systems, supply chains, and industrial applications have become primary targets for cyberattacks. The panel will be moderated by Cüneyt DELİKTAŞ.

Later, a keynote presentation will be given by Prof. Dr. Tamotsu MURAKAMİ of The University of Tokyo on "Method for Creative Machine Design," chaired by Prof. Dr. Yoshiyuki MATSUOKA.

During the remainder of the second day, there will be four parallel sessions in three time slots through the end of the day (12 sessions in total). Papers in the special sessions will address Monitoring Technology for Manufacturing in Taiwan; Design of Personalized Medical Devices; Data-Driven Modeling and AI Applications in Engineering; Design Science and Timeaxis Design; and Design and Human Interface. Three special sessions on Lifecycle Analysis of Modern Defense Systems will be arranged by ROKETSAN. One paper session will focus on Robotics, and another local-language session will focus on metal forming and hybrid manufacturing.

There will be sponsor presentations by ONPLUS and KAE SYSTEMS between the parallel-session slots.

The third-day program begins with a plenary session dedicated to celebrating the life and achievements of Prof. Dr. Turgut Tümer, who passed away in 2025. The session will be presented by Prof. Dr. Nevzat ÖZGÜVEN and chaired by Prof. Dr. Birol KILKIŞ. Next, Prof. Dr. Feza KORKUSUZ from Hacettepe University will deliver his keynote speech on "Motion Analysis: From Basics to AI-Based Tools," chaired by Prof. Dr. Nevzat ÖZGÜVEN.

During the remainder of the third day, there will be four parallel sessions in three time slots through the end of the day (10 sessions in total). The papers will address Mechanisms, Machine Components and Mechanical Performance; Machining Mechanics, Composite Drilling and Cutting-Force Modeling; Digital Manufacturing and Tool Dynamics; Industrial Machine Design, Automation and Human-Centred Manufacturing; and AI Applications and Optimization in Manufacturing. One additional special session will be dedicated to the memory of Prof. Dr. S. Turgut Tümer. There will also be four sessions presented in Turkish.

Sponsor sessions featuring presentations by MEGA DANIŞMANLIK and BELGİN OIL will be held before the parallel-session slots.

In summary, the scientific program brings together 99 contributions presented in special and general sessions.

We would like to express our sincere thanks to the Presidency and all members of Istanbul Technical University for hosting UMTIK 2026 and providing its facilities. We hope all participants will feel the warm and positive atmosphere at Istanbul Technical University.

We highly acknowledge the Honorary Chairpersons of the Conference, the presidents of the universities: Prof. Dr. Hasan MANDAL of Istanbul Technical University and Prof. Dr. Ahmet YOZGATLIGİL of Middle East Technical University.

We would like to express our sincere appreciation to Assoc. Prof. Tarkan GÜRBÜZ for his hard work in organizing and moderating the first-day panel, together with panelists Prof. Dr. Hasan MANDAL, Prof. Dr. Ahmet YOZGATLIGİL, Donald H. TAYLOR, and Suat BAYSAN. We would also like to thank our Honorary Keynote Speaker, Prof. Yusuf ALTINTAŞ, and all other keynote speakers: Prof. Dr. Alessandro BALSAMO, Prof. Dr. Tamotsu MURAKAMİ, Dr. Hakan YAVAŞ, Prof. Dr. Feza KORKUSUZ, Dr. Andy GLEADALL, and Dr. Emel MAHMUTYAZICIOĞLU.

The second panel moderator, Cüneyt DELİKTAŞ, and the panelists, Prof. Dr. Abdül Halim ZAİM, Prof. Dr. Şefik BAHTİYAR, Prof. Dr. Kemal BIÇAKÇI, Prof. Dr. İbrahim ÖZÇELİK, Prof. Dr. Alptekin KÜPÇÜ, and Prof. Dr. Mustafa ALKAN, are highly acknowledged for their valuable contributions.

All chairpersons, authors, and participants are highly acknowledged for their valuable contributions. Asst. Prof. Dr. Bahram LOTFİ and Assoc. Prof. Dr. Tanfer YANDAYAN are gratefully acknowledged for the tremendous time and effort they spent in every phase of the conference organization and in the editorial work for the Conference

Proceedings and the Book of Abstracts.

Last but not least, we would like to thank the silver and bronze sponsors, members of the International Program Committee, Conference Secretariat “ORIGINEMC,” Scientific Secretariat (Research Assistants Yunus Emre NEHRİ and Mehmet Furkan ÖZBEY), and all who contributed to the success of UMTIK 2026.

We wish all participants a highly memorable time during their stay in ISTANBUL.

The Organizing Committee

UMTIK 2026

August 19th–21st, 2026

İstanbul, Türkiye

# CONTENTS

## Keynote Papers


### Keynote Address

**Method for Creative Machine Design** 22
Tamotsu Murakami


## English Special Sessions


### Data-Driven Modeling and AI Applications

**AI-Based Interpretation of Technical Drawings for Variant-Specific Information Provision in Brownfield Assembly** 38
Max-Heiner Birk, Andreas Gaus, Christoph Reich, Michael Engler

**Structural Design Optimization of the Hybrid Composite Battery Enclosure of an Electric Vehicle** 54
N. Berk İçten, Erdem Acar

### Design and Human Interface

**Development of Augmented Hand Shadow Art System** 80
Hideo Miyachi

**An Approach to Mental-Image Based Cognition for Intuitive Human-Robot Interaction - Focusing on Human Ability of Problem Finding and Solving** 90
Masao Yokota, Rojanee Khummongkol

**Generation of 3D Models of Historical Japanese Castle Town for Virtual Production Use** 104
Towa Sakurai, Takahiro Yakoh

**Development and Evaluation of a Barrier-Free Tourism Support System Using AIoT Avatars** 120
Yuki Kida, Hiroko Inokuma, Takahiro Yakoh, Tetsuro Ogi

### Design Science and Timeaxis Design

**Effect of Unit Cell Size on Interface Pressure of 3D-Printed Gyroid Foam for Sitting Comfort** 130
Minh Tien Nguyen, Akinari Hirao

**Detecting Physical Fatigue and Drowsiness During Long-Term Truck Driving Using Center of Pressure Dynamics** 144
Akinari Hirao, Kai Suzuki

### In Memory of Prof. Dr. S. Turgut Tümer

**Effect of IMU Mounting Location on Vibration Behavior in Fixed-Wing UAV Fuselages: A Modal and Harmonic Finite Element Analysis** 154
Semih Nazlıgül, Alp Baykut, Hasan Çakır, Mustafa Bakkal

**Effect of Y2O3 Content on the Compressive and Hardness Behaviour of AZ91 Magnesium Matrix Composites Fabricated by Powder Metallurgy** 172
Mert İlbeyli, Türker Türkoğlu, Sare Çelik

**Investigation of 3-D Printing Potential of Bio-Inspired Cold Plates for Electric Vehicle Battery Thermal Management** 178
Fatih Furkan Beköz, Yusuf Ata Ertürk, Tuba Okutucu-Özyurt

# English General Sessions

### Manufacturing Process, Quality, Surface Engineering and Environmental Control

**Prediction of Tenacity and Elongation in Filament Drawing Process Using Motor Moment Based Mechanical Transformation** 188
Uscan Uskaner, Zeynep Parlar

### Structural Mechanics, Constitutive Modelling and Fracture Analysis

**One-Way Fluid-Structure Interaction (FSI) Analysis of a GFRP Wind Turbine Blade Under Different Wind Velocities** 202
Samet Akar, Ferit Sait, İclal Burcu Erciyas

### Robotics

**Development of Model Predictive Controlled 12-DoF Bipedal Robot** 216
Ozan Ecevit, Giray Cevher Eser, Bahram Lotfi, Hakkı Özgür Ünver

### Mechanisms, Machine Components and Mechanical Performance

**Friction Torque Loss in Relation to Flex Thickness on Rotary Shaft Seals** 236
Beliğ Tarık Otsay, Mustafa Cemal Çakır

**Inverse Position Analysis of a 4-RPR Planar Parallel Robot with Configurable Quadrilateral Platform** 244
İrem Beyza Ekici, Mustafa Özdemir

### Machining Mechanics, Composite Drilling and Cutting-Force Modelling

**Exploratory Milling of Muonionalusta Iron Meteorite Using CrN-, AlTiN-, and TiAlN-Coated Solid-Carbide End Mills: Preliminary Cutting-Force Analysis** 254
Nevzat Bircan Buğdaycı, Hasan Sinan Bank

### Industrial Machine Design, Automation and Human-Centred Manufacturing

**Development of a Process-Controlled Calendering Machine** 264
M. Çağrı Özkader, Barış Çetin, Öncü Akyıldız

# Turkish Special Sessions

### Lifecycle Analysis of Modern Defense Systems

**Yüksek Güvenilirlik Gerektiren Savunma Sanayii İmalat Süreçlerinde Yapay Zekâ Destekli Üretim ve Kalite Güvence Yaklaşımı** 270
Mehmet Can Baytekin, Beyzanur Zeybek

# Turkish General Sessions

## Savunma ve Enerji Sistemlerinde Yapısal Tasarım ve Analiz

**Kodlanmış Metayüzey Yöntemiyle Radar Kesit Alanı (RKA) Azaltma ve Analizi** **284**
Khangul Abdullayeva, Yavuz Kayıhan, Mete Kayıhan

## Makine, Mekanizma ve Robotik Sistem Tasarımı

**Sac İşleme Makineleri İçin Tam Otomatik Döndürme Sistemi** **300**
Emre Akagündüz, Mert Yalçıntaş

**SCARA Robot Tabanlı Frezeleme Sisteminin Tasarımı ve Geliştirilmesi** **316**
Sıla Betül Kirzuk, Furkan Durmaz, Osman Atsan, Kerem Yağız Karakaş, Yunus Emre Nehri, Ali Oral

# Method for Creative Machine Design

**Tamotsu MURAKAMI**, *murakami@mech.t.u-tokyo.ac.jp* The University of Tokyo, 113-8656, Tokyo, Japan

## ABSTRACT

In recent years, creative thinking and ability to generate new ideas for design have become increasingly important for creating artifacts that solve complex problems in people's lives, society, industry, economy, and environment, and deliver new value. Ideation is a complex cognitive activity involving a combination of conscious and unconscious processes, as well as logic and intuition. This keynote examines methods for creative mechanical design by drawing on insights from various fields, including design engineering, cognitive psychology, and cognitive neuroscience by exemplifying creative mechanical designs.

**Keywords:** Ideation, Ideation potential, Idea elicitation, Creativity

## 1. INTRODUCTION

Creativity is defined as, for example, “the ability to come up with ideas or artefacts that are new, surprising and valuable” [Boden, 2004]. Ideation for creative machine design is a complex thought process that combines various elements such as conscious and unconscious thought, logic and intuition, and knowledge related to the problem with seemingly unrelated but actually conducible knowledge. Nature of such ideation is gradually becoming clearer through recent research in various fields such as design engineering, cognitive psychology, and cognitive neuroscience. Based on findings in these fields, this keynote explains methods for creative machine design, using concrete examples.

## 2. NATURE OF IDEATION

1. **Four Steps of Idea Generation Process:** An early study on creative thinking process describes that the generation of ideas consists of four stages: Preparation, Incubation, Illumination, and Verification [Wallas, 2014].

- Preparation: “It includes the whole process of intellectual education.”, “The educated man has also acquired, by the effort of observation and memorizing, a body of remembered facts and words which gives him a wider range in the final moment of association” (p.39).

- Incubation: “during Incubation we do not voluntarily or consciously think on a particular problem”, “a series of unconscious and involuntary mental events may take place during that period” (p.41).

- Illumination: “the appearance of a new idea as instantaneous and unexpected. If we so define the Illumination stage as to restrict it to this instantaneous 'flash,' it is obvious that we cannot influence it by a direct effort of will” (p.46).

- Verification: “It is normally fully conscious, and men have worked out much the same series of mathematical and logical rules for controlling Verification by conscious effort as those which are used in the control of Preparation” (p.41).

2. **Correspondence between Empirical Rules and Cognitive Neuroscience:** The author noted a correspondence between the five-stage empirical rules for idea generation [Young, 2003], based on [Wallas, 2014], and recent findings in cognitive neuroscience [Goldberg, 2018] (Table 1).

Of these five stages, the first, second (Preparation), and fifth (Verification) are considered conscious processes, whereas the third (Incubation) and fourth (Illumination), the most critical stages for generating ideas, are considered unconscious. This explains why there is currently no direct method guaranteed to produce excellent ideas; consequently, the ideation method discussed in this keynote is essentially an indirect, consciously actionable activity to increase the likelihood that superior ideas will emerge through unconscious processes.

## 3. MODEL OF IDEATION ABILITY

The first step in Table 1 says that new ideas are not created in a vacuum, but they arise as novel configurations of the elements of previously formed ideas, solutions, and art forms [Goldberg, 2018].

For example, the inventor of a snap-off blade cutter knife (Figure 1) came up with the idea by knowing:

- that shoemakers on the street in the past used shards of glass to shave the soles of their shoes instead of blades and broke them with a stone for a new edge each time they became blunt, and

- the chocolate bars that American soldiers used to have in Japan after WWII [OLFA, 2026].

Table 1. Correspondence between Empirical Rules and Cognitive Neuroscience.

| Empirical Rules [Young, 2003] | Cognitive Neuroscience [Goldberg, 2018] |
|---|---|
| Step 1: "the gathering of raw materials - both the materials of your immediate problem and the materials which come from a constant enrichment of your store of general knowledge" (p.40). | "The ability to combine the elements of old ideas into new configurations is essential for generating new ideas and new concepts" (p.47), "this is how many important scientific ideas, technological inventions, and artistic creations have been born. As we already know, new ideas, solutions, and art forms are not created in a vacuum. To a very large extent, they arise as novel configurations of the elements of previously formed ideas, solutions, and art forms. The prefrontal cortex is uniquely equipped to configure and assemble bits of previously acquired knowledge and ideas in novel ways" (p.48). |
| Step 2: "the working over of these materials in your mind" (p.40), "after a while you will reach the hopeless stage. Everything is a jumble in your mind, with no clear insight anywhere" (p.31). | "The brain is in a state of task-specific hyperfrontality. The activated regions are likely to be quite disparate within the cortex; they are not integrated into a single strongly interconnected network" (p.133). |
| Step 3: "you make absolutely no effort of a direct nature. You drop the whole subject and put the problem out of your mind as completely as you can" (p.32). | "these disparate regions activated during the hyperfrontal state will constrain the 'mental wandering' that will come later. We will call the disparate locations activated within the network during the 'hyperfrontal' state neural anchoring points. When the hypofrontal mental wandering steps in, it almost literally 'fills the gaps.' It finds pathways between the initially disjointed neural anchoring points, which had been formed earlier during the "hyperfrontal" states" (p.133). |
| Step 4: "Out of nowhere the Idea will appear. It will come to you when you are least expecting it" (p.34). | "The cortical regions along these paths become integrated with the anchoring points, which were tagged earlier during the hyperfrontal state into a single interconnected network, which, with any luck, embodies the desired solution for a scientific puzzle or an artistic yearning" (p.133). |
| Step 5: "the final shaping and development of the idea to practical usefulness" (p.40). | - |
| "the important thing is to recognize their relationship and to grasp the fact that the mind follows these five steps in definite order - that by no possibility can one of them be taken before the preceding one is completed, if an idea is to be produced" (p.20). | "A creative process usually begins with a conscious idea of what needs to be accomplished, however vague and imprecise", "an innovative idea usually does not occur to someone who has never pondered the subject matter before; even when the subjective experience is one of the idea 'appearing out of nowhere,' it occurs to a prepared mind" (p.133), "in order for the mental wandering to be successful in finding the solution, it has to have been directed, and for chat to happen, the problem had to be tackled first in a deliberate "hyperfrontal" state" (p.134). |

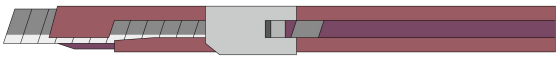


Figure 1. Snap-off Blade Cutter Knife. [OLFA, 2026]

The author models such idea generation process using a hypothetical conceptual space (Figure 2). Information, knowledge, and experience are stored as memories (depicted by solid circles in the figure). New ideas (depicted by hollow circle, diamond and triangle) emerge through conscious or unconscious conceptual manipulations such as recall, transformation, and combination (depicted by arrows) to the original memories. Consequently, ideation ability requires both richness of information, knowledge and experience to serve as raw material (the author defines it as “ideation potential”) and the conscious and unconscious abilities to perform these conceptual manipulations (the author defines it as “idea elicitation ability”) (Figure 3).

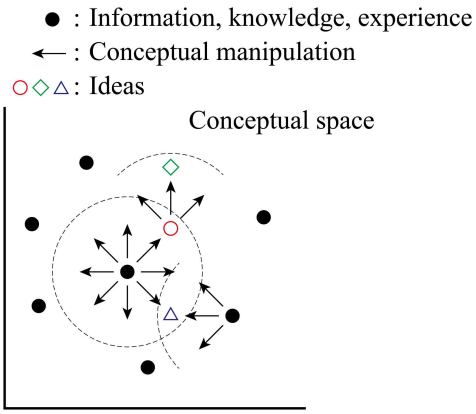



Figure 2. Materials for Ideation and Idea Emergence.

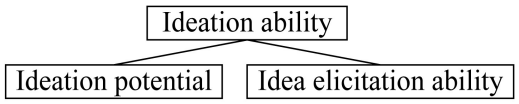



Figure 3. Ideation Potential and Idea Elicitation Ability as Elements of Ideation Ability.

## 4. ACTIVITIES IN DESIGN PROCESS

The author models design activities as shown in Figure 4. First, designers observe and understand people's lives and society to identify explicit or latent problems and needs. Next, they conceive, plan, and realize products to address these issues. The resulting products then deliver value to people's lives and society as user experience and functionality. Educational institutions, such as universities, cultivate future designers by fostering knowledge, critical thinking, and creativity.

When considering the factors behind excellent design within this framework, engineers might first point to the technologies equipped in products or to fabricate them. However, Walkman [Shinagawa, 2019], the world's first portable stereo music player, exemplifies excellence not in technology itself, but in the problem finding: the desire to take music with one outside.

Similarly, a bookend designed to tilt books in a convenient direction to prevent them from falling the wrong way (Figure 5) [MoMA, 2026] represents an example of an excellent problem solving, rather than problem finding or manufacturing. Thus, the factors for excellent design can be found not only in technology but also in each of the activities illustrated in Figure 4.

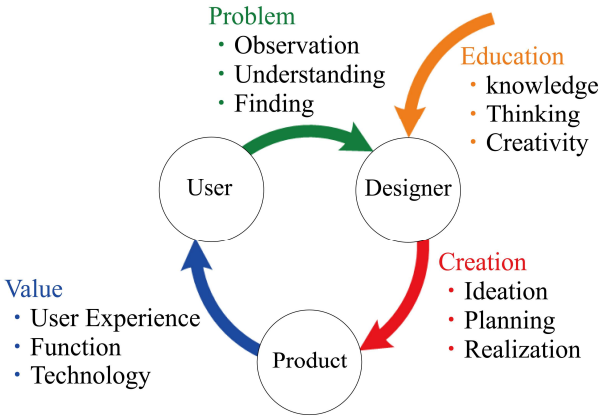



Figure 4. Activities in Design Process (Shaped as the Letter “d” for “Design”).

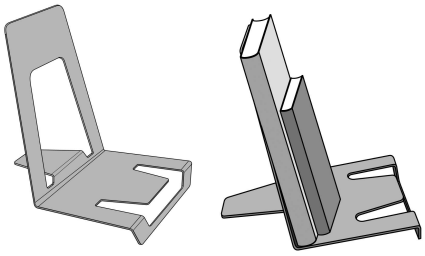


Figure 5. Bookend that Tilts Books in Advance [Bundoki, 2026].

The thought in such a design process is the combination of logic and intuition, as noted by Brooks: “Systematic design excluding intuition yields pedestrian follow-ons and knockoffs; intuitive design without system yields flawed fancies. How to weld intuition and systematic approach?” [Brooks, 2010] (p.ix). Therefore, the author believes that a methodology for creative mechanical design should not rely solely on logic but should also leave room for intuition.

As approaches to generating ideas for such creative mechanical design, the following sections introduce “Methods for Idea Elicitation” and an “Education Trial for Ideation Potential”.

## 5. METHODS FOR IDEA ELICITATION

As mentioned in 2.2, methods for idea elicitation are consciously actionable activity to increase the likelihood that superior ideas will emerge through unconscious processes. Among such methods, here the author describes technical-design-oriented methods rather than general methods such as analogy [de Bono, 2016] (pp. 147–153), brainstorming [Osborn, 2011] (pp. 297–308), the KJ method [Scupin, 1997], and Mind Mapping [Buzan, 2005].

### 1. **Managing Constraints for Ideation**

By identifying the necessary constraints regarding the problem at hand, one can accurately narrow the solution search space and avoid wasted mental effort. Conversely, by correctly

eliminating unnecessary constraints, one can prevent the effective search space from being unduly restricted, thereby increasing the likelihood of arriving at an excellent solution.

It has been noted that constraints fall into the following categories [Brooks, 2010] (p. 129).

Real constraints: Constraints that are generally applicable (e.g., a perpetual motion machine is theoretically impossible) or appropriate for the design problem.

Obsolete once-real constraints: For example, “welding aluminum is difficult” used to be true; nowadays, however, while it remains more difficult than welding steel, it is indeed possible.

Constraints misperceived as real: Aerodynamic theory for airplane design tended to frown on placing anything on top of the main wings, mainly because it increases aerodynamic drag. In a design of Honda Jet, however, they thought some way could be found to optimally position the engines on the main wings while still managing to reduce aerodynamic drag. Such a new mindset defied conventional wisdom, which led to success of Honda Jet [HondaJet, 2026].

Intentional artificial constraints: The design of wall-mounted CD player (Figure 6, right) was inspired by wall-mounted ventilation fans (Figure 6, left) which are typical in Japan. It features an interface where the power cord is used as a pull-switch to control CD playback and stopping, much like the pull-cord switches on those fans. However, the proposal to use the power cord as a pull-switch was initially rejected by several Japanese electronics manufacturers [Fukasawa, 2016]. This was because pulling on a power cord is generally considered a practice to be avoided with electrical appliances. Although that rule applies to strong force used to yank a plug from its socket, the cord can be designed to withstand the lighter force required to operate a pull-switch for playback control. In other words, the prohibition against pulling power cords is an intentional, artificial constraint. Relaxing it enabled an interface that is both intuitively understandable and engaging.

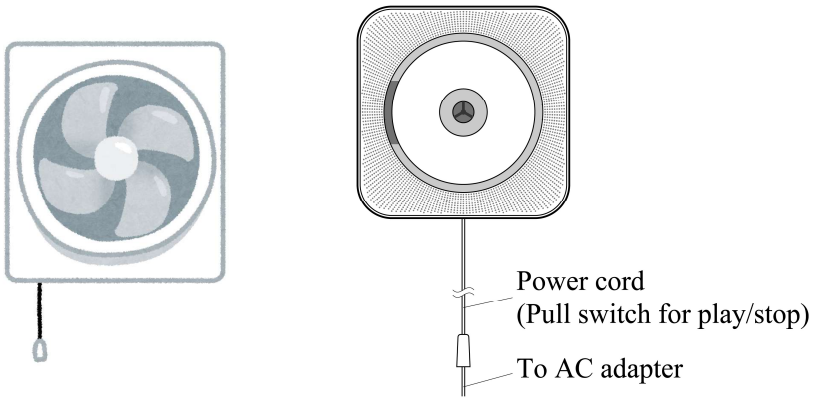



Figure 6. Wall Mounted CD Player [Fukasawa, 1999]

## 2. **Interaction among Function, Shape, Material and Process**

Design ideas can be developed by considering interaction among function, shape, material, and process (Figure 7) [Ashby, 2017]. For example, simply switching the process to 3D printing with the standard pliers (Figure 8) makes it difficult to realize the tool - specifically regarding the fabrication of the smooth-surfaced pin joint that serves as the movable pivot. However, if the material is changed to a flexible plastic suitable for 3D printing and the shape is modified to combine high-rigidity sections (using a dense lattice) with movable sections (using a sparse lattice), the shape, material, and process become compatible, which lead to achieving the functionality of pliers as shown in Figure 9 [O'Neal, 2016].

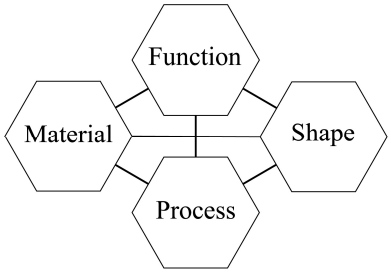



Figure 7. Interaction among Function, Shape, Material and Process [Ashby, 2017].

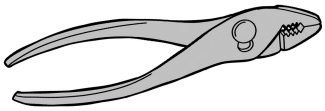


Figure 8. Standard pliers.

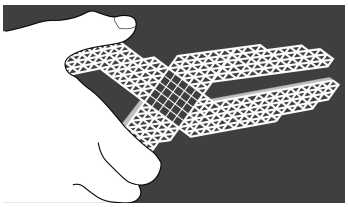
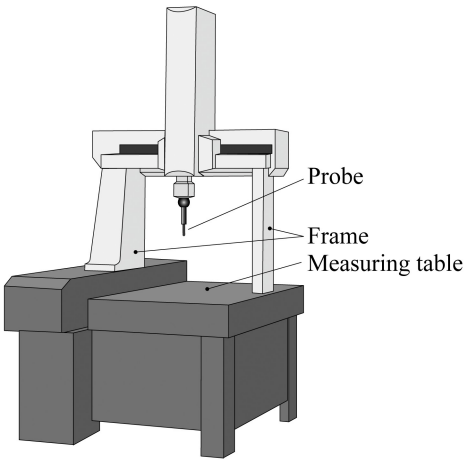
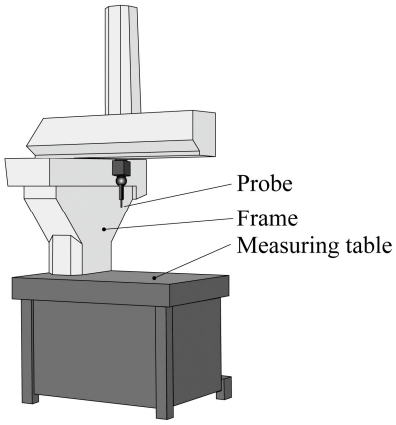


Figure 9. “Pliers” by 3D Printing [O’Neal, 2016].

An actual example of how altering shape can enhance function is found in the structural design of CNC coordinate measuring machine frames. Since deflection in the probe-supporting frame reduces measurement accuracy, these machines typically employ a both-ends-supported structure to minimize deflection (Figure 10, left) [Mitutoyo, 2025], which limits operator access to the measurement table from just the front and rear. In contrast, adopting a high-rigidity cantilever structure (Figure 10, right), while carefully balancing the design to avoid any impression of instability, enables operators to access the measurement table from three directions (front, rear, and right), thereby improving functionality regarding workpiece setup and measurement efficiency [Mitutoyo, 2019].




Both-ends-supported Structure [Mitutoyo, 2025].




High-rigidity Cantilever Structure [Mitutoyo, 2019].

Figure 10. Designs of CNC Coordinate Measuring Machine.

Generally, automobile body shapes are symmetrical, and door operation is also symmetrical. Consequently, the right and left doors are symmetrical (mirror images) to one another, which leads to improving efficiency in design by CAD and analysis by CAE. However, this symmetry means that the right and left doors are physically different in shape. In contrast, if the design utilizes physically identical parts for both the left and right doors, the vehicle body remains fundamentally symmetrical (Figure 11, left), but the door operation ceases to be symmetrical (Figure 11, right) [Citroën, 2026]. By modifying door shapes in this manner to achieve parts commonality as a cost-reduction measure, it becomes possible to offer electric mobility functionality at a lower price.

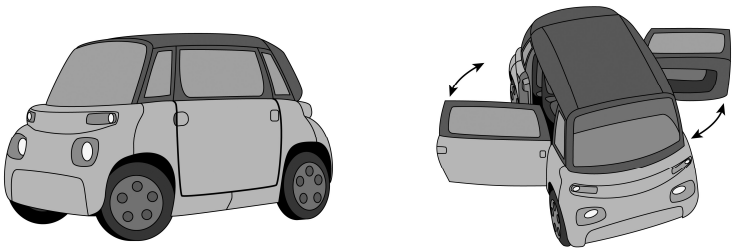


Figure 11. Standardization of Left and Right Door Units [Citroën, 2026].

The following are examples of excellent designs that utilize materials not typically or standardly used for such applications.

- Non-metallic wheelchair: With conventional metal wheelchairs, users must get off, walk with assistance through the metal detector at airport security checkpoints, and then get back into the chair. Designing a wheelchair made entirely of non-metallic materials such as wood or resin resolves this issue and facilitates barrier-free accessibility [JAL, 2011].

- Wooden satellites: Satellite bodies are typically constructed from lightweight, strong metals such as aluminum or titanium. Small satellites deployed in low Earth orbit must be disposed of by re-entering the atmosphere and burning up after their missions conclude, ensuring they do not remain as space debris. When aluminum bodies burn, however, they generate highly stable alumina particles that are thought to linger in the stratosphere for years. Replacing aluminum with wood as satellite material offers a potential solution to this problem. While wood has historically been a prime example of a lightweight, strong material, it was superseded by aluminum alloys in aircraft construction due to issues such as biological degradation and flammability. In the vacuum of space, however, the absence of air, water, and bacteria renders biological degradation and flammability non-issues. Against this backdrop, research and development are currently underway to launch wooden satellites [Murata, 2024] [NASA, 2025].

## 3. **Theory of Inventive Problem Solving (TRIZ)**

TRIZ is an acronym derived from the Russian phrase “Teoriya Resheniya Izobretatelskikh Zadatch (Теория решения изобретательских задач)” (Theory of Inventive Problem Solving).

The “Inventive Principles”, one component of the TRIZ framework, aims to generate creative problem-solving ideas by using a set of 40 principles to guide the thought process [Mann, 2007] (pp.270-289).

An example that can be explained using TRIZ Inventive Principles, though the idea itself was not originally derived from TRIZ, is the design of a robot hand system for accurately portioning and plating specific amounts of sticky, hard-to-handle food items (such as cooked noodles or prepared side dishes) into trays [ISHIDA, 2022] [Takahashi, et al., 2024]. Accurately measuring such ingredients with a single grasp of a robot hand is difficult. Another possible approach is to combine multiple hands, each having relatively low precision and some degree of variability in its grasp (Inventive Principle 16: Partial or Excessive Actions), into a single system (Inventive Principle 5: Merging). Sixteen hands (Figure 12, left) simultaneously grasp ingredients from a container, and the mass held by each is measured. Since the results show variation (Figure 12, right), all possible combinations of masses are calculated, and only those combinations falling within a preset lower and upper limit are selected. In the example shown in Figure 12 (right), three combinations fall within the range of 200g (lower limit) to 202g (upper limit):

- Release hands A, D, and F: 30.6g + 89.8g + 80.5g = 200.9g
- Release hands E, G, and J: 65.9g + 70.9g + 64.5g = 201.3g
- Release hands I, M, and N: 59.7g + 68.3g + 73.5g = 201.5g

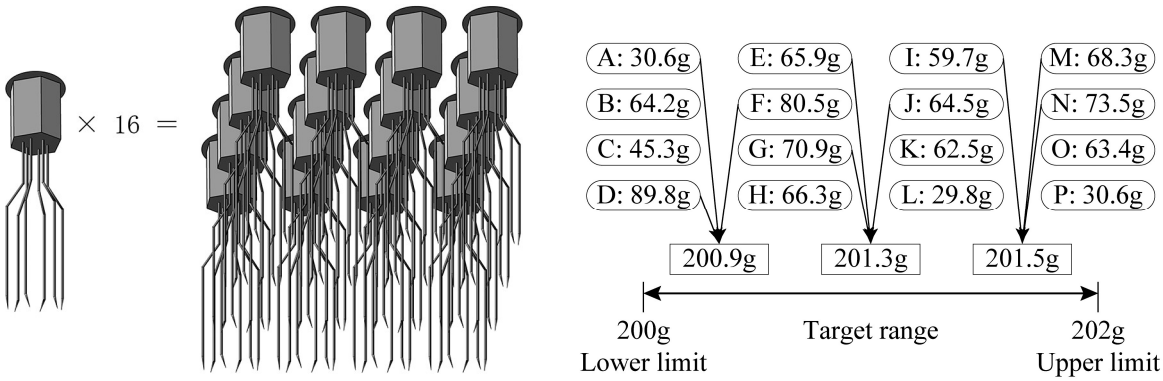
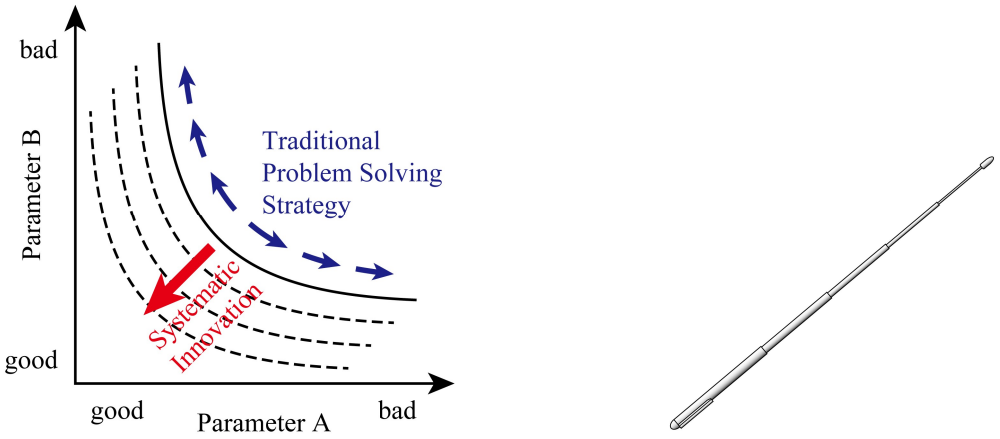



Figure 12. Gripping Combination Weighing [ISHIDA, 2022] [Takahashi, et al., 2024]

Another TRIZ method is the Contradiction Matrix, designed to resolve conflicts between two distinct characteristics such as "high strength" versus "low weight" [Mann, 2014] (p.464). TRIZ defines 39 specific features and constructs a 39 x 39 matrix representing every possible combination of a feature to be improved and a conflicting feature. Each cell where these features intersect lists the numbers of the "40 Inventive Principles" that have proven most successful for solving the specific type of contradiction.

Generally, a conflict between two distinct features can be represented by a graph as shown in Figure 13, left [Mann, 2007] (p.184). Traditional design strategies involve finding an acceptable pair of values for these conflicting features somewhere along the line plotted on the graph. In contrast, the TRIZ approach to conflict resolution aims to shift this line toward the graph's origin. For example, consider the design of a "portable pointer": if we treat "Length of stationary object" (long length is good for use) as the feature to improve and "Volume of moving object" (small volume is good for portability) as the feature that worsens, we can look at the intersecting cell in the matrix. From the listed principles such as "Inventive Principle 7: Nesting" one can conceive a "portable pointer" (Figure 13, right) that utilizes a telescoping structure.

As a related study, author has proposed a method for systematically handling the Contradiction Matrix by defining features based on SI physical quantity units, rather than limiting them to the standard set of 39 [Murakami, 2019].




Trade-off Elimination in TRIZ [Mann, 2007] (p.184). Telescopic Pointer.

Figure 13. Resolution of a Technical Contradiction between Two Features.

### 4. **Design Support Using Generative AI**

In recent years, there has been extensive research into design support utilizing generative AI, such as Large Language Models (LLMs). In design contexts where safety, reliability, and ethical considerations are important, accepting solutions generated by LLMs, whose process contains “black boxes”, without fully understanding them poses significant risks. One approach to addressing this issue is the use of Explainable AI (XAI) [Ortigossa et al., 2024], which introduces explainability into the AI's solution-generation process. The author conducted a study comparing outcomes between using an LLM alone and using an LLM supplemented by an XAI approach, specifically within the context of supporting divergent and convergent thinking during the conceptual design phase. As a result, the XAI approach significantly enhanced the objective originality and subjective credibility of the design solutions, whereas no differences regarding metrics for objective usefulness and feasibility were observed [Velasco Medina and Murakami, 2026].

## 6. EDUCATION TRIAL FOR IDEATION POTENTIAL

The author hypothesizes that the variety and volume of information, knowledge, and experience serving as raw material for ideation are linked to ideation potential (Section 3). Based on this hypothesis, the author has been piloting an educational approach aimed at enhancing ideation potential. In this course, students collect and present examples of excellent designs, problem-solving methods, intriguing artifacts, and biological phenomena. Through this process, participants accumulate a vast array of ideation materials, not naturally through everyday life but artificially as "supplements" for the mind. Since knowledge from fields

unrelated to the problem at hand often sparks ideas for excellent designs, students are not required to limit their examples to their own areas of specialization. This is essentially a design-oriented version of the practice found in the arts, where listening to a great deal of music is essential for creating good music, and viewing many paintings is necessary for producing good art.

Each year, the students (approximately 30, primarily first-year master's students) present new examples, distinct from those previously shared in the course web page, and engage in Q&A sessions, thereby sharing knowledge and efficiently expanding both the variety and volume of their knowledge base. To verify that a chosen example has not already been presented, students must review the archive of past examples (totaling 657 cases from the 2012–2025 academic years), which leads to their knowledge acquisition. Examples include the following:

- Bactericidal effect of the microstructure on cicada wings: The surfaces of cicada wings feature arrays of nanoscale protrusions that exert an antibacterial effect, killing bacteria through physical contact rather than chemical action [Ivanova, et al., 2012].

- Silicone-based bicycle gear crank: A battery-free assist gear system that achieves efficient, smooth rotation. It compresses internal silicone using the force of the pedal stroke and converts the resulting rebound into propulsive force for the opposite leg as it begins its own stroke [Cycle Olympic, 2023].

- Cat eyes that see well in the dark: As nocturnal animals, cats possess a reflective layer known as the tapetum lucidum behind the retina. This layer reflects incoming light back onto the retina, stimulating the retinal nerves twice, once upon entry and again upon reflection, thereby enhancing sensitivity. This mechanism is also the reason why cats' eyes appear to glow in the dark [Cat-World, 2023].

- Color image sensor utilizing diffraction for color separation: Unlike sensors that separate light through the selective absorption of wavelengths via color filters (resulting in 30‑50% transmittance), this sensor separates colors using diffraction via a deflector (achieving 100% transmittance). By avoiding the waste of light energy, it functions as a high-sensitivity color image sensor [Nishiwaki et al., 2013].

## 7. CONCLUSION

In this keynote, first the nature of ideation was examined by drawing on insights from various fields, including design engineering, cognitive psychology, and cognitive neuroscience. Then ideation ability to come up with creative mechanical design was modeled with two elements: ideation potential and idea elicitation ability. As methods that can be practiced consciously for

creative mechanical design, methods to support idea elicitation ability and education trial to increase ideation potential were reported.

## REFERENCES

1. **Boden, M. A., (2004),** The Creative Mind - Myths and Mechanisms, Second Edition, Routledge, New York, USA.

2. **Wallas, G., (2014),** The Art of Thought, Solis Press, Kent, England (First published in 1926).

3. **Young, J. W., (2003),** A Technique for Producing Ideas, McGraw-Hill Companies, New York, USA.

4. **Goldberg, E., (2018),** Creativity: The Human Brain in the Age of Innovation, Oxford University Press, New York, USA.

5. **OLFA, (2026),** The Birth of the Snap-off Blade Cutter Knife (https://www.olfa.co.jp/en/birth_of_olfa_cutter.html) (2026-06-24 access).

6. **Shinagawa, I., (2019),** Walkman Story: The Early Years of the Iconic Personal Cassette Player (https://www.nippon.com/en/japan-topics/g00726/) (2026-07-22 access).

7. **Bundoki.com, (2026),** MoMA Interlock Bookstand (https://www.bundoki.com/?pid=52302175) (2026-06-22 access).

8. **Brooks, F. P., (2010),** The Design of Design: Essays from a Computer Scientist, Addison-Wesley Professional, Boston, USA.

9. **de Bono, E., (2016),** Lateral Thinking: A Textbook of Creativity, Penguin Books, UK.

10. **Osborn, A. F., (2011),** Applied Imagination – Principles and Procedures of Creative Writing, Iyer Press, USA.

11. **Scupin, R., (1997),** “The KJ Method: A Technique for Analyzing Data Derived from Japanese Ethnology”, Human Organization, Vol. 56, No. 2, pp.233-237.

12. **Buzan, T. and Buzan, B. (auths.), Kanda, M. (trans.), (2005),** The Mind Map Book, Diamond, Inc., Tokyo, Japan (Japanese translation).

13. **HondaJet, (2026),** Unique Technologies and Products (https://global.honda/en/about/history-digest/75years-history/chapter3/section4_1/) (2026-06-29 access).

14. **Naoto Fukasawa Design, (1999),** Wall mounted CD Player (https://naotofukasawa.com/projects/540/) (2026-06-22 access).

15. **Fukasawa, N., (2016),** Before Thinking About Design (Part 2) (in Japanese) (https://www.designstoriesinc.com/special/tsuji-interview_naoto_fukasawa2/) (2026-06-29 access).

16. **Ashby, M. F., (2017),** Materials Selection in Mechanical Design, Fifth Edition, Butterworth-Heinemann, Oxford, UK, p.10.

17. **O'Neal, B., (2016),** Hasso-Plattner Institute Researchers Create Metamaterial Door Latch as Example of 3D Printing Versatility, 3DPrint.com, (https://3dprint.com/153102/hasso-plattner-institute-latch/) (2026-7-24 access).

18. **Mitutoyo, (2025),** CNC Coordinate Measuring Machine CRYSTA-Apex V PLUS Series (https://www2.mitutoyo.co.jp/eng/support/service/catalog/01/E16036.pdf) (2026-06-22 access).

19. **Mitutoyo, (2019),** CNC Coordinate Measuring Machine MiSTAR 555 (https://www.g-mark.org/en/gallery/winners/9e0d23df-803d-11ed-af7e-0242ac130002?years=2019) (2026-06-21 access).

20. **Citroën, (2026),** Citroën Ami 100% Electric Quadricycle (https://www.citroen.co.uk/ami) (2026-06-18 access).

21. **Japan Airlines, (2011),** Bamboo Wheelchairs (https://www.g-mark.org/en/gallery/winners/9d782556-803d-11ed-862b-0242ac130002?years=2011) (2026-07-25 access).

22. **Murata, K., (2024),** “Use of Wood in Space - The Impact of Outer Space on Wood”, Japan Technical Association of the Pulp and Paper Industry Journal, Vol. 78, No. 11, pp.930-933 (in Japanese).

23. **NASA, (2025),** JAXA’s First Wooden Satellite Deploys from Space Station (https://www.nasa.gov/image-article/jaxas-first-wooden-satellite-deploys-from-space-station/) (2026-07-25 access).

24. **ISHIDA, (2022),** Gripper Combination Weigher GCW-V (https://www.g-mark.org/en/gallery/winners/12344) (2026-06-25 access).

25. **Takahashi, A., Maeda, S., Naka, R., Tachikawa, S., Hojo, M. and Endo, G., (2024),** "Development of Gripping Combination Weighing Machine GCW-V," Journal of the Robotics Society of Japan, Vol. 42, No. 1, pp. 40-41 (in Japanese).

26. **Mann, D., (2007),** Hands-On Systematic Innovation for Business and Management, 2nd Edition, IFR Press, Clevedon, UK.

27. **Mann, D., (2014),** Hands-On Systematic Innovation, CrePS Institute, Chiba, Japan (Japanese translation).

28. **Murakami, T., (2019),** “Knowledge Management for Problem Solving Using Semistructured Contradiction Matrix Based on Physical Quantity Description”, 22nd International Conference on Engineering Design (ICED 2019), pp.1983-1992, doi: 10.1017/dsi.2019.204.

29. **Ortigossa, E. S., Gonçalves, T., and Nonato, L. G., (2024),** “EXplainable Artificial Intelligence (XAI) – From Theory to Methods and Applications”, IEEE Access, Vol. 12, pp.80799-80846, doi: 10.1109/ACCESS.2024.3409843.

30. **Velasco Medina, I. F. and Murakami, T., (2026),** “Explainable AI in Conceptual Design: An LLM-Powered Framework to Enhance Originality and Credibility”, Journal of Mechanical Design, pp.1-12, doi: 10.1115/1.4071544.

31. **Ivanova, E. P., Hasan, J., Webb, H. K., Truong, V. K., Watson, G. S., Watson, J. A., Baulin, V. A., Pogodin, S., Wang, J. Y., Tobin, M. J., Löbbe, C. and Crawford, R. J., (2012),** “Natural Bactericidal Surfaces: Mechanical Rupture of Pseudomonas aeruginosa Cells by Cicada Wings”, Small, Vol.8, No.16, pp 2489-2494, doi: 10.1002/smll.201200528.

32. **Cycle Olympic, (2023),** Free Power (https://www.olympic-corp.co.jp/cycle/freepower/en) (2026-07-25 access).

33. **Cat-World, (2023),** Cat Eyes: Anatomy, Function and Vision (https://cat-world.com/cats-eyes/) (2026-07-25 access).

34. **Nishiwaki, S., Nakamura, T., Hiramoto, M., Fujii, T. and Suzuki, (2013),** “Efficient Colour Splitters for High-pixel-density Image Sensors”, Nature Photonics, Vol.7, No.3, pp 240-246, doi: 10.1038/NPHOTON.2012.345.

# AI-BASED INTERPRETATION OF TECHNICAL DRAWINGS FOR VARIANT-SPECIFIC INFORMATION PROVISION IN BROWNFIELD ASSEMBLY

**Max-Heiner BIRK**, *max-heiner.birk@bosch.com* Furtwangen University, Robert-Gerwig-Platz 1, 78120, Furtwangen and Bosch Rexroth AG, An den Kelterwiesen 14, 72160 Horb am Neckar, Germany

**Andreas GAUS**, *andreas.gaus@bosch.com* Bosch Rexroth AG, An den Kelterwiesen 14, 72160 Horb am Neckar, Germany

**Prof. Dr. Christoph REICH**, *christoph.reich@hs-furtwangen.de* Furtwangen University, Robert-Gerwig-Platz 1, 78120, Furtwangen, Germany

**Prof. Dr.-Ing. Michael ENGLER**, *michael.engler@hs-furtwangen.de* Furtwangen University, Robert-Gerwig-Platz 1, 78120, Furtwangen, Germany

## ABSTRACT

In variant-rich brownfield assembly, technical drawings often contain essential target information for variant interpretation, but their unstructured PDF format prevents direct integration into automated workflows. This paper presents a modular AI-based pipeline for extracting machine-readable target information from such drawings. The method combines PDF rendering, title-block masking, YOLOv8-based detection, geometric filtering, left-right assignment and rule-based size classification. It was evaluated on 63 technical drawings from hydraulic component production. Within the investigated dataset, all drawings were processed correctly by the final workflow. The results indicate that the approach is suitable as a target-information module for downstream assembly automation.

**Keywords:** Brownfield assembly, technical drawing interpretation, variant-specific information, YOLOv8, assembly automation

## 1. INTRODUCTION

Variant-rich brownfield assembly environments are difficult to automate, even when individual assembly operations are technically feasible. A major reason is that increasing product variety leads to increasing manufacturing complexity in assembly systems, which in turn affects

process stability and operational performance [Hu et al., 2008]. In legacy production settings, this challenge is further intensified by historically grown system structures, heterogeneous information sources and the limited availability of directly usable digital product information.

In such environments, important target information is often not available as a directly usable digital data object, but remains distributed across existing documents and engineering records. Brownfield-oriented research therefore emphasizes that methods must be able to work with the source information that is realistically available in existing industrial environments [Sierla et al., 2022]. At the same time, recent manufacturing research highlights the importance of interlinked and machine-readable information flows for consistent downstream planning, execution and decision-making [Abdel-Aty and Negri, 2024]. This is particularly relevant in assembly contexts in which variant-specific process decisions still depend on the manual interpretation of technical drawings instead of structured digital interfaces.

A particularly relevant source of target information in assembly is the technical drawing. In many industrial contexts, drawings still contain essential information about relevant component views, geometric relations and variant-specific characteristics. However, technical drawings belong to the class of complex engineering documents, which typically combine text annotations, symbols and line-based graphical structures. Recent review work shows that the digitization of such documents is challenging and that earlier approaches based mainly on hand-crafted features and heuristics proved difficult to generalize robustly [Jamieson et al., 2024]. In practical brownfield settings, this means that the information required for downstream automation is frequently present, but not yet available in a form that can be processed automatically and reused consistently.

Against this background, the present work addresses the problem of converting technical drawings into machine-readable target information for downstream automation in brownfield assembly. The remainder of the paper is organized as follows. Section 2 summarizes relevant related work, Section 3 introduces the industrial problem and the required target information and presents the proposed method, Section 4 describes the experimental setup, Section 5 reports the results and discusses their implications and Section 6 concludes the paper.

## 2. RELATED WORK

Research relevant to the present work can be grouped into three areas: digitization of technical and engineering documents, deep-learning-based object detection and recent approaches for extracting structured information from engineering drawings.

A first important body of work addresses the general digitization of complex engineering documents. Recent literature emphasizes that engineering drawings and diagrams are

considerably more difficult to process than ordinary document images because they combine text, symbols, geometric primitives and connectivity information in a dense and often layout-dependent form [Jamieson et al., 2024]. The same review also shows that earlier approaches relied heavily on hand-crafted features and heuristics, limiting their robustness and transferability across varying document types and drawing layouts [Jamieson et al., 2024]. This observation is directly relevant for brownfield assembly settings, in which historical drawings often differ in structure, notation and visual organization.

A second relevant research area is object detection. Deep-learning-based object detection has become a widely established approach for jointly localizing and classifying objects in images [Zaidi et al., 2022]. Compared with classical rule-based image analysis, such methods offer greater flexibility when object appearance and layout vary, which is especially important in technical drawing applications. For the present problem, object detection is used as a localization mechanism for identifying the drawing regions that can subsequently be constrained, paired and interpreted through deterministic post-processing. This is consistent with the broader literature, where detection models serve as the basis for subsequent recognition, classification, or decision steps [Zaidi et al., 2022].

More recent studies have started to apply AI-based detection and parsing methods directly to engineering drawings. Ant et al. demonstrate that object detection can be used to recognize and localize parts in engineering drawings, showing the feasibility of AI-supported region interpretation in this document class [Ant et al., 2024]. Zhang et al. address the machine interpretation of raster engineering drawings through graph-based component segmentation, highlighting the importance of separating semantically distinct drawing elements before downstream reasoning [Zhang et al., 2023]. In addition, AI-based information extraction from 2D manufacturing drawings has also been discussed for broader production-related knowledge transfer. For example, Haar et al. describe a methodology for the extraction of information from 2D engineering and manufacturing drawings and explicitly motivate it by the continued industrial prevalence of 2D documents and legacy drawing archives [Haar et al., 2022]. Recent work by Maupou et al. further underlines the relevance of hybrid pipelines for raster mechanical engineering drawings by combining deep-learning-based detection with downstream interpretation steps [Maupou et al., 2024]. Title-block processing has also been identified as a relevant subproblem in engineering drawing organization, particularly for archived legacy documents and metadata-oriented retrieval workflows [Kashevnik et al., 2023]. Agritania and Isnaini further showed that drawing-view and dimension detection can support inspection-sheet generation in a manufacturing setting [Agritania and Isnaini, 2025]. More recently, Khan et al. reported a hybrid vision-language framework that links localized drawing

content to downstream manufacturing decisions, further supporting the relevance of modular drawing-interpretation pipelines for production use [Khan et al., 2026].

## 3. METHOD

The proposed method was designed as a modular Python-based pipeline for converting technical drawings in PDF format into structured target information for downstream assembly-related use. Its objective is not to generate a complete semantic understanding of an engineering drawing, but to identify and interpret those recurring drawing regions that are relevant for a subsequent variant-oriented decision logic. In the investigated use case, the task was to automatically detect two relevant housing views, to assign the detected regions to the left and right sides and subsequently derive a robust relative size interpretation from the final region pair. The method was implemented as a modular workflow combining data preparation, detection, deterministic post-processing and structured result export.

### 3.1 Overall pipeline concept

The proposed method follows a multi-stage workflow that combines document preprocessing, AI-based detection, deterministic post-processing and structured output generation. The sequence was chosen because technical drawings in brownfield environments contain recurring but not perfectly identical visual structures. A purely rule-based solution would be highly sensitive to layout variation, whereas a purely detector-based solution would not provide the deterministic consistency required for stable downstream interpretation.

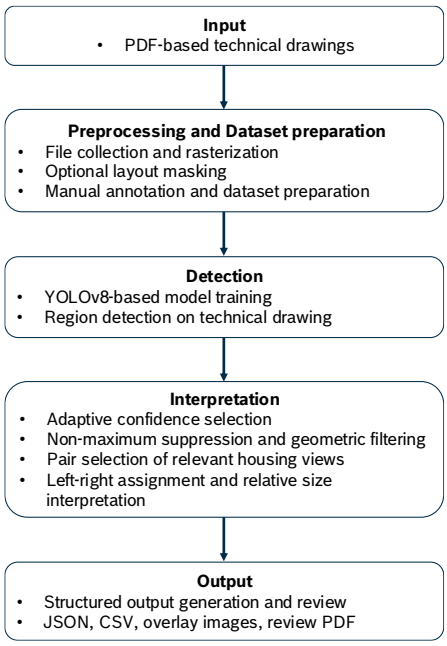



Figure 1. Overview of the proposed pipeline for extracting machine-readable target information from technical drawings.

### 3.2 Data acquisition and rasterization

As outlined in Figure 1, the pipeline starts with input handling and preprocessing. In the investigated implementation, PDF documents were used as the primary input format. Previously generated dataset and output folders were excluded from traversal in order to prevent the unintended re-use of derived files during repeated experiments.

Each PDF was converted into a raster image before further processing. The first page of each document was rendered at 300 DPI using PyMuPDF. This resolution was selected because it preserves fine line structures and relevant geometric contours while remaining computationally manageable for training and inference. The rendered page was then converted into a BGR image representation and if necessary, stripped of an alpha channel before entering the subsequent processing chain. The use of a fixed rasterization setting is important because it establishes a stable visual basis for both annotation and detection and avoids uncontrolled variation caused by inconsistent document rendering.

Before inference, optional masking of non-relevant layout regions was applied in order to suppress title block, tables and revision-related areas that might attract detections without contributing to the relevant drawing interpretation. In the investigated implementation, the rightmost 18 % of the image width and the bottom 22 % of the image height were replaced by white regions.

### 3.3 Dataset generation and annotation

For supervised object detection, a dedicated dataset was created from the drawing collection. As indicated in Figure 1, this stage comprised dataset structuring, manual annotation and validation split generation. The dataset followed the standard Ultralytics format with separate folders for training and validation images and labels, as well as a corresponding dataset configuration file. A single target class, housing, was defined because the method does not aim at generic component parsing, but focuses on one visually recurring drawing object class that is relevant for downstream interpretation.

Manual annotation was carried out using a dedicated graphical labeling interface implemented in Python with Tkinter. Rasterized drawing pages were displayed to the user and rectangular bounding boxes were placed around the relevant drawing regions. The annotated coordinates were then transformed back into the original image coordinate system and stored in normalized YOLO format, that is as relative center coordinates and relative box width and height. A task-specific annotation workflow was chosen because the target class was narrow, visually specific and closely tied to the actual drawing layout, making lightweight annotation more efficient than a more general external toolchain.

To obtain a reproducible validation subset, the dataset was split automatically into training and validation data. A validation fraction of 15 % and a fixed random seed of 42 were used. This ensured a stable train-validation partition while remaining suitable for the comparatively small dataset size used in the study. The experimental basis of the present work comprised 63 technical drawings.

### 3.4 Model training

Figure 1 includes the model-training stage as part of the overall detection workflow. The detection model was trained using Ultralytics YOLO with `yolov8s.pt` as the pretrained initialization. Transfer learning was considered appropriate because the task does not concern general object discovery in natural images, but adaptation to a narrow visual domain characterized by recurring technical drawing views. This choice is consistent with transfer-learning literature in computer vision, which shows that pretrained representations can improve performance in narrower target domains when only limited domain-specific data are available [Li et al., 2020].

The training and augmentation parameters are summarized in Table 1. The configuration was selected to preserve the line-based and orientation-dependent characteristics of technical drawings while allowing limited variation in position, scale and rotation.

Only mild geometric augmentation was applied because moderate variation in scale and layout must be tolerated, whereas arbitrary orientation changes, vertical flipping and color transformations are not meaningful for line-based technical drawings.

Table 1. Model training and augmentation parameters.

| Parameter category | Parameter | Value |
|---|---|---|
| Model | Pretrained initialization | YOLOv8s |
| Training | Input image size | 1280 x 1280 px |
| Training | Maximum epochs | 200 |
| Training | Batch size | 16 |
| Training | Optimizer | SGD |
| Training | Initial learning rate | 0.001 |
| Training | Weight decay | 0.0005 |
| Training | Early-stopping patience | 30 epochs |
| Augmentation | Rotation | ±3.0° |
| Augmentation | Translation | 0.05 |
| Augmentation | Scaling | 0.20 |
| Augmentation | Shear | 0.0 |
| Augmentation | Mosaic | 0.20 |
| Augmentation | Vertical flip | 0.0 |
| Augmentation | HSV augmentation | 0.0 |

YOLOv8s was selected as a pragmatic compromise between detection capability and computational effort, while larger detector variants or two-stage architectures would have increased training and inference complexity. Compared with larger YOLO variants and two-stage detectors such as Faster R-CNN, YOLOv8s was preferred because the investigated application required a lightweight and easily deployable detector rather than maximum benchmark performance. The adaptive confidence strategy was additionally selected because a single fixed threshold did not consistently provide a suitable candidate set across drawings with different visual densities.

### 3.5 Inference and adaptive detection strategy

Figure 2 illustrates the inference stage and the subsequent reduction of raw detector outputs to the final relevant region pair. Instead of relying on a single fixed confidence threshold, the method evaluated a descending sequence of thresholds and selected the first threshold for which the number of raw detections fell within a predefined interval of two to six candidate boxes. In the implemented configuration, the threshold schedule was defined as 0.95, 0.85, 0.75, 0.65, 0.55, 0.45, 0.35, 0.30, 0.25, 0.20, 0.15, 0.12, 0.10, 0.08 and 0.06.

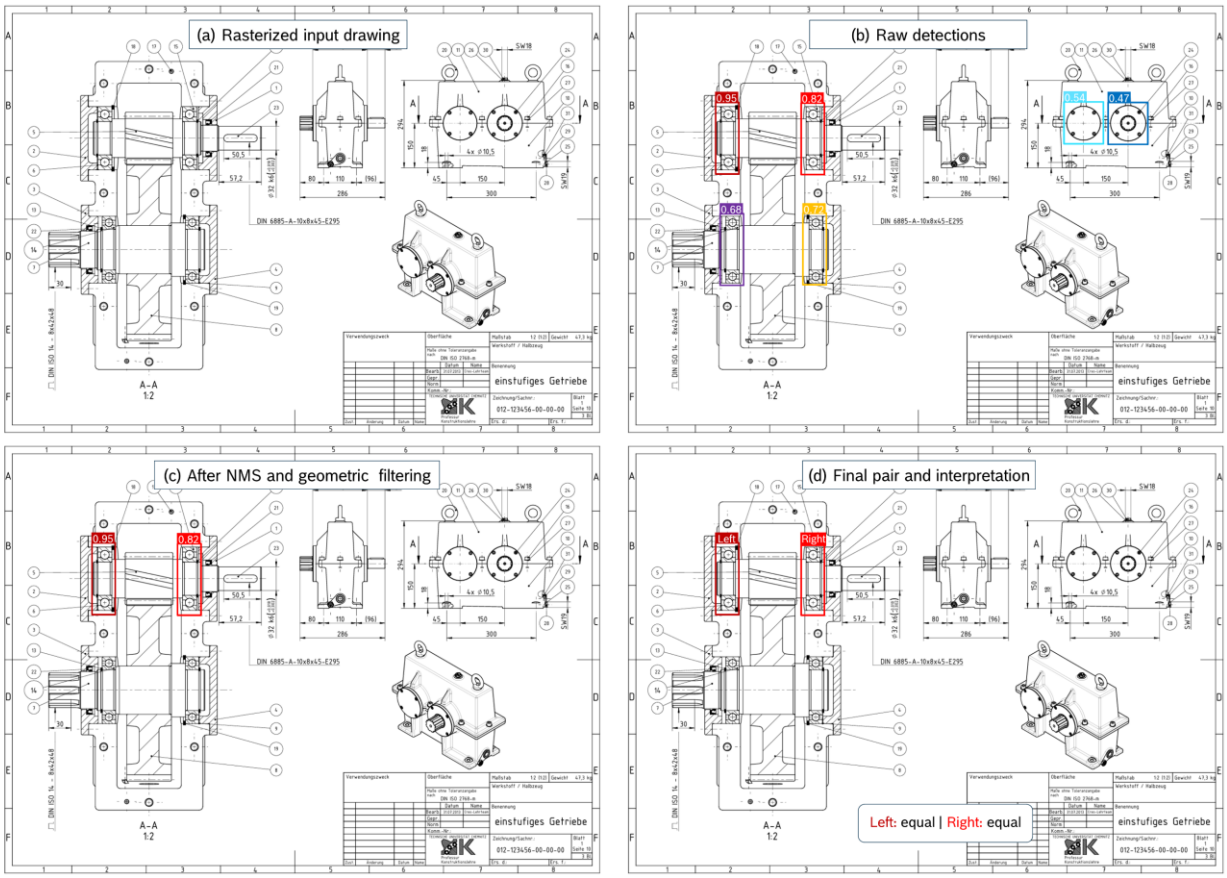



Figure 2. Exemplary technical drawing with added annotations for illustrating the inference and post-processing workflow, adapted from [Leidich, 2016].

The example in Figure 2(b) demonstrates that the detector may initially return several candidate regions with different confidence values. This adaptive strategy was introduced because a fixed threshold would either suppress valid detections in visually difficult drawings or admit too many false candidates in visually dense ones. By selecting the first threshold that yields a plausible number of raw candidates, the method stabilizes the downstream interpretation and provides a suitable starting point for deterministic post-processing.

Compared with a fixed confidence threshold, the adaptive strategy reduces the risk of suppressing valid regions in difficult drawings or retaining excessive candidates in visually dense drawings.

Inference was carried out with a square input size of 1280 x 1280 pixels and an IoU threshold of 0.50. For each accepted threshold, the detector returned bounding boxes and confidence scores for the candidate regions. These raw detections were then transformed into absolute image coordinates and passed to the subsequent post-processing stages. Figure 2(c) illustrates how the candidate set was further reduced by non-maximum suppression and geometric filtering before final pair selection was performed.

The final result of this process is shown in Figure 2(d). After reduction to the most plausible candidate set, the two relevant housing regions remain and can be assigned consistently to the left and right side. The resulting pair then forms the basis for the subsequent rule-based interpretation step.

### 3.6 Non-maximum suppression and geometric filtering

After inference, the raw detector outputs were refined by non-maximum suppression and geometric filtering before pair selection was performed. First, overlapping detections were reduced by non-maximum suppression with an IoU threshold of 0.50. This step was intended to remove redundant candidate boxes referring to the same visual region.

The remaining detections were then filtered geometrically. Candidates were rejected if their relative area was smaller than 0.2 % or larger than 20 % of the image area, or if their aspect ratio fell outside the interval from 0.35 to 3.5. This filtering step served as a geometric plausibility layer intended to remove extremely small, extremely large or strongly distorted candidates before pair selection.

### 3.7 Pair selection and left-right assignment

Because the downstream interpretation required exactly two relevant regions, the filtered detections were evaluated pairwise. Candidate boxes were first ranked by confidence and only the strongest candidates were considered for pair formation. Each possible pair was scored using a weighted combination of normalized horizontal distance, vertical overlap, height similarity, area similarity and mean confidence. Additional hard constraints required a minimum vertical overlap of 0.25 and a maximum height ratio of 1.8. Figure 3 schematically illustrates this selection logic. As shown there, pair selection was not based on confidence alone, but on a combined geometric and detection-based consistency score.

Candidate pairs with insufficient vertical overlap or strongly differing geometric proportions were therefore rejected, even if individual detections had relatively high confidence values. This made the final pair selection more robust against visually plausible but structurally unsuitable candidates. Once the best pair had been selected, the left-right assignment was derived from the horizontal center coordinates of the two boxes. The candidate with the smaller x-center was assigned to the left side and the other to the right side. This makes the downstream interpretation independent of the order in which the detector produced the boxes and stabilizes the semantic interpretation of the final result.

### 3.8 Rule-based variant interpretation

After the final pair had been established, the relative size class was determined through a transparent rule. Instead of estimating physical dimensions from the PDF representation, the pipeline compared only the vertical heights of the two final bounding boxes in pixels.

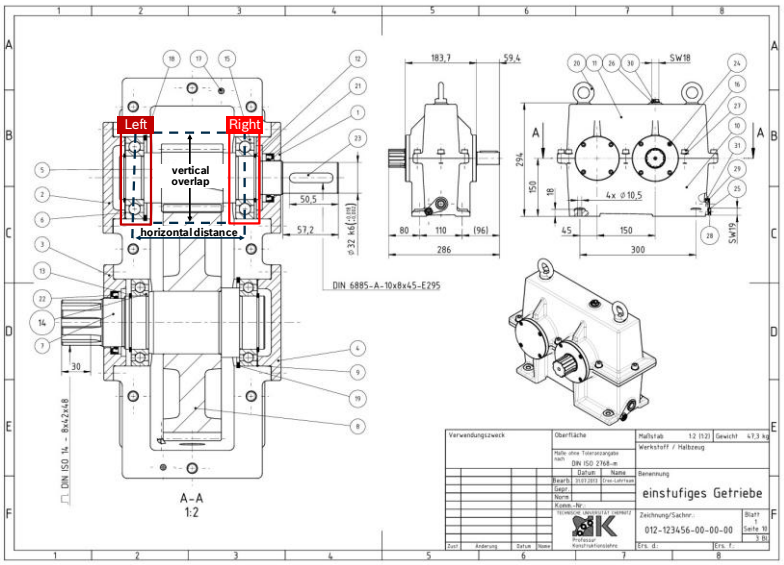



Figure 3. Schematic illustration of pair selection and left-right assignment, adapted from [Leidich, 2016].

If the relative height difference was less than or equal to 4 %, both sides were classified as equal. Otherwise, the larger box was assigned the label large and the smaller box the label small.

The relative difference was computed as the absolute difference between the two box heights divided by the larger of the two values. In this way, the interpretation was based on a normalized comparison rather than on absolute pixel values alone. An example of the resulting final interpretation is shown in Figure 2(d). The aim was not exact metric measurement, but a robust relative interpretation stable under rendering and layout variation.

### 3.9 Output generation and review

The final outputs were generated in several forms. For each processed drawing, the pipeline stored an overlay image showing the selected boxes and their side and size labels, as well as a JSON file containing the raw detections, filtered detections, selected pair, left-right assignment, class labels and box heights. In addition, a summary CSV file was generated to provide file-level review information such as the number of detections, minimum confidence, left/right availability, final class labels and box heights. Cases that do not satisfy the review criteria are copied into a dedicated `_review` folder together with the corresponding source file and overlay image. The review thresholds required at least two detections and a minimum confidence of 0.20. Finally, all overlay images could be merged into a multi-page PDF for compact visual inspection and documentation.

This output design supports both reproducibility and practical usability. The overlay images provide immediate interpretability for manual review, whereas the JSON, CSV and combined PDF outputs provide a structured basis for downstream processing, structured review and traceability.

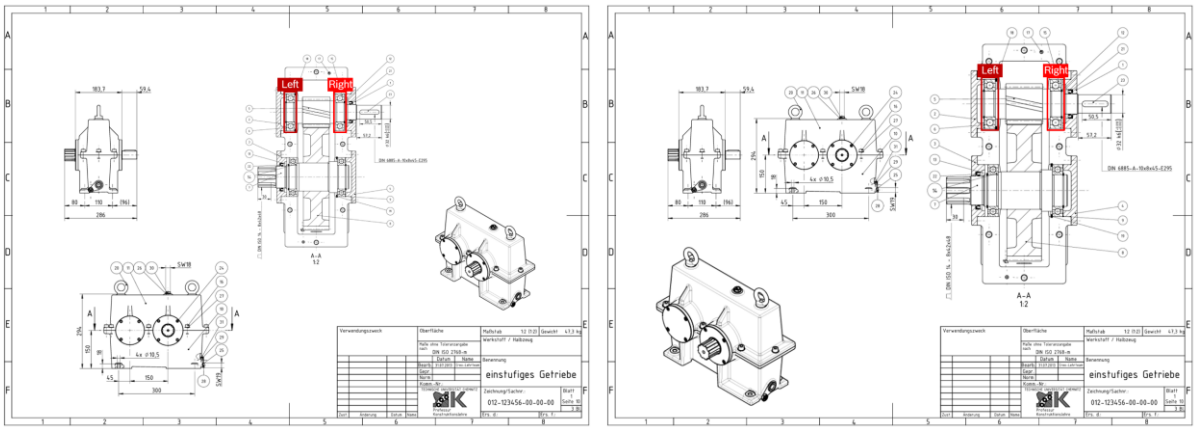



Figure 4. Illustrative detection in two different technical drawing layouts, demonstrating the applicability of the detection concept across varying document structures. Adapted from [Leidich, 2016].

## 4. EXPERIMENTAL SETUP

The proposed pipeline was evaluated in a controlled application-oriented setup that reflected the intended use of the method in a variant-rich brownfield environment. In contrast to a benchmark-style detector evaluation, the objective was the verification of an end-to-end target-information workflow from PDF drawing input to structured output generation.

Figure 4 provides an illustrative example of the pipeline applied to two different technical drawing layouts. The figure therefore illustrates the influence of layout variation on the detection task. Table 2 summarizes the main characteristics of the experimental setup and evaluation configuration. The investigated dataset comprised 63 technical drawings from a hydraulic component context. All documents were processed as PDF inputs in order to remain consistent with the intended industrial use case, in which the relevant target information is embedded in legacy technical drawings rather than in preprocessed image data. The evaluation criterion was defined at the drawing level. A drawing was counted as correctly processed only if the final pair of housing regions was identified correctly, assigned consistently to the left and right side and interpreted with the intended relative size relation. In this way, the evaluation focused on the correctness of the complete workflow rather than on intermediate detector outputs alone.

Table 2. Experimental setup and evaluation configuration.

| Property | Configuration |
|---|---|
| Industrial context | Hydraulic component production |
| Input format | Technical drawings in PDF format |
| Number of drawings | 63 |
| Pages evaluated per document | First page |
| Rasterization resolution | 300 DPI |
| Detection classes | Housing |
| Dataset split | 85% training, 15% validation |
| Random seed | 42 |
| Detector | YOLOv8s |
| Inference image size | 1280 x 1280 px |
| Inference IoU threshold | 0.50 |
| Adaptive confidence range | 0.95 to 0.06 |
| Expected final detections | Two housing regions per drawing |
| Evaluation level | Drawing-level end-to-end pipeline evaluation |
| Evaluation criteria | Correct pair selection, correct left-right assignment and correct relative-size interpretation |

## 5. RESULTS AND DISCUSSION

The final pipeline correctly processed all 63 drawings in the investigated dataset. A drawing was counted as correctly processed only if the final pair of housing regions was identified correctly, assigned consistently to the left and right sides and interpreted with the intended relative size relation. The corresponding quantitative drawing-level results are summarized in Table 3. These results refer to the complete workflow after detection and deterministic post-processing and do not imply unrestricted generalization to arbitrary engineering drawings.

According to Figure 5, the final left/right box height pairs can be assessed directly against the 4 % tolerance used for rule-based interpretation. This makes the final decision step transparent, because equal versus large/small classification is derived from an explicit geometric comparison rather than from a detector score alone. As shown in Figure 6, the retained final detections are associated with consistently high confidence values across the investigated drawing set. The plotted values correspond to the detections that remained after adaptive threshold selection and subsequent post-processing.

Thus, the figure does not summarize all raw detector responses, but the final detections entering the interpretation workflow. Taken together, Figures 5 and 6 show that the final workflow remained stable both at the rule-based interpretation level and at the retained-detection level across the investigated drawings. The results therefore indicate that the proposed combination of learning-based localization, deterministic post-processing and structured result generation can reliably transform a narrowly defined but practically relevant class of technical PDF drawings into machine-readable target information. The structured JSON, CSV and overlay outputs additionally support traceable downstream processing and manual review. At the same time, the reported results must be interpreted within the scope of the present study. The dataset size is limited, the target class is narrowly defined and the evaluated drawing family is visually related. A larger and more diverse dataset would introduce additional variation in drawing standards, layouts, scales and visual quality.

Table 3. Quantitative end-to-end evaluation results.

| Evaluation metric | Result |
|---|---|
| Evaluated drawings | 63 |
| Correctly detected final region pairs | 63/63 |
| Correct left-right assignments | 63/63 |
| Correct relative-size interpretations | 63/63 |
| Drawing-level end-to-end accuracy | 100% |

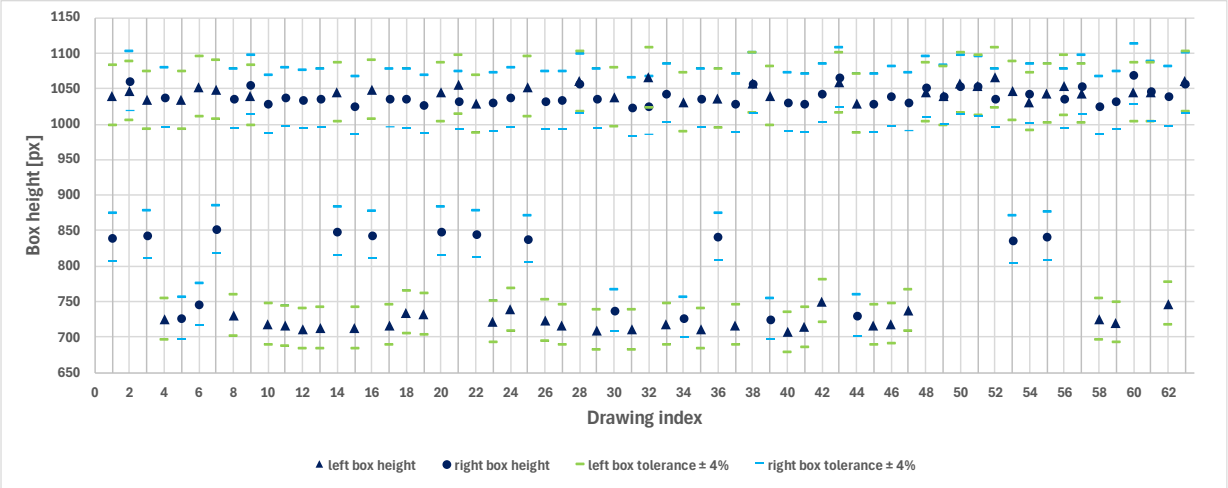



Figure 5. Per-drawing box heights of the final left/right detections with the 4 % decision tolerance for rule-based interpretation.

While additional training data could improve the learning-based localization stage, the geometric filters and pair-selection rules would also need to be re-evaluated for previously unseen drawing families. The method is therefore best understood as a feasible and application-oriented solution for a specific brownfield use case rather than as evidence of unrestricted generalization. Its transferability depends on several conditions: the relevant target regions must recur in a sufficiently consistent visual form, their spatial arrangement must support pair selection based on geometric consistency and relative box height must remain a valid proxy for the intended variant distinction. Under such conditions, the workflow is likely transferable to comparable drawing families.

By contrast, direct transfer cannot be assumed for drawings with substantially different layouts, conventions, target objects or tasks requiring exact metric recovery instead of relative comparison.

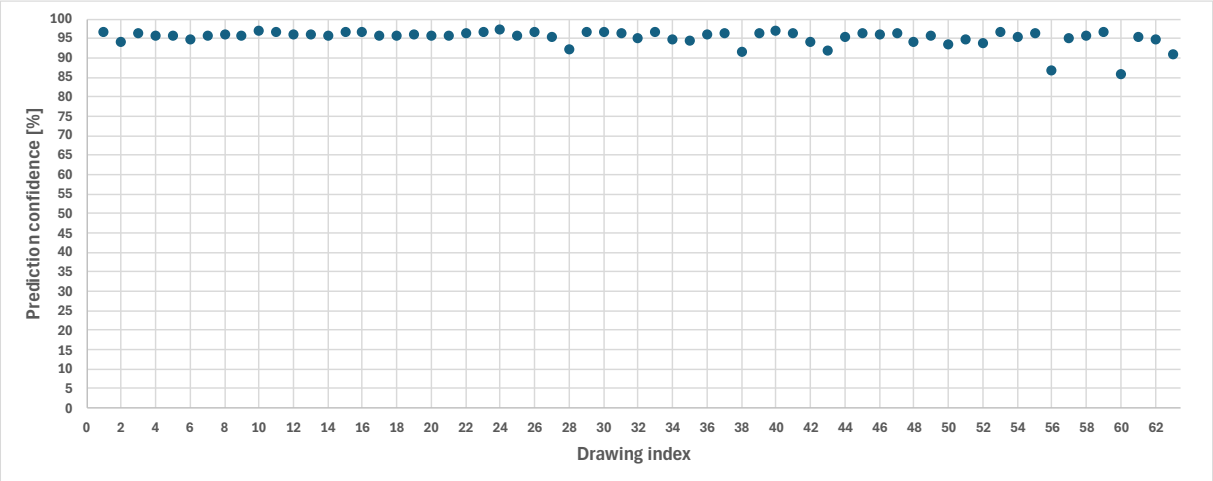



Figure 6. Confidence values of the retained final detections for each processed drawing.

Drawings with more than two relevant views would require an extension of the fixed pair-selection logic. Exact metric recovery would additionally require the detection and assignment of dimension lines, dimension text and drawing-scale information, for example by combining OCR with geometric line analysis.

Finally, the present evaluation is intentionally application-oriented and does not compare multiple detector architectures under benchmark conditions. Instead, the study prioritizes a transparent and practically usable target-information workflow. In the investigated industrial context, this emphasis is justified because downstream usability, deterministic behavior and traceable outputs are more critical than maximizing detector performance on a decontextualized image corpus.

## 6. CONCLUSION

The presented approach showed that the gap between information contained in legacy technical drawings and machine-readable target information for downstream automation can be reduced through a hybrid pipeline combining AI-based localization with deterministic post-processing.

In methodological terms, the main contribution of the paper does not lie in the detector alone, but in the integration of drawing preprocessing, region detection, pair selection and rule-based interpretation into a structured workflow for target-information provision. This workflow remains reproducible, reviewable and suitable for downstream industrial use.

The evaluation on 63 technical drawings from a variant-rich hydraulic component context showed that, within the investigated dataset, the final pipeline processed all drawings correctly according to the defined end-to-end criterion: relevant housing regions had to be detected, assigned consistently to the left and right side and interpreted correctly in relative size terms. This result should not be read as evidence of unrestricted generalization across arbitrary engineering drawings, but as a demonstration of feasibility and application-oriented robustness for the investigated drawing family. A further contribution lies in the structured output layer. Besides visual overlays, the pipeline provides machine-readable result objects that support downstream decision logic, traceability and review.

Overall, the results indicate that the proposed approach can serve as a feasible target-information provision module for downstream automation-related tasks in variant-rich brownfield assembly.

## 7. REFERENCES

1. **Abdel-Aty, T.A.**, and **Negri, E.**, (**2024**), “Conceptualizing the digital thread for smart manufacturing: a systematic literature review”, Journal of Intelligent Manufacturing, Vol. 35, No. 8, pp 3629–3653.

2. **Agritania, M.M.**, and **Isnaini, M.M.**, (**2025**), “Development of an engineering drawing detection and extraction algorithm for quality inspection using deep neural networks”, Procedia CIRP, Vol. 132, pp 135–140.

3. **Ant, J.L.**, **Doksanbir, A.**, **Dillenhofer, F.**, and **Kunne, B.**, (**2024**), “AI Object Detection of Parts in Engineering Drawings and a Concept of Integration in Engineering Education - AssistME”, Proceedings of NordDesign 2024, pp 342–351.

4. **Haar, C.**, **Kim, H.**, and **Koberg, L.**, (**2022**), “AI-Based Engineering and Production Drawing Information Extraction”, Flexible Automation and Intelligent Manufacturing: The Human-Data-Technology Nexus, Cham, pp 374–382.

5. **Hu, S.J.**, **Zhu, X.**, **Wang, H.**, and **Koren, Y.**, (**2008**), “Product variety and manufacturing complexity in assembly systems and supply chains”, CIRP Annals, Vol. 57, No. 1, pp 45–48.

6. **Jamieson, L.**, **Francisco Moreno-García, C.**, and **Elyan, E.**, (**2024**), “A review of deep learning methods for digitisation of complex documents and engineering diagrams”, Artificial Intelligence Review, Vol. 57, No. 6, pp 136.

7. **Kashevnik, A.**, **Shilov, N.**, **Teslya, N.**, **Hasan, F.**, **Kitenko, A.**, **Dukareva, V.**, **Abdurakhimov, M.**, **Zingarevich, A.**, and **Blokhin, D.**, (**2023**), “An Approach to Engineering Drawing Organization: Title Block Detection and Processing”, IEEE Access.

8. **Khan, M.T.**, **Chen, L.**, **Yong, Z.**, **Tan, J.M.**, **Feng, W.**, and **Moon, S.K.**, (**2026**), “From drawings to decisions: A hybrid vision-language framework for parsing 2D engineering drawings into structured manufacturing knowledge”, Robotics and Computer-Integrated Manufacturing, Vol. 99.

9. **Li, X.**, **Grandvalet, Y.**, **Davoine, F.**, **Cheng, J.**, **Cui, Y.**, **Zhang, H.**, **Belongie, S.**, **Tsai, Y.-H.**, and **Yang, M.-H.**, (**2020**), “Transfer learning in computer vision tasks: Remember where you come from”, Image and Vision Computing, Vol. 93.

10. **Maupou, C.**, **Yang, Y.**, **Fodop, G.**, **Qie, Y.**, **Migliorini, C.**, **Mehdi-Souzani, C.**, and **Anwer, N.**, (**2024**), “Automatic raster engineering drawing digitisation for legacy parts towards advanced manufacturing”, Procedia CIRP, Vol. 129, pp 234–239.

11. **Sierla, S.**, **Azangoo, M.**, **Rainio, K.**, **Papakonstantinou, N.**, **Fay, A.**, **Honkamaa, P.**, and **Vyatkin, V.**, (**2022**), “Roadmap to semi-automatic generation of digital twins for brownfield process plants”, Journal of Industrial Information Integration, Vol. 27.

12. **Zaidi, S.S.A.**, **Ansari, M.S.**, **Aslam, A.**, **Kanwal, N.**, **Asghar, M.**, and **Lee, B.**, (**2022**), “A survey of modern deep learning based object detection models”, Digital Signal Processing, Vol. 126.

13. **Zhang, W.**, **Joseph, J.**, **Yin, Y.**, **Xie, L.**, **Furuhata, T.**, **Yamakawa, S.**, **Shimada, K.**, and **Kara, L.B.**, (**2023**), “Component segmentation of engineering drawings using Graph Convolutional Networks”, Computers in Industry, Vol. 147.

14. **Leidich, E.**, (**2016**), “CAD-Aufbaukurs: Zeichnungserstellung Baugruppe", Technische Universität Chemnitz, pp 10.

# STRUCTURAL DESIGN OPTIMIZATION OF THE HYBRID COMPOSITE BATTERY ENCLOSURE OF AN ELECTRIC VEHICLE

**N. Berk İÇTEN**, *nicten@etu.edu.tr* TOBB ETÜ, 06560, Ankara, Türkiye

**Erdem ACAR**, *acar@etu.edu.tr* TOBB ETÜ, 06560, Ankara, Türkiye

## ABSTRACT

This study presents structural design and optimization of a carbon fiber and glass fiber reinforced hybrid battery enclosure for electric vehicles. Structural integrity of the battery enclosure is evaluated through static stiffness, vibration, and crash analyses using the commercial finite element analysis software LS-DYNA. To map the design space, a Latin hypercube sampling plan was established to develop five surrogate models: Artificial neural networks, Gaussian process regression, Support vector regression as well as Quadratic and Cubic response surface models. The study compares the prediction accuracy and optimization performance of these models. It is found that the optimized hybrid design achieves a comparable mass to the baseline aluminum design while offering significantly superior structural stiffness and enhanced safety margins.

**Keywords:** Battery Enclosure, Hybrid Composites, Surrogate Modeling, Structural Optimization.

## ÖZET

Bu çalışma, elektrikli araçlar için karbon fiber ve cam fiber takviyeli hibrit kompozit batarya muhafazasının yapısal tasarımını ve optimizasyonunu sunmaktadır. Batarya muhafazasının yapısal bütünlüğü, ticari sonlu elemanlar analizi yazılımı LS-DYNA kullanılarak statik direngenlik, titreşim ve çarpışma analizleri aracılığıyla değerlendirilmiştir. Tasarım uzayını taramak için yapay sinir ağları, Gauss süreç regresyonu, destek vektör regresyonunun yanı sıra karesel ve kübik tepki yüzeyi modelleri olmak üzere beş farklı vekil (surrogate) model geliştirmek için Latin hiperküp örnekleme yöntemi kullanılmıştır. Çalışma, bu modellerin tahmin doğruluğunu ve optimizasyon performansını karşılaştırmaktadır. Optimizasyon sonucunda, hibrit tasarımın referans alınan alüminyum modelle benzer bir kütle değerine sahip olduğu, ancak yapısal rijitlik bakımından daha üstün performans sergilediği saptanmıştır.

**Anahtar Kelimeler:** Batarya Muhafazası, Hibrit Kompozit, Vekil Modelleme, Yapısal Optimizasyon.

## 1. INTRODUCTION

Global targets for reducing carbon emissions and the increasing demand for sustainable energy have accelerated the transition from internal combustion engines to electric vehicles (EVs) in the automotive industry. However, the energy density stored by current battery technologies still offers a limited range compared to traditional vehicles. One of the most effective ways to overcome this limitation is the structural optimization and lightweighting of the battery enclosure, which accounts for a significant portion of the vehicle's total mass [Duddeck, 2008].

While lightweighting the battery enclosure provides an increase in range, compromising structural integrity brings serious safety risks. Mechanical damage to the enclosure can lead to catastrophic scenarios such as short circuits, thermal runaway, or fire [Xia et al., 2024]. Therefore, the design process should focus not only on mass reduction but also on multi-criteria performance indicators such as bending and torsional rigidity, natural frequencies, and impact resistance under various crash scenarios [Duddeck, 2008].

There are studies in the literature that evaluate the mechanical performance of battery packs using Finite Element Analysis (FEA) and optimize them with various algorithms [Zhang et al., 2015]. While many studies focus on conventional materials or uniform composites, hybrid structures consisting of a combination of Carbon Fiber Reinforced Polymer (CFRP) and Glass Fiber Reinforced Polymer (GFRP) offer superior potential in terms of cost and weight balance [Beardmore, 1986]. However, the computational cost of high-precision FEA simulations creates a bottleneck in multivariate composite optimizations.To overcome this challenge, surrogate modeling (metamodeling) methods stand out as an effective solution [Sacks et al., 1989]. Although Response Surface Methodology (RSM) is widely used in the literature due to its simplicity [Myers and Montgomery, 1995], more advanced machine learning techniques are needed to model complex design spaces [Bishop, 1995].

This study distinguishes itself from others in the literature by comprehensively comparing the prediction abilities of five different surrogate models (Artificial Neural Networks - ANN, Gaussian Process Regression - GPR, Support Vector Regression - SVR, Quadratic and Cubic RSM) and their effects on optimization outputs. In this study, the structural performance of the battery enclosure was analyzed using LS-DYNA simulations [Hallquist 2006], and a design space was created to train the models using the Latin Hypercube Sampling (LHS) method [McKay et al., 1979]. The accuracies of the surrogate models were evaluated using the "leave-

one-out cross-validation" (LOOCV) approach based on the generalized mean square cross-validation error (GMSE) and root mean square error (RMSE) metric [Acar and Rais-Rohani, 2009]. In the final stage, the lightest hybrid design parameters were determined using surrogate-based optimization, with model-specific strategies including Sequential Quadratic Programming (SQP) and Genetic Algorithm (GA) [Goldberg, 1989] approaches.

Building upon this methodological framework, this study provides three primary contributions to the literature. First, by systematically comparing five distinct surrogate models (ANN, GPR, SVR, Quadratic, and Cubic RSM), it identifies the most robust architecture for predicting non-linear structural responses in hybrid enclosures, setting up a clear benchmark for model selection. Second, it implements a sample-efficient optimization workflow that integrates FEA with surrogate modeling, effectively reducing computational cost without compromising predictive accuracy. Finally, the study demonstrates that the optimized CFRP/GFRP hybrid design provides superior structural efficiency compared to traditional metallic enclosures, achieving a competitive mass profile with enhanced torsional stiffness and impact resistance.

## 2. FINITE ELEMENT MODELING

The finite element model of the battery enclosure utilized in this study was developed by the Battery Technologies Research and Development Platform (BATEG) under the support of the TUBITAK 1004 Program and was adopted from the study by [Maral, 2025]. The mesh density and the material model MAT54 (Enhanced Composite Damage Model), which is based on the failure criteria proposed by [Chang-Chang, 1987] were validated in the aforementioned reference. A mesh convergence study conducted by [Maral ,2025] determined that an element size of 5 mm provides an optimum balance between computational efficiency and numerical accuracy. The battery enclosure consists of four main components: the top cover, bottom cover, frame, and energy absorber (Figure 1).

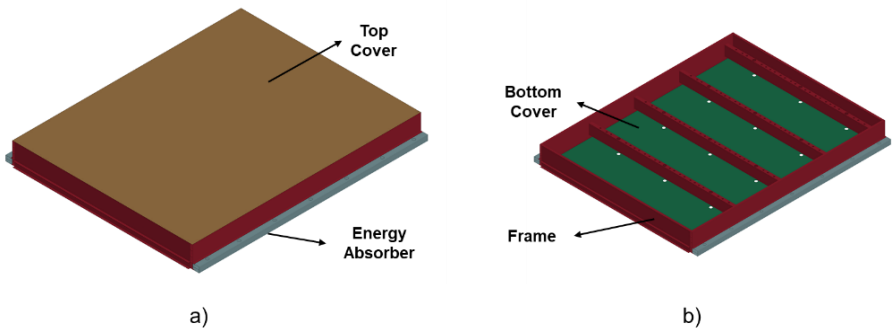



**Figure 1:** Battery Enclosure, a) With Top Cover, b) Without Top Cover

### 2.1 Hybrid Composite Structure and Material Properties

Two different composite material systems were preferred for the creation of the hybrid structure. IM7/8552 [Li, 2019] material, known for its high strength and lightweight, was used for carbon fiber reinforced layers; S-glass/epoxy [Hörmann and Wacker, 2005] material was used for glass fiber layers. The designed hybrid laminate structure consists of 8 layers in total.

In this configuration, CFRP was used in ±45° oriented layers to meet torsion and shear loads, and GFRP was used in 0° and 90° oriented layers (Figure 2).

$[90/+45/-45/0]_s$

| | |
|---|---|
| 90 | GFRP |
| +45 | CFRP |
| -45 | CFRP |
| 0 | GFRP |
| 0 | GFRP |
| -45 | CFRP |
| +45 | CFRP |
| 90 | GFRP |

**Figure 2:** HFRP Composite Material Structure.

### 2.2 Simulation Scenarios and Boundary Conditions

Five different structural analyses were conducted in this study for structural integrity assessment. The implicit analysis method was employed for bending, torsion, and natural frequency calculations. In contrast, for pole impact and obstacle analyses, explicit analysis was performed.

When the battery pack is mounted to the vehicle chassis, it functions as a beam along the longitudinal axis of the vehicle. Under the vertical loads generated by the passengers and the vehicle's own weight, the chassis tends to exhibit a sagging behavior. The bending stiffness ($K_b$) of the battery enclosure represents its resistance to this deformation. The formulation for bending stiffness is defined as follows [Aydoğdu et al., 2024]:

$$K_b = \frac{F}{\delta_{max}} \quad (1)$$

In this context, F represents the applied load, while $\delta_{max}$ denotes the maximum vertical displacement. The model prepared based on this calculation method is illustrated in Figure 3a. The battery enclosure was constrained in all degrees of freedom at the four corners, as indicated in Figure 3a. Bending loads of 500 N were applied to the midpoints of the long edges of the model, creating a total bending load of 1000 N. In this study, the bending stiffness of the battery enclosure is needed to be larger than 9000 N/mm.

When a vehicle corners, changes lanes, or when a wheel encounters an obstacle or pothole, a torsional moment is generated on the chassis. Due to its large cross-sectional area and

closed geometry, the battery pack contributes significantly to torsional resistance. The formulation for torsional stiffness is presented in Equation (2) [Aydoğdu et al., 2024]:

$$K_t = \frac{T}{\theta_{max}} \tag{2}$$

Torsional stiffness ($K_t$) is defined as the ratio of the applied torque (T) to the resulting twist angle (θ). The model prepared according to this calculation methodology is illustrated in Figure 3b. In the torsion analysis (Figure 3b), the battery enclosure was constrained in all degrees of freedom at the points indicated by triangles. A moment of 1500 Nm was applied to the exact midpoint of the line connecting two opposing holes, which were coupled via a Constrained Nodular Rigid Body (CNRB).

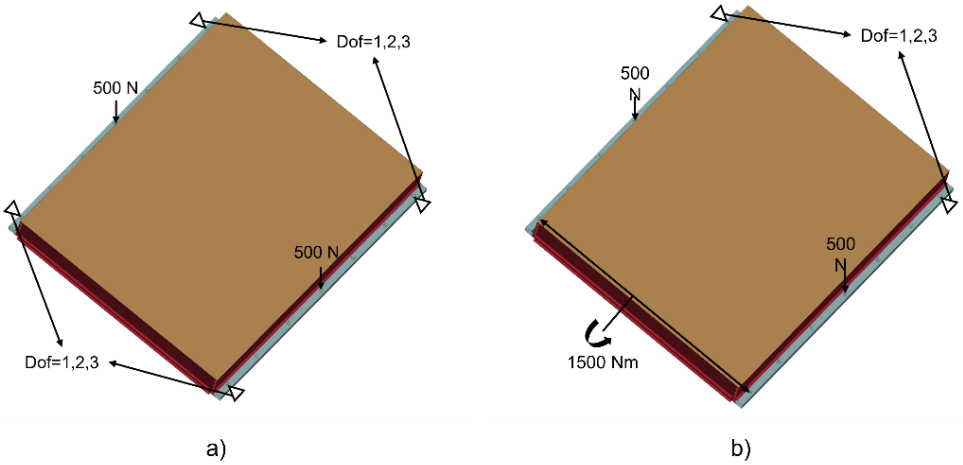



Figure 3. Boundary Conditions; a) Bending, b) Torsion

In the torsion analysis, the twist angle (Equation 3) is defined as the angle between the deformed and undeformed states of the battery enclosure (See Figure 4). In this study, the torsional stiffness of the battery enclosure is needed to be larger than 15000 Nm/°.

$$tan\theta_{max} = \frac{\delta_{max}}{0.5 \times width} \tag{3}$$

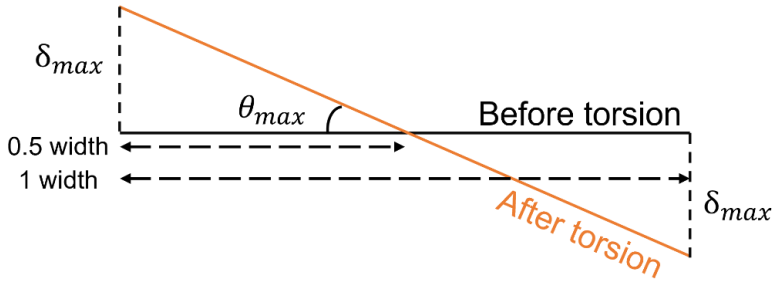
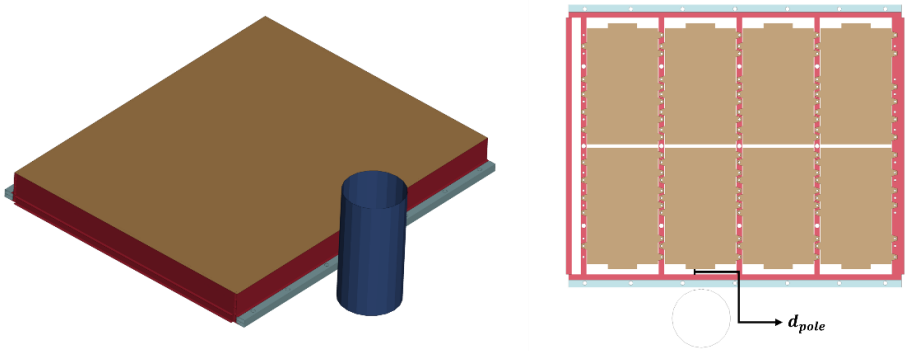



Figure 4. Description of twist angle

Every physical structure possesses natural vibration frequencies determined by its mass and stiffness distribution. The battery pack in electric vehicles is subjected to random vibrations originating from road conditions. If the first natural frequency $(\omega_1)$ of the battery pack falls within this range, resonance occurs [Zhang et al., 2015]. In the long term, resonance leads to uncontrolled amplitude increases and fatigue damage within the structure. In this study, the first natural frequency of the battery enclosure is required to be larger than 35 Hz.

Since battery packs occupy a large area on the vehicle floor, side impacts represent one of the most critical scenarios. In this study, an analysis was performed using the parameters specified for the Euro NCAP side pole impact test [Dagdeviren et al., 2016]. In the prepared model, the battery pack was impacted against a rigid pole (254 mm in diameter) at a velocity of 8 m/s. To satisfy the standard requirements, the rigid pole was constrained in all three translational and three rotational degrees of freedom. During the impact, the clearance between the wall struck by the pole and the module inside the battery enclosure was monitored. No contact should occur between them; any impact reaching the batteries could trigger thermal runaway, potentially resulting in fire or explosion. The side impact model is illustrated in Figure 5a [Maral, 2025]. In the side pole impact analysis, the distance between the module and the impact location is defined as $d_{pole}$. This distance is described in Figure 5b. In this study, no contact to the modules is allowed to occur, so $d_{pole} \geq 0$ should be maintained.

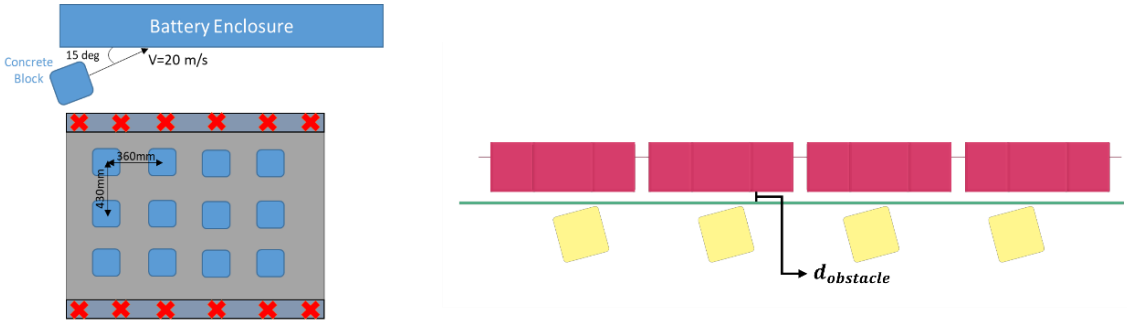



a) b)

Figure 5. Side impact model; a) Isometric view, b) Module to wall distance (d $_{pole}$)

Similar to the side impact scenario, the battery pack is susceptible to any impact originating from beneath the vehicle due to its underbody location. To ensure a realistic and challenging scenario, 12 concrete blocks (dimensions: 100 x 100 x 100 mm) were simultaneously impacted against the bottom surface of the battery pack at a constant velocity of 20 m/s with an oblique angle of 15°. The clearance between the bottom cover, where the collision occurs, and the lower section of the battery modules inside the enclosure is defined as d $_{obstacle}$. This distance

is illustrated in Figure 6b. In the simulations, the battery carrier was modeled as constrained in all degrees of freedom at the vehicle connection points. The primary objective of this test is to verify that the battery enclosure, even if deformed as a result of the impact, does not come into direct contact with the battery modules and that the carrier maintains its protective function. A schematic representation of the bottom impact scenario is provided in Figure 6a [Maral, 2025]. In this study, no contact to the modules is allowed to occur, so d $_{obstacle}$ ≥ 0 should be maintained.




a) b)

Figure 6. Obstacle model; a) Schematic view, b) Module to bottom cover distance (d $_{obstacle}$)

### 2.3 Design Variables and Component Architectures

In the optimization of the battery enclosure, three design variables were defined to establish the design space: CFRP layer thickness ($t_2$), stacking orientation ($\theta$), and the thickness ratio (r), that is the ratio of the GFRP layer thickness ($t_1$) to the CFRP layer thickness ($t_2$). To reduce design complexity and enhance computational efficiency, the thickness relationships between the enclosure components were fixed at specific ratios. In this configuration, the bottom cover's reference thickness was set as 8T; accordingly, the energy absorber and frame were proportioned to 3T, while the top cover was set to 2T relative to this reference (Figure 7). All design values were derived based on the thickness of the bottom cover, ensuring a consistent distribution across the entire structure.

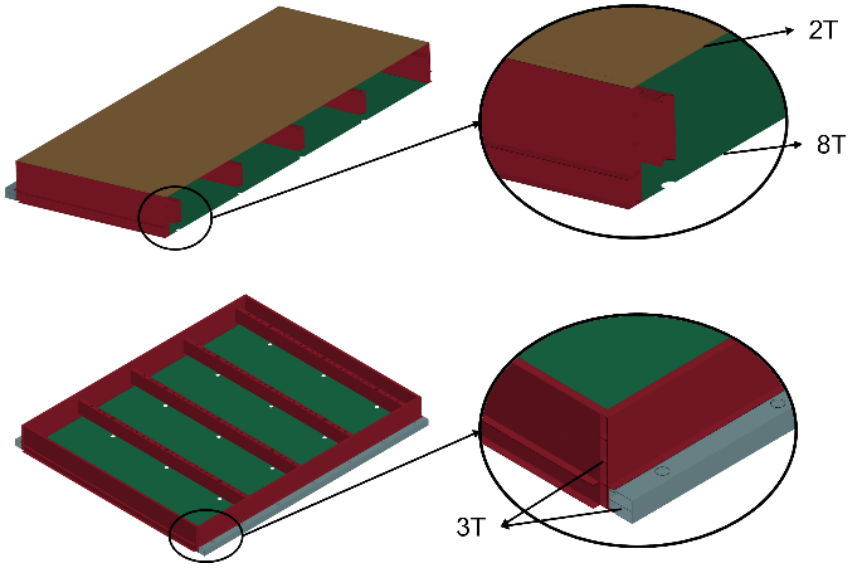



Figure 7. Thickness proportion of the enclosure components

## 3. SURROGATE MODELS and OPTIMIZATION

This section describes the surrogate-based design optimization framework developed to enhance the structural performance of the hybrid battery enclosure. The process begins with the design of experiments and progresses through the construction of surrogate models, accuracy assessment and finally, the implementation of optimization algorithms to achieve the target mass and performance constraints. The overall surrogate-based structural design optimization flowchart implemented in this study is illustrated in Figure 8.

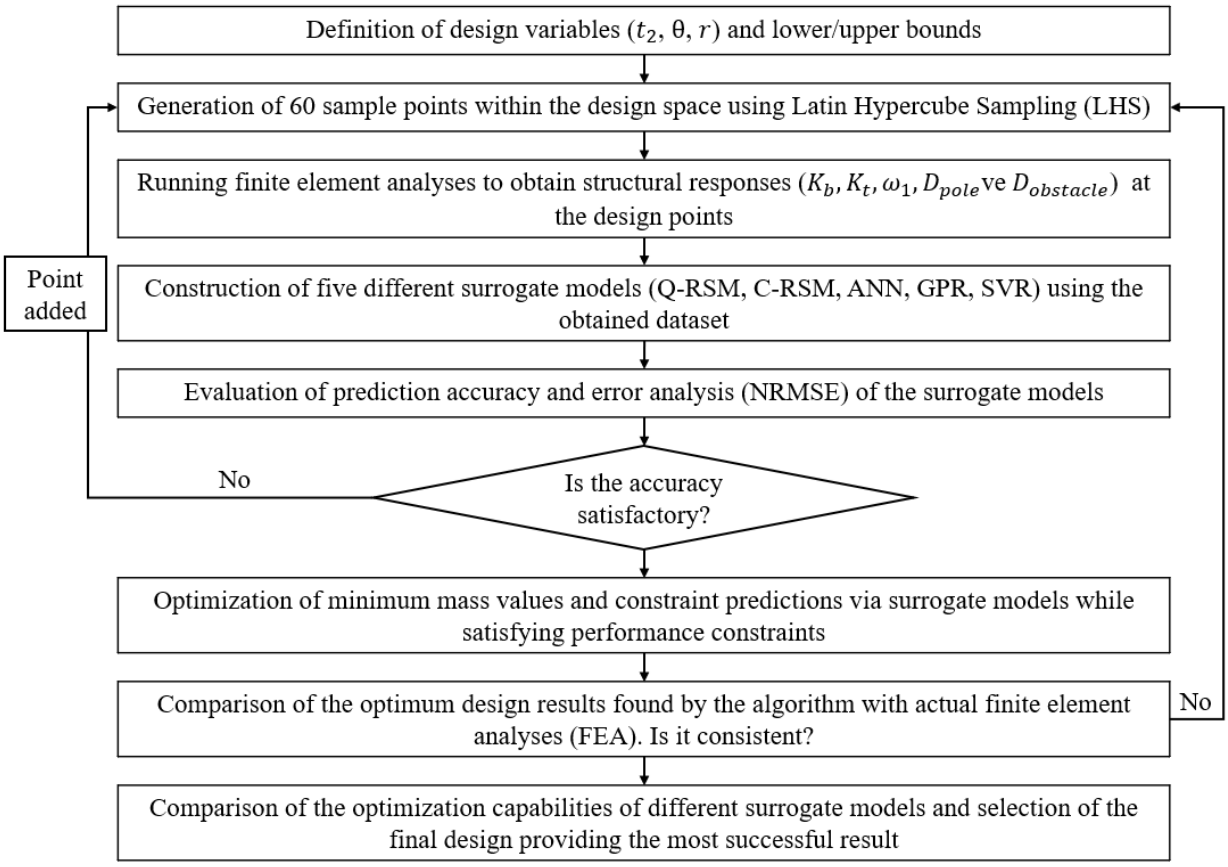



Figure 8. Flowchart of the surrogate-based structural design optimization.

### 3.1 Design of Experiments

The dataset required for surrogate model training was generated using the Latin Hypercube Sampling (LHS) method. LHS divides the value range of each design variable into N equal sub-intervals and selects exactly one sample from each, providing a more homogeneous representation of the design space with significantly fewer points compared to simple random sampling [McKay et al., 1979]. In this study, an LHS set of 60 points was generated for three design variables (CFRP thickness $t_2$ [2, 4] mm, fiber orientation angle $\theta \in$ [0°, 90°], and thickness ratio r ∈ [0.429, 2.333]); the structural responses for each point were calculated via Finite Element Analysis (FEA). The calculated outputs consist of six structural responses: mass *M* (kg), bending stiffness $K_b$ (N/mm), torsional stiffness $K_t$ (Nm/°), first natural frequency $\omega_1$ (Hz), side impact deformation d $_{pole}$ (mm), and bottom impact deformation d $_{obstacle}$ (mm). The primary objective of the optimization problem is to minimize the total mass *M* while ensuring the structural integrity and safety criteria of the enclosure. Accordingly, the established mathematical model and constraints are as follows:

$$\begin{aligned}
&\text{Find:} && t_2,\ \theta,\ r \\
&\text{Minimize:} && M\ (t_2,\ \theta,\ r) \\
&\textit{Subject to:} && K_b \geq 9000\ N/mm, \\
& && K_t \geq 15000\ Nm/°, \\
& && \omega_1 \geq 35\ Hz \\
& && d_{pole} \geq 0\ mm \\
& && d_{obstacle} \geq 0\ mm \\
& && 2 \leq t_2 \leq 4\ mm \\
& && 0° \leq \theta \leq 90° \\
& && 0.429 \leq r \leq 2.333
\end{aligned} \tag{4}$$

### 3.2 Surrogate Models

Literature indicates that a single surrogate model may not consistently provide the best results, as prediction accuracy varies depending on the structure of the design space (linear, non-linear, or noisy) [Forrester et al., 2008]. Therefore, five different surrogate models were independently trained and compared for each structural response. To evaluate model accuracy, the Leave-One-Out Cross-Validation (LOOCV) method was applied: in each iteration, one point was set aside as a test point, the model was retrained using the remaining

59 points, and the prediction error at the test point was recorded. The normalized root-mean-square error (LOOCV-NRMSE) were utilized as performance metrics:

$$LOOCV\text{-}NRMSE(\%) = \frac{\sqrt{\frac{1}{n}\sum_{i=1}^{n}(y_i - \hat{y}_i)^2}}{y_{max} - y_{min}} \times 100 \tag{5}$$

n: Total number of simulation points (n=60 for this study).

$y_i$: Actual response obtained from Finite Element Analysis (FEA).

$\hat{y}_i$:Predicted response at the $i^{th}$ point obtained from a model trained without that specific point.

Quadratic and cubic response surface models (Q-RSM, C-RSM):

RSM aims to predict the physical behavior of the battery enclosure using interpretable and computationally inexpensive polynomial functions. While the quadratic model is expressed by a 10-term polynomial consisting of constant, linear, quadratic, and two-way cross-interaction terms, the cubic model reaches 20 terms with the addition of pure cubic and quadratic-linear

cross-interaction terms. The general forms of these polynomial expressions and the derivation of the term counts are detailed in Appendix A. In both models, the coefficients are calculated analytically using the least squares method; therefore, iterative optimization is not required. To prevent the scale differences of the design variables from adversely affecting the coefficient calculation, all variables have been normalized to the [0, 1] range.

Artificial neural networks (ANN):

The primary advantage of ANNs is their potential to approximate any continuous function with the desired accuracy, due to their complex activation functions [Hornik et al., 1989]. This characteristic can be decisive for complex, multimodal response surfaces where the polynomial structure of RSM remains insufficient. However, utilizing this capacity with limited data requires caution because it is widely known that as the architecture becomes more complex, the risk of overfitting increases. Therefore, the most suitable architecture and neuron count for this dataset were determined through a systematic comparison. Five different network architectures Multi-Layer Perceptron (MLP), Radial Basis Function (RBF) Network, Generalized Regression Neural Network (GRNN), Cascade Forward Neural Network (CFNN) and Fitnet were evaluated in combination with five different neuron counts [3, 5, 8, 10, 15]. For each structural response, 25 architecture-neuron pairs were compared based on the LOOCV-NRMSE metric. A single hidden layer was used in all models, as the use of two hidden layers led to observed overfitting within the limited dataset. Weight optimization was performed using the Bayesian Regularization algorithm (see Appendix B), which is particularly effective for small datasets to prevent overfitting.

Support vector regression (SVR):

The working principle of SVR is based on constructing the prediction function such that it remains within a tube of width ε (epsilon): prediction errors within this tube are not considered losses, while those outside the tube are penalized via the C (penalty weight) parameter [Vapnik, 1995]. This structure provides SVR with an inherent robustness against numerical noise, which is inevitable in FEA simulations. Non-linear relationships are handled through kernel transformation, where the input space is mapped into a high-dimensional feature space where a linear model is established. For each structural response, five different kernel functions were compared: the Gaussian (RBF) kernel, polynomial kernels (2nd, 3rd, and 4th degrees), and the linear kernel (see Appendix C). For each kernel, hyperparameters (C, ε, and σ (kernel scale)) were determined using Bayesian optimization. The most successful kernel was selected based on the highest LOOCV $R^2$ value.

Gaussian process regression (GPR):

GPR fundamentally distinguishes itself from other models by representing the system as a stochastic process rather than a deterministic function. For any given point x, GPR generates not only a predicted value (mean $\hat{\mu}(x)$) but also a measure of uncertainty (variance $\hat{\sigma}^2(x)$) that quantifies the confidence in that prediction [Sacks et al., 1989]. The variance approaches zero at the training points (high confidence), while it increases in regions lacking data (low confidence). This characteristic is the primary attribute that differentiates GPR from other models and grants it strategic importance regarding constraint uncertainty management. For each structural response, eight different kernels were compared: standard versions of squared exponential (SE), Matérn 5/2, Matérn 3/2, rational quadratic, and exponential kernels, alongside Automatic Relevance Determination (ARD) versions of the SE, Matérn 5/2, and Matérn 3/2 kernels (see Appendix D). In all GPR models, hyperparameters were determined using the Maximum Likelihood Estimation (MLE) method.

### 3.3 Optimization

To ensure a fair and unbiased comparison, the exact same optimization strategy was applied to all five surrogate models. During this process, a hybrid approach combining a Genetic Algorithm (GA) with Sequential Quadratic Programming (SQP) was chosen. First, a global exploration of the design space was performed by the GA to avoid getting trapped in local minima. Once the most promising region was identified, this point was passed to the SQP algorithm as the initial starting value. Then, a local search was performed by the SQP algorithm to find the exact global optimum. This setup was implemented using MATLAB's HybridFcn command, which starts SQP automatically when GA finishes. Finally, the obtained optimum design was validated using Finite Element Analysis (FEA). This step confirmed the surrogate model's accuracy and ensured that all constraints were strictly met. The error formulation utilized for the comparison between the surrogate model predictions and the FEA results is given in Equation 6.

$$Error = \frac{FEA - Prediction}{FEA} \times 100 \tag{6}$$

## 4. RESULTS

### 4.1 Performance Evaluation of Surrogate Models

All surrogate models learned the mass (*M*) function, which exhibits a highly linear character with respect to the design variables, with near-perfect precision, achieving Test-NRMSE values equal to 0.0% (Table 1). When the structural constraints $K_b$, $K_t$, and $\omega_1$ are examined, it is observed that the GPR, ANN, and SVR models exhibited consistent success across all three error metrics, predicting these complex non-linear responses with a maximum error margin of 3.3%. In contrast, traditional Q-RSM and C-RSM models underperformed compared to modern machine learning algorithms, particularly in the $K_t$ parameter, yielding LOOCV-NRMSE errors of 7.8% and 6.9%, respectively. As expected, due to the physical nature of the problem, the highest error rates were observed in the $d_{pole}$ and $d_{obstacle}$ constraints, which involve complex crash dynamics. It is noteworthy that the $d_{pole}$ results possess significantly higher error values compared to $d_{obstacle}$. While the lowest Test-NRMSE error for $d_{pole}$ was provided by the GPR model at 5.6%, the SVR model also remained at a reasonable level with a Test-NRMSE of 6.6%. The GPR model offered the highest accuracy in all constraints except for $d_{pole}$, it was found that the SVR model exhibited a more robust performance in the $d_{pole}$ constraint compared to GPR. The general performance decrease in the crash constraints is attributed to the extremely complex and highly non-linear character of the impact tests. The fact that polynomial-based RSM models yielded the poorest results across these constraints shows that the use of advanced surrogate models is a necessity for the optimization of complex hybrid composite structures. According to Table 1, GPR outperforms all other surrogate models in five out of six structural responses based on Test-NRMSE. It achieves exceptional precision in stiffness and vibration metrics. In the $d_{obstacle}$ crash constraint, the ANN model shows a statistically negligible advantage over GPR (3.8% vs. 4.0%). These results prove that GPR provides the highest global prediction accuracy for this multidisciplinary design space.

Table 1. Surrogate models error metrics.

| Models | Error Metrics (%) | M | $K_b$ | $K_t$ | $\omega_1$ | d $_{pole}$ | $d_{obstacle}$ |
|---|---|---|---|---|---|---|---|
| **Q-RSM** | LOOCV-NRMSE | 0.0 | 2.6 | 7.8 | 2.6 | 8.7 | 5.8 |
| | Test-NRMSE | 0.0 | 1.8 | 6.8 | 2.0 | 7.4 | 5.5 |
| **C-RSM** | LOOCV-NRMSE | 0.0 | 1.5 | 6.9 | 2.8 | 11.6 | 7.7 |
| | Test-NRMSE | 0.0 | 1.1 | 4.5 | 1.6 | 6.6 | 4.8 |
| **GPR** | LOOCV-NRMSE | 0.0 | 0.6 | 0.4 | 0.5 | 8.5 | 4.9 |
| | Test-NRMSE | 0.0 | 0.2 | 0.2 | 0.3 | 5.6 | 4.0 |
| **ANN** | LOOCV-NRMSE | 0.0 | 1.2 | 2.6 | 0.7 | 7.3 | 5.3 |
| | Test-NRMSE | 0.0 | 0.5 | 2.0 | 0.5 | 7.0 | 3.8 |
| **SVR** | LOOCV-NRMSE | 0.0 | 1.8 | 3.1 | 2.6 | 6.4 | 4.9 |
| | Test-NRMSE | 0.0 | 1.1 | 3.3 | 2.1 | 6.6 | 4.9 |

**Note:** $t_2$, d $_{pole}$ *and* $d_{obstacle}$ *are in mm,* θ *in degrees, M in kg,* $K_b$ *in* $N/mm$, $K_t$ *in Nm/° and* $\omega_1$ *in Hz.*

### 4.2 Hybrid Optimization and FEA Validation

The optimization results presented in Table 2 reveal that $t_2$ (CFRP thickness) reached the upper limit of 4.0 mm across all models, identifying it as the active constraint required to satisfy structural stiffness requirements. The concentration of fiber angles *Θ* within a narrow range between 50.5° and 56.4° confirms a consistent global optimum region. While the traditional RSM suggested the heaviest design at 45.7 kg, the GPR model successfully achieved the lightest configuration at 43.6 kg. FEA validations confirmed that all models correctly identified $K_b$ (bending stiffness) as a primary active constraint. However, the precision of these predictions varied significantly; while the GPR model showed an exceptional precision with only a 0.2% error, the Q-RSM model exhibited a much higher deviation of 4.4%, indicating its limited capability in capturing the exact structural behavior. The discrepancy between the models became most apparent in the crash-related d $_{pole}$ constraint. Both ANN and RSM-based models struggled with d $_{pole}$ predictions due to the highly non-linear and discontinuous nature of impact dynamics. In particular, the Q-RSM and ANN models showed significant deviations of -19.0% and -15.8%, respectively. These errors indicate that second-order polynomial-based RSMs struggle with high-order nonlinearities, whereas the ANN model potentially suffers from insufficient training data in this design space. In contrast, GPR and SVR-based hybrid optimization proved to be much more robust, providing the most reliable framework for the design of complex hybrid composite structures by maintaining significantly lower deviations in these challenging constraints.

Table 2. Optimization results and errors (%) compared to FEA.

| | Q-RSM | % | C-RSM | % | GPR | % | ANN | % | SVR | % |
|---|---|---|---|---|---|---|---|---|---|---|
| $t_2$ | 4.0 | - | 4.0 | - | 4.0 | - | 4.0 | - | 4.0 | - |
| $\Theta$ | 52.1 | - | 50.5 | - | 56.4 | - | 53.2 | - | 52.2 | - |
| $r$ | 1.1 | - | 1.0 | - | 1.0 | - | 1.0 | - | 1.0 | - |
| $M$ | 45.7 | -0.2 | 43.9 | 0.1 | 43.6 | -0.1 | 43.7 | 0.0 | 43.8 | -0.1 |
| $K_b$ | 9000 | 4.4 | 9000 | 0.4 | 9000 | 0.2 | 9000 | 0.5 | 9000 | 0.3 |
| $K_t$ | 22986 | 12.8 | 24951 | 4.8 | 24005 | 0.8 | 24737 | 2.6 | 24895 | 3.2 |
| $\omega_1$ | 37.9 | -1.0 | 37.7 | -2.2 | 36.3 | 0.5 | 36.3 | -0.5 | 36.8 | -0.3 |
| $d_{pole}$ | 13.7 | -19.0 | 11.8 | -1.5 | 11.6 | -5.5 | 12.6 | -15.8 | 11.2 | 2.2 |
| $d_{obstacle}$ | 8.9 | 0.3 | 9.2 | -1.7 | 9.0 | -1.80 | 8.7 | 2.6 | 8.9 | 1.9 |

**Note:** $t_2$, $d_{pole}$ *and* $d_{obstacle}$ *are in mm,* $\theta$ *in degrees, M in kg,* $K_b$ *in* $N/mm$, $K_t$ *in Nm/° and* $\omega_1$ *in Hz.*

### 4.3 Hybrid Optimization via Adaptive Sampling and FEA Validation

To minimize the validation errors between the optimization and FEA, an adaptive sampling strategy was executed. The predicted optimum design points from each individual surrogate model were verified via high-fidelity FEA simulations. These model-specific data points were then appended to the baseline training matrix, expanding the dataset to 61 samples. The surrogate models were subsequently retrained on this updated space to enhance their mathematical convergence around the global optimum. The optimized design variables, final mass values, and corresponding FEA validation errors obtained after the refinement process are summarized in Table 3. The implementation of adaptive sampling led to a consistent reduction in validation errors across nearly all structural constraints, providing marginal refinements in some responses and substantial improvements in others. Most notably, the $d_{pole}$ prediction error of the second-order Q-RSM model dropped from -19.0% to -9.5%, while the ANN model's error was successfully reduced from -15.8% to 5.0%. These error mitigations prove that integrating optimization outputs back into the training data effectively enhances the predictive reliability of metamodels without the necessity of massive global datasets. Also, advanced models like GPR and SVR maintained exceptional robustness, keeping their validation errors under 1.5% across the most critical constraints.

Table 3. Optimization results and errors (%) compared to FEA after adaptive sampling.

| | Q-RSM | % | C-RSM | % | GPR | % | ANN | % | SVR | % |
|---|---|---|---|---|---|---|---|---|---|---|
| $t_2$ | 4.0 | - | 4.0 | - | 4.0 | - | 4.0 | - | 4.0 | - |
| $\Theta$ | 52.2 | - | 50.5 | - | 56.3 | - | 52.1 | - | 52.3 | - |
| $r$ | 1.1 | - | 1.0 | - | 1.0 | - | 1.0 | - | 1.0 | - |
| $M$ | 45.2 | -0.2 | 43.9 | 0.2 | 43.4 | 0.2 | 43.7 | 0.2 | 43.7 | 0.1 |
| $K_b$ | 9000 | 3.4 | 9000 | 0.4 | 9000 | 0.2 | 9000 | 0.2 | 9000 | 0.3 |
| $K_t$ | 23554 | 10.0 | 25448 | 2.9 | 24142 | 0.4 | 25271 | 1.9 | 25621 | 0.3 |
| $\omega_1$ | 37.6 | -0.8 | 37.3 | -1.2 | 36.4 | 0.3 | 36.8 | -0.2 | 36.5 | 0.5 |
| $d_{pole}$ | 13.2 | -9.5 | 11.7 | -1.1 | 11.0 | -1.3 | 11.1 | 5.0 | 11.4 | 0.9 |
| $d_{obstacle}$ | 8.9 | 0.7 | 9.1 | -1.0 | 8.9 | -0.7 | 8.9 | 1.9 | 9.1 | -1.3 |

**Note:** $t_2$, $d_{pole}$ *and* $d_{obstacle}$ *are in mm,* $\theta$ *in degrees, M in kg,* $K_b$ *in* $N/mm$, $K_t$ *in Nm/° and* $\omega_1$ *in Hz.*

### 4.4 Comparison with the Reference Aluminum Design

The performance of the optimized hybrid GPR design is benchmarked against a reference aluminum battery enclosure design obtained from the study by [Maral 2025]. The comparative results, including the percentage changes, are summarized in Table 4. The hybrid model (43.5 kg) exhibits a marginal mass increase of 2.4% compared to the reference aluminum model (42.5 kg). This difference is directly linked to the established upper-bound constraint on theCFRP thickness ($t_2 \leq 4\ mm$). In the optimization process, once the maximum allowable CFRP thickness was reached, the algorithm utilized GFRP layers to satisfy the remaining structural requirements for bending stiffness ($K_b$). Due to the higher density and lower stiffness of GFRP relative to CFRP, a greater volume of material was required to achieve the targeted mechanical performance, which resulted in the observed increase in total mass. Despite this slight mass penalty, the hybrid design demonstrates superior structural characteristics. Most notably, a 28.9% increase in torsional stiffness $K_t$ was achieved, indicating that the hybrid configuration is significantly more resistant to twisting loads than the aluminum reference. Furthermore, $d_{pole}$ increased from 5.8 mm to 11.0 mm. This higher clearance indicates that the hybrid design provides a much larger safety margin against battery intrusion during a crash. Consequently, the optimized hybrid GPR design is proven to be a high-performance alternative, offering a substantial boost in both structural rigidity and safety clearance with a negligible difference in mass.

Table 4. Comparison of the optimized hybrid design with the reference aluminum design.

| | M | $K_b$ | $K_t$ | $\omega_1$ | d $_{pole}$ | $d_{obstacle}$ |
|---|---|---|---|---|---|---|
| Referenced Aluminum | 42.5 | 9003 | 18782 | 39.7 | 5.8 | 9.5 |
| Hybrid GPR (FEA) | 43.5 | 9020 | **24236** | 36.5 | **11.0** | 8.9 |
| Change (%) | 2.4% | 0.2% | **28.9%** | -8.1% | **90.1%** | -6.5% |

**Note:** $t_2$, d $_{pole}$ *and* $d_{obstacle}$ $are\ in\ mm$, θ *in degrees, M in kg,* $K_b\ in\ N/mm, K_t$ *in Nm/° and* $\omega_1$ *in Hz.*

## 5. CONCLUSION AND FUTURE WORK

In this study, a hybrid composite battery enclosure was optimized using five surrogate models to achieve minimum mass while satisfying structural and boundary conditions. The optimization results demonstrated that $t_2$ and $K_b$ act as the primary active constraints in the design space. Furthermore, the implementation of an adaptive sampling strategy successfully mitigated prediction errors in the models. The optimized hybrid GPR design achieved a mass of 43.5 kg, which is only 2.4% higher than a reference aluminum enclosure, even though the CFRP thickness ($t_2$) was restricted to a maximum of 4 mm. However, this slight mass penalty is significantly offset by a 28.9% increase in torsional stiffness and by a 90.1% improvement in safety clearance during side impact, showing the superior structural efficiency of hybrid composite materials. Overall, the surrogate architectures implemented in this study provided highly reliable predictions for the battery enclosure optimization. While the polynomial-based RSM models underperformed compared to the GPR, SVR, and ANN, the GPR model demonstrated the highest predictive capability in terms of both error metrics and prediction consistency. Ultimately, these findings indicate that properly optimized hybrid designs can truly challenge traditional metallic structures in the automotive industry.

Future research will first investigate the lightweighting potential of increasing the CFRP thickness ($t_2$). Subsequent studies will address industrial feasibility by integrating manufacturing constraints (specifically targeting manufacturable layer thicknesses and feasible fiber orientation angles) and adding cost-optimization as a design objective.

## ACKNOWLEDGEMENTS

The authors acknowledge the support provided by the Scientific and Technological Research Council of Türkiye (TÜBİTAK) Project No. 22AG024 under Program No. 22AG001.

## REFERENCES

1. **Duddeck, F.** (2008), "Multidisciplinary optimization of car bodies", Structural and Multidisciplinary Optimization, Vol. 35, No. 4, pp. 375-389.
2. **Xia, Y., Wierzbicki, T., Sahraei, E. and Zhang, X.** (2014), "Damage of cells and battery packs due to ground impact", Journal of Power Sources, Vol. 267, pp. 78-97.
3. **Zhang, J., Hu, S., Guo, X. and Zhou, Q.** (2015), "Multidisciplinary Design Optimization of BEV Body Structure", SAE Technical Paper 2015-26-0229.
4. **Beardmore, P.** (1986), "Composite structures for automobiles", Composite Structures, Vol. 5, No. 3, pp. 163-176.
5. **Sacks, J., Welch, W.J., Mitchell, T.J. and Wynn, H.P.** (1989), "Design and analysis of computer experiments", Statistical Science, Vol. 4, No. 4, pp. 409-423.
6. **Myers, R.H. and Montgomery, D.C.** (1995), Response Surface Methodology: Process and Product Optimization Using Designed Experiments, 1st ed., John Wiley & Sons, New York.
7. **Bishop, C.M.** (1995), Neural Networks for Pattern Recognition, Oxford University Press, Oxford.
8. **Hallquist, J.O.** (2006), LS-DYNA Theory Manual, Livermore Software Technology Corporation (LSTC), Livermore, California.
9. **McKay, M.D., Beckman, R.J. and Conover, W.J.** (1979), "A comparison of three methods for selecting values of input variables in the analysis of output from a computer code", Technometrics, Vol. 21, No. 2, pp. 239-245.
10. **Acar, E. and Rais-Rohani, M.** (2009), "Ensemble of metamodels with optimized weight factors", Structural and Multidisciplinary Optimization, Vol. 37, No. 3, pp. 279-294.
11. **Goldberg, D.E.** (1989), Genetic Algorithms in Search, Optimization and Machine Learning, Addison-Wesley, Reading, Massachusetts.
12. **Maral, M.E.** (2025), "Bir Elektrikli Aracın Kompozit Batarya Taşıyıcısının Sonlu Elemanlar Yöntemiyle Yapısal Analizi", M. Sc. Thesis, TOBB ETU Institute of Sciences, Ankara.
13. **Chang, F.K. and Chang, K.Y.** (1987), "A progressive damage model for laminated composites containing stress concentration", Journal of Composite Materials, Vol. 21, No. 3, pp. 283-296.

14. **Li, A.** (2019), "Optimization of Composite Structures for Crashworthiness", M. Sc. Thesis, TU Delft Aerospace Engineering, Delft.
15. **Hörmann, M. and Wacker, M.** (2005), "Simulation of the crash performance of crash boxes based on advanced thermoplastic composite", 5th European LS-DYNA Users Conference, Birmingham.
16. **Aydoğdu, B., Karpat, F. and Kaya, N.** (2025), "Design and Optimization of an EV Battery Enclosure Using Machine Learning", Makina Tasarım ve İmalat Dergisi, Vol. 23, No. 1, pp. 1-7.
17. **Dagdeviren, S., Yavuz, M., Kocabas, M.O., Unsal, E. and Esat, V.** (2016), "Structural crashworthiness analysis of a ladder frame chassis subjected to full frontal and pole side impacts", International Journal of Crashworthiness, Vol. 21, No. 5, pp. 477-493.
18. **Forrester, A.I.J., Sobester, A. and Keane, A.J.** (2008), Engineering Design via Surrogate Modelling: A Practical Guide, John Wiley & Sons, Chichester.
19. **Hornik, K., Stinchcombe, M. and White, H.** (1989), "Multilayer feedforward networks are universal approximators", Neural Networks, Vol. 2, No. 5, pp. 359-366.
20. **Foresee, F.D. and Hagan, M.T.** (1997), "Gauss-Newton approximation to Bayesian learning", Proceedings of the International Joint Conference on Neural Networks (IJCNN'97), Houston, Vol. 3, pp. 1930-1935.
21. **Specht, D.F.** (1991), "A general regression neural network", IEEE Transactions on Neural Networks, Vol. 2, No. 6, pp. 568-576.
22. **Vapnik, V.** (1995), The Nature of Statistical Learning Theory, Springer, New York.
23. **Rasmussen, C.E. and Williams, C.K.I.** (2006), Gaussian Processes for Machine Learning, MIT Press, Cambridge, Massachusetts.

## APPENDIX

### A. Polynomial Response Surface Models (Q-RSM and C-RSM)

The polynomial response surface model $\hat{f}(x)$ is used as a surrogate for the actual response f(x). The general form of a second-order (quadratic) model for L design variables is expressed as follows [Myers and Montgomery, 1995]:

$$\hat{f}(x) = b_0 + \sum_{i=1}^{L} b_i x_i + \sum_{i=1}^{L} b_{ii} x_i^2 + \sum_{i=1}^{L-1} \sum_{j=i+1}^{L} b_{ij} x_i x_j \tag{7}$$

To model more complex curvatures, the cubic model adds higher-order interaction and pure cubic terms:

$$\hat{f}_{cubic}(x) = \hat{f}_{quadratic}(x) + \sum_{i=1}^{L} b_{iii} x_i^3 + \sum_{i \neq j}^{L} b_{iij} x_i^2 x_j + \sum_{i<j<k}^{L} b_{ijk} x_i x_j x_k \tag{8}$$

Where $b_0, b_i, b_{ii}, b_{ij}, b_{iii}, b_{iij}, b_{ijk}$ represent the unknown coefficients determined via least squares method.

### B. Artifical Neural Networks (ANN)

In this study, five different ANN architectures were evaluated and categorized into two primary groups based on their learning mechanisms and mathematical formulations.

Feedforward architectures (MLP, CFNN, and Fitnet)

This group includes MLP, CFNN, and Fitnet architectures. The fundamental processing unit in these architectures is the neuron, where the output of the $j^{th}$ neuron in the $l^{th}$ layer $a_j^{(l)}$ is computed as follows:

$$a_j^{(l)} = g\left( \sum_{i=1}^{N_{l-1}} w_{ji}^{(l)} a_i^{(l-1)} + b_j^{(l)} \right) \tag{9}$$

Where $w_{ji}^{(l)}$ represents the weights, $b_j^{(l)}$ is the bias term, and $g(\cdot)$ is the activation function [Hornik et al., 1989]. In this study, the hyperbolic tangent (tanh) function was employed for hidden layers:

$$g(z) = \frac{e^z - e^{-z}}{e^z + e^{-z}} \tag{10}$$

For the Cascade-Forward (CFNN) architecture, the connection matrix is expanded such that each layer receives signals from all previous layers, including the input layer:

$$a_j^{(l)} = g\left(\sum_{k=0}^{l-1}\sum_{i=1}^{N_k} w_{ji}^{(l,k)} a_i^{(k)} + b_j^{(l)}\right) \tag{11}$$

Bayesian regularization (weight optimization)

The weight optimization for MLP, CFNN, and Fitnet was performed using the Bayesian Regularization (trainbr) algorithm [Foresee and Hagan, 1997]. Unlike standard

backpropagation, this algorithm minimizes a cost function (F) that penalizes both the sum of squared errors ($E_D$) and the sum of squared weights ($E_W$):

$$F = \beta E_D + \alpha E_W = \beta \sum_{i=1}^{n} (y_i - \hat{y}_i)^2 + \alpha \sum_{j=1}^{m} w_j^2 \tag{12}$$

The objective parameters $\alpha$ and $\beta$ are automatically updated within a Bayesian framework to optimize the network's effective number of parameters. This mechanism is critical for the limited dataset used in this study to prevent overfitting.

Radial basis function (RBF) network

The RBF network, constructed via the (newrb) function, utilizes hidden neurons that compute the Euclidean distance between the input vector and a center $\boldsymbol{c_i}$:

$$\phi_i(x) = \exp\left(-\frac{|x - c_i|^2}{2\sigma^2}\right) \tag{13}$$

The final output is a linear combination of these radial basis functions: $\hat{y}(x) = \sum_{i=1}^{m} w_i \phi_i(x) + b$. The second-layer weights ($w_i$) are calculated deterministically using the Ordinary Least Squares (OLS) method.

Generalized regression neural network (GRNN)

The GRNN architecture is based on the Nadaraya-Watson kernel regression [Specht, 1991]. The prediction function is formulated as:

$$\hat{y}(x) = \frac{\sum_{i=1}^{n} y_i \exp\left(-\frac{|x - x_i|^2}{2\sigma^2}\right)}{\sum_{i=1}^{n} \exp\left(-\frac{|x - x_i|^2}{2\sigma^2}\right)} \tag{14}$$

Each training point $\boldsymbol{x_i}$ acts as a kernel center. Since the weights are directly assigned from the training data, the model is built in a single pass without the need for iterative gradient-based training.

### C. Support Vector Regression (SVR)

SVR is a kernel-based regression method that utilizes an ϵ-insensitive loss function [Vapnik, 1995]. The primary objective is to find a function that is as flat as possible while allowing for a maximum deviation of ϵ from the actual values of the training points.

For the linear ϵ-SVR formulation $f(x) = \boldsymbol{w^T x} + b$, the primal optimization problem is defined as follows:

$$min_{(w,b,\xi,\xi^*)} \quad \frac{1}{2}|\mathrm{w}|^2 + C\sum_{i=1}^{n}(\xi_i + \xi_i^*) \tag{15}$$

Under constraints:

$$y_i - w^T x_i - b \le \varepsilon + \xi_i, \qquad w^T x_i + b - y_i \le \varepsilon + \xi_i^*, \qquad \xi_i, \xi_i^* \ge 0$$

Here, C is the penalty parameter (BoxConstraint), ϵ is the tube width, and $\xi_i, \xi_i^*$ are the slack variables representing deviations outside the tube. Errors remaining within the tube are not counted as losses; this ε-insensitive structure provides SVR with a natural robustness against numerical noise in FEA simulations.

Dual formulation and prediction: By solving the dual problem in terms of Lagrange multipliers $(\alpha_i, \alpha_i^*)$, the prediction function is obtained as follows:

$$\hat{f}(x) = \sum_{i=1}^{n}(\alpha_i - \alpha_i^*)\langle x_i, x\rangle + b \tag{16}$$

Points that satisfy the condition $\alpha_i \neq 0$ or $\alpha_i^* \neq 0$ are called support vectors; the prediction is formed solely by the contribution of these points.

Non-linear expansion, kernel transformation: For non-linear relationships, instead of the inner product $\langle x_i, x \rangle$, a kernel function $K(x_i, x) = \langle \phi(x_i), \phi(\{x) \rangle$ is used; thus, the input space is mapped into a high-dimensional feature space without the need for explicit closed-form computation. The prediction function takes the following form:

$$\hat{f}(x) = \sum_{i=1}^{n} (\alpha_i - \alpha_i^*) K(x_i, x) + b \tag{17}$$

The kernel functions evaluated in this study are presented in Table 5.

Table 5. SVR Kernel Functions

| Kernel | Expression | Hyperparameters |
|---|---|---|
| **Linear** | $K(x_i, x_j) = x_i^T x_j$ | $C, \varepsilon$ |
| **Gaussian (RBF)** | $K(x_i, x_j) = exp(-\| x_i - x_j \|/2\sigma^2)$ | $C, \varepsilon, \sigma$ |
| **Polynomial ($d^{th}$degree)** | $K(x_i, x_j) = (1 + x_i^T x_j)^d, d \in \{2,3,4\}$ | $C, \varepsilon, d$ |

**D. Gauss Process Regression (GPR)**

GPR is a non-parametric approach that models the system response not as a deterministic function, but as a zero-mean Gaussian stochastic process [Rasmussen and Williams, 2006]. The model is expressed in the following form:

$$y(x) = h(x)^T \beta + f(x) + \varepsilon \tag{18}$$

Here, $h(x)^T \beta$ is the known basis function (constant mean in this study), $f(x) \sim GP(0, k(x, x'))$ is the zero-mean latent Gaussian process, and $\varepsilon \sim N(0, \sigma^2)$ is the independent measurement noise.

Prediction and uncertainty: When conditioned on the data X and y consisting of n training points, the conditional distribution for any test point $x^*$ is analytically obtained as follows:

$$\hat{\mu}(x^*) = h(x^*)^T\hat{\beta} + k(x^*, X)[K(X,X) + \sigma^2 I]^{-1}\left(y - H\hat{\beta}\right) \quad (19)$$

$$\hat{\sigma}^2(x^*) = k(x^*, x^*) - k(x^*, X)[K(X,X) + \sigma^2 I]^{-1}k(X, x^*) \quad (20)$$

The $(i, j)$ element of the covariance matrix $K(X,X)$ is calculated using the kernel function $k(x_i, x_j)$; meanwhile, $k(x^*, X)$ is the covariance vector between the test point and all training points. As seen in Equation (20), GPR produces not only a point estimate but also a variance

value that quantifies the reliability of that estimate; this feature makes GPR strategic in terms of constraint uncertainty management.

Hyperparameter estimation: The hyperparameters $\theta$ of the kernel function (length scale $\ell$, signal variance $\sigma_f^2$, and noise variance $\sigma^2$) are automatically determined via maximum likelihood estimation (MLE):

$$\hat{\theta} = arg\ max_{(\theta)}\left[-\frac{1}{2}log|K_\theta| - \frac{1}{2}y^T K_\theta^{-1} y - \frac{n}{2}log\ 2\pi\right] \quad (21)$$

Kernel functions: Eight different kernels were compared for each structural response. The standard kernel formulas in terms of the Euclidean distance $r = |x - x'|$ are presented in Table 6.

Table 6. GPR Kernel Formulas

| Kernel | Formula |
|---|---|
| **Squared Exponential (SE)** | $k(r) = \sigma_f^2 exp\left(-r^2/(2\ell^2)\right)$ |
| **Matérn 5/2** | $k(r) = \sigma_f^2\left(1 + \sqrt{5}r/\ell + 5r^2/(3\ell^2)\right)exp\left(-\sqrt{5}r/\ell\right)$ |
| **Matérn 3/2** | $k(r) = \sigma_f^2\left(1 + \sqrt{3}r/\ell\right)exp\left(-\sqrt{3}r/\ell\right)$ |
| **Rational Quadratic** | $k(r) = \sigma_f^2\left(1 + r^2/(2\alpha\ell^2)\right)^{-\alpha}$ |
| **Exponential** | $k(r) = \sigma_f^2 exp(-r/\ell)$ |

While standard kernel versions utilize a single length scale $\ell$ for all inputs, Automatic Relevance Determination (ARD) versions of the SE, Matérn 5/2, and Matérn 3/2 kernels learn an independent length scale $\ell_i$ for each input variable $(t_2, \theta, r)$. This approach allows the model

to identify the relative importance of each design parameter. In ARD cases, the squared Euclidean distance $r^2$ is redefined as follows:

$$r^2 = \sum_{i=1}^{L} \frac{(x_i - x_i')^2}{\ell_i^2} \tag{22}$$

# DEVELOPMENT OF AUGMENTED HAND SHADOW ART SYSTEM

**Hideo MIYACHI**, miyachi@tcu.ac.jp Tokyo City University, 2248551, Yokoyama, Japan

## ABSTRACT

Shadow puppetry is an art form created by projecting three-dimensional objects onto a two-dimensional screen. In Japan, in particular, hand shadow puppetry, using human hands, has been a beloved part of Japanese culture since the 17th century. However, since many shadow puppet performances are educational shows aimed at children, it is difficult to operate them on a self-sustaining basis, and they tend to be supported by subsidies from the national government and local authorities for the purpose of cultural preservation. This research aims to enhance the artistic value of hand shadow puppetry and achieve economic sustainability by developing an advanced system. The proposed system employs image processing and AI to add color to typically monochromatic images and enables a single performer to manipulate multiple shadows simultaneously. This paper presents the proposed prototype system and the enhanced shadow puppetry video created as a trial.

**Keywords:** Shadow puppetry, Augmented hand shadow, Image processing, Pose estimation

## 1. INTRODUCTION

Shadow puppetry is an art form created by projecting three-dimensional objects onto a two-dimensional screen, and it is performed widely across the world. Several forms of shadow puppetry are inscribed on the UNESCO Representative List of the Intangible Cultural Heritage of Humanity, including Indonesia's "Wayang Puppet Theatre" (No. 00063, 2008), Turkey's "Karagöz" (No. 00180, 2009), and "Chinese Shadow Puppetry" (No. 00421, 2011) [1]. These traditional performing arts use puppets made from animal skins to tell stories through shadow puppetry.

In contrast to puppet-based methods, Hand Shadow Puppetry—which uses human hands and fingers instead of physical puppets—has been a popular art form in Japan since the Edo period(1603-1868). To this day, theater companies such as "Kageboushi" continue to give public performances. However, organizations dedicated to preserving traditional performing arts, including shadow puppetry, face serious challenges such as a shortage of

successors and difficulties in securing financial stability. As a result, many groups find themselves forced to rely on the tourism industry or on cultural preservation grants from the national and local governments. With the goal of enhancing the artistry of hand shadow puppetry, the authors have begun developing an advanced system that integrates information technology. This project is conducted with the cooperation of Mr. Shuichi Iida [2], a performer from "Kakashiza"—Japan's first professional shadow play theater troupe, which disbanded in 2025. This manuscript presents an overview of the system and introduces videos created as a trial.

## 2. RELATED WORKS

Research on shadow puppetry can be categorized into three primary areas: puppet making techniques, the preservation and transmission of traditional skills, and the expansion of artistic expression. In the field of puppet making techniques, studies focus on the relationship between three-dimensional (3D) forms and two-dimensional (2D) silhouettes. Notable examples include a study that calculates 3D volumes from input shadow images [3] and a method for rapidly creating digital shadow puppets using classified templates [4]. Regarding the transmission of hand shadow puppetry skills, a system has been proposed to simulate the joint movements of fingers required to reproduce specific shadow shapes from a given input image [5]. In terms of expanding the expressive potential of shadow puppetry—which is also the objective of this study—a system called "Shadow Play" has been proposed, where generative AI collaborates with human performers. However, specific artistic outputs or case studies from this system are not clearly documented in the literature [6]. Another system proposed by Qi Guo et al. [7] also aims for human-AI collaboration; however, its implementation is limited to controlling the movement of shadow puppets based on poses estimated via MediaPipe. In this case, the system serves merely as a control interface for shadow avatars rather than a means to enhance the inherent artistry of the performance.

Similar to "Shadow Play," our proposed system captures hand shadows via camera and employs AI and image processing to elevate the artistic quality. However, our approach does not rely primarily on generative AI. Instead, it maintains the hand shadow itself as the central element, utilizing AI and image processing specifically to extend and augment its expressive capabilities. The following sections report on the specific system configuration and the prototype videos produced.

## 3. RELATED WORKS

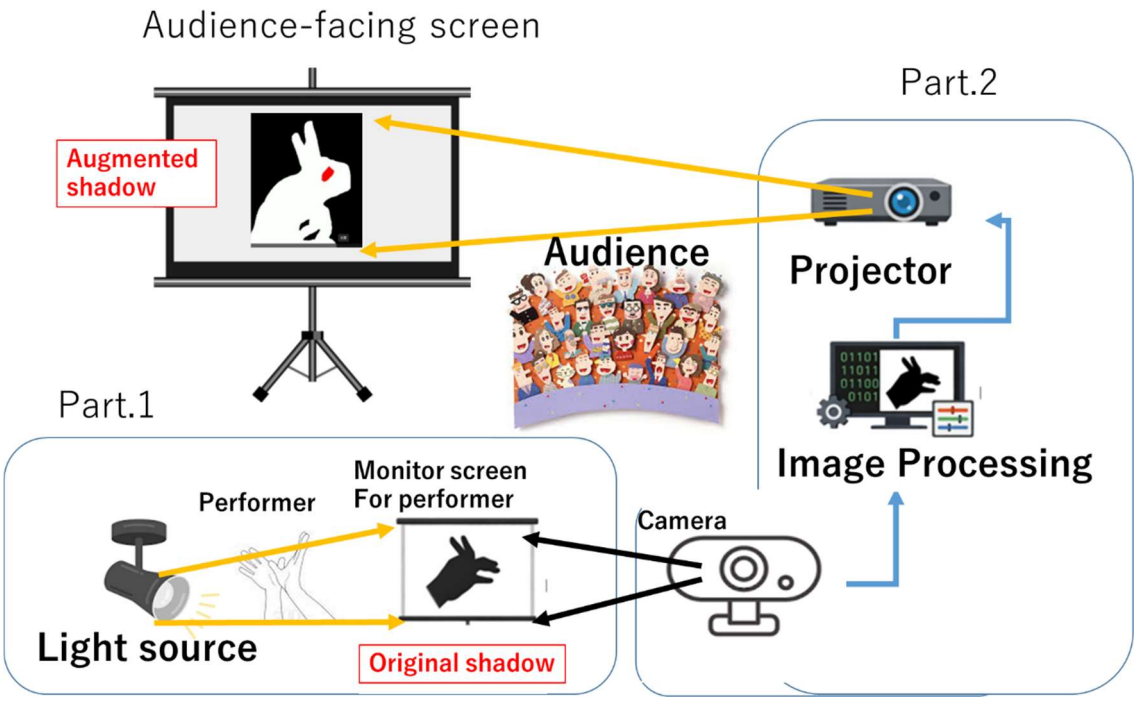



Fig.1 Overview of the augmented hand shadow system

The configuration of the proposed system is shown in Figure 1. The system consists of two parts. Part 1 (as indicated in Fig. 1) represents the existing conventional hand shadow puppetry setup. Part 2 represents the expanded component, with the image processing phase within this part being the primary focus of this paper. In the final implementation, the camera will capture the shadow images from Part 1 as they appear on the screen, and the system will provide the audience with an enhanced visual experience (Augmented Shadow Puppetry) in real-time through image processing. In this manuscript, we present three types of prototype videos generated by applying these enhancements to captured hand shadow footage.

Part 1 remains unchanged from conventional setups because the performers do not act by looking at the physical shape of their hands; rather, they perform by monitoring the images projected onto the screen. Performers must navigate the spatial relationship between their hands, the light source, and the screen. For example, when representing two eyes using both hands, it is often impossible to place both hands at an equal distance from the screen. If the hands are crossed, one hand will inevitably be closer to the screen while the other is further away. If the performer simply forms identical circles with both hands, the shadow of the rear hand would appear larger than the front one. To compensate for this, players recognize subtle differences in distance and adjust their fingers while observing the silhouette on the screen to ensure the shadow forms the correct intended shape. Therefore, it is essential that the configuration of Part 1 remains the identical shadow play set that the performers use in their daily practice.

Part 2 is the augmented component proposed in this study. A camera captures the hand shadows from the same perspective as a typical audience member. This footage then undergoes image processing, and the resulting augmented shadows are projected onto the audience-facing screen.

## 4. IMAGE PROCESSING TRIALS

### 4.1 Colorization of shadows

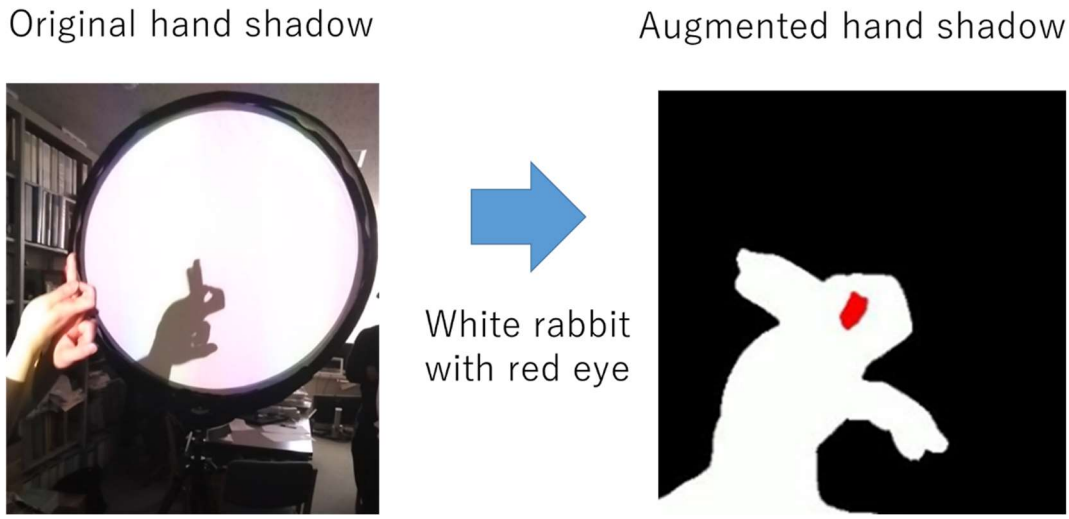



Fig.2 Augmented hand shadow of a rabbit with a white body and red eyes.

Shadow puppetry is fundamentally a monochrome medium. Regardless of the actual color of the subject—such as a white rabbit—the resulting shadow remains black. To address this limitation, our first trial involved binarizing and inverting the input image to render the rabbit white against a black background. Figure 2 shows the first example of augmented shadow art. The original image was binarized, and by inverting the black and white values, the rabbit was rendered white and the background black. Furthermore, we applied a colorization process to the eye area, rendering it in red. The resulting video demonstrates a departure from traditional silhouettes by introducing specific color elements to enhance the character's identity. The computational load for this image processing is minimal due to its simplicity. However, it should be noted that the original shadow images are not true binary images. The luminance of the white background varies depending on the distance from the light source, and the edges of the shadows are often blurred rather than sharp due to light diffraction (penumbra). While the original footage for this study utilizes a projector as the light source, if a flame-based light source were used instead, the flickering of the flames would become an integral part of the performance. Therefore, it is necessary to treat the binary image as a mask and generate the final video by taking the luminance distribution of the original image into careful consideration.

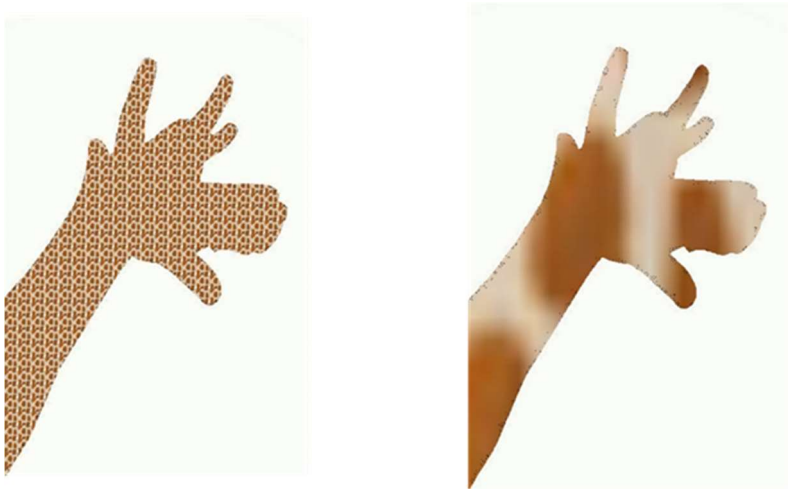


Fig.3 Augmented hand shadow of a giraffe with a color pattern texture applied by parallel projection mapping

Another example of colorizing shadows is shown in Figure 3. In this case, while maintaining the white background, a texture—such as a giraffe-like pattern—is applied to the black shadow regions using parallel projection mapping. With simple parallel projection mapping, the applied patterns do not follow the movement of the animal silhouettes. It makes an impression that the shadows are acting as "windows" through which a static background pattern is visible. To ensure that the patterns track the movement of the shadows, UV mapping is required. Assigning appropriate UV coordinates to a dynamic two-dimensional shadow is another challenge.

### 4.2 Applying video into the background

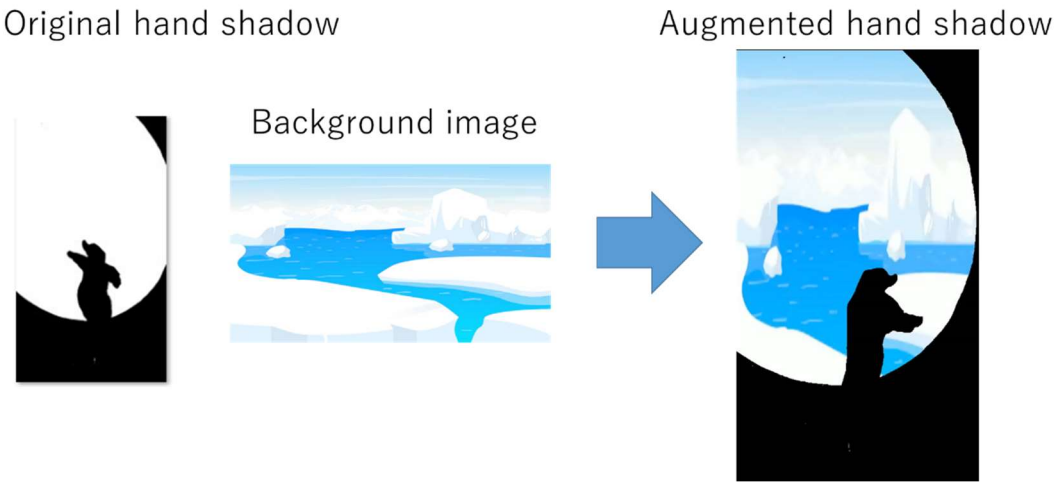



Fig.4 Augmented hand shadow of a penguin with an Antarctic-like landscape as the background.

The second trial involves the application of imagery to the background. While the augmented shadow in Figure 3 mapped a texture onto the shadow area itself, the 2nd augmented shadow in Fig.4 demonstrates a case where the image is mapped onto the background region instead. This process is a straightforward operation where the binary image is used as a mask to perform a summation (blending) of images. Compared to the approach in Figure 3, this method preserves the original shadow exactly as it is, which we believe helps maintain the authentic aesthetic of the shadow play. In the prototype video, a dynamic visual effect is created by scrolling the background image to the left. Furthermore, by applying the hand pose estimation discussed in the next section, it appears feasible to control the direction and speed of the background scrolling in response to the penguin's movements.

### 4.3 Shadow duplication

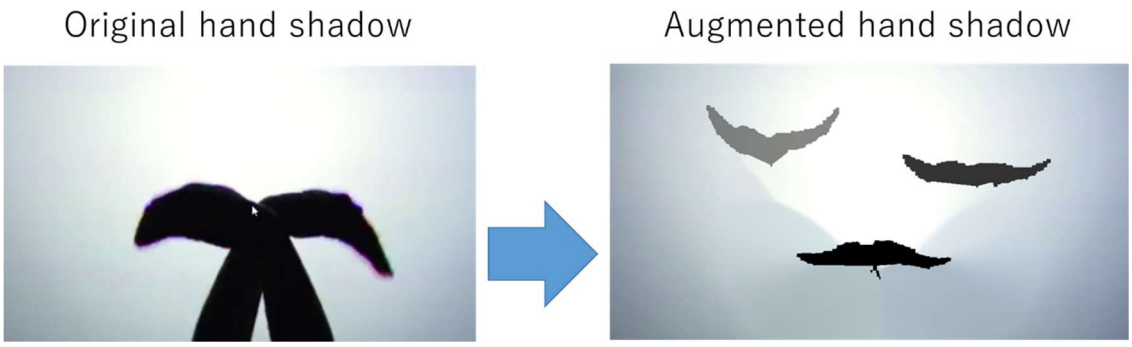



Fig.5 Augmented hand shadow of a single bird transformed into a formation of three birds flying (the original shadow puppet footage is from reference [8]).

The third augmented shadow involves extracting a single bird shadow and duplicating it to create a visual of three birds flying in formation. In this case, we implemented an expansion of the hand shadow puppetry by utilizing pose estimation. By performing fine-tuning on YOLO's human pose estimation [9] data with approximately 50 additional frames of hand shadow images, we achieved highly accurate pose estimation for the shadows.

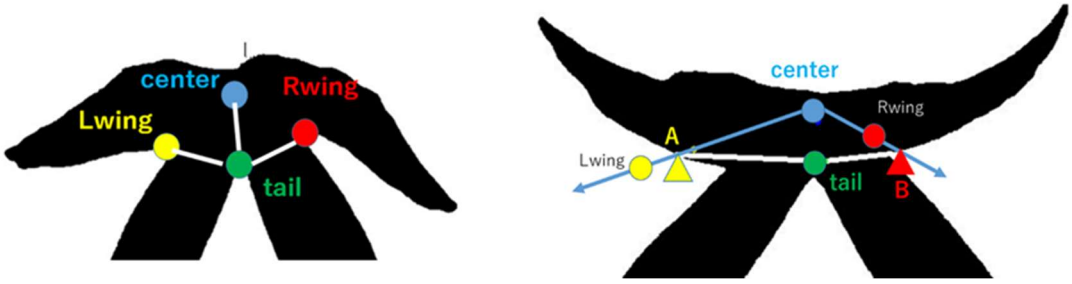



Fig.6 (a) Four key points used in estimating bird posture (b) Separation line to separate the bird and the shadow of the wrist

This pose estimation was designed to separate the bird silhouette from the wrist portion of the performer. As shown in Figure 6(a), we trained the model on four specific key points: "Rwing" and "Lwing" representing the boundaries between the wings and the wrist, "tail" at the intersection of the two wrists, and "center" at the perceived center of the bird. Theoretically, if Rwing, Lwing, and the tail are located precisely on the boundary between black and white, the bird could be extracted along the lines connecting these three points. However, since the estimated key points do not exactly on the boundaries, we employed a searching method indicated in Fig. 6(b). Starting from the "center," the search tracks pixels along a ray extending toward Rwing (or Lwing) until it reaches the first white pixel, defined as Point B (or A). The bird is then isolated using the lines connecting Point A, the tail, and Point B. Through this process, we obtained a time-series dataset of the bird shadow isolated from the wrists. To create the three-bird formation, the following steps were taken:

1. Background Generation: A background image (bright in the center and dark toward the edges) was generated by interpolating the shadow regions of the original image.

2. Duplication and Scaling: The bird image was scaled down to 50% of its original size and arranged in an inverted triangle formation (Fig. 5).

3. Depth Cues: To simulate depth, the further away the bird is, the higher the percentage of white background blended in.

4. Time-offset playback: Since the three birds lack natural variation if their movements are perfectly synchronized, each frame was composited with a bird shifted by two frames from the time-series bird data.

Note that this extraction method shown in Figure 6 was specifically designed for only this video; it is not universally applicable to all shadow types, meaning appropriate methods must be devised for each performance. In this example, shadow pose estimation was used to separate the shadow's wrist from the bird. However, it would also be possible to apply pose estimation to the augmented shadow process for rabbits described in Section 4.1 and map the image to the eye position.

## 5. CONCLUSION

In this paper, we proposed a system designed to enhance the expressive potential of hand shadow puppetry by integrating image processing and machine learning while preserving the original silhouette's essence as much as possible. Based on this proposal, we introduced three types of prototype augmented shadow videos. It should be noted that these prototype videos were created by processing pre-recorded footage and were not generated in real-time. Furthermore, the algorithms used to produce these augmented shadows were specifically tailored to these three videos and currently lack general applicability. In the future, we plan to

develop a real-time processing system and explore more versatile augmented shadow puppet creation algorithms that can be applied to wider range of contents.

**Acknowledgements**

The authors would like to express their sincere gratitude to Mr. Shuichi Iida, a shadow play artist, for his invaluable lectures on puppetry and for providing the performance data essential to this research.

**References**

[1] UNESCO Intangible Cultural Heritage website https://ich.unesco.org/en/home

[2] Kakashiza Shadow Play Theatre: An Interview with Shuichi Iida, 2019/5/3 Interview

PAPET PLACE NEWS, https://puppetplace.wordpress.com/

https://puppetplace.wordpress.com/2019/05/03/kakashiza-shadow-play-theatre-an-interview-with-shuichi-iida/

[3] MITRA N. J., PAULY M.: Shadow art. ACM Transactions on Graphics 28(5),(2009), 1-7, https://doi.org/10.1145/1618452.1618502

[4] Teng Li, Weiqun Cao: Research on a method of creating digital shadow puppets based on parameterized templates, Multimedia Tools and Applications 80 (2021),20403-20422

[5] Aalok Gangopadhyay, Prajwal Singh, Ashish Tiwari, Shanmuganathan Raman: Hand Shadow Art: A Differentiable Rendering Perspective, Pacific Graphics (2023) https://doi.org/10.48550/arXiv.2505.21252

[6] Jesse Josua Benjamin, Joseph Lindley : Shadowplay: An Embodied AI Art Installation, The 18th International Conference on Tangible, Embedded, and Embodied Interaction,(2024)

[7] Qi Guo, Yixuan Li, Yaoxi Kuang, Shuanbo Qin, Tao Chen, Junying Zeng : Lightweight Dual-Agent Architecture for 2D Shadow Puppetry: Real-Time Edge Deployment and Evaluation, IEEE Access PP(99):1-1, (2026), DOI:10.1109/ACCESS.2026.3674872

[8] Gekidan Kakashiza [Shadow Play Theatre KAKASHIZA]. (2020, March 5). Oshiete! Kagejo!! -Kagee joshi no tekagee koza- Dai-ikkai "Kayoppe no shomen-dori" [Teach me! Shadow Woman!! -Shadow play girls' hand shadow puppet workshop- Lesson 1 "Kayoppe's Front-facing Bird"] [Video]. YouTube. https://www.youtube.com/watch?v=Sb2xom5H_po

[9] D. Maji, S. Nagori, M. Mathews, and P. Poddar, "YOLO-Pose: Enhancing YOLO for Multi Person Pose Estimation Using Object Keypoint Similarity Loss," in Proceedings of the

IEEE/CVF Conference on Computer Vision and Pattern Recognition (CVPR) Workshops, 2022, pp. 2637-2646.

# An Approach to Mental-Image Based Cognition for Intuitive Human-Robot Interaction --- Focusing on Human Ability of Problem Finding and Solving ---

**Masao Yokota**, *yokota@fit.ac.jp* Fukuoka Institute of Technology, Fukuoka, Japan

**Rojanee Khummongkol**, *rojanee.k@ku.ac.th* Kasetsart University, Kamphaeng Saen Campus, Nakhon Pathom, Thailand

## ABSTRACT

A methodology is proposed to provide robots with problem finding/solving ability based on a mental image model.

**Keywords:** human-robot interaction, artificial intelligence, natural language understanding, cognition model, problem finding/solving

## INTRODUCTION

Nowadays, great progress in artificial intelligence (AI) and robotics may well predict a world in the very near future where ordinary people and home robots will be interacting very naturally in casual scenes, finding and solving various problems cooperatively. Particularly, in the field of AI, deep-learning (DL) based methodologies have been widely utilized to simulate some aspects of human cognition, such as pattern recognition (based on discriminative AI) and natural language processing (based on generative AI (GAI) with large language models (LLMs)), with remarkable outcomes. In fact, GAI improves technical effectiveness in this field in comparison with traditional rule-based AI. However, many conventional AI models, particularly those based on DL, are not transparent or explainable in reasoning, which makes it difficult to understand how they make decisions. Moreover, all benchmarks of the applications [e.g., Fatemi, 2024] are based on behaviorism and do not require the process from input to output to be cognitively human-like in the sense of strong psychological equivalence [Winograd, 1978], [ Levesque, 2011], [Yokota, 2019]. Actually, several serious limitations of GAI are issued in its application to real robots where well-coordinated integration of perception, action, and knowledge is required for human-like interaction with the physical world [Yokota, 2019], [Obrenovic, 2025], [Ma, 2026].

Just reflecting our daily cognitive experiences, for example, natural language understanding (NLU) by human is essentially an inferential process that creatively comprehends meaning based on the mental images (or imagery) evoked or recalled by natural language (NL) expressions, rather than a probabilistic process based on specific statistics concerning natural language expressions [Yokota, 2019]. However, the specific cognitive and neural mechanisms of such mental-image-based cognition (including NLU) remain under exploration in the fields of brain and mind research such as computational neuroscience and artificial intelligence [Daniel & Langland-Hassan, 2024]. At the present stage, neuroimaging can be the most powerful tool to observe real-time neuronal activities in the brain but has not yet come to be able to map complex semantic contents of external expressions (e.g., descriptions in natural language) to neuronal activities as mental images that people experience self-reflexively [Papanicolaou, 2023].

Considering the importance of mental-image based cognition and the difficulty of conducting research on mental image itself, Yokota, M. has proposed a computational model of mental image in his original semantic theory named Mental Image Directed Semantic Theory (MIDST), within traditional rule-based AI. MIDST has been applied to simulation of human mental-image based NLU, demonstrating its adequacy, theoretically by good applicability to formal computation and experimentally by good agreement with human performances [Khummongkol & Yokota, 2016; 2023]. In MIDST, mental images, not limited to visual but ominisensory, are modelled as abstract line-drawings discerned with symbolic tags, called loci in attribute spaces, in a perfectly language-free way, to be formalized in a formal language $\boldsymbol{L_{md}}$, a logic-based knowledge representation language (KRL) [Yokota, 2019]. In contrast to the widespread adoption of black-box DL-based methodologies, this implies that formal logic can be applied to transparent multimedia understanding, enabling AI to fully understand information elements expressed individually in various media such as language, images, and gestures, and to enable translation between different media, as shown in Figure 1.

Actually, the application system named conversation management system (CoMaS) can semantically process natural language, town map, and animation in a uniform way via $\boldsymbol{L_{md}}$ expression [Khummongkol & Yokota, 2016; 2023].

The present paper describes a problem finding/solving (PFS) methodology based on $\boldsymbol{L_{md}}$ representation to be expected in such a symbiotic world of ordinary people and robots as mentioned above. Here, ordinary people are usually assumed to be faithful to their innate cognition in everyday life. For example, they are more likely to produce intuitive or subjective

S1 and are considered less likely to produce scientific S2 unless they face inconveniences or serious situations like a physics exam [Yokota, 2019]. In other words, we ordinary people are accustomed to cognizing and expressing things as we percept since childhood, even though the truth is often otherwise as known well by various kinds of visual illusions.

(S1) We are seeing stars deep in space.

(S2) We are seeing the past images of stars deep in space.

The following is composed of 5 sections. The first section presents some essential features of mental images as natural language word concepts in correspondence with the cognitive processes to acquire them. The second section gives a brief description about the mental image model and its formulation language $L_{md}$ proposed in MIDST. The third section describes the methodology for PFS in $L_{md}$. The fourth section introduces the application system CoMaS, focusing on its PFS mechanism in NLU. Lastly, the fifth section discusses the adequacy of the work and concludes the paper.

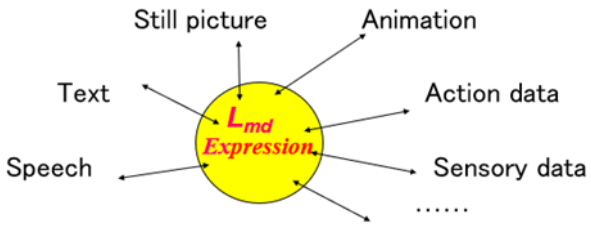



Figure 1. Intermedia translation via $L_{md}$ expression

## NATURAL LANGUAGE, COGNITION AND MENTAL IMAGE

Figure 2 shows the PFS environment intended here, so called, intuitive human-robot interaction, where robots sense and act in the work field to find and solve problems there, communicating with ordinary people, in a multi-modal way centered on human (natural) language.

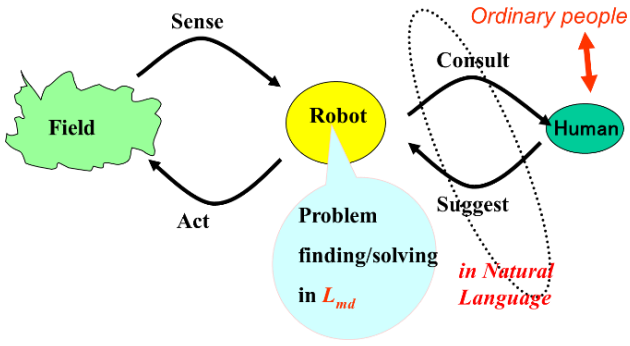



Figure 2. Intuitive human-robot interaction centered on natural language

The most essential capability for the robots there is that of integrative multimedia understanding, namely, total comprehension of natural language, robotic sensation, and robotic action, translated to $\boldsymbol{L_{md}}$ expressions, accepting such intuitive expressions as S3 and S4 referring to the same scene. This seemingly contradiction can be resolved by taking into account the differences in the scanning direction of human attention along the path [Yokota, 2019].

(S3) The ladder goes down to the waterway.

(S4) The ladder comes up from the waterway.

Therefore, it is quite obvious that we ordinary people acquire and form concepts of things as mental images through our innate sensory systems before and after language acquisition, hereafter to be called natural concepts, regardless of whether they are referred to by words or not. MIDST makes a special effort to formalize abstractness, vagueness, and subjectivity of natural concepts to be computable for systematic NLU, especially for spatiotemporal (4D) language understanding. For example, the seemingly semantic inconsistency between S3 and S4 concerns subjectivity (of the observer). As for abstractness and vagueness, consider the assertion S5 and the questions S6-S9. Perhaps, S6 and S7 are easily affirmed by consulting the mental image of S5 but it is not informative enough to answer S8 or S9. That is, the meaning of S5 is too abstract to affirm or deny S8 or S9. It is noticeable that we can imagine only *vaguely* the regions of Quebec and London S5.

(S5) Kate traveled with the box from Quebec to London.

(S6) Did the box move from Quebec to London.

(S7) Did Kate carry the box from Quebec to London?

(S8) Did Kate carry the box *in her pocket*?

(S9) Was the box *colorful*?

That is, word images and its composition, namely, sentence images are essentially abstract and vague but have logical structures definite enough to entail other sentences as images in the same level of abstractness. The mental image evoked by S5 could be modeled as shown in Figure 3, where *the circles refer to the regions occupied by the named entities according to Venn diagram; the names are alternatives for ultimate conceptual or general images of their referents; the broken arrow indicates Kate's replacement from Quebec to London; the used colors are absolutely meaningless.*

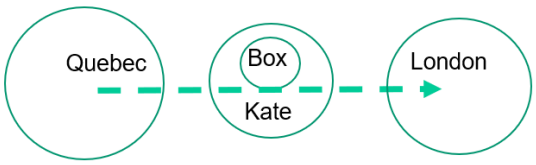



Figure 3. Exemplification of abstract mental image of S5.

However, it would be semantically not clear or interpretable *without its caption in italic given above*. What is worse is that such a mental image model is not general, limited to some special kinds of spatiotemporal relations among physical entities. For another example of abstractness, consider the transitive verb "(x) pass (y)" with reference to S10–S13. As can be easily imagined, S11–S13 concretize the abstract situation in S10 in the form of the kinetic effect from Jim to the apple. This suggests that the kinetic effect, and more broadly causal effects, must ultimately be symbolized because they are abstract in the mental representation. In MIDST, "effect from A upon B" is to be symbolized as "A→B".

(S10) Jim passed me the apple.

(S11) Jim passed me the apple by throwing it.

(S12) Jim passed me the apple by tossing it.

(S13) Jim passed me the apple by rolling it.

As a result, this fact provides a legitimate reason to assign specific special symbols to abstract matters in mental images, as indicated by the names shown in Figure 3. This is also the case for modeling negated mental image. For example, consider S14. It is most likely for us to recall a certain image of lion, tagged with a special *symbol* to negate it (or followed by a special *operation* to eliminate it), corresponding with "~" in the logical formula "~lion(A)" [Yokota, 2019].

(S14) The object A is not a lion.

## MENTAL IMAGE MODEL AND $L_{md}$

In MIDST, mental images are modeled as Loci in Attribute Spaces. For example, consider the triangular red object shown in Figure 4, which moves in a sinusoidal trajectory. We then assume that a corresponding sensation (i.e., an image) arises in the observer's mind. The moving triangular red object is then perceived in the observer's mind as loci in three attribute spaces: Location, Color, and Shape. As can be easily imagined, attribute spaces here correspond to the human sensory systems, and loci represent sensations of phenomena inside or outside the human mind. From the perspective of artifacts, such attribute spaces represent

specific measuring instruments or sensors such as chronographs, barometers, and thermometers, and loci represent the movements of their indicators.

As shown in Figure 5, loci in attribute space are articulated with *Atomic Locus* over a certain *absolute time* interval $[t_i, t_f]$ and formulated in the formal language $\boldsymbol{L_{md}}$ for predicate logic as a formula (1) called *atomic locus formula*, where the first two arguments are sometimes referred to as Event Causer and Attribute Carrier, respectively. Here, the interval $[t_i, t_f]$ is suppressed and, as necessity, indicated explicitly by an additional atomic locus in the attribute space of 'Time point' corresponding to the chronograph [Yokota, 2019]. A logical combination of atomic locus formulas defined as a well-formed formula (i.e., wff) is simply called *locus formula*.

$$L(x,y,p,q,a,g,k) \quad (1)$$

The following is the intuitive interpretation of the atomic locus formula (1).

***Matter 'x' causes Attribute 'a' of Matter 'y' to keep (p=q) or change (p ≠ q) its values temporally (g=Gt) or spatially (g=Gs) over a certain absolute time-interval, where the values 'p' and 'q' are relative to the standard 'k'.***

The locus indicates monotonic change (or constancy) of the attribute in time domain ($g=G_t$) or spatial domain ($g=G_s$). The former is called *temporal change event*, and the latter is called *spatial change event*. These types of events correspond to *temporal gestalt* and *spatial gestalt*, so called in psychology, and for example, they are applied respectively as (2) and (3) in distinguishing between S15 and S16 (LOC: attribute Location).

(S15) The truck runs from Nagasaki to Fukuoka.

(S16) The expressway runs from Nagasaki to Fukuoka.

$$(\exists x,y,k)\ L(x,y,\text{Nagasaki},\text{Fukuoka},\text{LOC},G_t,k) \wedge \text{truck}(y) \quad (2)$$

$$(\exists x,y,k)\ L(x,y,\text{Nagasaki},\text{Fukuoka},\text{LOC},G_s,k) \wedge \text{expressway}(y) \quad (3)$$

Suppose that a locus in an attribute space is the scan path of attention controlled by the observer. These representations reflect differences in the spatiotemporal relationship between the attribute carrier (y) and the observer's focus of attention (FAO). That is, in S15, it is assumed that the FAO moves together with the truck, whereas in S16, it is assumed to move alone along the expressway.

For example, the natural concept “(x) fetches (y)” is a temporal change event concept, whose locus is shown in Figure 6, and is formulated as in (4). Here, the symbol λ is used to explicitly specify free variables, and the special symbols • and Π are tempo-logical connectors, called “Consecutive AND” and “Simultaneous AND”, and are specially introduced into the knowledge representation and reasoning system to indicate both logical and temporal relationships.

$$(\lambda x,y)\text{fetch}(x,y)\Leftrightarrow(\lambda x,y)\ (\exists p_1,p_2,k)\ L(x,x,p_1,p_2,LOC,G_t,k)\bullet$$

$$(L(x,x,p_2,p_1,LOC,G_t,k)\Pi L(x,y,p_2,p_1,LOC,G_t,k))\wedge x\neq y\wedge p_1\neq p_2, \quad (4)$$

As another example, the natural concept “(x) is between (y and z)” is a concept of spatial change event illustrated in Figure 7, involving an unreal and purely psychological matter or product called “Imaginary Spatial Region (ISR)”, formulated as (5), where DIR represents the attribute Direction.

$$(\lambda x,y,z)\text{between}(x,y,z)\Leftrightarrow(\lambda x,y,z)(\exists u,w,p,k_1,k_2)\ (L(w,u,x,y,LOC,G_s,k_1)\bullet L(w,u,y,z,LOC,G_s,k_1))$$

$$\Pi L(w,u,p,p,DIR,G_s,k_2)\wedge ISR(u)\wedge x\neq y\wedge y\neq z\wedge z\neq x \quad (5)$$

The ISR here is assumed to be the linear spatial gestalt among the three objects, to be scanned by FAO. An object (e.g., *x*) placed at a value term is to represent its value (e.g., the location occupied by *x*) at the time. It is noticeable that the DIR value *p* allows any perceivable direction with or without a name such as “right” and “upward”, quite distinct from conventional approaches based on text-data learning such as GAI with LLM.

MIDST defines every kind of word concept in a specific format articulated attribute by attribute as shown above. For example, an entity (e.g. oil, rock, rain) is conceptualized as an integration of perceptible events in which it is involved, to be utilized for its recognition or its prediction about what will happen about it, namely, its ontology, implying its potential as well. According to this scheme, for example, snow can be defined in a simplified form as (6), reading “Snow usually moves from the sky to the ground (being allowed to move otherwise), has no length, is always cold, sometimes changes from solid into liquid (being allowed not to melt), is usually white (being allowed to be dyed otherwise in such a condition as environmental pollution), …”.

$$(\lambda x)\text{snow}(x)\Leftrightarrow(\lambda x)(L^{\Diamond}(_,x,Sky,Ground,LOC,G_t,_)\wedge L^{*}(_,x,/,/,LNG,G_t,_)\wedge$$

$$L^{\circ}(_,x,Sld,Lqd,QLT,G_t,_)\wedge L^{*}(_,x,Cld,Cld,TMP,G_t,T_p)\wedge L^{\Diamond}(_,x,Wht,Wht,COL,G_t,_)\wedge\ \ldots) \quad (6)$$

Here,

LNG, QLT, TMP, COL: “length”, “temperature”, “quality”, “color” (as attributes);

_: abbreviation of some variable bound by ∃; *: “always”; °: “sometimes”; ◊: “usually”;

/ : “no value” (=abbreviation of ~(∃p)); Sld: “solid” in quality; Lqd: “liquid” in quality; Cld: “cold” as perceived temperature ($T_p$); Wht: “white” in color.

This definition format is used to infer the possibility of an entity in order to detect semantically unusual expressions, such as “short snow,” in conjunction with the natural concept of “short” as defined in (7). This contradicts (6) in the value of length (LNG). NLU systems based on MIDST are designed to sense such semantic anomaly for robots not to honestly obey to such a mischievous or ridiculous order as “find short snow in the fields” only to make them work in vain [Yokota, 2019].

$$(\lambda x)\mathrm{short}(x)\Leftrightarrow(\lambda x)(\exists y,p,k)\mathrm{L}(y,x,p,p,\mathrm{LNG},G_t,k)\wedge p<k \qquad (7)$$

Here, “$p < k$” indicates that the value ($p$) is less than a specific reference value ($k$).

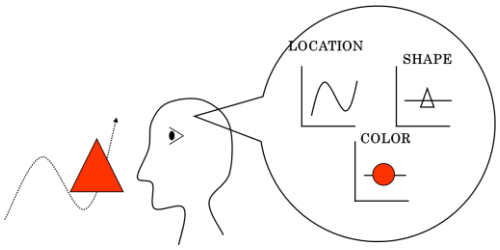



Figure 4. Mental image model as loci in attribute spaces

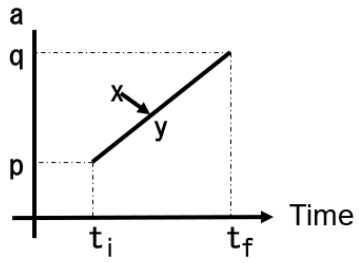



Figure 5. Atomic locus

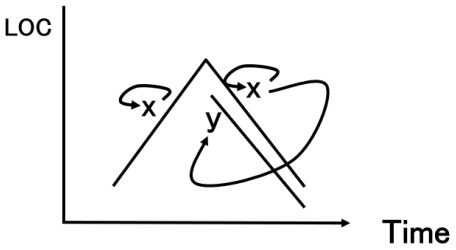



Figure 6. Locus of “(*x*) *fetch* (*y*)”

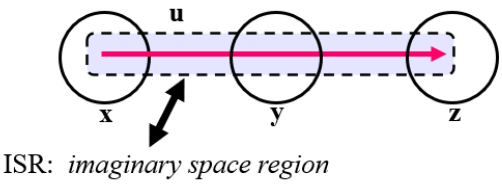



Figure 7. Pictorial interpretation of (5)

## PROBLEM FINDING / SOLVING IN *Lmd*

In the real world, robots must confront with complex problems quite different from well-structured simple ones in certain game or toy worlds for which problem-solving is almost solution-searching within a definite problem space [Newell and Simon, 1972]. Heylighen, F. emphasized the importance of representation to formulate or structure complex problems well enough for systematic computation or solution in his metatheory about problem-formulation [Heylighen, 1988]. However, the most important unresolved issue regarding PFS to date has

been how to design a KRL for systematic representation and computation that can be applied to complex real-world problems. To challenge this difficulty, Yokota, M. has proposed $\boldsymbol{L_{md}}$ as a candidate for such a KRL, considering its application to such an environment as shown in Figure 3 where well-coordinated integration of perception, action, and knowledge is required for robots to collaborate with ordinary people [Yokota, 2019]. The formal language $\boldsymbol{L_{md}}$ has already shown a remarkable adequacy and uniqueness in representation and computation of spatiotemporal knowledge in PFS concerning NLU [Khummongkol and Yokota, 2016; 2023]. The following describes how $\boldsymbol{L_{md}}$ works for problem finding and solving within predicate logic.

Definition of problem and task:

According to Heylighen, F. [Heylighen, 1988], these problems may fall into the category of *Exploration problems* for robots that are partially or completely unfamiliar with their environment. These can be broadly classified into two subcategories: A) Creation problems and B) Maintenance problems [Yokota, 2019]. In general, the former is considered more difficult than the latter, and robots would often come to solve it in cooperation with people while the latter can be simple enough for them to find and solve autonomously.

A) Creation Problem: goods designing, novel writing, etc.

B) Maintenance Problem: security keeping, housekeeping, etc.

Imagine a situation where a robot must find and solve related problems in order to accomplish a task assigned by a human in such an environment as shown Figure 2. The robot is required to determine tasks in order to solve problems in the world. Generally, in the process of solving such problems, it must interpolate some transition event $X_T$ between the two events, *Current Event* ($X_C$) and *Goal Event* ($X_G$), as shown in (8).

$$X_C \bullet X_T \bullet X_G \tag{8}$$

According to this formalization, a problem $X_P$ is defined as $X_T \bullet X_G$, and the robot's task is defined as its realization, similar to traditional AI as described by Russell, J.J. and Norvig, P. [Russell & Norvig, 2010], etc. In traditional AI, the problem is defined as the difference or gap between the current state and the goal state, and the task is defined as its cancellation. Here, the term event is preferred over the term state, and instead, states are defined as static events corresponding to level loci. Events in the world are described as loci in particular attribute spaces, and problems are detected by units of atomic loci. For example, using $\mathbf{P_{V2}}$ (*Postulate of Identity of Assigned Values*), which signifies the continuity of attribute values, event X in (9) is inferred as (10) where the cause of the event z' may be different from z. For brevity, in the

following formulation, (∀…) and (∃…) mean all the variables but those bound otherwise are bound by the very quantifiers.

$L(x,y,q_1,q_2,a,g,k)\bullet X\bullet L(z,y,q_3,q_4,a,g,k)$ (9)

$L(z',y,q_2,q_3,a,g,k)$ (10)

**$P_{V2}$.** $(\forall\ldots)L(x,y,p_1,q_1,a,g,k)\bullet L(z,y,p_2,q_2,a,g,k).\supset.q_1=p_2$

Creation problem finding and solving:

Consider such a verbal command as S17 to a robot named Robby from a human. Robby is operating a helicopter. He interprets S17 as (11), the goal event $X_G$ here, concerning the attribute of the *helicopter* ($H_6$), *Height* (*HGT*) at the *metric standard* (*M*), with the *event causer* (or *actor*) *himself* (*R*). If the current event $X_C$ is given by (12), (13) with the transit event $X_T$ underlined can be inferred as the problem corresponding to S17.

(S17) Robby, please have helicopter $H_6$ hover 100 to 110 meters high.

$(\exists\ldots)L(R,H_6,q,q,HGT,G_t,M)\wedge 100m\leq q\leq 110m$ (11)

$(\exists\ldots)L(z_0,H_6,p,p,HGT,G_t,M)$ (12)

$(\exists\ldots)\underline{L(R,H_6,p,q,HGT,G_t,M)}\bullet L(R,H_6,q,q,HGT,G_t,M)\wedge 100m\leq q\leq 110m$ (13)

For this problem, Robby is to execute the expected task (13) by deploying the altimeter to sense the height and the collective lever to raise or sink the helicopter. How Robby uses the devices of the helicopter is to be given in $\boldsymbol{L_{md}}$ case by case.

Maintenance problem finding and solving:

In general, the goal event $X_G$ for a maintenance problem is that for another creation problem such as S17 given possibly by humans and solved by the robot in advance. That is, in this case, the task is to autonomously restore the pre-created goal event $X_G$ in advance to the current event $X_C$, as shown in (14). Here, $X\text{-}_T$ is an event that has already been detected as abnormal with the attribute value range of $X_T$ reversed. For example, if $X_G$ is given in advance in (11), $X_T$ is represented by the underlined part in (13), and $X_{-T}$ is represented in (15) (the event causer $z_1$ may differ from Robby, such as airflow in the vertical direction). Therefore, the task here is almost the same as the task for Robby described in the previous section.

$X_G\bullet X\text{-}_T\bullet X_C\bullet X_T\bullet X_G$ (14)

$L(z_1,H_6,q,p,HGT,G_t,M)$ (15)

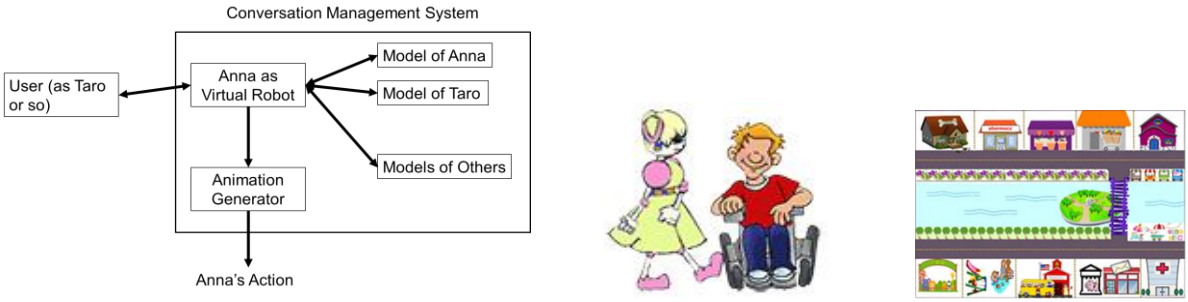
## CONVERSATION MANAGEMENT SYSTEM (CoMaS)

Overview:

The application system CoMaS is designed to work based on the principle shown in Figure 1. Its configuration is shown in Figure 8 (a), together with the icons of Anna and Taro (b), and part of the town map (c) involved here [Khummongkol & Yokota, 2016; 2023]. Anna, a virtual robot, is envisioned to act as an agent for CoMaS, conversing with users (such as Taro) in natural language, referencing knowledge models about specific environments such as maps of people and towns, and responding with animations as needed.

The imaginary scenario of Anna and Taro is as follows: Taro has a physical disability, uses a wheelchair, and lives in the town. Anna is a household robot that supports Taro's life. Anna is almost a stranger to Taro, as she has only recently come to his home.

Anna has been given the ability to process various types of information - NL expression, map, and animation - in a uniform way via $\boldsymbol{L_{md}}$ expression. Details of these functional items are described in Yokota's monograph [Yokota, 2019].




(a) Configuration (b) Anna & Taro (c) Town map (part)

Figure 8. Conversation Management System (CoMaS)

Problem finding/solving by Anna:

Consider that Taro asks Anna for a task by the utterance S18 and that Anna understands it as (16) to be illustrated in Figure 9.

(S18) Anna, go to the table with the box between the vase and the chair.

((L(_,ISR,Vase,Box,LOC,Gs,_)•L(_,ISR,Box,Chair,LOC,Gs,_))ΠL(_,ISR,?q,?q,DIR,Gs,_))•
(L(Anna,Anna,F1,F1,LOC,Gt,_)•$X_T$•(L(Anna,Anna,?p,Table,LOC,Gt,_)
Π(Anna,Box,Anna,Anna,LOC,Gt,_)) (16)

where

$X_C$ = L(Anna,Anna,F1,F1,LOC,Gt,_),

$X_T$ = L(Anna,Anna,F1,?p,LOC,Gt,_)•L(Anna,Box,?p,Anna,LOC,Gt,_),

and

$X_G$ = L(Anna,Anna,?p,Table,LOC,Gt,_)Π(Anna,Box,Anna,Anna,LOC,Gt,_).

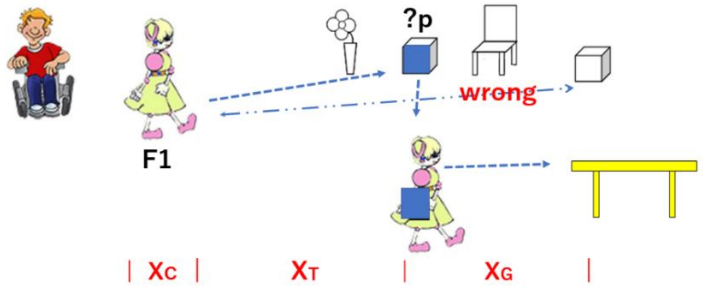



Figure 9. Illustration of Anna's understanding of S18.

Figure 10 shows the result of Anna's reactions to Taro's utterances. The process is a pure theorem proving by inference rules for first order predicate logic and a set of postulates concerning mental operation upon mental image in human.

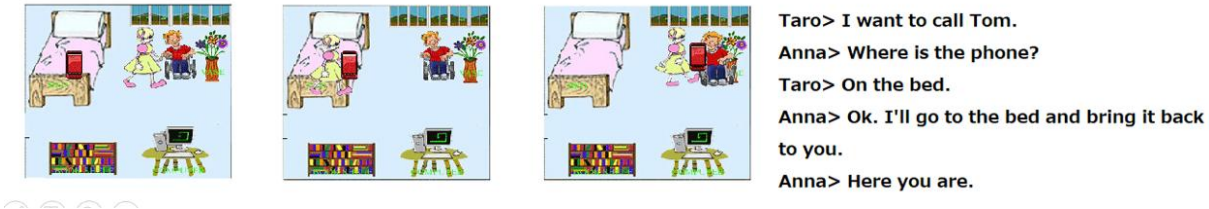



Figure 10. Example of Anna's conversation with Taro, and her reactions in language and animation.

## DISCUSSION AND CONCLUSION

This paper, based on MIDST, described a methodology within traditional rule-based AI for human and robot to find/solve problems cooperatively through language-centered communication. The definition of problem can be very simple and clarified in the context of (8) in the use of CANDs, more broadly, tempo-logical connectives [Yokota, 2019], which is one of the most noteworthy aspects of MIDST and is quite different from other spatiotemporal knowledge representation schemes [e.g., Valentin & Rumberg, 2025]. The application system CoMaS has shown its effectiveness in PFS concerning various interactions between Anna and Taro given in 4D expressions [Khummongkol & Yokota, 2016; 2023]. CoMaS performs reasoning within predicate logic, which is quite transparent and very simple with the benefit of $L_{md}$ expressions normalized by atomic locus formulas in a language-independent form, quite distinctly from other language-dependent approaches such as Vision-Language-Action models

[Ma, et al., 2026] and many conventional AI models, especially, based on DL of text data. The core technology of CoMaS based on MIDST is integrative understanding of natural language, sensor data, and motor data uniformly represented in $L_{md}$. The quality of CoMaS depends not on machine learning, but on the quality of the concepts and assumptions of the words introduced or defined by our own careful introspection. Therefore, CoMaS can only be scaled at a much slower rate than GAI systems using LLM until some innovative technology is brought about to extract mental images from the human brain as interpretable data. However, given the current state of this kind of technology, it might be more practical to first provide CoMaS with basic word concepts (e.g., basic English) in $L_{md}$, and then with compound word concepts explained by the basic ones through its NLU facility. In future research, we plan to realize this idea of enriching CoMaS in lexical knowledge, and implement it in actual robots in real-world environments.

**Acknowledgement**

This work was partially funded by the Grants from Ministry of Education, Culture, Sports, Science and Technology, Japanese Government, KAKENHI numbered 62580024, 62210013, 62210010, 63633519, 01633014, 03245221, 05241105, 07207124, 08207118, 08680419, 09204110, 10111106, 14580436, 17500132, 23500195, and 19K12109.

**REFERENCES**

1. **Yokota, M. (2019)**, Natural language understanding and cognitive robotics. CRC press.

2. **Fatemi, B., Kazemi, M., Tsitsulin, A., Malkan, K., Yim, J., Palowitch, J., Seo, S., Halcrow, J., and Perozzi, B., (2024)**, “Test of Time: A Benchmark for Evaluating LLMs on Temporal Reasoning,” arXiv:2406.09170 [cs.CL]

3. **Khummongkol, R. andYokota, M. (2016)**, “Computer simulation of humanrobot interaction through natural language,” Artificial Life and Robotics, doi:10.1007/ s10015 01603065, pp. 1 10, SpringerVerlag.

4. **Heylighen, F. (1988)**, “Formulating the Problem of ProblemFormulation,” In Trappl, R. (ed.), Cybernetics and Systems '88, Kluwer Academic Publishers, Dordrecht, pp. 949 957.

5. **Russell, S.J. and Norvig, P. (2010)**, Artificial Intelligence: A Modern Approach (3rd ed.). Upper Saddle River: Prentice Hall.

6. **Ma,Y., Song, Z., Zhuang, Y., Hao, J., and King, I. (2026)**, “A Survey on Vision Language Action Models for Embodied AI,” arXiv:2405.14093 https://arxiv.org/ August 19-21, 2026, Istanbul, Türkiye

7. **Daniel, G. and Langland-Hassan, P. (2024)**, "Inner Speech", The Stanford Encyclopedia abs/2405.14093. https://plato.stanford.edu/archives/sum2024/entries/innerspeech/.

8. **Khummongkol, R. and Yokota, M. (2023)**, Towards robotic deep spatiotemporal language understanding based on mentalimagedirected semantic theory. Artif Life Robotics 29, 70–80 (2024). https://doi.org/10.1007/s10015023009058.

9. **Winograd, T. (1978)**, “On primitives, prototypes, and other semantic anomalies,” Proceedings of conference on Theoretical Issues in Natural Language Processing, pp.25 32, Univ. of Illinois.

10. **Yokota, M. and Khummongkol, R. (2014)**, “Representation and computation of human intuitive spatiotemporal concepts as mental Imagery,” Proc. of The IEEE 6th International Conference on Awareness Science and Technology, Paris France.

11. **Yokota, M. and Khummongkol, R. (2019)**, “Modeling of Human MentalImage Based Understanding of Spatiotemporal Language for Intuitive HumanRobot Interaction,” Proc. of Workshop on Speaking of Location 2019: Communicating about Space colocated with 14th International Conference on Spatial Information Theory (COSIT 2019), pp.2946.

12. **Levesque, H.J. (2011)**, “The Winograd schema challenge. AAAI Spring Symposium: Logical Formalizations of Commonsense Reasoning,” Palo Alto CA.

13. **Obrenovic, B., Gu, X., Wang, G. Godinic, D., and Jakhongirov, I. (2025)**, “Generative AI and human–robot interaction: implications and future agenda for business, society and ethics,” AI & Soc 40, pp.677–690. https://doi.org/10.1007/s00146024018890

14. **Papanicolaou, A.C. (2023)**, “NonInvasive Mapping of the Neuronal Networks of Language,” Brain Sci. 2023, 13, 1457. https://doi.org/10.3390/brainsci13101457

15. **Newell, A. and Simon, H.A. (1972)**, Human Problem Solving, (PrenticeHall, Englewood Cliffs).

16. **Valentin, G. and Rumberg, A. (2025)**, "Temporal Logic", The Stanford Encyclopedia of Philosophy (Summer 2025 Edition), Edward N. Zalta & Uri Nodelman (eds.). https://plato.stanford.edu/archives/sum2025/entries/logictemporal/ <Comment> The authors would like to choose to submit an extended abstract for the conference proceedings.

# Generation of 3D models of historical Japanese castle town for virtual production use

**Towa SAKURAI**, *sakurai.towa@keio.jp* Keio University, 223-8526, Yokohama, Japan

**Takahiro YAKOH**, *yakoh@keio.jp* Keio University, 223-8526, Yokohama, Japan

## ABSTRACT

This paper proposes a generative AI system for reconstructing Japanese castle towns. The system generates three-dimensional (3D) models that incorporate historical town configuration rules, detailed town planning, such as specific town types and block sizes, and topographical correlations, based on given location, era, and scale parameters, to ensure historical accuracy. This paper validates spatial accuracy through comparison with historical records and demonstrates the flexibility to generate various town models tailored to user-defined parameters.

**Keywords:** residential planning, generative AI, Japanese castle town analysis

## 1. Introduction

This chapter introduces the research background and objectives of this paper. Our research methodology and the structure of this paper are also explained briefly.

### Research background

In recent years, the Japanese entertainment industry has been growing rapidly. In 2025, the total market capitalization of the nine major entertainment companies increased by 30% to 57 trillion yen, surpassing the automotive industry [Nikkei, 2025]. The value of overseas exports of broadcast content has been rising steadily since 2015, reaching approximately 83.58 billion yen in fiscal year 2023, indicating continued growth in Japan's content market [Ministry of Internal Affairs and Communications, 2024]. The entertainment industry has become an important pillar contributing to the Japanese economy. Furthermore, Japan's content market is expanding due to the proliferation of video streaming services and accelerating global expansion, leading to an increase in the market size for video-related software [Ministry of Internal Affairs and Communications, 2026].

Virtual Production (VP) is increasingly being adopted in video production settings. VP is a technique that performs real-time compositing of live-action footage with 3D CG backgrounds displayed on LED screens, offering the benefits of eliminating weather and time constraints while reducing production costs. In Japan, the popularity of historical castle towns necessitates the rapid generation of 3D models for virtual production. However, there is a challenge: producing the 3D urban models that constitute these backgrounds is time-consuming and costly. While the expansion of general-purpose assets has been considered a solution to this challenge, such an approach risks compromising model diversity. Moreover, even with general-purpose assets, the task of arranging architectural models according to maps to form a city remains. We have considered whether using generative AI to produce these urban models could resolve these issues.

**Research Objectives**

This study aims to develop an automated generation tool for 3D urban models of historical castle towns, designed to provide efficient background assets for virtual production. By algorithmically implementing fundamental rules of historical urban structures — specifically, topography and land subdivision — our approach enables the generation of diverse, historically grounded city models based on user-defined parameters. Through the evaluation of the generated models, this research clarifies the practical utility and versatility of this method in the professional workflow of virtual production.

**Research Methodology**

In this study, we propose a method for generating virtual historical urban models to reconstruct the urban structure of castle towns. First, we analyzed and modeled the fundamental requirements for model generation by describing the urban structure of castle towns based on topographic data and historical literature in a rule-based manner. Next, we automated the modeling process using Python scripts to construct models in Blender. Finally, we verified the geometric fidelity of the generated castle town models to the urban structure and evaluated the effectiveness of the proposed method.

The remainder of this paper is organized as follows. Chapter 2 introduces some related works. Our analysis and modeling of the rules of Japanese historical castle town design are explained in Chapter 3. Chapter 4 describes the design and implementation of the proposed system. Some experimental evaluations are shown in Chapter 5. Finally, this paper is concluded in Chapter 6.

## 2. Related Work

Huang et al. (2025) developed a high-quality 3D architectural model generation AI by decomposing architectural components using *BuildingBlock* [Huang et al., 2025]. Chen et al. (2024) proposed a method to generate virtual city models of contemporary car-oriented cities by applying weights to road and lot generation [Chen et al., 2024]. While prior research has already explored AI models focusing exclusively on architecture, generation methods for contemporary virtual cities, and urban model generation in foreign contexts, research on virtual city model generation for historical cities, particularly those in Japan, remains limited.

This study introduces a novel approach by training models on Japan-specific and subdivision rules (*chiwari* in Japanese) and the relationship between topography and urban structure, thereby enabling the generation of historical Japanese urban models.

## 3. Analysis of Castle Towns and Tool Development

In this chapter, we analyze and model the rules of Japanese historical castle town design.

### Historical Background of Castle Towns

Japanese castle towns are cities systematically constructed by feudal lords (*daimyo*) around their own castles, with the entire town planned from the top down by the lord. Unlike other towns that developed unintentionally or only through individual human activity, Japanese castle towns were planned and strongly reflected the lord's intentions. The urban structures also differed by lord, each possessing unique characteristics.

A castle town consisted of the castle where the lord resided, *samurai* residences where warriors who defended the castle lived, and merchant districts where merchants and craftsmen lived. Although the detailed layout of these residences varied depending on the location and the lord, it can generally be said that *samurai* residences were located in the vicinity of the castle, while merchant districts extended into the outer areas.

### Generative Framework for Castle Town Reconstruction

This study proposes a generative framework that translates historical castle-town configurations into code for cross-regional application. By hierarchically stacking processes—from the urban structural foundation to individual architectural placement—this framework embodies the rule-based nature of historical castle towns. The generation process consists of three steps: (1) creation of urban blocks reflecting logic and topography, (2) subdivision of residential lots based on historical literature, and (3) placement of architecture tailored to these lots.

In the first step, the urban structural foundation is generated by modeling road layouts based on topographic and historical data, using Osaka and Edo Castles as representative archetypes to create structural variations. The second step subdivides these urban blocks into residential lots. Drawing on historical records, the process incorporates size distribution rules to capture both the distinct differences between castle types and the fine variations within each layout. In the third step, individual architectural assets are placed. By analyzing site geometries, an algorithm automatically adjusts architectural sizes to fit diverse site conditions. By chaining these processes, this framework serves as a dynamic system capable of reconstructing historical models while adapting to various regions and user inputs.

## 4. Design and Development of a Generative System/Tool

This chapter explains the step-by-step procedure for generating the Japanese castle town model. Before that, some notations are introduced in Table 1 to simplify the explanation. Figure 1 illustrates the abstracted layout of a typical Japanese castle town as well as these notations.

Table 1. Notation of parameters

| | | |
|---|---|---|
| User's Input | $type$ | Urban type, where $type \in \{Osaka, Edo\}$ |
| | $S_c$ | Side length of the castle precinct [m] |
| | $A_S$ | Area of the *samurai* residential district [m$^2$] |
| | $r$ , $i$ | Terrain adaptation parameters (radius and influence) |
| Given or Derived parameters | $A_C$ | Area of the castle precinct [m$^2$], where $A_C = S_c^{\,2}$ |
| | $B_{mj}$ | Merchant district grid, representing the structural unit of urban blocks |

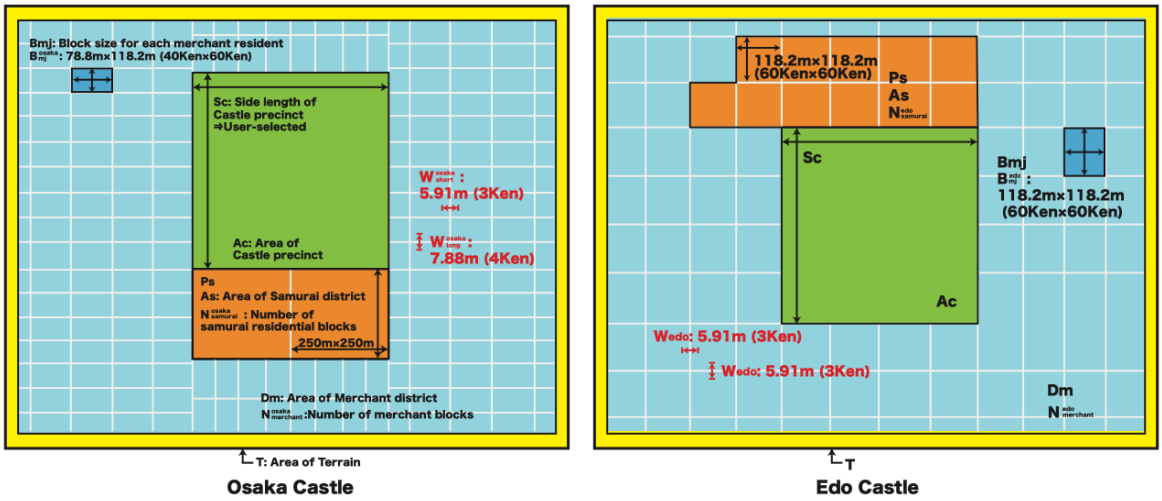



Figure 1. Abstracted Layout of Japanese Castle Town

**Step 0: topography acquisition and reproduction logic**

Baseline topographic and architectural data for historical city reconstruction are acquired and processed using BlenderGIS [domlysz, 2026], an open-source Blender add-on. The data acquisition pipeline follows a standardized workflow to ensure spatial consistency:

I. Topographic Data Integration: Geographic base map imagery is captured via the BlenderGIS interface. Subsequently, terrain relief is generated by wrapping a base plane mesh around elevation data derived from the SRTM (Shuttle Radar Topography Mission) global digital elevation model, accessed through the Open Topography web service.

II. Urban Data Incorporation: Building footprints are imported from OpenStreetMap (OSM) datasets. To enhance visual fidelity, these footprints are extruded based on either metadata or a randomized height threshold and projected onto the terrain mesh using the 'Elevation from object' function.

**Step 1: creation of urban blocks through road generation**

Definition of Parameters: To formalize the process of urban block generation via road network construction, we use the notation summarized in Table 1 and the subdivision models illustrated in Figure 1. Although all subsequent values are expressed in meters, historical literature often uses the traditional Japanese length unit, *Ken* ($1\,Ken = 1.97\,m$). Consequently, both units may be provided for clarity.

The zoning configuration is determined by the input parameters $S_c$ and $A_s$. The castle precinct is positioned at the center of the terrain mesh $T$, occupying an area of $A_C = S_c^{\,2}$.

The merchant district $D_m$ (represented as the blue area in Figure 1, left) is tentatively defined as the remaining area of the terrain mesh, as shown in Equation (1).

$$D_m = T \setminus (A_c \cup A_s) \tag{1}$$

Osaka logic: Based on the historical analysis by Matsuo, the *samurai* residential area is concentrated on the south side of the castle [Matsuo, 2015]. Therefore, *samurai* residential plots $P_s$ (represented as the orange area in Figure 1, left) of $250\,m \times 250\,m$ are placed in this area, and the number of plots $N_{samurai}^{osaka}$ (represented as the number of subdivisions in the orange area of Figure 1 left) is calculated as Equation (2).

$$N_{samurai}^{osaka} = \left\lfloor \frac{A_S}{(250 + W_{short}^{osaka})^2} \right\rfloor \tag{2}$$

The merchant district $D_m$ is subdivided into urban blocks $B_{mj}$ based on historical urban layouts. Osawa states that the city blocks in the merchant districts of Osaka Castle were based on $78.8\,m \times 118.2\,m$ $(40\,Ken \times 60\,Ken)$ rectangular plots, and that the *Uemachi* district to the west of the castle featured vertical town layout where the long side of the block faced the center of the castle [Osawa, 2018]. Therefore, the urban block $B_{mj}^{osaka}$ (represented as the small blue squares in Figure 1 , left) is determined as Equation (3).

$$B_{mj}^{osaka} = 78.8\,m \times 118.2\,m \quad (40\,Ken \times 60\,Ken) \tag{3}$$

$$Orientation \;: long \;\; side \perp castle \;\; center \tag{4}$$

Regarding road width, Yoshida et al. analyzed the block configuration before and after the excavation of the *Nagahori* River using a reconstructed map of the *Shimanouchi* district [Yoshida and Matsuguchi,1993]. Based on their reconstruction, the road width $W$ (indicated in red in Figure 1, left) is given by Equations (5) and (6).

$$W_{long}^{osaka} = 7.88\,m \quad (4\,Ken) \;; along \;\; the \;\; long \;\; side \;\; of \;\; B_{mj} \tag{5}$$

$$W_{short}^{osaka} = 5.91\,m \quad (3\,Ken) \;; along \;\; the \;\; short \;\; side \;\; of \;\; B_{mj} \tag{6}$$

We apply this subdivision logic to the merchant district. The total number of merchant blocks $N_{merchant}^{osaka}$ (represented as the number of subdivisions in the blue area of Figure 1, left) is calculated using Equation (7).

$$N_{merchant}^{osaka} = \frac{D_m}{\left(78.8 + W_{long}^{osaka}\right) \times \left(118.2 + W_{short}^{osaka}\right)} \tag{7}$$

Following the construction of the road network, the road layout is deformed to conform to the terrain mesh $T$. As noted by Abe et al., roads in Osaka were frequently routed along valley lines to ensure efficient drainage. Therefore, we deform the road network along the terrain.

Edo Castle: Based on Masai's historical analysis, *samurai* residential zones tended to be concentrated in the northern and northwestern sectors of the castle, forming continuous areas such as *Bancho*, *Ichigaya*, and *Surugadai* [Masai, 1975]. Therefore, the *samurai* residential plots $P_s$ (represented as the orange area in Figure 1 right) are configured to be placed within these northern and northwestern sectors based on the user-specified area $A_s$. It is widely accepted that the road layout of Edo Castle is based on $118.2\,m \times 118.2\,m$ $(60\,Ken \times 60\,Ken)$ square blocks, regardless of whether they are in merchant districts or *samurai* residential areas Edo Castle's road layout is based on $118.2\,m \times 118.2\,m$ $(60\,Ken \times 60\,Ken)$ square blocks, regardless of their district [Tamai, 1986]. Based on this historical structure, we define the urban

block $B_{mj}^{edo}$ (represented by the small blue squares in Figure 1, right) with these dimensions , as defined in Equation (8).

$$B_{mj}^{edo} = 118.2\,m \times 118.2\,m \quad (60\,Ken \times 60\,Ken) \tag{8}$$

and the number of plots $N_{samurai}^{edo}$ (represented as the number of subdivisions in the orange area of Figure 1, right) is calculated by Equation (9).

$$N_{samurai}^{edo} = \lfloor \frac{A_S}{118.2^2} \rfloor \tag{9}$$

Roads are generated at the boundaries of these blocks, and the road width $W_{edo}$ (indicated in red in Figure 1, right) is uniformly defined as Equation (10).

$$W_{edo} = 5.91\,m \quad (3\,Ken) \tag{10}$$

We apply this subdivision logic to the merchant district. The total number of merchant blocks $N_{merchant}^{edo}$ (represented as the number of subdivisions in the blue area of Figure 1, right) is obtained as Equation (11).

$$N_{merchant}^{edo} = \frac{D_m}{(118.2 + W_{edo})^2} \tag{11}$$

Terrain adaptation was implemented in the same manner as for Osaka Castle.

**Step 2: subdivision of residential lots based on historical literature**

Osaka Castle: Following the construction of urban blocks, each merchant district block $B_{mj}^{osaka}$ is further subdivided into individual residential lots. Based on the historical urban structure described by Osawa, the residential lots in Osaka Castle typically featured a *ryogawa-cho* (towns facing each other across a street) configuration. In this layout, a rear property line is established along the east-west axis of the block [Osawa, 2015]. We implement this by dividing each block $B_{mj}^{osaka}$ into two equal segments along its long side (Figure 2 left [1]). Subsequently, the frontage along the long-side road is subdivided into individual lots (Figure 2 left [2]). Regarding the frontage size $F_s$, we refer to the research by Saito et al. on the town divisions in *Gujo-Hachiman* [Saito and Miura, 2011]. Historical trends indicate that frontages ranging from 3.94 to 5.91 m (2–3 $Ken$) and 5.91 to 7.88 m (3–4$Ken$) account for 46% and 25% of the total distribution, respectively. Based on this, we established a subdivision logic for the frontage size $F_s$ using weighted random selection, as expressed in Equation (12).

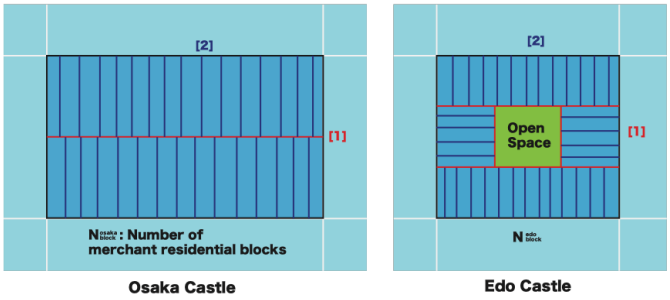



Figure 2. Residential subdivision models for Osaka and Edo Castle towns

$$F_s = \begin{cases} U(3.94\ ,\ 5.91)m \ \ with \ \ probability \ \ P_1 \approx 2/3 \\ U(5.91\ ,\ 7.88)m \ \ with \ \ probability \ \ P_2 \approx 1/3 \end{cases} \quad (12)$$

The expected frontage size $E[F_s]$ is defined to represent the average subdivision density based on the historical trends as shown in Equation (13).

$$E[F_s] = (P_1 \cdot 4.925) + (P_2 \cdot 6.895) \quad (13)$$

By applying this lot subdivision logic, the number of residential lots per block segment $N_{block}^{osaka}$ (represented as the number of subdivisions in the blue area of Figure 2 , left) and the designed total number of residential lots $N_R^{osaka}$ is given with Equation (22) and (23), where $L_{long}$ represents the length of the long side of the block.

$$N_{block}^{osaka} = 2 \cdot \lfloor \frac{118.2}{E[F_s]} \rfloor \quad (14)$$

$$N_R^{osaka} = N_{block}^{osaka} \cdot N_{merchant}^{osaka} \quad (15)$$

Edo Castle: In the case of Edo Castle, the framework is the same as that of Osaka Castle, but the residential lot subdivision logic differs. It is a widely accepted theory that in the Edo Castle lot subdivision, plots with a depth of 39.4m (20 $Ken$) were allocated along the four sides of the urban blocks(Figure 2 right [1]).; consequently, in the $118.2\,m \times 118.2\,m$ $(60\,Ken \times 60\,Ken)$ blocks of Edo Castle, $118.2\,m \times 118.2\,m$ $(60\,Ken \times 60\,Ken)$ open space (represented as the green area in Figure 2 right) was left in the center [Tamai, 1986]. Therefore, we constructed a logic to subdivide the urban blocks with lines $39.4\,m$ $(20\,Ken)$ from each side, and protected the remaining $39.4\,m \times 39.4\,m$ $(20\,Ken \times 20\,Ken)$ area at the center as an open space to prevent further subdivision of the frontage.

The lot subdivision logic based on frontage was applied in the same manner as for Osaka Castle, with modifications to the subdivision orientation to ensure that the frontage faces the road (Figure 2, right [2]).

With this subdivision logic, the number of residential lots per block $N_{block}^{edo}$ (represented as the number of subdivisions in the blue area of Figure 2 right) and the derived total number of residential lots $N_R^{edo}$ are defined as follows:

$$N_{block}^{edo} = 2 \cdot \left( \lfloor \frac{118.2}{E[F_s]} \rfloor + \lfloor \frac{118.2 - 78.8}{E[F_s]} \rfloor \right) \tag{16}$$

$$N_R^{edo} = N_{block}^{edo} \cdot N_{merchant}^{edo} \tag{17}$$

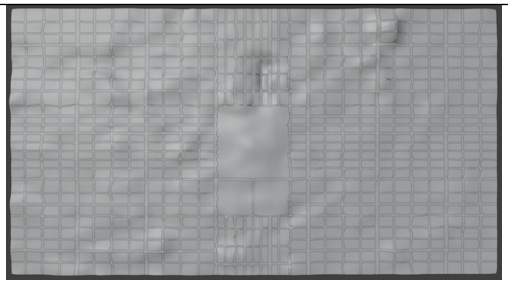
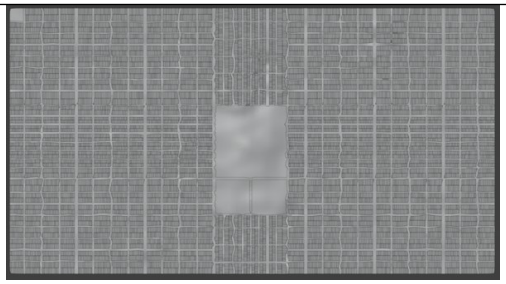
**Step 3: placement of architecture tailored to the residential lots**

The following is the logic for generating architecture tailored to the residential lots generated thus far. As the span between columns in a *machiya* (traditional townhouse) is 1 $Ken$ (1.97m), we analyze each lot's dimensions to determine its size in Ken and then place the vertical and horizontal columns accordingly. Centered on these columns, we form the walls and roof, and the design is intended to place the largest possible building within the lot boundaries, oriented along the road. This logic is implemented identically for both Osaka Castle and Edo Castle.

## 5. Evaluations & Verifications

Firstly, the two types of castle town models were generated by the developed system, representing Osaka Castle and Edo Castle, as shown in Figure 3. It looks feasible.

To quantitatively assess the fitness of the design model, the number of *samurai* residential urban blocks was compared across three *samurai* residential area patterns. Table 2 shows the number of *samurai* residential urban blocks of the Edo Castle type. It has been verified that the proposed system can create an appropriate urban model with a similar number of *samurai* residential blocks to the design model.

| Type | Generated Road Network | Generated Residential Lots |
|---|---|---|
| Osaka Castle |  |  |

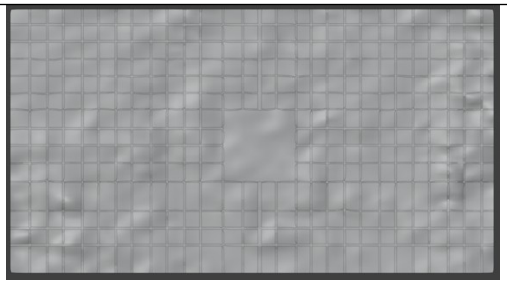
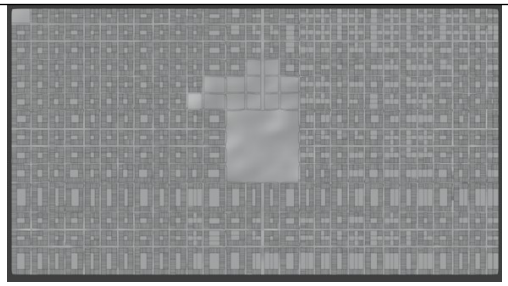
| | | |
|---|---|---|
| Edo Castle |  |  |

Figure 3. Generated 3D models of historical town configurations

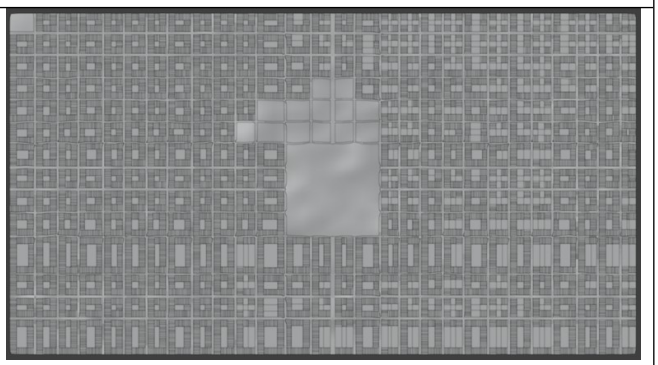
Table 2. Comparison of the number of *samurai* residential blocks $N_{samurai}^{edo}$

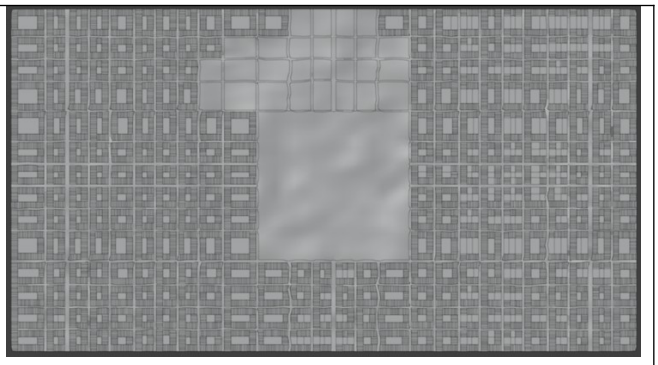
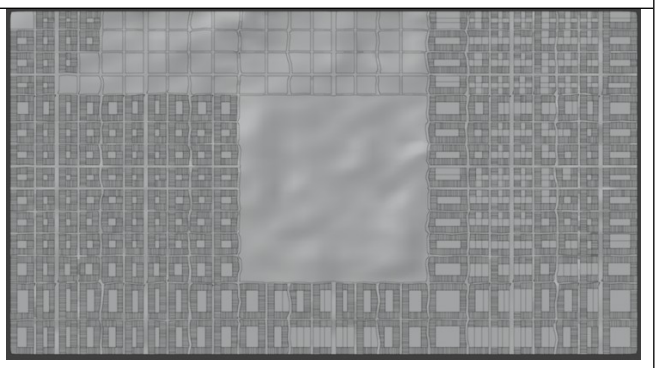
| $A_S$ | Target number calculated with the design model | Result number counted in the generated model |
|---|---|---|
| 162,000 | 11 | 13 |
| 414,720 | 29 | 27 |
| 648,000 | 46 | 59 |

Table 3. Comparison of the number of merchant blocks $N_{merchant}^{edo}$

| $S_c$ | $A_C$ | $A_S$ | $T$ | $D_m$ | Target number | Result number |
|---|---|---|---|---|---|---|
| 500 | 250,000 | 162,000 | 6,000,000 | 5,588,000 | 362 | 362 |
| 800 | 640,000 | 414,720 | 6,000,000 | 4,945,280 | 321 | 301 |
| 1,000 | 1,000,000 | 648,000 | 6,000,000 | 4,352,000 | 282 | 241 |

Table 4. Residential lot generation results in various castle areas

| $S_c$ | $A_C$ | $A_S$ | Residential lot generation results |
|---|---|---|---|
| 500 | 250,000 | 162,000 |  |

| | | | |
|---|---|---|---|
| 800 | 640,000 | 414,720 |  |
| 1000 | 1,000,000 | 648,000 |  |

The number of merchant blocks was also compared across three patterns. Table 3 shows the number of merchant blocks. The comparison shows that the proposed system can create an appropriate urban model with a similar number of merchant blocks to the design model.

The generated results for the residential lots, corresponding to various user-specified scales for castles and *samurai* residences, are illustrated in Table 4.

Table 5 presents the quantitative results for residential lot generation. We performed a residential subdivision in the merchant district, where the area varies according to the castle and *samurai* residential parameters. Based on the calculated expected lot frontage of 5.58 m, we estimated the number of residential lots within each urban block. Subsequently, we derived the designed total number of lots for the entire merchant district based on the previously calculated block count. Comparing the designed values with the resulting number of generated lots, significant discrepancies were observed in some cases. This is primarily attributed to the stochastic nature of the lot-generation model, including the randomized determination of frontage widths. However, the generated lot counts follow the overall trend of the target values, confirming the validity of the proposed model.

Buildings were generated based on the size of the residential lots, as illustrated in Figure 4. The merchant district buildings were designed to fit the residential lots around Osaka Castle and Edo Castle, thereby forming the castle town.

During the road network generation process, generated roads undergo topographic adaptation. Without this adaptation, the road network and residential lots are generated based on basic requirements, resulting in straight road segments and rectangular blocks. Topographic adaptation fixes the road width and deforms the road by shifting the vertices of the straight segments to conform to the terrain's elevation, as demonstrated in Figure 5.

Table 5. Comparison of the number of residential lots $N_{R\text{-}edo}$

| $A_C$ | $D_m$ | $E[F_s]$ | $N_{merchant}^{edo}$ | $N_{block}^{edo}$ | Target number | Result number |
|---|---|---|---|---|---|---|
| 250,000 | 5,588,000 | 5.58 | 362 | 56.49 | 20,499 | 34,086 |
| 640,000 | 4,945,280 | 5.58 | 321 | 56.49 | 18,133 | 18,474 |
| 1,000,000 | 4,352,000 | 5.58 | 282 | 56.49 | 15,930 | 14,874 |

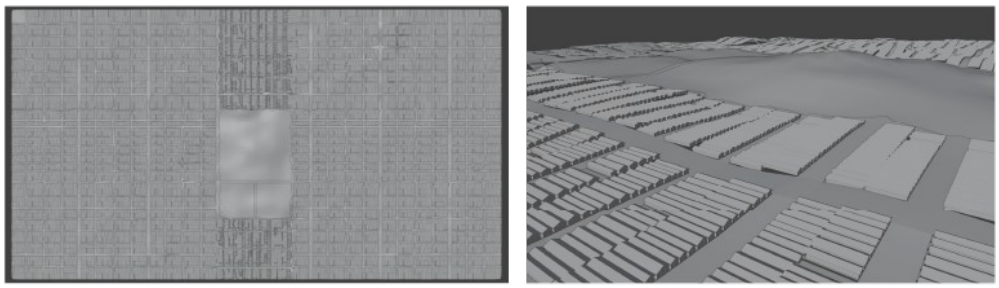


Figure 4. Generated result of residential and 3D architectural structures

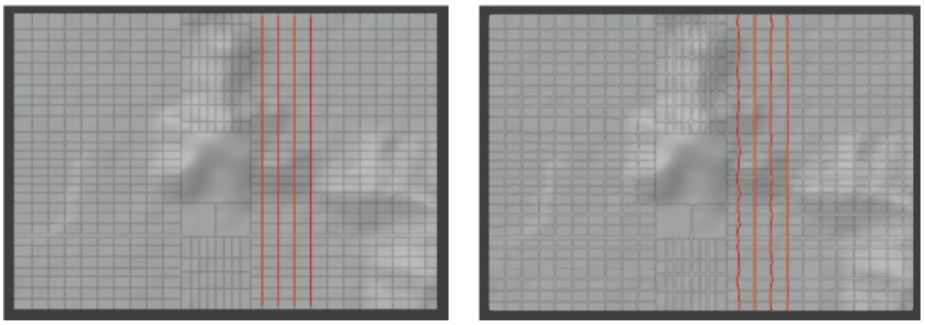



Figure 5. Impact of topographic adaptation on road network generation.

Next, we verify the applicability of the proposed system to regions with remaining historical castle town layouts in both Japan and other countries. In Japan, we selected Nagoya Castle, a castle town that developed during a similar era. For the other countries' cases, we selected the Château Comtal in Carcassonne, France, a fortified city, and Prague Castle in the Czech Republic, where the castle town extends beyond the city walls. The urban and road network configurations for each city are illustrated in Figures 6, 7, and 8.




Figure 6. Road network configuration in Château Comtal [Source: Map data © Google]




Figure 7. Road network configuration in Prague Castle [Source: Map data © Google]




Figure 8. Road network configuration in Nagoya Castle [Source: Map data © Google]

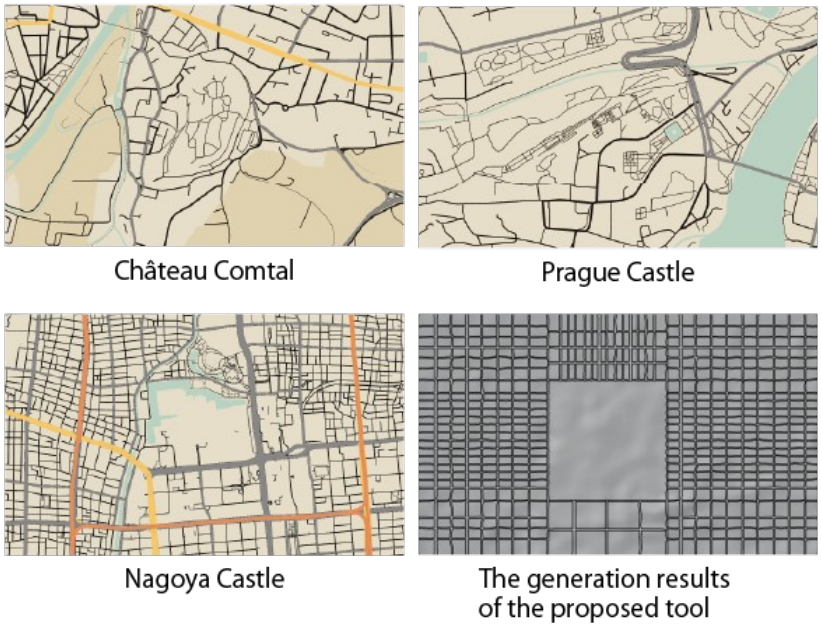



Figure 9. Road network configurations and the generation result of the proposed tool

[Source: Map data © Google]

We compared these disparate road configurations in three countries' contexts with the road layout of Osaka Castle generated by the proposed system, as illustrated in Figure 9.

The Château Comtal is oval, unlike the square castle shape produced by the proposed system. The road network of this fortified city consists primarily of curved roads that follow the castle's shape, in sharp contrast to the straight, grid-based road network generated by the proposed system. These differences indicate that the urban structure generated by the proposed system differs significantly from that of the Château Comtal, and consequently, the proposed system fails to reproduce the Château Comtal and its surrounding castle town.

Prague Castle also has an elongated east-west shape, unlike the square castle shape produced by the proposed system. The castle town has developed horizontally east-west from the castle, and the roads extend extensively in the same direction. Comparing Prague Castle with the road layout of the castle town generated by the proposed system reveals that, similar to the Château Comtal, the castle town differs significantly from the one generated by the proposed system.

In the case of Nagoya Castle in Japan, its shape is nearly square, resembling the castle constructed by the proposed system. Traces of large land subdivisions for *samurai* residences remain on the south side of the castle, and the size of these blocks is successfully reproduced by the proposed system's settings for *samurai* residential areas on the south side. In other areas, the base roads are arranged linearly, indicating that the castle town generated by the proposed system aligns with the land subdivision and road layout of Nagoya Castle.

These comparisons between Japanese and other countries' castle towns suggest that we have successfully generated cities similar to Japanese castle towns, demonstrating that the proposed system can produce the urban structure characteristic of them.

## 6. Conclusions

In this study, we proposed and implemented a generative system for reconstructing 3D urban models of historical Japanese castle towns. By algorithmically integrating rules for historical urban structures - specifically, topographic adaptation and land subdivision - our system enables the automated generation of diverse, historically grounded city models based on user-defined parameters. First, we conducted a quantitative assessment of the generation process, confirming that the output counts are broadly consistent with designed values and thereby validating the fundamental logic of our urban modeling framework. Furthermore, through comparative analysis between Japanese and international castle towns, we demonstrated that our method effectively reproduces the unique spatial configurations characteristic of Japanese castle towns. These results confirm that our approach provides a practical and effective solution for the rapid generation of 3D urban assets within the virtual production workflow.

As the future work, we have developed and validated the proposed generative system. Future work will assess its practical utility and evaluate the extent to which it can reduce production costs for 3DCG assets. While this study focused on the top-down urban development driven by feudal lords, our future efforts will expand the framework to incorporate diverse modes of urban formation, such as organic settlement growth, thereby enhancing the diversity of cities that can be constructed.

## REFERENCES

1. **Nikkei, (2025),** "Market Capitalization of Entertainment Industry Surpasses Automotive Industry", Nikkei Electronic Edition, June 30.

2. **(2024),** "Current Analysis of Overseas Expansion of Broadcast Content (FY2023)", Ministry of Internal Affairs and Communications.

3. **(2026),** "Content Market", White Paper on Information and Communications in Japan 2026, Ministry of Internal Affairs and Communications.

4. **Huang, J., Wang, C., Li, L., Huang, C., Dai, Q., and Xu, W., (2025),** "BuildingBlock: A Hybrid Approach for Structured Building Generation", SIGGRAPH Conference Papers '25, Article No. 3730705.

5. **Chen, Z., Song, P., and Ortner, F. P., (2024),** "Hierarchical Co-generation of Parcels and Streets in Urban Modeling", Computer Graphics Forum, Vol. 43, No. 2.

6. **domlysz, (2026),** "Quick start · domlysz/BlenderGIS Wiki", GitHub, https://github.com/domlysz/BlenderGIS/wiki/Quick-start

7. **Matsuo, N. (2015),** "Toyotomi-jidai no Fushimi-jokamachi to Osaka-jokamachi", Osaka Rekishi Hakubutsukan Kenkyu Kiyo, Vol.13, pp 35-45.

8. **Osawa, K. (2018),** "On the 'Suji' of the Toyotomi Osaka Castle Town: A Trial Theory from the Perspective of the Urban Construction Process", Bulletin of the Osaka Museum of History, Vol. 16, pp 19-33.

9. **Yoshida, T. and Matsuguchi, T. (1993),** "On the Town Planning and Subdivision of Simanouchi Area: A study on the town planning and the formation of Osaka Castle town Part 1", Journal of Archit. Plann. Environ. Engng, AIJ, No. 454, pp 165-172.

10. Masai, Y. (1975), "1:20,000 Urban Land Use Map of Edo (Tokyo) ca. 1860", Chizu (Map), Vol. 13, No. 1, pp 9-16.

11. **Tamai, T. (1986),** "Edo: Ushinawareta toshi kukan o yomu", Heibonsha, Tokyo, pp 24-27.

12. **Osawa, K. (2015),** "Bunken shiryo kara mita Toyotomi zenki Osaka-jo no bukeyashiki bukechi", Bulletin of the Osaka Museum of History, Vol. 13, pp 1-18.

13. **Saito, C. and Miura, T. (2011),** "An investigation report of castle town's zoning and composition in Gujo-Hachiman: An analysis of material of pictures and literatures", Journal of the City Planning Institute of Japan, Vol. 46, No. 3, pp 733-738.

# DEVELOPMENT AND EVALUATION OF A BARRIER-FREE TOURISM SUPPORT SYSTEM USING AIOT AVATARS

**Yuki KIDA**, *ykida@keio.jp*, Keio University, 223-8526, Yokohama, Japan

**Hiroko INOKUMA**, *h.inokuma@keio.jp*, Keio University, 223-8526, Yokohama, Japan

**Takahiro YAKOH**, *yakoh@keio.jp*, Keio University, 223-8526, Yokohama, Japan

**Tetsuro OGI**, *ogi.z6@keio.jp*, Keio University, 223-8526, Yokohama, Japan,
*ogi_tetsuro@asia-u.ac.jp,* Asia University, 180-8629, Tokyo, Japan

## ABSTRACT

When people with disabilities engage in tourism, they require prior research of accessible routes and facilities, while some information may still be difficult to obtain on-site. This study aims to enable access to information without such preparation by developing a barrier-free tourism support system using AIoT avatars. These avatars are anthropomorphized objects created using generative AI and engage users in autonomous conversations. Experiments were conducted at a hotel, souvenir shop, and cafe. The results suggested that the system provided users with the information necessary for tourism activities, enabling them to correctly reach their destinations or place orders and make purchases.

**Keywords:** IoT, Avatar, Generative AI, Barrier-Free, Tourism

## 1. INTRODUCTION

People with disabilities often need to gather extensive information before visiting tourist destinations, particularly regarding accessible routes and facilities. For example, wheelchair users need to confirm in advance whether accessible routes are available, whether steps are present, and whether facilities such as elevators and accessible restrooms are provided. However, some of this information can only be confirmed after arriving at the destination, while other information is often unavailable or insufficiently provided. As a result, they may experience difficulty reaching their destinations smoothly or spend considerable time searching for accessible routes and necessary facilities at tourist sites. This study aims to create an

environment in which people with disabilities can easily obtain the information they need when and where they need it without requiring extensive prior preparation.

Examples of methods for providing tourism information include digital signage [1,2] and guide robots [3,4]. In recent years, robotic avatars that enable remote users to interact with local users have also been actively studied [5-7], and are expected to support tourism activities. However, these approaches may be limited in terms of installation locations because of constraints such as the available installation space at tourist sites. Consequently, it is difficult to deploy a sufficient number of systems to provide information wherever users need it.

Therefore, we developed a barrier-free tourism support system that uses AIoT avatars to provide essential tourism information to users. AIoT avatars are created by attaching compact IoT devices to objects already present in tourist facilities, enabling these objects to engage in autonomous conversations using generative AI. In this paper, we evaluate the effectiveness of the proposed system through experiments conducted in actual tourist facilities, including a hotel, a souvenir shop, and a cafe. The remainder of this paper describes the concept of AIoT avatars, the design of the proposed system, and the evaluation of its effectiveness through the experiments.

## 2. CONCEPT OF AIOT AVATAR

The development of Internet of Things (IoT) technology has enabled various objects to be connected to the Internet and exchange data. In our previous studies, we proposed the concept of IoT avatars, in which real-world objects are not only capable of transmitting and receiving data but are also anthropomorphized as avatars that can communicate with people in a human-like manner [8].

An IoT avatar is created by attaching a compact IoT avatar device, equipped with a camera, microphone, and speaker, to an object in the environment. Each IoT avatar is operated by a remote user. Through the camera, microphone, and speaker of the IoT avatar device, the remote user communicates with local users as if they were the object itself. We have also developed a system in which multiple IoT avatars are deployed at different locations within a facility [9]. A remote user can switch between IoT avatars to continuously communicate with a local user while following the user's movements. However, although a remote user can communicate while switching between IoT avatars, it is not possible to simultaneously operate and communicate through multiple IoT avatars. To overcome this limitation, we proposed AIoT avatars by incorporating a generative AI-based voice communication function into IoT avatars, enabling them to communicate autonomously without the involvement of remote users [10].

The system proposed in this study transforms objects located at tourist sites into AIoT avatars and deploys them at multiple locations. Through autonomous conversations with users, each AIoT avatar provides users with the necessary tourism information in real time at its respective location. Consequently, the entire tourist environment can provide the barrier-free information required by users at the right place and time.

## 3. SYSTEM DESIGN OF A BARRIER-FREE TOURISM SUPPORT SYSTEM

### IoT Avatar Device

In this study, AIoT avatars were created by attaching the IoT avatar device shown in Figure 1 to various objects in the environment. The IoT avatar device consists of a Raspberry Pi 5, a compact Bluetooth speaker (aGO Mini), a camera (Raspberry Pi Camera V2), and a compact USB microphone. The enclosure of the IoT avatar device measures 92 mm in length, 61 mm in width, and 52 mm in height, and was fabricated from PLA using a 3D printer. In addition, an LED (NeoPixel Ring) was embedded inside the enclosure and designed to illuminate through the surface of the device. When the AIoT avatar is available for interaction, the LED lights up as shown in Figure 1(a) or Figure 1(b), allowing users to recognize its availability visually. As shown in Figure 1(a), two LED segments are illuminated to resemble the eyes of the AIoT avatar when the device is attached to ordinary objects. In contrast, as shown in Figure 1(b), the LED is illuminated in a ring shape when the device is attached to objects that already have eyes, such as dolls.

### Communication Function

The voice communication function was implemented using the OpenAI Realtime API. We developed a web application that responds to users' voice input in real time. The web application runs in a web browser on the IoT avatar device, enabling the AIoT avatar to communicate with users autonomously.

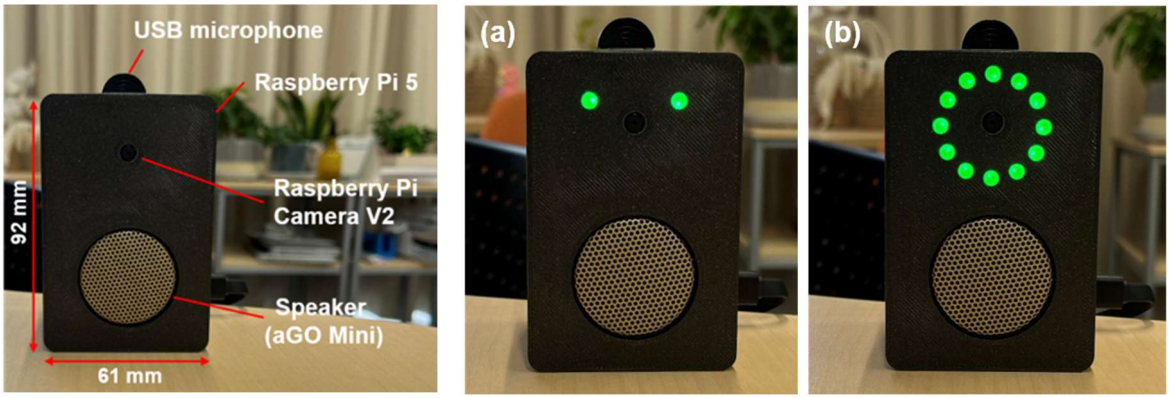



Figure 1. IoT Avatar Device

Prompts were designed for the AIoT avatars so that each avatar would converse as if it were the object to which it was attached. Figure 2 shows part of the prompt. In the actual experiments, the prompts were written in Japanese, and the AIoT avatars communicated with users in Japanese. In addition, the prompts included information specific to each experimental site, such as facility information, available products, and ordering or purchasing procedures for the hotel, souvenir shop, and cafe, allowing the AIoT avatars to provide appropriate guidance to users.

**Barrier-Free Tourism Support System Using AIoT Avatars**

In this study, we developed a support system intended for wheelchair users. AIoT avatars installed in tourist facilities detect wheelchair users and initiate guidance. To detect wheelchair users, we used MediaPipe Pose, a pose estimation library developed by Google, to obtain human posture information from camera images. Because wheelchair users generally remain seated, we adopted a method for detecting seated users based on the hip joint angle calculated from the shoulder, hip, and knee. In other words, the system detects users in a seated posture, and the AIoT avatar then speaks to them. However, when a user passes close to the AIoT avatar from outside the camera's field of view, parts of the lower body, such as the knees, may not be captured in the camera image, making it impossible to calculate the hip joint angle. In such cases, the system initiates guidance when the user's face or upper body is detected.

Regarding the conversation function, users are allowed to communicate with the AIoT avatar only while they are detected. If no user is detected, the conversation is disabled. However, once a user has been detected, the conversation is not terminated immediately when detection is temporarily lost. Instead, depending on the experimental site, the conversation remains available for thirty seconds, one minute, or three minutes. The duration was determined for

```
## System Prompt ##
### Basic Policy
-  Role: You are a houseplant. As a houseplant, provide facility guidance in a polite and friendly manner.
-  Responses should basically be in Japanese and consist of only a short, polite, and friendly one-sentence
   utterance (do not speak at length).
-  When providing facility guidance or facility information, use only one line of content from the Facility
   Guidance & Facility Information below in a single response. (Do not combine multiple pieces of
   information into one response.)
:

### Facility Guidance & Facility Information
-  You are located in the Tower Building of the Imperial Hotel.
-  Your current location is the corridor in front of the guest rooms on the 20th floor of the Tower
   Building.
-  If you are asked about the location or direction of the elevator, respond with:
   "Please exit the door and proceed down the corridor to your left.“
:

### If you are asked about facilities or information that are not included in this prompt:
- Do not provide any information that is not contained in this prompt.Do not make up information.
:
```

Figure 2. Part of the System Prompt

each experimental site by considering factors such as the distances between the AIoT avatars deployed at each location.

Figure 3 shows the pose estimation process using MediaPipe Pose. AIoT avatars deployed at different locations throughout the tourist facility continuously capture camera images and estimate human posture using MediaPipe Pose. When the estimation result indicates that a user has been detected, the LED on the AIoT avatar is illuminated, and the AIoT avatar initiates guidance by speaking to the user. Through conversations with the AIoT avatars deployed throughout the facility, users can obtain information about facility accessibility, product information, ordering procedures, and purchasing procedures.

## 4. EXPERIMENTS

To evaluate the effectiveness of the proposed system, we conducted experiments in actual tourist facilities. The experiments were carried out in Tokyo, Japan, at the Imperial Hotel and Toyosu Senkyaku Banrai, specifically at Toyosu Engimono, a souvenir shop, and Toyosu Fukurasuzume, a cafe. The souvenir shop and the cafe were located next to each other within the same facility. Ten wheelchair users participated in the experiments.

Figure 4 shows the experiments conducted at the hotel. The experiments were conducted on the guest room floor and in the banquet lobby. On the guest room floor, four AIoT avatars were deployed along the corridor to provide guidance on accessible routes and facility information while directing participants to their destination (the elevator). Each participant completed the task twice. After completing the two trials, the participants answered the questionnaire shown in Table 1 using a seven-point Likert scale. In the banquet lobby, three AIoT avatars were deployed at different locations to guide participants to the taxi stand and provide facility information. Each participant also performed the task twice. After completing the two trials,



Figure 3. Pose Estimation Process Using MediaPipe Pose

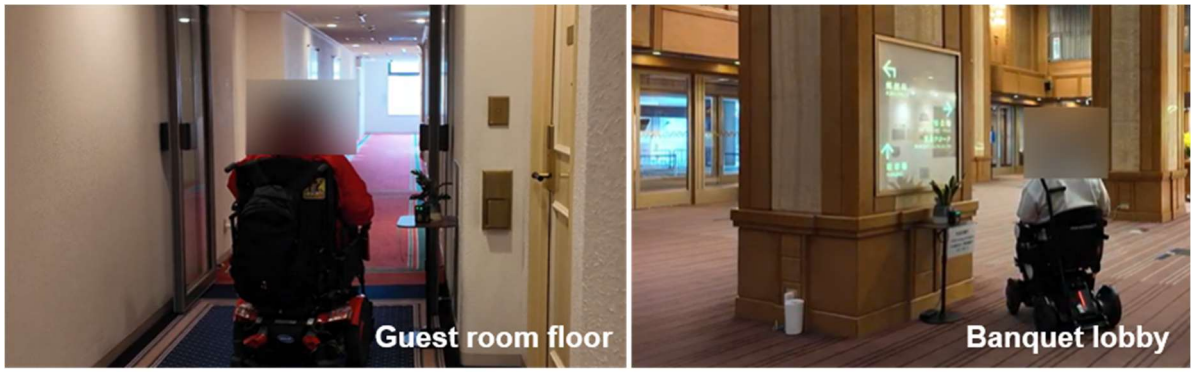



Figure 4. Experiments Conducted at the Hotel

Table 1 Questionnaire

| |
|---|
| Q1: I was able to have a natural conversation with this system. |
| Q2: I was able to obtain the information I needed through this system. |
| Q3: I was able to correctly reach my destination using this system. (hotel)<br>I was able to correctly place orders or make purchases using this system. (souvenir shop, cafe) |
| Q4: I felt that I was talking with the houseplant. (hotel)<br>I felt that I was talking with the sparrow. (souvenir shop, cafe) |
| Q5: I felt that I was talking with a remote person. |
| Q6: I felt that I was talking with an AI. |
| Q7: I felt that each houseplant had the same personality. (hotel)<br>I felt that each sparrow had the same personality. (souvenir shop, cafe) |
| Q8: I felt that each houseplant shared information with the others. (hotel)<br>I felt that each sparrow shared information with the others. (souvenir shop, cafe) |
| Q9: I thought this system was effective. |
| Q10: I would like to use this system. |

the participants answered the same questionnaire. In the hotel experiments, houseplants placed throughout the facility were used as AIoT avatars. When houseplants were used as AIoT avatars, the LEDs were illuminated using the pattern shown in Figure 1(a).

Figure 5 shows the experiments conducted at the souvenir shop and the cafe. In the souvenir shop, four AIoT avatars were deployed to provide information necessary for shopping, including product descriptions, directions to the sales areas, and payment procedures. Each participant performed the shopping task twice using the four AIoT avatars. After completing the two trials, the participants answered the questionnaire shown in Table 1 using a seven-point Likert scale. In the cafe, three AIoT avatars were deployed to provide information about menu items and guidance on the ordering procedure. Each participant performed the ordering task twice using the three AIoT avatars. After completing the two trials, the participants




Figure 5. Experiments Conducted at the Souvenir Shop and the Cafe

answered the same questionnaire. In the souvenir shop and cafe experiments, sparrow dolls were used as AIoT avatars. Since sparrow dolls had already been placed in the facility, identical sparrow dolls were prepared and used as AIoT avatars. When sparrow dolls were used as AIoT avatars, the LEDs were illuminated using the pattern shown in Figure 1(b).

## 5. RESULTS AND DISCUSSION

Figures 6 and 7 show the questionnaire results obtained from the hotel and the souvenir shop/cafe experiments, respectively. First, regarding the effectiveness of the proposed system, high scores were obtained for Q2 and Q3 in both the hotel and the souvenir shop/cafe experiments. These findings suggested that the proposed system enabled participants to obtain the information they needed for tourism activities, allowing them to correctly reach their destinations and complete ordering and shopping tasks. In addition, the high scores for Q9 and Q10 suggested that the proposed system was effective as an information support system for tourist facilities in this experiment and that participants were willing to use the system.

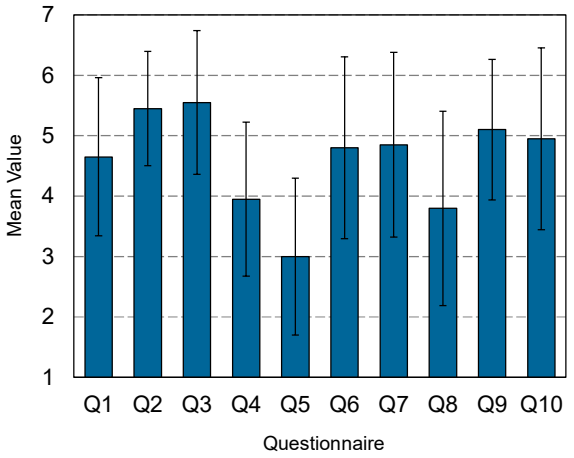



Figure 6. Hotel Results

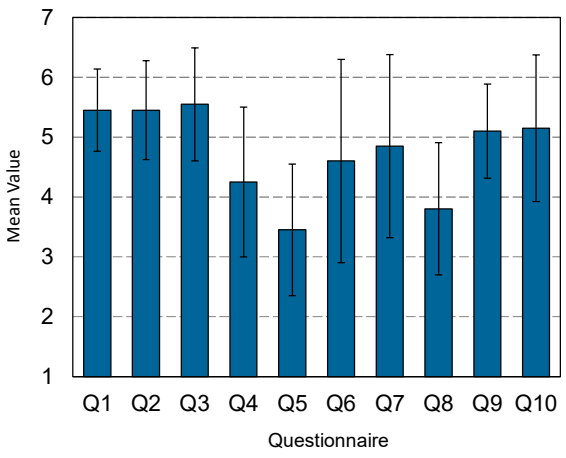



Figure 7. Souvenir Shop/Cafe Results

Regarding the naturalness of the conversation (Q1), the average score exceeded 4.5 in both the hotel and the souvenir shop/cafe experiments, indicating that participants were generally able to communicate naturally with the AIoT avatars. However, the score in the hotel experiment was lower than that in the souvenir shop/cafe experiment. A possible reason for this difference is the lighting environment in the hotel. Specifically, some areas, such as the corridors, were relatively dark, which occasionally caused unstable user detection by the camera. As a result, the initiation of conversations was sometimes delayed, which may have affected participants' evaluation of conversational naturalness.

Regarding the perceived communication partner (Q4, Q5, and Q6), participants reported some sense of talking with the houseplants or sparrow dolls (Q4), while they reported a relatively high sense of talking with an AI (Q6). These findings suggested that participants perceived themselves as communicating with an autonomous AI through real-world objects.

The results of Q7 and Q8 suggested that participants tended to perceive each houseplant or sparrow doll as having the same personality. However, they did not perceive that information was shared among the different houseplants or sparrow dolls. In the current system, each AIoT avatar is assigned an independent prompt and communicates independently. As a result, conversation histories are not shared among AIoT avatars, and conversations are not transferred between them. Consequently, the same guidance can be repeated by different AIoT avatars. A possible improvement is to allow AIoT avatars to share conversation histories with one another. Implementing such a system remains an important topic for future work.

In addition, participants provided feedback regarding user identification, travel direction estimation, and the eye expressions of the AIoT avatars. Although user identification and travel direction estimation have not yet been implemented in the current system, these functions are considered important for providing personalized information to individual users. By identifying whether a user has interacted with an AIoT avatar at another location and recognizing the direction in which the user is moving, the system could provide more detailed information and guidance according to the user's situation. This would enable the proposed system to provide more personalized support and realize a more useful barrier-free tourism support system. Possible approaches include identifying users and estimating their travel direction using cameras or utilizing information from users' smartphones.

Furthermore, to encourage users to perceive AIoT avatars as familiar and approachable entities, rather than simply passing by them, it is also important to improve nonverbal expressions, such as eye movements generated by the LEDs. These improvements are expected to make the AIoT avatars more effective in attracting users' attention and providing

guidance. Implementing these functions and improving such expression methods remain important directions for future work.

## 6. CONCLUSION

In this study, we developed a barrier-free tourism support system using AIoT avatars that utilize generative AI. The objective was to create an environment in which people with disabilities can obtain the information they need at the appropriate locations without requiring prior research. Experiments were conducted at a hotel, a souvenir shop, and a cafe. The results suggested that participants were able to obtain the information they needed and correctly reach their destinations or place orders and make purchases. Overall, these results suggested the effectiveness of the proposed system.

Future work includes enabling AIoT avatars to share conversation histories for continuous guidance across multiple locations. Another important direction is to implement user identification and travel direction estimation to provide personalized information according to each user's situation.

## ACKNOWLEDGMENT

This research was supported by JKA promotion funds from KEIRIN RACE (2024M-549) and the Tokyo Metropolitan Government's Barrier-Free Tourism Promotion Project Utilizing Advanced Technologies.

The authors would like to express their sincere gratitude to Imperial Hotel, AUC Corporation, Hinomaru Limousine, AliiTravel, A&A, and Mirairo for their valuable cooperation and support throughout this project.

## REFERENCES

1. **Koto, Z. and Bandung, Y. (2016),** "Interactive Digital Signage architecture to improve user interaction on tourism information services", In International Symposium on Electronics and Smart Devices (ISESD), pp. 380-385.

2. **Ogi, T., Ito, K. and Ukegawa, S. (2017),** "Multilingual information service based on combination of smartphone and digital signage", In International Conference on Network-Based Information Systems, pp. 644-653.

3. **Al-Wazzan, A., Al-Farhan, R., Al-Ali, F. and El-Abd, M. (2016),** "Tour-guide robot", In International Conference on Industrial Informatics and Computer Systems (CIICS), pp. 1-5.

4. **Rosa, S., Randazzo, M., Landini, E., Bernagozzi, S., Sacco, G., Piccinino, M. and Natale, L. (2024),** "Tour guide robot: a 5G-enabled robot museum guide", Frontiers in Robotics and AI, 10, 1323675.

5. **Park, S., Kim, J., Lee, H., Jo, M., Gong, D., Ju, D., Won, D., Kim, S., Oh, J., Jang, H., and Bae, J. (2023),** "A whole-body integrated AVATAR system: Implementation of telepresence with intuitive control and immersive feedback", IEEE Robotics & Automation Magazine, 32(2), 60-68.

6. **Elobaid, M., Dafarra, S., Ranjbari, E., Romualdi, G., Chaki, T., Kawakami, T., Yoshiike, T. and Pucci, D. (2024),** "Remote telepresence over large distances via robot avatars: case studies", In 2024 IEEE Conference on Telepresence, pp. 183-187.

7. **Dafarra, S., Pattacini, U., Romualdi, G., Rapetti, L., Grieco, R., Darvish, K., Milani, G., Valli, E., Sorrentino, I., Viceconte, P. M., Scalzo, A., Traversaro, S., Sartore, C., Elobaid, M., Guedelha, N., Herron, C., Leonessa, A., Draicchio, F., Metta, G., Maggiali, M. and Pucci, D. (2024),** "icub3 avatar system: Enabling remote fully immersive embodiment of humanoid robots", Science Robotics, 9(86), eadh3834.

8. **Kida, Y., Chiba, T. and Ogi, T. (2025),** "IoT avatar: various objects in real space are anthropomorphised as avatars", International Journal of Web and Grid Services, Vol.21, No.1, pp.42-57.

9. **Tsukada, S., Chiba, T., Kida, Y. and Ogi, T. (2025),** "Construction of a Continuous Communication System Using Multiple IoT Avatars", JSME D&S 2025. (in Japanese)

10. **Kida, Y., Muto, H., Chiba, T. and Ogi, T. (2025),** "Comparative Evaluation of Communication via Remote User Operation and Generative AI in IoT Avatar", VRSJ Annual Conference 2025. (in Japanese)

# EFFECT OF UNIT CELL SIZE ON INTERFACE PRESSURE OF 3D-PRINTED GYROID FOAM FOR SITTING COMFORT

**Minh Tien NGUYEN**, *nb24501@shibaura-it.ac.jp*, Shibaura Institute of Technology, 135-8548, Tokyo, Japan

**Akinari HIRAO**, *hirao@shibaura-it.ac.jp*, Shibaura Institute of Technology, 135-8548, Tokyo, Japan

## ABSTRACT

Prolonged sitting can increase discomfort and physical stress on the human body, making seat foam comfort an important factor in user experience and seating design. Recently, 3D-printed foam structures have received increasing attention for seating applications because of their lightweight characteristics and design flexibility. However, previous studies have mainly focused on physical testing and prototype development, with limited use of simulation methods. In this study, a combined testing and finite element simulation approach was used to investigate the mechanical behavior of gyroid structures under sitting conditions. Pressure distribution and surface displacement obtained from physical tests were used to validate the simulation results. After validation, the simulation model was applied to investigate the influence of unit cell size, one of the main design parameters of gyroid structures, on contact pressure distribution. The results indicate that the proposed approach can support design based on simulation for improved sitting comfort.

**Keywords:** 3D-printed foams, Gyroid structure, Finite element method

## 1. INTRODUCTION

Three-dimensional (3D) printing technology has been widely used in many fields because it can manufacture complex structures [Shahrubudin, N., 2019]. In recent years, a promising application of this technology is developing seating systems to improve sitting comfort [Pagliari, C., 2025, Hogeveen, T., 2023, De la Rosa, S., 2024]. Nowadays, people spend a significant amount of time sitting in vehicles, workplaces, and homes. Therefore, improving seat comfort has become an important research topic. Prolonged sitting can cause discomfort and increase the physical load on the body. This highlights the need for effective seat designs.

Previous studies suggest that seat design should consider several factors, including lightweight construction, comfort, and environmental sustainability [Hogeveen, T., 2023]. To

achieve these objectives, researchers have investigated different materials and structural designs. In addition, some studies have focused on specific seating applications. For example, foam structures designed for wheelchair users have been developed to improve pressure distribution and sitting comfort during extended use [De la Rosa, S., 2024]. These studies show continued efforts to develop seating systems that provide better support for users.

Because additive manufacturing offers greater design freedom, 3D-printed foams are attracting increasing attention as an alternative to traditional foam materials. By using lattice structures, these materials can significantly reduce overall weight while maintaining the mechanical performance required for seating. Furthermore, many 3D-printable materials have favorable properties, such as elasticity, shape recovery, and durability under repeated loading [Hogeveen, T., 2023]. The flexibility of 3D printing also allows the production of complex foam structures that are difficult to manufacture using conventional methods. As a result, 3D-printed foams are expected to have potential in future seating and cushioning applications.

Previous studies have commonly improved the performance of 3D-printed foams by combining regions with different structural densities based on pressure distribution maps [De la Rosa, S., 2024, Lu, C., 2023]. Although these approaches have shown promising results, the influence of individual geometric design parameters on interface pressure is still insufficiently understood. A better understanding of these parameters would provide a more systematic basis for foam design and optimization. Finite element analysis is an efficient tool for investigating the relationship between geometric design parameters and pressure distribution. However, its application to the mechanical behavior and pressure response of 3D-printed seating foams is still limited [Nguyen, M.T., 2025].

In the development of 3D-printed gyroid foam, three primary design parameters are considered: unit cell size (s), surface coefficient (solidity) (d), and wall thickness (t). These parameters define the geometric characteristics of the lattice structure. They are also expected to influence its mechanical behavior and pressure response. Among them, the unit cell size directly determines the scale of the lattice structure. This scale can affect the deformation behavior and load transfer mechanism of the foam under compression. However, its exact influence on contact pressure remains unclear.

Therefore, this study evaluates the effect of unit cell size on the pressure distribution of 3D-printed gyroid foam through experimental testing and finite element analysis. Contact pressure is widely regarded as an important indicator of seated comfort, so it is employed here to evaluate the different foams. By combining experimental testing with finite element analysis, this study aims to provide a comprehensive understanding of the relationship between unit cell size and pressure distribution. Ultimately, this will offer useful guidance for the future design and optimization of 3D-printed seating foams.

## 2. METHODS

### 1. Simulation Method

The study used LS DYNA for simulation with a simplified human body model based on the full-body model developed by Liu [Liu, S., 2023]. The original model was simplified into 37 parts (Fig. 1), including buttock, thigh, pelvis models, corresponding to approximately 10% of the original number of parts. The removed body parts were represented by applying equivalent mass to the remaining model at pelvis and knees [Yadav, S. K., 2021].

In this study, a quasi-static analysis was conducted using an explicit finite element solver. The human body model was freely dropped at a very small distance from the seat surface to reduce unnecessary movement before contact. The initial velocity of the model was set to zero, and the load was applied through gravitational acceleration. The 3D-printed foam was placed on a rigid plate representing the supporting surface. The rigid plate was fully constrained in all six degrees of freedom to simulate a fixed support.

The main contact interfaces included the contact between the human body and the foam, and the contact between the foam and the rigid plate. In addition, contact definitions were assigned between different parts of the human body model, as well as self-contact within each individual part. These contact settings were used to prevent penetration between different parts and between elements within the same part.

### 2. Design Method

Figure 2 illustrates the gyroid unit cell and the foam prototype used in this study. The geometry of the gyroid foam was defined by three primary design parameters: unit cell size (s), surface coefficient (d), and wall thickness (t).

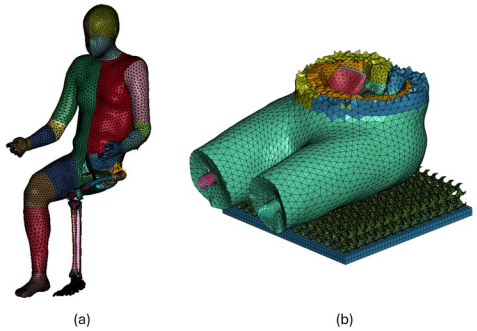



Fig. 1. Human model: (a) - Full body model; (b) - Simplified body model

These parameters govern the geometric characteristics of the lattice structure and may influence its mechanical behavior under loading conditions. These parameters were inputed independently using Fusion 360 (s, d) and then using ELEGOO Cura for thickness (t).

Three foam prototypes with dimensions of 400 × 440 × 60 mm were designed and manufactured for experimental evaluation and finite element model verification. The prototypes were designed with different surface coefficients (Fig. 2) while the remaining design parameters and printing conditions were kept constant.

## 3. **Testing Method**

Material property test:

In this study, the gyroid structure was modeled directly in the finite element simulation rather than using a homogenized model. Therefore, it was necessary to determine the material properties of the printed gyroid structure to more accurately represent its mechanical behavior.

Several previous studies on the simulation of 3D-printed materials have determined material properties by testing individual 3D-printed filaments, including tensile tests [Ahmadi Soufivand, A., 2020] and compression tests [Amirpour, M., 2022]. However, using the mechanical properties of a single 3D-printed filament to represent an entire 3D-printed structure may not accurately reflect its actual mechanical behavior. Experimental observations showed a clear difference in the failure mechanisms. Under axial tensile loading, a single 3D-printed filament exhibited high ductility. In contrast, 3D-printed specimens loaded perpendicular to the printing plane (Z-direction) showed a mixed failure mode. The fracture involved not only interlayer separation but also fracture of the printed roads themselves. This behavior suggests that the thermomechanical manufacturing process, together with the formation of stress concentration, results in mechanical behavior that differs from that of a single 3D-printed filament. Therefore, to obtain material properties that are more representative of the actual gyroid foam used in the finite element model, tensile tests were performed on straight specimens using an A&D MCT-1150 testing machine at a loading rate of 10 mm/min (Fig. 3). TPU 95A was used for specimens and prototypes at 230°C nozzle and 50°C print bed.

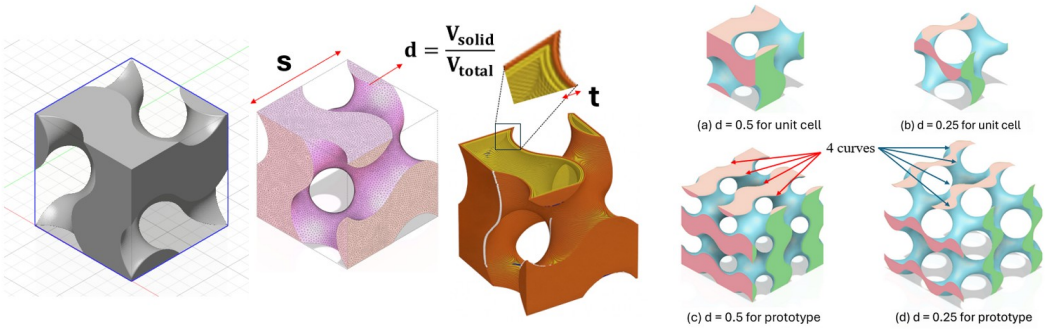



Fig. 2. Unit cell and description of d variation in the structure

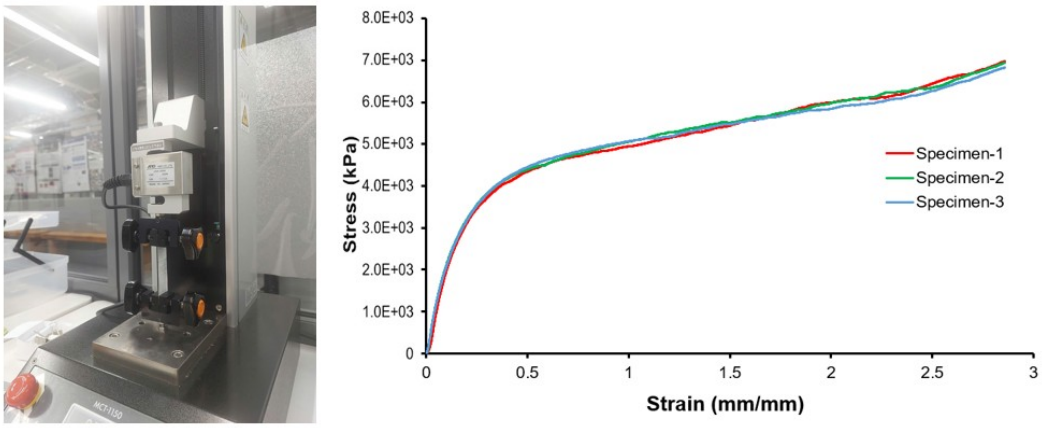



Fig. 3. Testing machine and properties curve

This approach was adopted to minimize differences in geometry and manufacturing conditions between the material specimens and the simulated gyroid structure. The specimens were stretched to an engineering strain of approximately 3, and the force-displacement curves were recorded. The experimental data were then processed to obtain the engineering stress-strain curve of the material during tensile deformation, which was used to define the material model in this study.

The TPU material was modeled using the MAT_181 (SIMPLIFIED_RUBBER/FOAM) material card with a density of $1.2 \times 10^{-6}$ kg/mm$^3$, a bulk modulus of $333 \times 10^3$ kPa, and a Poisson's ratio of 0.495. It was treated as a rubber-like material, and a first-order Ogden material model was used to fit the compression behavior in MATLAB. The first-order Ogden equation is given by:

$$P = \mu\left(\lambda^{\alpha-1} - \lambda^{-0.5\alpha-1}\right) \quad (1)$$

Where: P is stress; $\mu$ is the shear modulus coefficient, representing the first material constant of the Ogden model; $\lambda$ is the stretch ratio; and $\alpha$ is the material exponent, representing the second material constant of the Ogden model and serving as the exponential parameter.

Prototype test:

Sitting tests with human subjects were conducted to validate the simulation process can be trusted for analysis of the new model without prototyping. Interface pressure during sitting was measured using a pressure sensor system (Fig. 4). A volunteer was asked to sit on 3 prepared prototypes, and ten times for each prototype to collect pressure data. The physical characteristics of the subject were as follows: age 24 years, height 176 cm, body mass 72 kg, and a Body Mass Index (BMI) of 23.24 kg/m², which represents a normal physique. The results for each prototype were then averaged to reduce random errors between the repeated trials. Although the subjects were instructed to maintain a consistent upright posture, slight differences in sitting conditions were unavoidable across trials.



Fig. 4. Testing scene

In addition to pressure measurements, vertical foam displacement was recorded to provide further validation of the model. A physical probe inserted through the foam was used to measure the vertical displacement directly beneath the right ischial tuberosity. After the foam displacement stabilized, the probe displacement was recorded and used as the final foam displacement value for comparison with the simulation results.

## 3. RESULTS AND DISCUSSION

### 1. **Simulation Validation**

To evaluate the reliability of the finite element model, the simulated contact pressure and foam surface displacement were directly compared with the testing results. The corresponding design parameters of prototypes are summarized in Table 1. In all test cases, the measured pressure consistently reached its maximum value at the ischial tuberosities, which are located at the lower part of the pelvis and directly bear the body weight during sitting. Both the testing and simulation results showed a gradual decrease in pressure from the ischial tuberosities toward the thighs. The thigh region acted as a secondary load-bearing area with moderate pressure levels, contributing to the redistribution of body weight (Fig. 5). The ability of the finite element model to capture this characteristic pressure distribution, in good agreement with the experimental observations, provides initial evidence that the applied boundary conditions and contact definitions are reasonable.

However, the simulation results showed a localized increase in pressure at the thigh region near the front edge of the foam. This phenomenon can be explained by the limitations of the simplified human body model, the absence of foot support in the simulation. The simplified model already differs from the full body model, so some differences between the simulation results and the actual measurements are unavoidable. As shown in Fig. 5b, this pressure increase was relatively small (1-2 kPa) and did not significantly affect the primary pressure distribution around the ischial tuberosities. Therefore, this difference is considered acceptable.

Table 1. Prototype parameters for validation

| Prototype | Unit cell (mm) | | | Printer (mm) | |
|---|---|---|---|---|---|
| | s | t | d | Nozzle | Wall |
| P1 | 30 | 0.6 | 0.25 | 0.6 | 1 |
| P2 | 30 | 0.6 | 0.35 | 0.6 | 1 |
| P3 | 30 | 0.6 | 0.50 | 0.6 | 1 |

Although the current model is suitable for this study, future modeling approaches can be considered to further improve accuracy. These include adjusting the initial thigh angle, modifying the added mass distribution, or further simplifying non-critical regions to prevent unwanted localized pressure.

To further validate the model quantitatively, the peak interface pressures below the left and right buttocks (P.P_L and P.P_R) and the foam's maximum vertical displacement below the right buttock (P.D_R) were extracted from both the simulations and tests, as summarized in Table 2.

Overall, the simulation demonstrated good accuracy in predicting the peak contact pressure. The largest difference in peak pressure was approximately 12% for two cases, while the remaining cases exhibited errors below 10% (Table 2). Considering the complexity of the human-seat contact interface and the detailed human body model employed, pressure prediction differences within the range of 10-12% have been widely reported in previous studies [Zhang, T.,2023, Huang, S., 2015, Huang, S., 2022, Wang, X., 2019]. Regarding the maximum vertical displacement, the test and simulation results showed good agreement, with most differences ranging from 5% to 10%.

To provide a clearer visualization of the mechanical response under different structures, the comparison results are presented in Fig. 6. The average peak pressures of both buttocks (Fig. 6a) exhibited a clear increasing trend as the surface coefficient (d) increased. Both the test and simulation results consistently showed that the lowest average peak pressure was recorded at d = 0.25, while the highest was observed at d = 0.50. Averaging the peak pressures from the left and right regions helps minimize test differences caused by slight, unavoidable asymmetrical sitting postures across trials. While the test results showed a small pressure difference between d = 0.25 and d = 0.35, the simulation showed a larger increase; however, this difference remains acceptable within the allowed range (7.33%).

Table 2. Comparison between test and simulation results

| Result | P1 | | | P2 | | | P3 | | |
|---|---|---|---|---|---|---|---|---|---|
| | P.P_L (kPa) | P.P_R (kPa) | P.D_R (mm) | P.P_L (kPa) | P.P_R (kPa) | P.D_R (mm) | P.P_L (kPa) | P.P_R (kPa) | P.D_R (mm) |
| Test | 16.61 | 16.67 | 17.1 | 16.68 | 16.79 | 6.7 | 19.32 | 19.28 | 5.8 |
| Simulation | 16.21 | 14.62 | 15.31 | 17.92 | 16.30 | 7.24 | 21.78 | 19.04 | 6.10 |
| Difference | 2.42% | 12.27% | 10.47% | 7.44% | 2.89% | 8.06% | 12.74% | 1.24% | 5.17% |

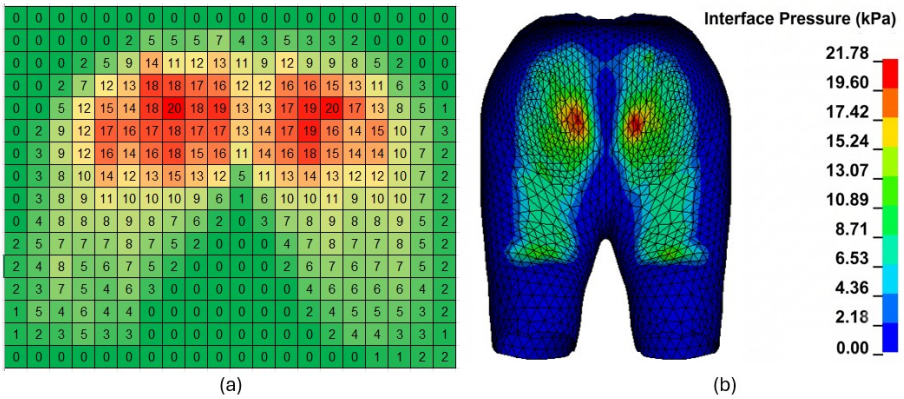



Fig. 5. Pressure distribution - P3 (kPa): Test (a) and Simulation (b)

Overall, the simulation successfully captured the general relationship between the surface coefficient of the gyroid foam and the interface pressure response.

A similar trend was observed for the vertical displacement of the three prototypes. As the surface coefficient (d) decreased, the gyroid foam contained larger internal voids, resulting in greater structural displacement under loading (Fig. 6b). When d = 0.25, the displacement increased substantially in both the test and simulation results, indicating that the proposed finite element model was able to capture the structural softening associated with the reduction in d. This agreement provides additional confidence in the model's reliability and its suitability for the subsequent analyses.

## 2. **Effect of Unit Cell Size on Interface Pressure**

Following the successful validation of the finite element model, a parametric study was conducted to investigate the influence of unit cell size (s) on interface pressure distribution. Five simulation models (M1-M5) with unit cell sizes ranging from 30 mm to 50 mm were designed and analyzed. For this evaluation, only the unit cell size was varied, while the remaining two design parameters were kept constant (Table 3). The corresponding simulation results are summarized in Table 4.

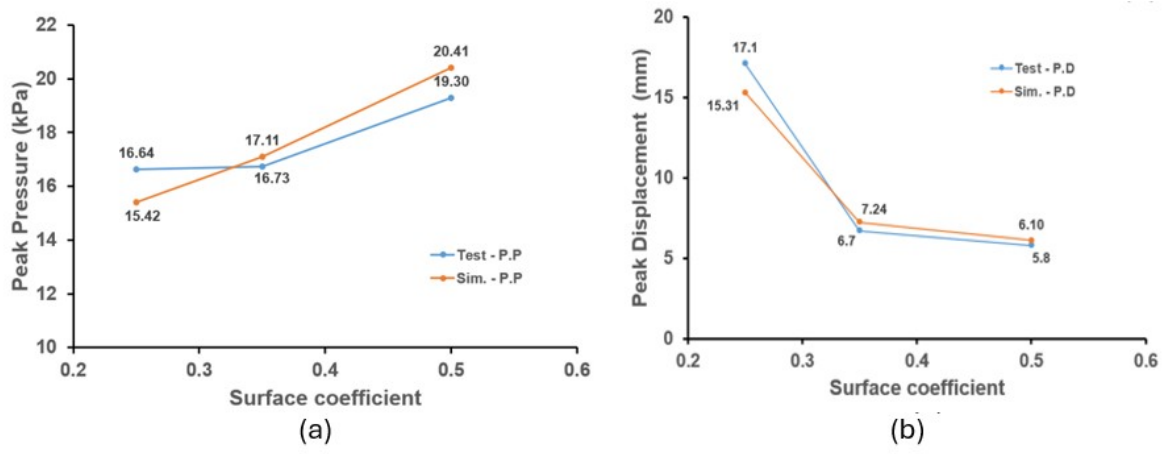



Fig. 6. Comparison graph: (a) - Average peak pressure; (b) - Peak displacement

Table 3. Design parameters for unit cell size variations

| Model | Unit cell (mm) | | |
|---|---|---|---|
| | s | t | d |
| M1 | 30 | 0.6 | 0.35 |
| M2 | 35 | 0.6 | 0.35 |
| M3 | 40 | 0.6 | 0.35 |
| M4 | 45 | 0.6 | 0.35 |
| M5 | 50 | 0.6 | 0.35 |

Table 4. Summary of peak pressure and displacement simulation results

| Result | Model | | | | |
|---|---|---|---|---|---|
| | M1 | M2 | M3 | M4 | M5 |
| P.P_L (kPa) | 17.92 | 19.54 | 17.74 | 14.18 | 12.77 |
| P.P_R (kPa) | 16.30 | 22.36 | 16.03 | 13.59 | 12.04 |
| P.P_AVG (kPa) | 17.11 | 20.95 | 16.89 | 13.89 | 12.41 |
| P.D_R (mm) | 7.24 | 9.30 | 11.10 | 18.00 | 22.10 |

From the simulation results, it can be observed that increasing the unit cell size resulted in larger surface displacement of the foam, increasing from 7.24 mm to 22.10 mm. However, the average peak contact pressure did not exhibit a monotonic increasing or decreasing trend. Instead, the highest average peak pressure was observed for Model M2 (35 mm), reaching approximately 20.95 kPa. To better explain the pressure increase observed in M2, cross-sectional views through the location of the maximum contact pressure were extracted for model M1, M2, and M3 (Fig. 7). In M2, the lowest point of the ischial tuberosity is located directly above a vertical wall of the gyroid structure. This alignment transfers the load directly through the load-bearing region of the lattice, resulting in higher local contact pressure. In contrast, in M1 and M3, the contact point is shifted slightly away from the vertical wall. Consequently, the load is distributed over the surrounding gyroid structure, resulting in lower local contact pressure.

At larger cell sizes, structural softening increases the contact area and reduces the pressure. These results suggest a nonlinear relationship between the unit cell size and both the average interface pressure and the structural displacement (Fig. 8). Quadratic trend lines were added to show the overall trend of the data. Since only five data points were available, the fitted equations and $R^2$ values are provided for trend observation only and should not be considered as accurate prediction models.

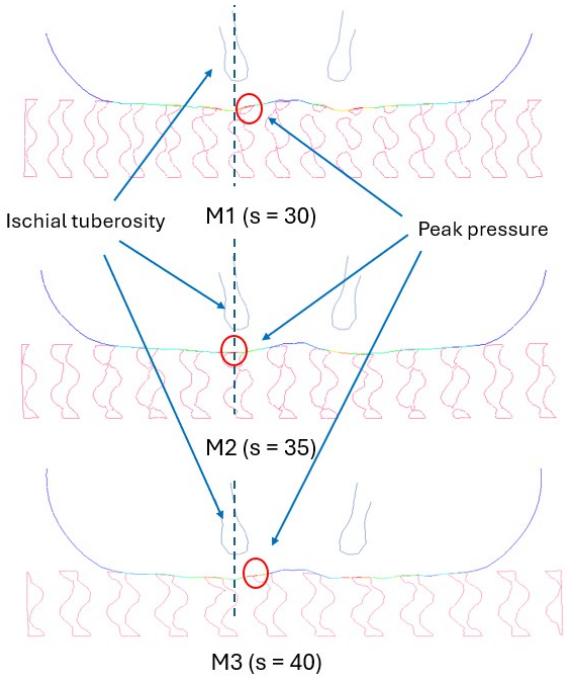



Fig. 7. Cross-sectional views at peak pressure location

The observed trends suggest that unit cell sizes of 30 mm and 40 mm provide a better balance between pressure reduction and structural stiffness. Compared with the 35 mm model, both configurations produced lower peak pressures while maintaining greater structural support than the 45 mm and 50 mm models.

In contrast, the 50 mm model exhibited the largest surface deformation. This larger displacement increased the contact area between the human body and the foam, allowing the body load to be distributed over a wider area and consequently reducing the contact pressure.

To further clarify the influence of the design parameters on sitting comfort, the Seat Pressure Distribution index (SPD%) was employed to evaluate pressure distribution uniformity.

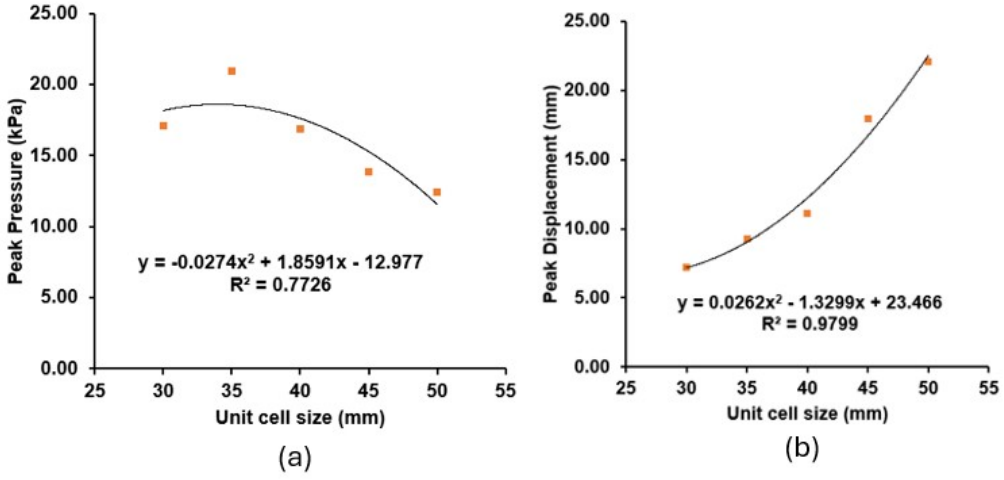



Fig. 8. Quadratic trendlines with fitted equations and $R^2$ values.
(a) - Average peak pressure; (b) - Peak displacement

A lower SPD% indicates a more uniform pressure distribution, which is generally associated with improved sitting comfort [Lu, C., 2023, Mehdi, A., 2002, Jiayi, B., 2021]. The SPD% was calculated using Equation (2):

$$SPD\,\% = \frac{\sum_{i=1}^{n} (p_i - p_m)^2}{4np_m^2} \times 100$$

Where: $p_i$ is the pressure at the i-th measurement cell, $p_m$ is the average pressure, n is number of measurement cell.

However, this index was originally developed for pressure maps obtained from experimental measurements. To extend its application to finite element simulations using triangle mesh elements, a spatial interpolation procedure was implemented in MATLAB. Through this process, the pressure values obtained from the finite element model were converted into a uniform pressure map, as illustrated in Fig. 9. The pressure distribution calculated on triangle elements was interpolated onto a common two-dimensional pressure map consisting of 256 cells (16×16), enabling direct calculation of the SPD% index. Based on the interpolated pressure maps, the SPD% values were calculated for all five foam models. The corresponding results are summarized in Table 5.

The SPD% results showed a trend that was generally consistent with the peak contact pressure. A similar trend was observed as the unit cell size varied, indicating that both evaluation indices reflected the influence of unit cell size on pressure distribution. The combined trends of peak pressure and SPD% are presented in Fig. 10.

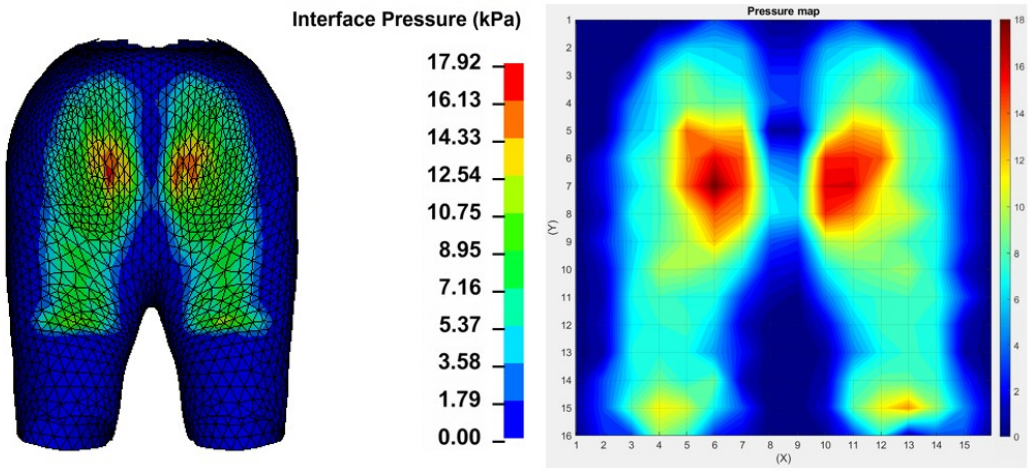



Fig. 9. Conversion of simulation results into a pressure map (M1)

Table 5. Summary of SPD% results

| Result | Model | | | | |
|---|---|---|---|---|---|
| | M1 | M2 | M3 | M4 | M5 |

| | | | | | |
|---|---|---|---|---|---|
| Average Pressure (kPa) | 5.87 | 5.94 | 6.17 | 5.79 | 5.59 |
| SPD% | 6.71% | 8.01% | 6.39% | 5.08% | 4.78% |

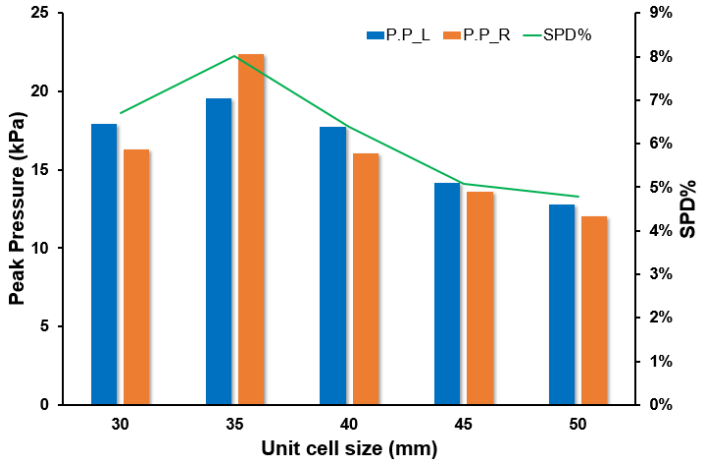



Fig. 10. Combined trends of peak contact pressure and SPD%

The SPD% index depends not only on the peak pressure but also on the overall pressure distribution. As illustrated in Fig. 9, although the 30 mm and 40 mm unit cell sizes produced similar peak pressures, the 40 mm design achieved a more uniform pressure distribution, resulting in a lower SPD% value. In contrast, the increase in pressure at the 35 mm unit cell size caused greater local pressure concentration, reduced the uniformity of the contact pressure distribution, and led to the highest SPD% value (8.01%). As the unit cell size increased from 40 mm to 50 mm, both peak pressure and SPD% decreased. 45 mm and 50 mm size are small differences than orthers. Therefore, the 45 mm size seems to be good. Future issues are more size to be simulated.

## 4. CONCLUSION

This study investigated the influence of unit cell size (s), one of the primary geometric design parameters of 3D-printed gyroid foam, on sitting comfort indicators, including peak contact pressure and the SPD% index, using a finite element simulation approach.

The results demonstrated that the unit cell size has a nonlinear influence on the contact pressure at the human-foam interface. Larger unit cell sizes produced greater foam displacement, which increased the contact area between the occupant and the foam and consequently reduced the peak contact pressure.

The proposed finite element model demonstrated satisfactory reliability by showing good agreement with the testing results for both peak contact pressure and maximum foam displacement in most validation cases. Nevertheless, further improvements to the human body

model are still necessary to achieve higher prediction accuracy and reliability. In future work, a more detailed human body model should be adopted.

The test validation was conducted using a single participant while evaluating multiple foam prototypes. This approach eliminated the influence of individual differences and enabled a clearer assessment of the effect of unit cell size. However, the findings may not fully represent the variation in body characteristics across a wider population. Future studies should therefore include a larger and more diverse group of participants to improve the generalizability of the results.

Furthermore, the SPD% index was successfully extended to finite element simulations through the proposed spatial interpolation procedure. The SPD% results exhibited trends that were consistent with those of the peak contact pressure, indicating that this index can serve as a useful quantitative indicator for future simulation-based evaluations of sitting comfort.

In addition to improving the finite element model, future work will focus on a more comprehensive investigation of the combined effects of multiple geometric design parameters on pressure distribution and sitting comfort. Such studies are expected to provide a deeper understanding of the design characteristics of 3D-printed seating foams and support their further optimization.

## REFERENCES

1. **Shahrubudin, N., Lee, T.C. and Ramlan, R. (2019),** "An Overview on 3D Printing Technology: Technological, Materials, and Applications", Procedia Manufacturing, Vol.35, pp 1286-1296.

**2. Pagliari, C., Montalti, A., Frizziero, L. and Liverani, A. (2025),** "Enhancing ergonomic comfort: A study on customized cushion design using 3D scanning and additive manufacturing", Results in Engineering, Vol.25, 104256.

**3. Hogeveen, T., Ballemans, M., Strijker, A., Ammerlaan, B. and Vink, P. (2023),** "Towards an environment friendly comfortable aircraft seat", Proceedings of the Fourth International Comfort Congress, Amberg, Germany, pp 17-20.

**4. De la Rosa, S., Mayuet, P.F., Silva, C.S., Sampaio, A.M. and Rodríguez-Parada, L. (2024),** "Design and characterization of 3D-printed TPU-based lattice structures. Application to methodology for the design of personalized therapeutic products", Rapid Prototyping Journal, Vol.30, No.11, pp 72-86.

**5. Lu, C., Chen, Z., Li, Y., Fu, X. and Tang, Y. (2023),** "Hole Matrix Mapping Model for Partitioned Sitting Surface Based on Human Body Pressure Distribution Matrix", Healthcare, Vol.11, No.6, 895.

**6. Nguyen, M.T. and Hirao, A. (2025),** "Finite Element Modeling of Human-Seat Interaction and the Integration of 3D-Printed Foam in Enhancing Sitting Comfort: A Systematic Review", Appl. Sci., Vol.15, No.18, 10193.

**7. Liu, S., Beillas, P., Ding, L. and Wang, X. (2023),** "PIPER adult comfort: an open-source full body human body model for seating comfort assessment and its validation under static loading conditions", Front. Bioeng. Biotechnol., Vol.11, 1170768.

**8. Yadav, S. K., Huang, C., Mo, Fuhao., Li, J., Chen, J., Xiao, Z. (2021),** "Analysis of seat cushion comfort by employing a finite element buttock model as a supplement to pressure measurement", International Journal of Industrial Ergonomics, Vol. 86, 103211.

**9. Ahmadi Soufivand, A., Abolfathi, N., Hashemi, S.A. and Lee, S.J. (2020),** "Prediction of mechanical behavior of 3D bioprinted tissue-engineered scaffolds using finite element method (FEM) analysis", Additive Manufacturing, Vol.33, 101181.

**10. Amirpour, M. and Battley, M. (2022),** "Study of manufacturing defects on compressive deformation of 3D-printed polymeric lattices", Int. J. Adv. Manuf. Technol., Vol.122, pp 2561-2576.

**11. Zhang, T. and Ren, J. (2023),** "A design method for contact contour based on the distribution of target contact pressure", Int. J. Mech. Mater. Des., Vol.20, pp 251-267.

**12. Huang, S., Zhang, Z., Xu, Z. and He, Y. (2015),** "Modeling of human model for static pressure distribution prediction", Int. J. Industrial Ergon., Vol.50, pp 186-195.

**13. Huang, S., Sun, D., Zhang, L., Zhou, J. and Wang, Z. (2022),** "Comfort Assessment and Optimization Based on FE Simulation for High-Speed Train Seats: Comparison with Different Design Parameters", Sustainability, Vol.14, No.22, 15185.

**14. Wang, X., Savonnet, L., Theodorakos, I., Beurier, G. and Duprey, S. (2019),** "Biomechanical human models for seating discomfort assessment", DHM Posturography, pp 643-656.

**15. Mehdi, A., Michael S. T. (2002),** "Alternative Test Methods for Long Term Dynamic Effects of Vehicle Seats", SAE Technical paper series, 2002-01-3082.

**16. Jiayi, B., Qianxiang, Z., et al (2021),** "Comfort Evaluation of Slow-Recovery Ejection Seat Cushions Based on Sitting Pressure Distribution", Front. Bioeng. Biotechnol. (9), 759442.

# DETECTING PHYSICAL FATIGUE AND DROWSINESS DURING LONG-TERM TRUCK DRIVING USING CENTER OF PRESSURE DYNAMICS

**Akinari HIRAO**, *hirao@shibaura-it.ac.jp* Shibaura Institute of Technology, 135-8548, Tokyo, Japan

**Kai SUZUKI**, *CY22044@shibaura-it.ac.jp* Shibaura Institute of Technology, 135-8548, Tokyo, Japan

## ABSTRACT

In truck transportation, preventing accidents caused by drowsiness and physical distress during long-duration driving is a critical challenge. While existing systems focus on drowsiness, methods to decouple these two fatigue factors remain unestablished. This study proposes a non-intrusive method to differentiate mental and physical fatigue using Center of Pressure (COP) dynamics. We conducted a 100-minute continuous driving experiment using a driving simulator with 12 participants. The experiment revealed distinct behavioral patterns: increased physical distress significantly elevated both COP path length and standard deviation (SD), whereas increased drowsiness significantly increased SD but had no significant effect on path length. Based on these findings, we developed a four-quadrant model to classify driver states. Physiological data, including core body temperature, validated the model's accuracy. This approach enables specific interventions, such as recommending either a nap or a stretch, based on the identified fatigue source.

**Keywords:** Physical fatigue, Drowsiness, Pressure distribution, Driving

## 1. INTRODUCTION

In modern global logistics networks, road freight transport plays a fundamental role in supporting social infrastructure. However, the global shortage of drivers and the tightening of labor regulations have made it more difficult than ever to achieve both operational safety and efficiency [International Road Transport Union, 2024] [Jaydarifard et al., 2024]. To overcome this challenge, monitoring technologies that can grasp driver status in real-time are indispensable [Öztürk et al., 2026]. Nevertheless, many currently popular systems are biased toward detecting "Drowsiness" based on visual information such as eye closure (PERCLOS) [Abe, 2023] [Hassan et al. (2026)], often failing to sufficiently consider the impact of "Physical

Discomfort" associated with prolonged sitting postures [Kyung and Nussbaum, 2008] [Lecocq et al., 2022]. Professional truck drivers, in particular, are forced into fixed postures specific to heavy-duty vehicles for long periods; thus, physical distress often arises even while the driver is awake, becoming a significant factor in inducing distractions and human errors [Jongkol et al., 2026] [Williamson et al., 2011].

This study aims to decouple and quantify the characteristics of the effects that central "mental fatigue" and peripheral "physical fatigue" have on driver behavior. Ergonomics research has demonstrated that physical discomfort is not merely a lack of comfort but a physiologically independent response [Helander and Zhang, 1997], and its accumulation has been reported to manifest as involuntary "postural fidgeting" [Sammonds et al., 2017].

In our experiments, we conducted long-duration simulations replicating a heavy-duty truck driving environment and established a multimodal measurement system consisting of core body temperature, heart rate variability (HRV), and postural imaging. In this report, while utilizing these diverse physiological and behavioral indicators as evidence to support the differentiation of fatigue types, we ultimately focus on the dynamics of the "Center of Pressure (COP)". We examine the effectiveness of COP fluctuation characteristics—measurable non-intrusively from the seat surface—in aggregating and representing these different types of fatigue. This effort represents an attempt to evolve existing knowledge on the relationship between postural changes and body pressure distribution [Na et al., 2005] and the prediction of discomfort via seat pressure [Gyi and Porter, 1999] into a decoupled fatigue evaluation method for modern long-duration driving.

## 2. METHODS

1. **Participants and Environment:** Twelve healthy male participants (mean age: 22.0 ± 1.5 years, height: 174.5 ± 5.8 cm, weight: 64.5 ± 9.3 kg) who drive on a daily basis participated in the experiment. They were instructed to obtain sufficient sleep (equivalent to or more than their usual amount) on the night prior to the experiment, and their physical condition was confirmed to be normal on the day of the study.

The laboratory was maintained as a quiet environment with the room temperature controlled at approximately 23°C, excluding external auditory stimuli.

2. **Experimental Setup and Simulation:**

Cockpit: A dedicated cockpit was constructed using an aluminum frame based on actual truck blueprints. The steering angle was fixed at 25° to emulate a heavy-duty truck. For steering and

pedal operations, a steering controller with force feedback, the Force Feedback Truck Control System manufactured by HORI, was utilized.

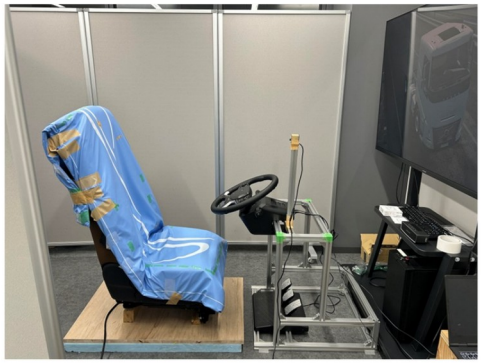
Seat: A seat for heavy-duty vehicles (manufactured by Tachi-S) was employed to reproduce the upright seating posture characteristic of trucks.

Driving Simulator Software: "Euro Truck Simulator 2" was adopted to precisely simulate the physical behavior (inertia, suspension, engine torque, etc.) of a full cab-over vehicle (Volvo FH). The driving screen is shown in Figure 1.

Driving Task: Participants performed a 100-minute continuous drive on the M25 motorway in the UK (3 lanes, gentle curves). To induce monotony and control arousal levels, the traffic volume was set to 0.1 times the normal level, and participants were instructed to cruise at a speed of 80–90 km/h.



Driving simulator screen



Experimental environment setup

Figure 1. Driving simulator screen image and experimental environment.

3. **Measurements and Feature Extraction:**

Subjective Measures (Every 10 min):

Physical Fatigue Index (PFI) [Hirao et al., 2006]: Subjective fatigue levels for eight body parts (neck, shoulders, back, lower back, buttocks, arms, thighs, and legs) were collected on a 6-point scale from 0 to 5. The Physical Fatigue Index (PFI) was calculated using Sheridan' s weighting factors (e.g., neck: 0.5, back: 0.5, buttocks: 0.4) according to the following formula:

$$PFI(t) = \sum w_i \cdot S_i(t) \quad (1)$$

Karolinska Sleepiness Scale (KSS) [Gillberg et al., 1994]: Drowsiness was assessed using a 9-point scale ranging from 1 (extremely alert) to 9 (very sleepy). The Japanese translation of the KSS [Uchida and Nakajima, 2024] was employed for this study.

Physical Measures:

COP Dynamics: Center of Pressure (COP) coordinates were extracted using a seat pressure sensor (Sumitomo Riko SR Soft Vision Full Body Version; 5 Hz).

Path Length: The sum of the Euclidean distances between COP coordinates recorded every second over a one-minute interval.

Standard Deviation: Calculated as the combined standard deviation of the center of gravity on the X and Y axes using the following formula:

$$SD_{Total} = SD_x^{\,2} + SD_y^{\,2} \quad (2)$$

Postural Data: Using the Microsoft Azure Kinect Body Tracking Function, coordinates for 12 joints were acquired. The "neck angle" and "trunk angle" were then calculated from vectors connecting the tragus, T1, and the ischial tuberosity.

Physiological Measures:

Heart Rate: Heart rate was measured at 1 Hz using a smartwatch (Garmin Vivoactive 5).

Core Body Temperature: Core body temperature was measured at 1 Hz using a belt-type monitor (CORE Body Technology).

Drowsiness Indicators: Using a web camera (60 fps), PERCLOS (the proportion of time the eyes were closed over a specific period) and the frequency of "long blinks" (microsleeps) lasting 0.5 seconds or longer were calculated.

Data Synchronization and Preprocessing: To integrate the different sampling frequencies from multiple measurement devices (e.g., 60 Hz for video, 5 Hz for pressure, and 1 Hz for physiological sensors), all data were synchronized and resampled to a common frequency of 1 Hz. Subsequently, features (e.g., mean, standard deviation, or cumulative values) were calculated for each one-minute interval to serve as the units for analysis.

## 3. FOUR-QUADRANT MODEL FOR DRIVER STATE

In this study, we defined a four-quadrant model to categorize the driver's state using two primary axes: central "mental fatigue" (drowsiness) and peripheral "physical fatigue" (physical distress).

The thresholds for the four quadrants were established based on the Subjective Measures as follows:

Horizontal Axis (Drowsiness): Reduced arousal is defined as KSS≥6 (the midpoint between "neither alert nor sleepy" and "sleepy").

Vertical Axis (Physical Fatigue): The presence of physical distress is defined as PFI≥4.2. This threshold represents the level at which the subjective scores for the major body parts (neck, lower back, and buttocks) reach "3: feel."

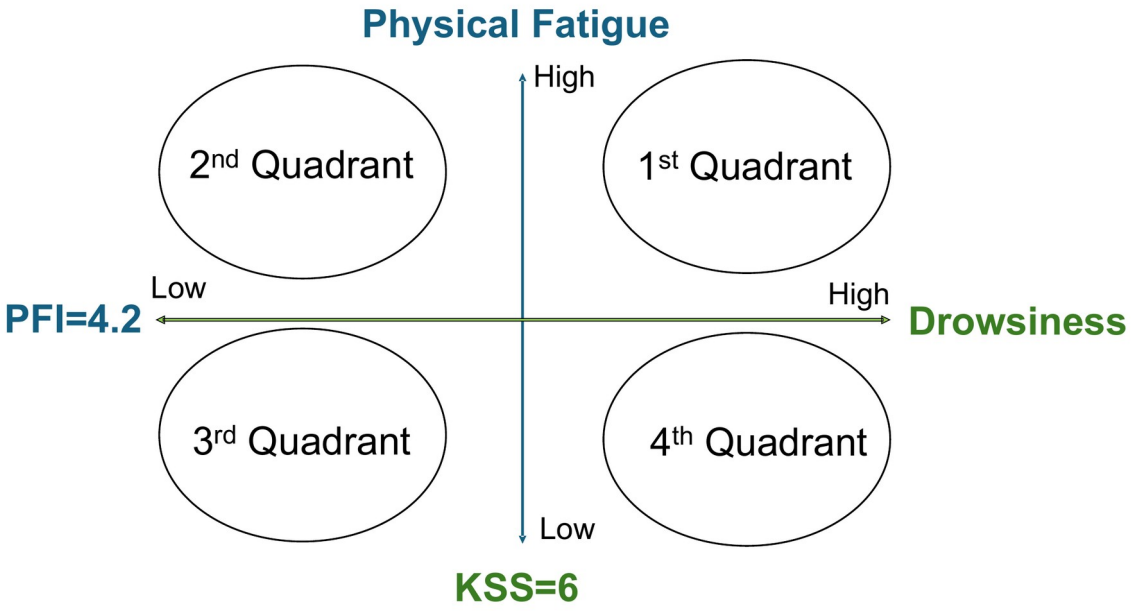



Figure 2. Four-Quadrant Model for Driver State

This study aims to capture central "mental fatigue" (drowsiness) and peripheral "physical fatigue" (physical distress) through Center of Pressure (COP) dynamics. To this end, the following two hypotheses have been defined:

Hypothesis 1 (Drowsiness): Drowsiness causes a relaxation of antigravity muscles (diminished postural maintenance capacity), which leads to an increase in COP fluctuations (Standard Deviation).

COP Standard Deviation (Fluctuations)= The variability (SD) of the center of pressure (COP) position.

Hypothesis 2 (Physical Fatigue): Physical distress leads to "postural fidgeting" (re-sitting) to relieve discomfort, resulting in an increase in COP displacement (Path Length).

COP Path Length (Displacement)=The total distance of center of pressure (COP) movement over a 1-minute interval.

## 4. RESULTS AND DISCUSSION

1. **Validity of Fatigue States:** As the driving session progressed, both the Physical Fatigue Index (PFI) and the Karolinska Sleepiness Scale (KSS) increased, showing an extremely strong positive correlation (r=0.99). Simultaneously, a decrease in core body temperature

(r=−0.98) and a reduction in heart rate (r=−0.79) were observed, providing objective evidence that the participants were in a physiological sleep onset stage (a state of reduced arousal).

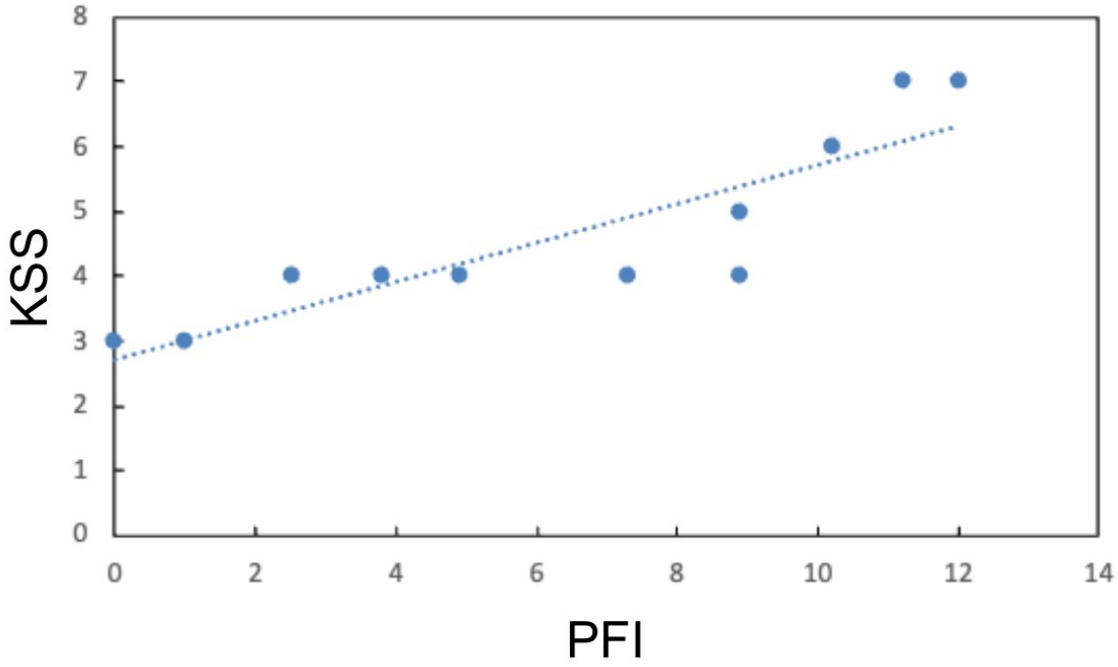



Figure 3. Relationship between PFI and KSS

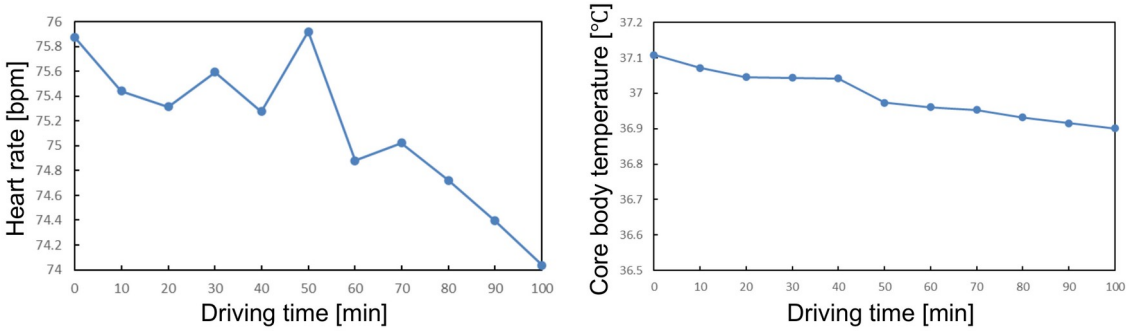



Figure 4. Transition of Heart rate and core body temperature

2. **Decoupling Drowsiness and Physical Fatigue:**

Drowsiness (Hypothesis 1): In the "low arousal group" (KSS≥6), the COP standard deviation significantly increased ($p<0.01$). Conversely, no statistically significant difference was observed in the COP path length compared to the high arousal group ($p>0.15$). This suggests that the relaxation of antigravity muscles caused by drowsiness induces "static fluctuations" but does not involve active physical displacement. This static fluctuation in COP was also aligned with the tendency of increased PERCLOS and altered neck angles.

Physical Fatigue (Hypothesis 2): In the "high fatigue group" (PFI≥4.2), the COP path length significantly increased compared to the low fatigue group ($p<0.01$). This is attributed to active postural fidgeting (re-sitting) performed to alleviate physical discomfort. The increase in path

length coincided with transient shifts in trunk angles captured by body tracking, supporting the occurrence of conscious re-sitting.

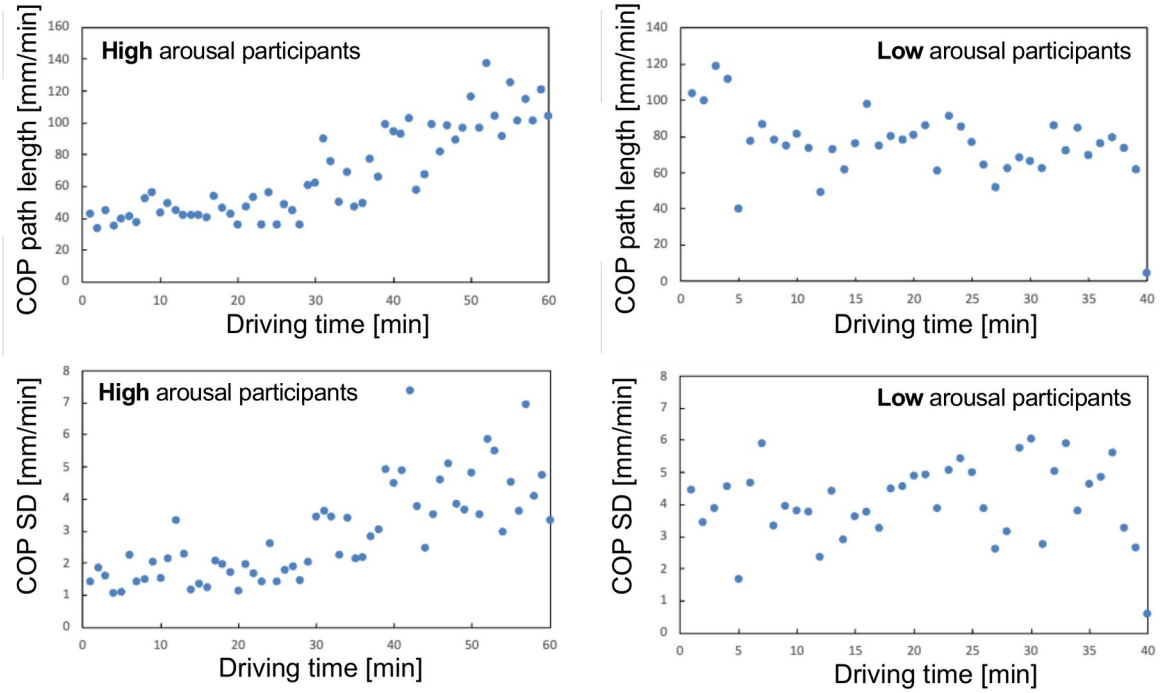



Figure 5. Drowsiness and COP dynamics

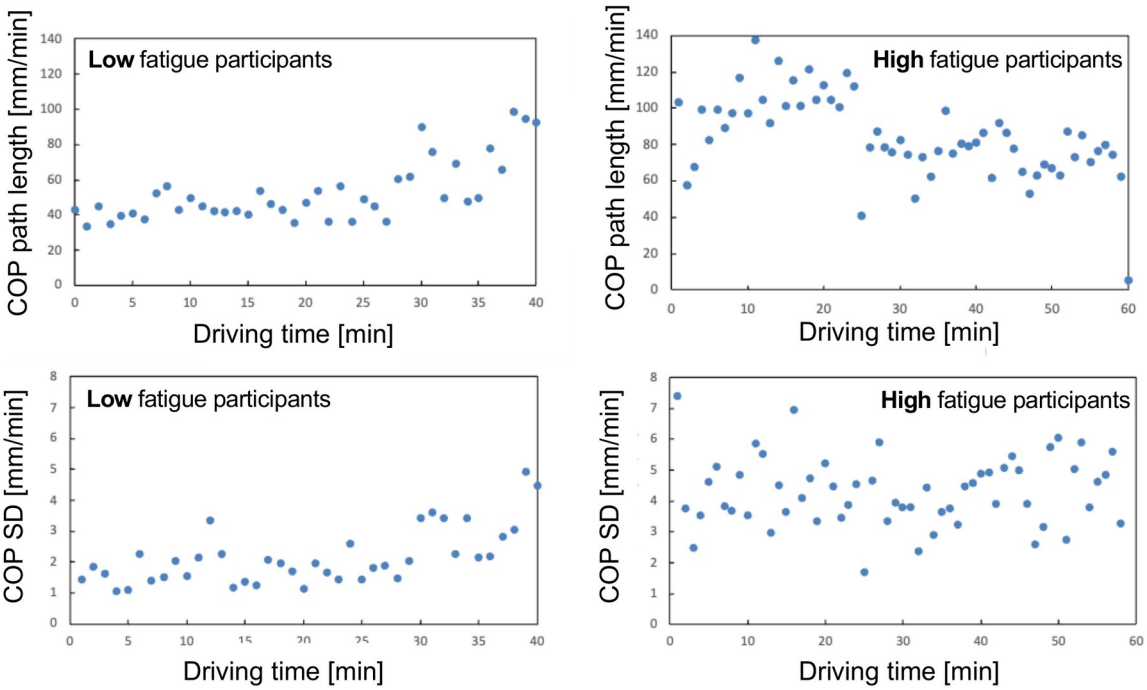



Figure 6. Physical Fatigue and COP dynamics

3. **Proposal of Four-Quadrant State Classification Model:** Based on the findings mentioned above, we propose a "Four-Quadrant State Classification Model" using COP standard

deviation (SD: postural stability) on the X-axis and COP path length (displacement) on the Y-axis. The states within these four quadrants are defined as follows:

3rd Quadrant (Stable State): A stable driving condition characterized by high arousal and minimal physical distress.

2nd Quadrant (Physical Fatigue): A state where the path length is large, and conscious postural fidgeting (re-sitting) is dominant.

4th Quadrant (Low Arousal State): A state where the path length remains small, but micro-fluctuations (SD) increase due to reduced postural stability.

1st Quadrant (Combined Fatigue): A state where both indicators increase, representing the highest risk for driving.

The thresholds for classifying driver states using these four quadrants were established by adding twice the standard deviation (2SD) to the mean values of the stable condition observed during the first 40 minutes of the experiment of all participants (baseline: KSS≤5 and PFI<4.2).

Regarding the observed state transitions, participants were located in the 3rd Quadrant (Stable) during the initial 40 minutes of the experiment. However, as time progressed, a dynamic transition was confirmed, with participants shifting through the 4th Quadrant and ultimately into the 1st Quadrant.

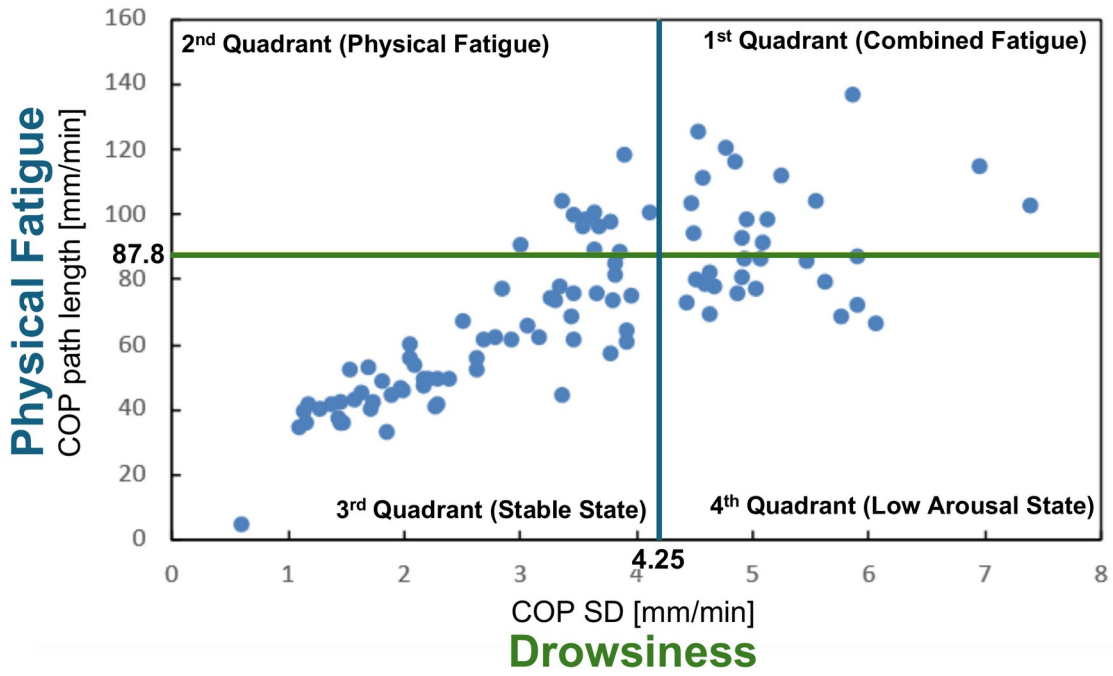



Figure 7. Four-Quadrant State Classification Model

4. **Limitation of this study:** This study was conducted with a small number of participants from a limited age group. Therefore, further validation is required, as the COP dynamics are

expected to be significantly influenced by the wider age range of professional truck drivers, as well as individual differences in physique, muscle strength, and the presence of pre-existing conditions such as chronic lower back pain.

Furthermore, as these results were obtained in a static laboratory environment, validation under real-world driving conditions is essential.

## 5. CONCLUSION

This study demonstrated that the dynamic analysis of the Center of Pressure (COP) enables the decoupled evaluation of drowsiness and physical distress during long-duration driving—a distinction that has traditionally been difficult to achieve—through physical metrics based on COP fluctuations.

This methodology serves as a fundamental technology that allows for specific intervention decisions, such as determining whether to encourage stretching to relieve physical pain or to recommend a nap to address mental fatigue, using only non-intrusive pressure sensors embedded in the seat.

Future work includes the detailed analysis of individual state transition patterns over time and the validation of algorithms that account for diverse participants and the impact of vehicle vibrations and accelerations present in real-world driving environments.

## REFERENCES

1. International Road Transport Union (IRU) (2024), "Global truck driver shortage report 2024", IRU Intelligence Briefing.

2. Jaydarifarda, S. et al. (2024), "Driver fatigue in taxi, ride-hailing, and ridesharing services: a systematic review", Transport Reviews, Vol.44, No.3, pp 572–590.

3. Öztürk, İ et al. (2026), "Does acceptance of driver monitoring systems differ across countries? A latent profile analysis approach", Accident Analysis & Prevention, Vol.233, 108590.

4. Abe, T. (2023), "PERCLOS-based technologies for detecting drowsiness: current evidence and future directions", SLEEP Advances, Vol.4, No.1, zpad006.

5. Hassan, O. F. et al. (2026), "Intelligent driver monitoring systems: a survey of drowsiness detection technologies for road safety", Artificial Intelligence Review, Vol.5, 137.

6. Kyung,G. and Nussbaum, M. A. (2008), "Driver sitting comfort and discomfort (Part II): Relationships with and prediction from interface pressure", International Journal of Industrial Ergonomics, Vol.38, No.5–6, pp 526-538.

7. Lecocq, M. et al. (2022), "Perceived discomfort and neuromuscular fatigue during long-duration real driving with different car seats", PLoS ONE, Vol.17, No.12, e0278131.

8. Jongkol, P. et al. (2026), "Understanding Driver Acceptance of Ergonomics and Fatigue Warning Applications Among Low and High Physical Discomfort Groups", Applied Sciences, Vol.16, No.9, 4085.

9. Williamson, A. et al., (2011), "The link between fatigue and safety", Accident Analysis and Prevention, Vol.43, pp 498–515.

10. Helander, M. G. and Zhang, L. (1997), "Field studies of comfort and discomfort in sitting", Ergonomics, Vol.40, No.9, pp 895-915.

11. Sammonds et al., (2017), "Effect of long term driving on driver discomfort and its relationship with seat fidgets and movements (SFMs)", Applied Ergonomics, Vol.58, pp 119-127.

12. Na, S. et al. (2005), "Evaluation of driver's discomfort and postural change using dynamic body pressure distribution", International Journal of Industrial Ergonomics, Vol.35, No.12, pp 1085-1096.

13. Gyi, D. E. and Porter, J. M. (1999), "Interface pressure and the prediction of car seat discomfort", Applied Ergonomics, Vol.30, No.2, pp 99-107.

14. Hirao, A. et al. (2006), "Development of a new driving posture focused on biomechanical loads", SAE Paper, 2006-01-1302.

15. Gillberg, M., (1994), "Relations Between Performance and Subjective Ratings of Sleepiness During a Night Awake", Sleep, Vol.17, No.3, pp 236–241.

16. Uchiyama, Y. and Nakajima, K. (2024), "Convergent Construct Validity of Japanese Version of Karolinska Sleepiness Scale Conforming to European Union Law", Transactions of Society of Automotive Engineers of Japan, Vol.55, No.3, pp 579-586. (In Japanese)

# EFFECT OF IMU MOUNTING LOCATION ON VIBRATION BEHAVIOR IN FIXED-WING UAV FUSELAGES: A MODAL AND HARMONIC FINITE ELEMENT ANALYSIS

**Semih NAZLIGÜL**, *nazligul21@itu.edu.tr*, Department of Mechanical Engineering, Istanbul Technical University, Istanbul, Türkiye

**Alp BAYKUT**, *baykuta22@itu.edu.tr*, Department of Mechanical Engineering, Istanbul Technical University, Istanbul, Türkiye

**Hasan ÇAKIR**, *h.cakir@yilmazdynamics.com*, Yılmaz Machine, Türkiye

**Mustafa BAKKAL**, *bakkalmu@itu.edu.tr*, Department of Mechanical Engineering, Istanbul Technical University, Istanbul, Türkiye

## ABSTRACT

Inertial Measurement Units (IMUs) are essential components of unmanned aerial vehicle (UAV) flight control systems, providing real-time orientation, angular rate, and acceleration data. However, motor and propeller-induced structural vibrations propagate through the airframe and corrupt IMU readings, leading to attitude estimation errors and degraded flight stability. This study presents a numerical investigation into the effect of IMU mounting location on vibration-induced measurement error in a fixed-wing UAV fuselage, using modal and harmonic finite element analysis (FEA) in ANSYS. Six natural frequencies of the airframe were extracted, with the first two wing-bending modes (37.378 Hz and 40.949 Hz) found to overlap directly with the operational frequency range of small UAV propulsion units. Harmonic analysis was performed across a 48–300 Hz frequency sweep to evaluate the structural response under motor-induced excitation. At the critical 48 Hz excitation frequency, total deformation reached a maximum of 5.682 mm at the wing tips, while the fuselage exhibited near-zero deformation across all extracted modes. A node-by-node comparison of eleven candidate points within the fuselage nose region revealed a consistent amplitude gradient along the longitudinal axis, ranging from 0.286 mm at the foremost nose tip to 0.444 mm near the wing-fuselage junction — a 55% increase in vibration amplitude over the sampled region. Balancing this vibration gradient against the need to keep the IMU close to the vehicle's center of gravity, a mounting zone located approximately 725–780 mm forward of the wing root is identified as the

recommended placement region, offering amplitude values of 0.312–0.332 mm — close to the observed minimum while avoiding excessive displacement from the center of gravity. A lever-arm error analysis indicates that this 60–80 mm reduction in center-of-gravity offset corresponds to a measurement error reduction of approximately 0.19–0.26 m/s² (20–26 mg) under representative maneuver conditions, quantitatively validating the proposed trade-off. The proposed methodology offers a low-cost, simulation-based approach for sensor placement optimization that can be applied during the early design stages of fixed-wing UAV platforms.

**Keywords:** Inertial Measurement Unit (IMU), fixed-wing UAV, finite element analysis, modal analysis, harmonic analysis, vibration, sensor placement

## 1. INTRODUCTION

Unmanned aerial vehicles (UAVs) have become increasingly prevalent across civilian, commercial, and military domains, with fixed-wing platforms in particular experiencing rapid growth due to their long endurance, extended range, and aerodynamic efficiency compared to multi-rotor configurations. The fixed-wing UAV market is projected to grow at a compound annual growth rate of approximately 10% through 2030, driven by applications in surveillance, mapping, and reconnaissance missions.

At the core of every UAV flight control system lies the Inertial Measurement Unit (IMU), a sensor package combining accelerometers, gyroscopes, and often magnetometers to provide real-time data on the vehicle's orientation, angular velocity, and linear acceleration. The accuracy of this data directly determines the quality of attitude estimation and, consequently, the stability of the flight control loop. Any corruption of IMU signals propagates through the estimation and control chain, potentially resulting in degraded flight performance or, in severe cases, loss of control.

A persistent challenge in UAV design is that motor and propeller assemblies generate mechanical vibrations that propagate through the airframe structure. These vibrations occur predominantly at the fundamental rotational frequency of the propulsion system and its harmonics, typically spanning a range of 45–250 Hz depending on motor RPM and propeller blade count. When these excitation frequencies coincide with the natural frequencies of the airframe structure, resonance amplification occurs, significantly increasing the vibration amplitude experienced by onboard avionics, including the IMU.

While the importance of vibration isolation for IMUs is widely acknowledged in the UAV community, mounting location selection is often guided by intuition or convenience rather than systematic structural analysis. Common practice places the IMU near the fuselage centerline

based on the general assumption that this region experiences lower vibration than the wings or tail. However, this assumption has rarely been verified through quantitative structural analysis specific to fixed-wing airframes.

This study addresses this gap by performing a coupled modal and harmonic finite element analysis of a fixed-wing UAV fuselage to (1) identify the natural frequencies and mode shapes of the structure, (2) characterize the frequency response of the airframe under simulated motor excitation, and (3) quantitatively compare vibration amplitudes at multiple candidate mounting locations within the fuselage nose region. The objective is to provide a numerically grounded recommendation for IMU placement that minimizes vibration-induced measurement error.

## 2. LITERATURE REVIEW

Vibration-induced sensor error in UAV platforms has been examined from several distinct perspectives in the existing literature, each addressing a different aspect of the problem without providing a complete, UAV-specific placement methodology.

Structural vibration characteristics of fixed-wing UAV airframes under ground engine test conditions have been documented in recent work, with findings indicating that the highest deformation amplitudes occur at the wing tips and in the immediate vicinity of the engine mount, while the fuselage body remains comparatively quiescent. First and second wing bending modes were identified in the 12–18 Hz range for the tested platform, though no attempt was made to translate these findings into sensor placement guidance.

Modal characterization of composite UAV wing structures using both finite element simulation and experimental modal analysis has demonstrated good agreement between numerical and physical results for low-order bending and torsional modes, validating the use of FEA as a predictive tool for UAV structural dynamics. However, this body of work focuses exclusively on wing-level dynamics and does not extend to fuselage-mounted avionics.

From a more general structural health monitoring perspective, finite element-based optimization frameworks have been developed for vibration sensor placement, in which a large set of candidate node locations is systematically reduced to a small number of optimal positions based on correlation criteria applied to modal displacement data. While methodologically relevant, such frameworks have not been applied to UAV airframes or to IMU-specific placement requirements.

Finally, signal-processing approaches have addressed the consequences of vibration-corrupted IMU data by designing Kalman filters informed by combined turbulence and motor vibration models for fixed-wing UAVs. While effective at the signal level, these approaches

treat vibration exposure as a fixed input rather than a parameter that can be reduced through informed sensor placement.

Table 1 summarizes the key contributions and limitations of these studies in relation to the present work.

Table 1. Summary of related literature and the gap addressed by this study.

| Reference | Focus | Key Finding | Gap Addressed by This Study |
|---|---|---|---|
| González et al. (2026) | Fixed-wing UAV ground engine vibration testing | Highest vibration amplitudes concentrate at wing tips and near the engine; first two wing bending modes near 12–18 Hz | No IMU placement analysis performed |
| Dessena et al. (2025) | Composite UAV wing modal analysis | FEM and experimental modal results show good agreement for low-order bending modes | Wing-focused; fuselage and sensor placement not addressed |
| Shin et al. (2022) | Vibration sensor placement optimization via FEM | 24,252 candidate nodes reduced to 10 optimal sensor locations using correlation-based ranking | General structural framework, not validated on UAV airframes |
| Bréda et al. (2023) | Fixed-wing UAV Kalman filter design | Combined Dryden turbulence and motor vibration models used as filter input | Addresses filtering, not the underlying placement problem |
| **This Study** | **Fixed-wing UAV fuselage IMU placement via modal + harmonic FEA** | **Quantitative, node-level comparison of vibration amplitude across candidate mounting locations in the fuselage nose** | **Fills the identified gap** |

As summarized in Table 1, no existing study combines finite element-based modal and harmonic analysis with a quantitative, node-level comparison of candidate IMU mounting locations specifically for fixed-wing UAV fuselages. This study addresses that gap.

## 3. METHODOLOGY

### 3.1 Geometry and Material Properties

The geometry used in this study represents a small-class fixed-wing UAV fuselage with attached wings and tail surfaces, modeled in ANSYS Workbench. The structure was assigned the material properties of an aluminum alloy (Young's modulus E = 69 GPa, Poisson's ratio ν = 0.33, density ρ = 2700 kg/m³), representative of lightweight metallic UAV airframe construction. The model was discretized using a tetrahedral mesh suitable for capturing the geometric complexity of the fuselage-wing-tail assembly.

### 3.2 Boundary Conditions

Fixed support boundary conditions were applied at the wing-fuselage attachment surfaces, representing the most structurally rigid connection points in the airframe under flight loading conditions. This boundary condition configuration is consistent with approaches used in prior UAV structural dynamics studies and reflects the load-bearing interface through which motor-induced vibrations are most directly transmitted into the fuselage structure.

### 3.3 Modal Analysis

A free-vibration modal analysis was performed to extract the first six natural frequencies and corresponding mode shapes of the airframe. This analysis serves two purposes: first, to identify resonant frequencies that may coincide with motor excitation frequencies, and second, to identify regions of the structure that exhibit consistently low displacement across multiple modes — candidate "nodal" regions for sensor placement.

### 3.4 Harmonic Analysis

A steady-state harmonic analysis was conducted to evaluate the forced response of the structure under simulated motor excitation. A frequency sweep from 48 Hz to 300 Hz was selected to encompass the typical operational range of small UAV propulsion systems, including the fundamental motor frequency and its first harmonics. The excitation load was applied as a concentrated force at the motor mounting location, oriented along the vertical (Z) axis, consistent with the dominant direction of propeller-induced vibration.

Total deformation results were extracted across the frequency sweep for the overall structure, and additionally for eleven discrete node locations within the fuselage nose region at the critical 48 Hz excitation frequency, corresponding to the lower bound of the motor operating range and the point of maximum system-level response amplitude.

### 3.5 Candidate Mounting Locations

Eleven node locations distributed along the fuselage nose region, from the foremost tip toward the wing-fuselage junction, were selected for direct amplitude comparison. This region was selected based on preliminary modal results indicating consistently low displacement across the fuselage body relative to the wings and tail, making it the primary candidate region for IMU mounting. The objective of the node-level comparison was to determine whether vibration amplitude varies meaningfully within this candidate region, and if so, to identify the sub-region offering the lowest exposure.

## 4. RESULTS

### 4.1 Modal Analysis Results

The first six natural frequencies of the airframe were extracted and are summarized in Table 2. The first two modes, at 37.378 Hz and 40.949 Hz, correspond to first and second wing bending modes respectively, with maximum total deformation occurring at the wing tips (Figures 1 and 2). These frequencies fall directly within the operational range of small UAV propulsion systems (typically 45–97 Hz depending on RPM), indicating a significant risk of resonance amplification under motor excitation.

Table 2. First six natural frequencies and mode shape characteristics of the fixed-wing UAV airframe.

| Mode | Frequency (Hz) | Mode Shape Description | Significance |
|---|---|---|---|
| 1 | 37.378 | First wing bending mode — maximum deformation at left wing tip | Critical — overlaps motor operating range |
| 2 | 40.949 | Second wing bending mode — maximum deformation at opposite wing tip | Critical — overlaps motor operating range |
| 3 | 52.314 | Fuselage bending mode | Moderate significance |
| 4 | 56.107 | Torsional mode | Moderate significance |
| 5 | 106.86 | Higher-order bending mode — maximum deformation at right wing/tail surface | Low significance |
| 6 | 139.88 | Higher-order mode | Low significance |

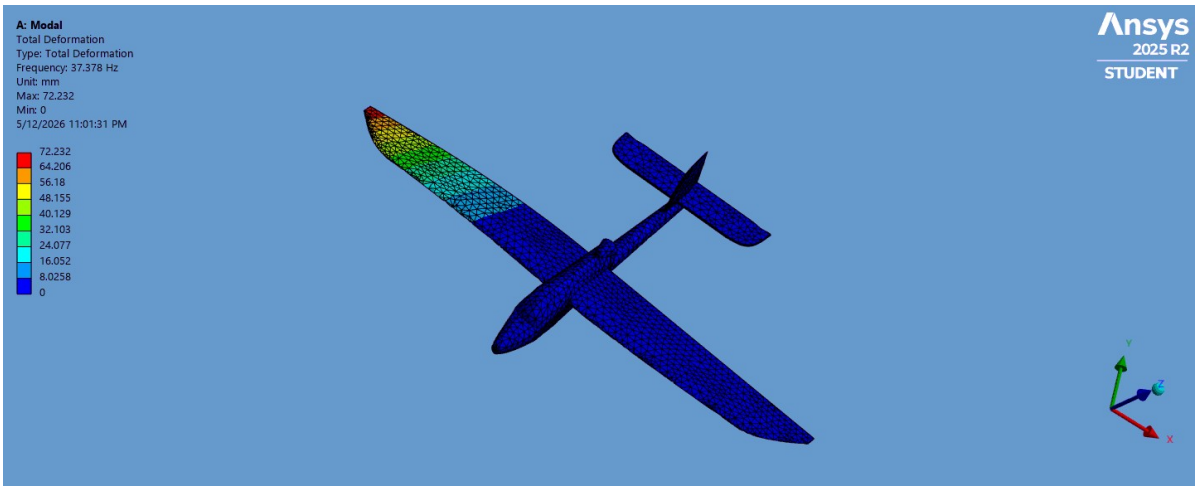



Figure 1. Mode 1 (37.378 Hz) — First wing bending mode. Maximum total deformation (72.232 mm) occurs at the left wing tip, while the fuselage body shows near-zero deformation.

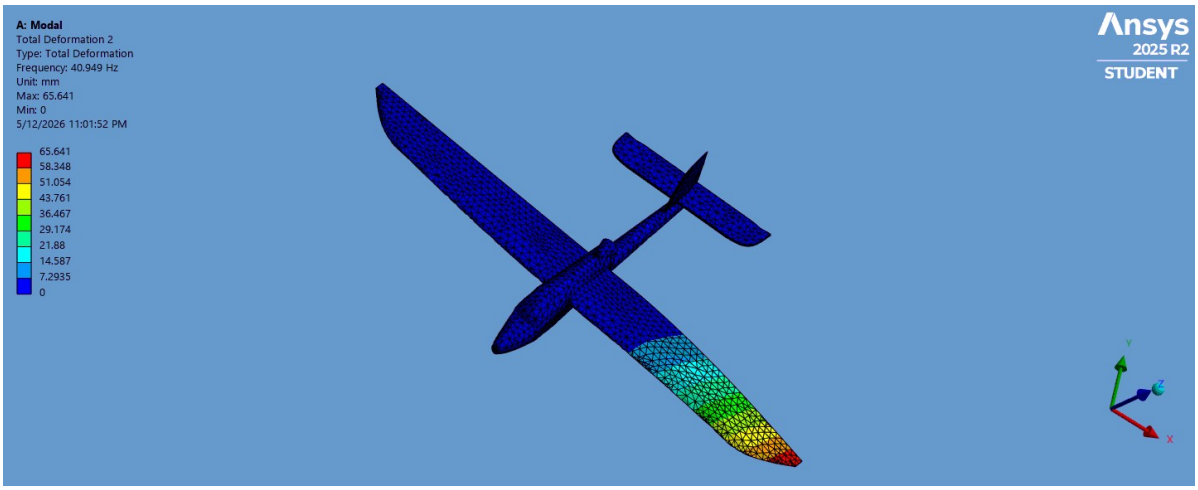



Figure 2. Mode 2 (40.949 Hz) — Second wing bending mode. Maximum total deformation (65.641 mm) occurs at the opposite wing tip; the fuselage body again shows near-zero deformation.

A consistent pattern emerges across all six extracted modes: the highest deformation amplitudes are concentrated in the wings and tail surfaces, while the fuselage body — particularly the nose region — exhibits near-zero displacement regardless of which mode is excited. This behavior is illustrated further in Figure 3, which shows Mode 5 (106.86 Hz), a higher-order bending mode in which deformation is again localized to the wing and tail assembly.

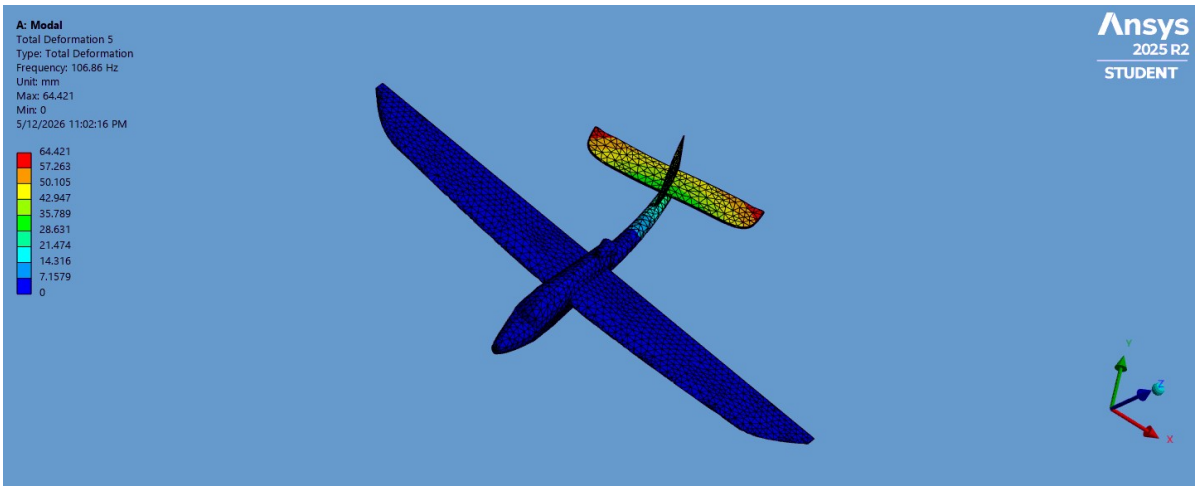



Figure 3. Mode 5 (106.86 Hz) — Higher-order bending mode. Maximum total deformation (64.421 mm) is concentrated in the wing and tail assembly; the fuselage remains near-zero across the full mode shape.

This consistent behavior across multiple modes — spanning a frequency range of nearly 4:1 (37.4 Hz to 139.9 Hz) — provides strong initial evidence that the fuselage body represents a structurally favorable region for vibration-sensitive sensor placement, independent of which vibration mode dominates under a given flight condition.

### 4.2 Harmonic Analysis — System-Level Frequency Response

The harmonic analysis results, shown in Figure 4, present the frequency response of the overall structure across the 48–300 Hz sweep. The amplitude curve exhibits a maximum value of 0.1726 mm at the lower bound of the sweep (48 Hz), corresponding to the typical idle/low-RPM frequency of small UAV motors. The amplitude decreases sharply with increasing frequency, reaching a local minimum of approximately 0.0049 mm in the 100–130 Hz range, before rising again to a second local maximum of 0.1726 mm near 210 Hz — a secondary resonance associated with the higher-order wing/tail modes identified in the modal analysis.

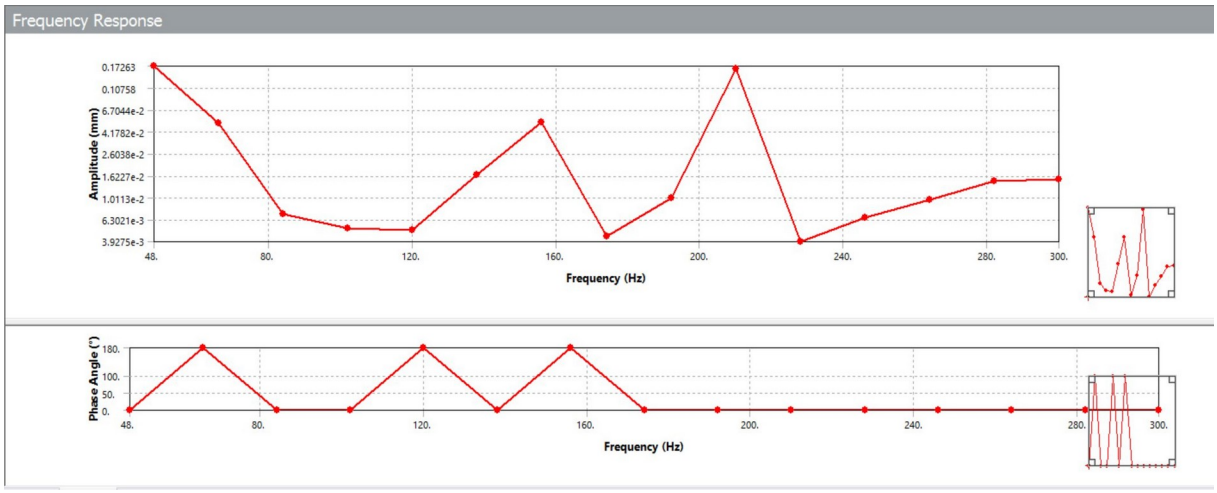



Figure 4. System-level frequency response (48–300 Hz). Top: amplitude (mm) vs. frequency (Hz). Bottom: phase angle (°) vs. frequency, with 180° transitions indicating resonance crossings.

The phase angle plot in Figure 4 (bottom) provides additional confirmation of resonance behavior: each 180° phase transition corresponds to a resonance crossing, occurring at approximately 70 Hz, 120 Hz, and 155 Hz. These crossings align closely with the higher-order natural frequencies identified in the modal analysis (Table 2), confirming consistency between the two analysis stages.

Two frequency ranges identified as "safe zones" — 100–130 Hz and 165–170 Hz — exhibit amplitude values below 0.01 mm, more than an order of magnitude lower than the peak response at 48 Hz and 210 Hz. Notably, the cruise-RPM operating frequency of typical small UAV motors (approximately 83–97 Hz) falls within or close to the first of these safe zones, suggesting that steady cruise flight may impose substantially lower vibration loading on the airframe than idle or low-RPM conditions.

To examine the spatial distribution of deformation at the most critical excitation frequency (48 Hz), the total deformation contour of the full structure was extracted (Figure 5). The maximum deformation of 5.682 mm occurs at the wing tips, consistent with the wing-bending mode shapes identified in the modal analysis (Figures 1 and 2). In contrast, the fuselage body — including the nose region — shows deformation values approaching zero (minimum recorded value: $2.01 \times 10^{-19}$ mm), confirming that the spatial distribution of vibration energy observed in the modal analysis persists under realistic harmonic excitation.

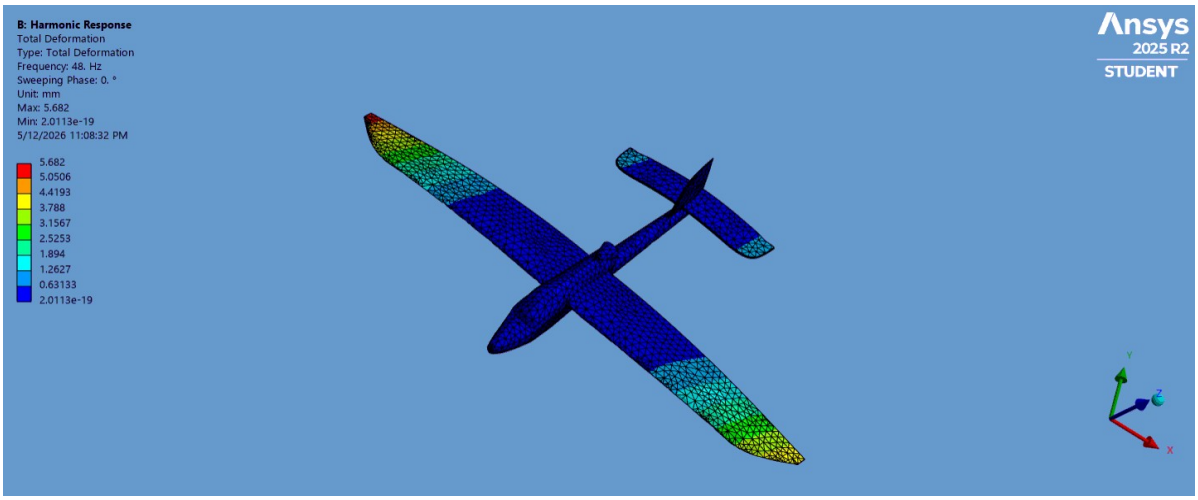



Figure 5. Total deformation contour at 48 Hz excitation frequency. Maximum deformation (5.682 mm) occurs at the wing tips; the fuselage body shows near-zero deformation throughout.

### 4.3 Node-Level Comparison Within the Fuselage Nose Region

Given the consistently low deformation observed across the fuselage in both modal and harmonic results, the fuselage nose was identified as the primary candidate region for IMU placement. To determine whether vibration amplitude varies meaningfully within this region — and to identify the most favorable sub-region — total deformation values at 48 Hz were extracted for eleven discrete node locations distributed along the longitudinal (X) axis, from the foremost nose tip toward the wing-fuselage junction (Figure 6).

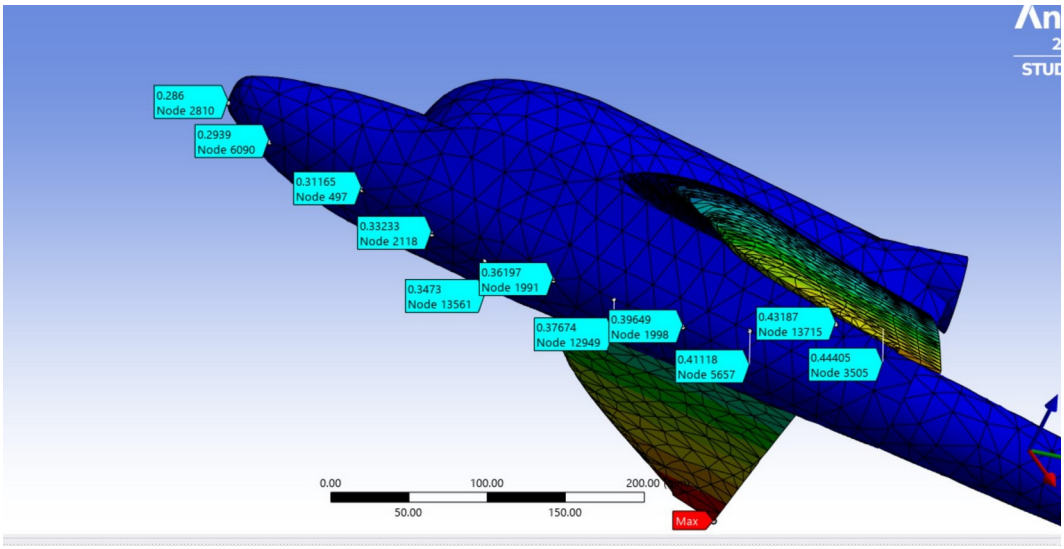



Figure 6. Total deformation values (mm) at eleven node locations within the fuselage nose region, extracted at 48 Hz excitation frequency.

The results, summarized in Table 3 and ordered from the foremost nose tip to the fuselage body near the wing root, reveal a clear and monotonic amplitude gradient along the X axis.

The lowest amplitude, 0.286 mm, occurs at the foremost nose tip (X = -845.6 mm), while the highest amplitude among the sampled points, 0.444 mm, occurs near the wing-fuselage junction (X = -605.7 mm) — an increase of approximately 55% over the sampled region. Figure 7 presents this relationship graphically.

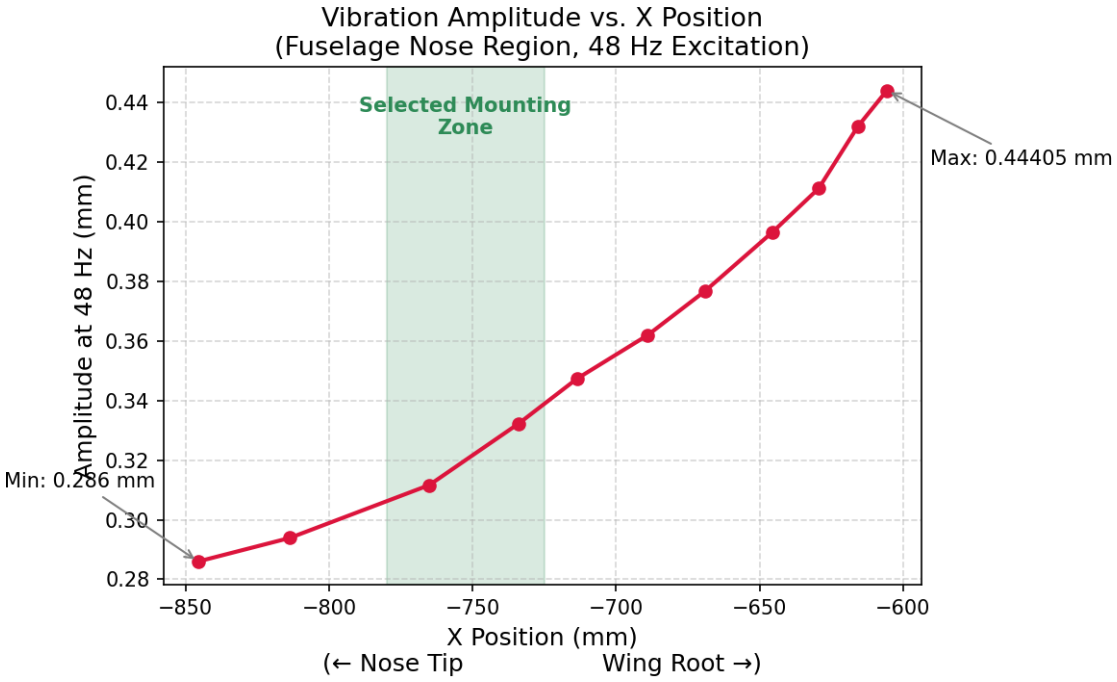



Figure 7. Vibration amplitude at 48 Hz as a function of longitudinal (X) position. The amplitude decreases monotonically toward the nose tip; the shaded region (X = -780 to -725 mm) indicates the recommended IMU mounting zone.

Table 3. Total deformation amplitude at eleven candidate IMU mounting locations within the fuselage nose region, at 48 Hz excitation frequency, ordered from nose tip to fuselage body. Highlighted rows (Node 497 and Node 2118) fall within the recommended mounting zone.

| Node ID | X Position (mm) | Approximate Location (Nose Tip → Fuselage) | Amplitude at 48 Hz (mm) | Relative Position |
|---|---|---|---|---|
| Node 2810 | -845.59 | Nose tip (foremost point) | 0.2860 | 0% (reference) |
| Node 6090 | -813.70 | Near nose tip | 0.2939 | 10% |
| **Node 497** | -765.07 | Forward nose region | **0.3117** | 20% |
| **Node 2118** | -733.86 | Forward-mid nose | **0.3323** | 30% |
| Node 13561 | -713.67 | Mid nose region | 0.3473 | 40% |
| Node 1991 | -688.96 | Mid nose region | 0.3620 | 50% |
| Node 12949 | -669.00 | Mid-aft nose | 0.3767 | 60% |
| Node 1998 | -645.55 | Aft nose region | 0.3965 | 70% |
| Node 5657 | -629.42 | Near fuselage junction | 0.4112 | 80% |
| Node 13715 | -615.85 | Fuselage transition | 0.4319 | 90% |
| Node 3505 | -605.67 | Fuselage body (near wing root) | 0.4441 | 100% (reference) |

This gradient indicates that, although the entire fuselage nose region experiences substantially lower vibration than the wings and tail (by more than an order of magnitude relative to the 5.682 mm wing-tip deformation in Figure 5), the amplitude is not uniform within this region. Vibration amplitude decreases progressively toward the nose tip — the point of maximum structural distance from the wing-mounted motor/propeller assembly.

### 4.4 Optimal Mounting Zone: Vibration Gradient and Lever-Arm Trade-Off

The amplitude-vs-position curve in Figure 7 reveals two distinct behavioral regimes. In the region X = -845.6 mm to X = -780 mm (closest to the nose tip), amplitude decreases steeply from 0.286 mm to approximately 0.311 mm. Beyond X = -780 mm toward the wing root, the rate of decrease diminishes markedly — the curve flattens and amplitude changes only from

0.312 mm to 0.332 mm across the X = -780 to -725 mm interval (Node 497 and Node 2118, highlighted in Table 3). This inflection in the gradient is the key observation for mounting zone selection.

While the foremost nose tip (X = -845.6 mm) exhibits the absolute minimum amplitude (0.286 mm), it simultaneously represents the point of maximum longitudinal offset from the vehicle's center of gravity. IMU performance for angular rate measurement is known to degrade with increasing center-of-gravity offset, as lever-arm effects introduce a systematic acceleration error that scales with maneuver intensity. Selecting the nose-tip extreme therefore trades a marginal further reduction in vibration amplitude (from ~0.311 mm to 0.286 mm, i.e., ~8%) for an additional 60–80 mm of lever-arm distance, incurring a measurable and systematic measurement penalty.

### 4.5 Lever-Arm Error Quantification

To quantify this penalty, the lever-arm acceleration error is estimated using the standard rigid-body kinematic relationship. For an IMU at distance r from the center of gravity, the measured specific force differs from the true value by:

$$a_error = \alpha \times r + \omega^2 \times r \quad (1)$$

where the first term is the tangential error due to angular acceleration α (rad/s²), and the second term is the centripetal error due to angular velocity ω (rad/s). Using representative values for a moderate fixed-wing UAV maneuver — ω = 60°/s (1.047 rad/s) and α = 120°/s² (2.094 rad/s²), consistent with a coordinated turn or step control input — the error corresponding to lever-arm distances of 60 mm and 80 mm (the bounds of the offset reduction achieved by the recommended zone) is given in Table 4.

Table 4. Lever-arm acceleration error for 60–80 mm center-of-gravity offset (ω = 60°/s, α = 120°/s²).

| Lever-Arm Distance, r | Tangential Error (α×r) | Centripetal Error (ω²×r) | Total Error |
|---|---|---|---|
| 60 mm | 0.126 m/s² | 0.066 m/s² | 0.192 m/s² (≈ 19.5 mg) |
| 80 mm | 0.168 m/s² | 0.088 m/s² | 0.255 m/s² (≈ 26.0 mg) |
| **Reduction achieved by recommended zone vs. nose-tip extreme** | — | — | **0.19–0.26 m/s²** |

The resulting error, 0.19–0.26 m/s² (approximately 20–26 mg), is comparable to the bias stability and noise floor of consumer-grade MEMS accelerometers used in small UAV platforms. Crucially, this error is systematic and persistent: unlike random vibration noise which may be filtered, lever-arm error scales directly with maneuver rate and does not average out over time, making it a direct contributor to attitude estimation drift during dynamic flight phases.

Taken together, Figure 7 and Table 4 define the basis for the final placement recommendation. The vibration amplitude gradient (Figure 7) shows that the greatest marginal reduction in vibration occurs in the X = -845 to -780 mm interval; beyond that, additional forward displacement yields diminishing returns in vibration reduction. The lever-arm error analysis (Table 4) shows that this same interval corresponds to a systematic measurement penalty of 0.19–0.26 m/s². The recommended mounting zone at X = -725 to -780 mm therefore represents the point of optimal balance: it captures the largest portion of the available vibration reduction (amplitude 0.312–0.332 mm, within 9–16% of the global minimum) while avoiding the lever-arm penalty associated with the extreme nose-tip location.

## 5. DISCUSSION

The combined modal and harmonic analysis results provide convergent evidence regarding the spatial distribution of vibration energy within the fixed-wing UAV airframe under study. Three key observations emerge from this convergence.

First, the modal analysis demonstrates that across six natural frequencies spanning 37.4–139.9 Hz — representing a wide range of structural deformation patterns — the fuselage body consistently exhibits near-zero displacement, while deformation is concentrated in the wings and tail. This is not the behavior of a single mode but a structural characteristic that persists across multiple, dynamically distinct mode shapes, suggesting that the fuselage's favorable vibration characteristics are robust to changes in excitation frequency, and therefore to changes in motor RPM during flight.

Second, the harmonic analysis confirms that this modal behavior translates directly into forced-response behavior under realistic motor excitation. At 48 Hz — the frequency at which the system-level response amplitude is maximized — the fuselage deformation remains near zero even as the wing tips reach 5.682 mm. This indicates that the favorable vibration characteristics of the fuselage are not merely a property of unforced natural vibration but persist under the most demanding excitation condition examined in this study.

Third, and most significantly for practical sensor placement decisions, the node-level comparison reveals that the fuselage is not vibrationally uniform. A 55% increase in amplitude

was observed along the X axis between the foremost nose tip and the fuselage region nearest the wing root. The combined vibration gradient and lever-arm analysis (Sections 4.4 and 4.5) quantitatively identifies the X = -725 to -780 mm zone as the optimal balance point between minimizing vibration exposure and minimizing center-of-gravity offset.

It is also worth noting that the first two natural frequencies of the airframe (37.378 Hz and 40.949 Hz) fall within the typical idle-to-low-RPM operating range of small UAV motors. This represents a structural design consideration independent of sensor placement: if these resonances can be shifted outside the operational RPM range through structural modification (e.g., stiffening of the wing structure or mass redistribution), the overall vibration environment — and consequently the baseline IMU error — could be reduced for any mounting location.

## 6. CONCLUSION

This study performed a coupled modal and harmonic finite element analysis of a fixed-wing UAV fuselage to quantitatively assess the effect of IMU mounting location on vibration-induced measurement error. The following conclusions can be drawn from the results:

Modal analysis identified six natural frequencies between 37.4 Hz and 139.9 Hz, with the first two modes — corresponding to wing bending — falling within the typical operational frequency range of small UAV propulsion systems, representing a resonance risk.

Across all six extracted modes, the fuselage body exhibited consistently near-zero deformation, while maximum deformation was concentrated in the wings and tail, indicating that the fuselage represents a structurally favorable region for vibration-sensitive sensor placement.

Harmonic analysis across a 48–300 Hz sweep identified 48 Hz and 210 Hz as resonance-driven amplitude peaks, and 100–130 Hz and 165–170 Hz as low-amplitude "safe zones" coinciding approximately with typical cruise-RPM excitation frequencies.

At the critical 48 Hz excitation frequency, total deformation reached 5.682 mm at the wing tips while remaining near-zero across the fuselage, confirming the modal-analysis findings under forced excitation.

A node-level comparison of eleven candidate locations within the fuselage nose revealed a monotonic, 55% increase in vibration amplitude along the X axis, from the foremost nose tip (0.286 mm, X = -845.6 mm) to the region nearest the wing root (0.444 mm, X = -605.7 mm).

Balancing vibration exposure against proximity to the center of gravity, a mounting zone between X = -725 mm and X = -780 mm is recommended, offering amplitude values of 0.312 –0.332 mm — within 9–16% of the global minimum — while reducing the longitudinal offset from the center of gravity by 60–80 mm relative to the nose-tip extreme.

A lever-arm error analysis quantified this 60–80 mm offset reduction as corresponding to an acceleration measurement error reduction of approximately 0.19–0.26 m/s² (20–26 mg) under representative maneuver conditions (ω = 60°/s, α = 120°/s²), confirming that the recommended mounting zone provides a measurable benefit beyond geometric convenience.

These findings provide a quantitative, simulation-based basis for IMU placement recommendations in fixed-wing UAV design, complementing existing qualitative guidance with node-level amplitude data. The proposed methodology — combining modal characterization, harmonic response analysis, and node-level amplitude comparison — is computationally inexpensive relative to full aeroelastic or experimental vibration testing and can be readily incorporated into early-stage UAV structural design workflows.

**Future Work**

Experimental validation through accelerometer measurements at the candidate mounting locations identified in this study, for direct comparison with simulation predictions.

Extension of the harmonic analysis to additional excitation directions and multi-frequency (combined harmonic) loading conditions representative of real flight maneuvers.

Investigation of composite fuselage materials and their effect on the modal characteristics and resulting nodal regions identified in this study.

Integration of the identified vibration frequency content into adaptive filter design (e.g., notch or Kalman filtering) for residual vibration compensation at the selected mounting location.

Extension of the methodology to multi-rotor and VTOL configurations, where multiple simultaneous excitation sources create more complex vibration interaction patterns.

## REFERENCES

[1] **González, J. et al. (2026)**. Structural Vibration Analysis of UAVs Under Ground Engine Test Conditions. Sensors, 26(2), 583.

[2] **Dessena, G. et al. (2025)**. Composite UAV Wing Modal Analysis — Finite Element and Experimental Validation. Journal of Aerospace Engineering.

[3] **Shin, S. et al. (2022)**. Vibration Sensor Placement Optimization via Finite Element Method. Structural Health Monitoring, 21(4).

[4] **Bréda, P. et al. (2023)**. Kalman Filter Design for Small FixedWing UAVs with Combined Dryden Turbulence and Motor Vibration Models. Aerospace Science and Technology. August 1921, 2026, Istanbul, Türkiye

[5] **Rotax Aircraft Engines (2003)**. Service Letter SL912010: Vibration Analysis. BRP August 19-21, 2026, Istanbul, Türkiye Rotax GmbH & Co KG.

[6] **Grand View Research (2024)**. FixedWing UAV Market Size, Share & Trends Analysis Report.

# EFFECT OF Y2O3 CONTENT ON THE COMPRESSIVE AND HARDNESS BEHAVIOUR OF AZ91 MAGNESIUM MATRIX COMPOSITES FABRICATED BY POWDER METALLURGY

**Mert ILBEYLI**, *mert.ilbeyli@balikesir.edu.tr* Balıkesir University, 10145, Balıkesir, Türkiye

**Turker TURKOGLU**, *turker.turkoglu@balikesir.edu.tr* Balıkesir University, 10145, Balıkesir, Türkiye

**Sare CELIK**, *scelik@balikesir.edu.tr* Balıkesir University, 10145, Balıkesir, Türkiye

## ABSTRACT

AZ91 magnesium alloy was reinforced with 5, 10, and 15 wt.% $Y_2O_3$ by ball milling and uniaxial hot pressing at 550 °C under 100 MPa in argon. Vickers microhardness and uniaxial compression tests showed that both properties increased with reinforcement content and reached a maximum at 10 wt.% $Y_2O_3$, where the compressive strength rose from 185 to 258 MPa and the hardness from 82 to 121 $HV_1$. Further addition up to 15 wt.% caused a partial decline (245 MPa, 110 $HV_1$), attributed to $Y_2O_3$ agglomeration. The optimum at 10 wt.% is explained by combined Hall-Petch, Orowan, thermal-mismatch, and load-transfer mechanisms.

**Keywords:** AZ91, Y2O3, magnesium matrix composite, powder metallurgy, hot pressing.

## 1. INTRODUCTION

Magnesium and its alloys remain the lightest structural metals in practical engineering use, offering an attractive combination of low density, high specific strength, and good damping behaviour. Among commercial magnesium alloys, AZ91 (Mg-9Al-1Zn) is by far the most widely produced, yet its monolithic form is limited by moderate absolute strength, poor wear resistance, and a marked drop in mechanical performance at elevated temperatures. Reinforcing AZ91 with hard particles is one of the established routes for addressing these limitations [Kelen, 2025; Ding, 2026].

Several ceramic and intermetallic systems have been investigated as reinforcement for magnesium-based composites. Boron carbide additions in AZ31 produced by powder metallurgy have been shown to raise both tensile and compressive strength up to an optimum content of about 2.25 wt.%, beyond which particle clustering and porosity reverse the trend [Sharma, 2026]. A similar non-monotonic response has been documented for Mg-$TiO_2$ nanocomposites, where 3 vol.% $TiO_2$ was identified as the optimum reinforcement level [Faris, 2026]. SiCp-reinforced AZ31 composites consolidated by hot pressing and subsequent extrusion have also been examined in detail with respect to their hot-deformation behaviour

[Wang, 2026]. AZ91-hydroxyapatite composites processed by deformation-driven metallurgy have been reported in the biomedical context [Jamshidi, 2025].

Rare-earth oxides, and $Y_2O_3$ in particular, are of long-standing interest as reinforcement for magnesium because of their high thermodynamic stability, high hardness, and the well-documented role of yttrium-containing oxide films in improving the high-temperature oxidation resistance of AZ91 [Bak, 2009]. Despite this favourable background, the room-temperature mechanical response of AZ91- $Y_2O_3$ composites produced by solid-state powder metallurgy has not received attention comparable to that given to AZ91 reinforced with carbides, nitrides, or carbon-based phases. The present study was designed to fill this gap. AZ91- $Y_2O_3$ composites containing 0, 5, 10, and 15 wt.% $Y_2O_3$ were produced by ball milling followed by uniaxial hot pressing and were evaluated in terms of Vickers microhardness and uniaxial compression. The aim was to identify the optimum reinforcement level and to clarify the strengthening and damage mechanisms that govern the composition-property relationship in this system.

## 2. MATERIALS AND METHOD

Each Commercial AZ91 powder and $Y_2O_3$ powder, both finer than 325 mesh (≈ 44 μm), were used as the matrix and reinforcement, respectively. Four compositions were prepared: unreinforced AZ91 as the reference, and AZ91 containing 5, 10, and 15 wt.% $Y_2O_3$. The powder mixtures were homogenised in a planetary ball mill at 250 rpm for 2 h.

The blended powders were poured into a cylindrical hot-work tool steel die and consolidated by uniaxial hot pressing. The die was heated to 550 °C at a rate of 5 °C/min in flowing argon, held at this temperature for 30 min under a uniaxial pressure of 100 MPa, and cooled under load. This temperature is slightly above the eutectic temperature of the AZ91 alloy and was selected to promote densification through sintering while preserving the $Y_2O_3$ reinforcement. The resulting cylindrical specimens measured 15 mm in diameter and 10 mm in height.

Vickers microhardness was measured at a load of 1 kgf ($HV_1$), with several indents per sample to obtain a representative mean value. Uniaxial compression tests were performed at room temperature on the as-produced cylindrical specimens at a constant crosshead speed of 1 mm/min, following the general framework of ASTM E9. At least three specimens per composition were tested and the average values are reported. The uniaxial compression test setup used in this study is shown in Figure 1.



Figure 1. Uniaxial compression test setup of the composite specimen.

## 3. RESULTS AND DISCUSSION

The unreinforced AZ91 reference specimen exhibited a compressive strength of 185 MPa and a hardness of 82 $HV_1$, which is consistent with previously reported values for solid-state-processed AZ91. The addition of 5 wt.% $Y_2O_3$ produced a modest but consistent improvement, raising the compressive strength to 205 MPa and the hardness to 96 $HV_1$. The largest improvement was recorded for the 10 wt.% composite, which reached 258 MPa and 121 $HV_1$, corresponding to relative gains of approximately 40 % and 48 % over the unreinforced reference. Increasing the $Y_2O_3$ content further to 15 wt.% did not continue this trend; both quantities decreased to 245 MPa and 110 $HV_1$.

The concurrent improvement of hardness and compressive strength up to 10 wt.% $Y_2O_3$ is consistent with the combined action of several established strengthening mechanisms operating in particle-reinforced magnesium composites. The $Y_2O_3$ particles act as obstacles to grain-boundary migration during consolidation, refining the α-Mg matrix in accordance with the Hall-Petch relationship. The rigid $Y_2O_3$ particles also act as obstacles to dislocation motion via Orowan looping. The large mismatch in the coefficient of thermal expansion between α-Mg (≈ 26 x $10^{-6}$ $K^{-1}$) and $Y_2O_3$ (≈ 8 x $10^{-6}$ $K^{-1}$) generates geometrically necessary dislocations around the reinforcement during cooling from the processing temperature, raising the matrix dislocation density. Finally, the considerably higher elastic modulus of $Y_2O_3$ enables load transfer from the soft matrix to the harder reinforcement under compression, provided that the matrix-particle interface remains sound. This combination of mechanisms is well established in the literature on magnesium matrix composites and has been invoked to explain the strengthening response of Mg-$TiO_2$ [Faris, 2026] and AZ31-$B_4C$ [Sharma, 2026] systems produced by powder metallurgy.

The decline observed at 15 wt.% $Y_2O_3$ is, in our view, the most informative feature of the dataset. The fact that hardness and compressive strength decrease together points to a cause other than distributed porosity alone, because indentation hardness is relatively insensitive to homogeneous porosity but quite sensitive to localised microstructural defects beneath the

indenter. A more consistent explanation is that, beyond a certain volume fraction, $Y_2O_3$ particles begin to agglomerate during ball milling and consolidation, forming clusters that reduce the effective interfacial area between matrix and reinforcement, introduce localised porosity within the clusters, and act as preferential sites for crack initiation under both indentation and compressive loading. This optimum-and-decline behaviour is fully consistent with previous reports on powder-metallurgy magnesium matrix composites, where a clear strengthening peak has been documented at intermediate reinforcement contents (3 vol.% in Mg-$TiO_2$ [Faris, 2026] and 2.25 wt.% in AZ31-$B_4C$ [Sharma, 2026]) followed by an agglomeration-controlled deterioration at higher contents. As shown in Figure 2, both the ultimate compressive strength and Vickers microhardness reached a maximum at 10 wt.% $Y_2O_3$ and declined at 15 wt.%. As shown in Figure 2, both the ultimate compressive strength and Vickers microhardness reached a maximum at 10 wt.% $Y_2O_3$ and declined at 15 wt.%.

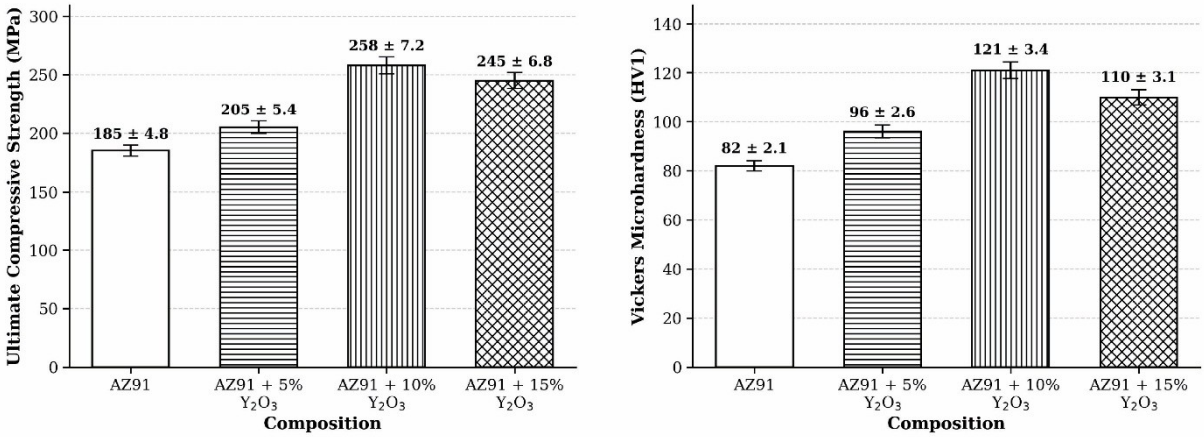



Figure 2. Compressive and Hardness test results.

The present processing research, 10 wt.% $Y_2O_3$ therefore represents the balance point between the increasing density of strengthening obstacles and the onset of agglomeration-controlled damage.

## 3. CONCLUSIONS

AZ91-$Y_2O_3$ composites containing 0, 5, 10, and 15 wt.% $Y_2O_3$ were successfully produced by ball milling and uniaxial hot pressing at 550 °C and 100 MPa in argon. Both Vickers microhardness and ultimate compressive strength increased with $Y_2O_3$ content up to 10 wt.%, reaching 121 $HV_1$ and 258 MPa (gains of 48 % and 40 % relative to the unreinforced reference), and then decreased at 15 wt.% to 110 $HV_1$ and 245 MPa. The optimum at 10 wt.% reflects the combined action of Hall-Petch refinement, Orowan looping, thermal-mismatch strengthening, and load transfer, while the subsequent decline is attributed to $Y_2O_3$ agglomeration and the resulting microstructural defects. Under the present processing conditions, 10 wt.% $Y_2O_3$ emerges as the most effective reinforcement level for AZ91 magnesium alloy.

## REFERENCES

1. **Bak, S.-H. and Lee, D.-B., (2009),** "Effect of Y and $Y_2O_3$ on oxidation of AZ91D Mg alloys between 400 °C and 500 °C", Transactions of Nonferrous Metals Society of China, Vol.19, pp 871-874.

2. **Ding, Y., Wang, H., Gong, X., Le, Q. and Chen, Z., (2026),** "Strong interfacial bonding and high mechanical properties of copper-decorated carbon nanotubes reinforced AZ91 magnesium matrix composite", Journal of Composite Materials, Vol.60, No.5, pp 399-412.

3. **Faris, S.Z., Eqal, A.K., Mohammed, B.R. and Hussein, H.A., (2026),** "Mechanical and microstructural properties of $TiO_2$-enhanced magnesium composites prepared by powder metallurgy", Next Materials, Vol.10, p 101470.

4. **Jamshidi, K., Jamaati, R. and Jamshidi Aval, H., (2025),** "Microstructure and corrosion resistance of AZ91-Hydroxyapatite composites processed via deformation-driven metallurgy", Journal of Materials Science: Materials in Medicine, Vol.36, p 81.

5. **Kelen, F., Gavgali, M. and Aydoğmuş, T., (2025),** "TiNi Particle-Reinforced Magnesium Matrix Composites: Production, Microstructure, Phase Transformations, and Mechanical Properties", Advanced Engineering Materials, Vol.27, p 2402277.

6. **Sharma, S.K., Pradhan, R., Sharma, L.K., Sharma, Y. and Sharma, M., (2026),** "Optimized low-content $B_4C$ reinforcement in AZ31 alloy composites fabricated by powder metallurgy", Materials Letters, Vol.410, p 140284.

7. **Wang, Z., Zhao, L., Zhu, S., Wang, D., Wang, Q., Xiao, B. and Ma, Z., (2026),** "Hot deformation behavior and dynamic recrystallization mechanism of 15 vol% SiCp/AZ31 magnesium matrix composite by powder metallurgy", Journal of Alloys and Compounds, Vol.1054, p 186344.

# INVESTIGATION OF 3-D PRINTING POTENTIAL OF BIO-INSPIRED COLD PLATES FOR ELECTRIC VEHICLE BATTERY THERMAL MANAGEMENT

**Fatih Furkan BEKÖZ**, *bekoz23@itu.edu.tr*, Istanbul Technical University, 34469, Istanbul, Türkiye

**Yusuf Ata ERTÜRK**, *erturky22@itu.edu.tr*, Istanbul Technical University, 34469, Istanbul, Türkiye

**Tuba OKUTUCU-ÖZYURT**, *okutucuozyurt@itu.edu.tr*, Istanbul Technical University, 34469, Istanbul, Türkiye

## ABSTRACT

A bio-inspired cold plate compatible with 3-D printing steps is developed for the thermal management of electric vehicle batteries. Gyroid-based cooling channels with high heat transfer potential are designed. To reduce the inherent hydraulic resistance of gyroid structures, Murray's Law is utilized as a design criterion. Field-Driven Design is utilized to grade the gyroid wall thicknesses based on local flow parameters. Validations via Lattice Boltzmann simulations proved that multi-field grading achieves an optimized pressure drop and stable flow within standard pump capacities. This framework establishes a highly efficient, optimized hydraulic foundation for subsequent thermal analyses directly influencing battery performance.

**Keywords:** Battery Thermal Management, Additive Manufacturing, Gyroid TPMS, Murray's Law, Field-Driven Design, LBM.

## 1. INTRODUCTION

The performance, safety, and cycle life of electric vehicles (EVs), particularly in heavy-duty applications like electric buses, are fundamentally dictated by the thermal management of the battery packs [1]. Conventional liquid cooling plates with hollow channels often suffer from limited convective heat transfer coefficients due to the presence of core flow that bypasses the channel walls. To overcome this limitation, Triply Periodic Minimal Surface (TPMS) structures, specifically gyroid lattices, have emerged as a high-performance alternative due to their exceptional surface area-to-volume ratios [2].

However, integrating complex micro-architectures increases hydraulic resistance. This study adopts a bio-inspired optimization strategy to mitigate pressure drop. Murray [3] described the fundamental principle of minimum work in the vascular system, establishing that for an efficient fluid network, the cubic radius of a parent vessel must relate to its daughter branches as:

$$r_0^3 = \sum_{i=1}^{n} r_i^3 \quad (1)$$

By applying this bio-inspired cubic relationship as an optimization constraint, this work proposes a homogenized gyroid cold plate designed to maximize heat transfer while maintaining hydraulic efficiency.

## 2. DESIGN METHODOLOGY

The internal volume of the cold plate is modeled using implicit modeling within the computational design software nTop. Based on geometric constraints where the narrowest channel is 10 mm, a gyroid unit cell size of 10 x 10 x 10 mm is selected. This sizing ensures structural integrity and prevents flow choking at critical junctions.

To ensure uniform flow distribution and manage hydraulic loads, a Field-Driven Design (FDD) approach is implemented. Following the methodology for functionally graded lattice structures established by Maskery et al. [4], the wall thickness of the gyroid is algorithmically varied rather than being kept constant. Using a ramp function driven by local velocity and pressure fields, thicknesses were reduced to 0.3 mm in high-velocity zones to lower resistance and increased to 0.8 mm in stagnant regions to redirect flow. The integration of these spatial variations follows the systematic optimization workflow presented in Figure 1.

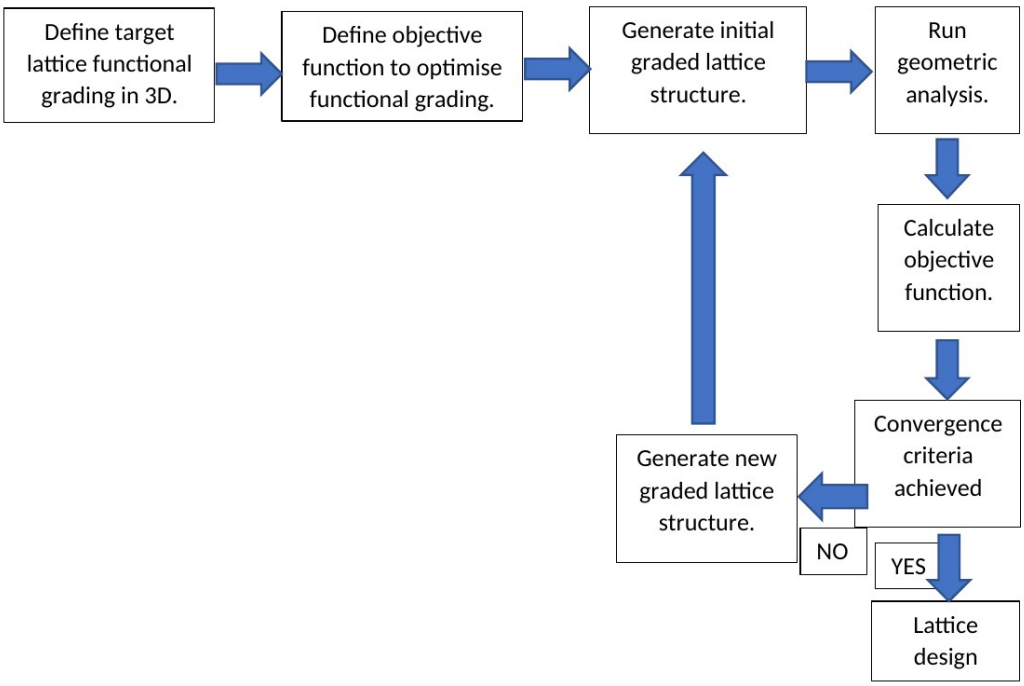



**Figure 1:** Optimization flowchart for functionally graded lattice structures (adapted from Maskery et al. [4]).

## 3. RESULTS AND DISCUSSION

### 3.1. Stage 1 Validation: Idealized Newtonian Fluid

The first validation stage is performed using a straight pipe geometry with a length $L$ = 1 m and an internal diameter, $D$ = 20 mm. The simulation utilized an idealized Newtonian fluid with a density of $\rho = 1000\ \mathrm{kg/m^3}$ and a kinematic viscosity $v = 100\ \mathrm{mm^2/s}$. At a constant flow velocity $V = 10\ \mathrm{mm/s}$, the pressure drop is analytically calculated using the Darcy–Weisbach equation (2) for a laminar regime $f = \frac{64}{\mathrm{Re}}$

$$\Delta P = f \cdot \left(\frac{L}{D}\right) \cdot \frac{\rho v^2}{2} \tag{2}$$

As shown in Figure 2, at the cell size of 0.25 mm (the limit of our current computational capacity), the LBM solver yielded a pressure drop that perfectly matched the analytical value of 80 Pa, confirming the accuracy of the numerical scheme.

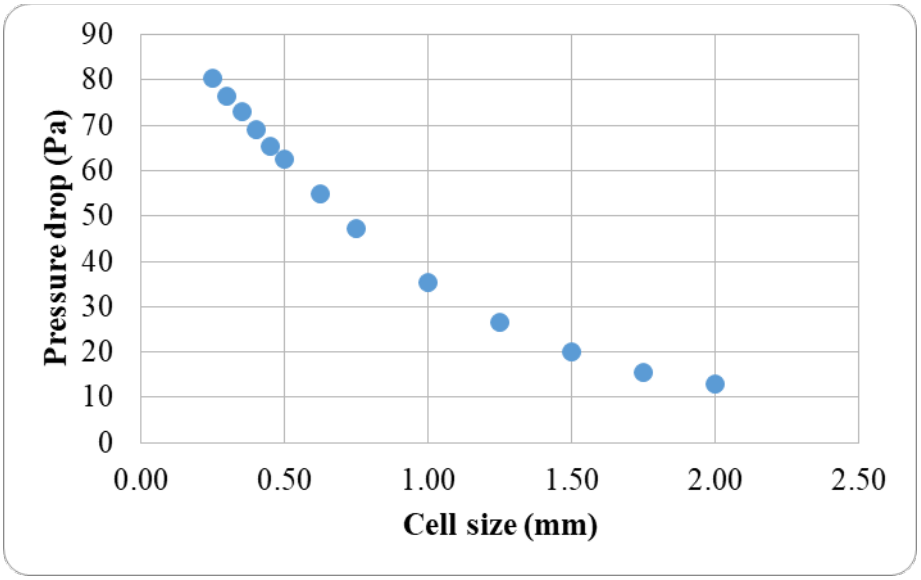
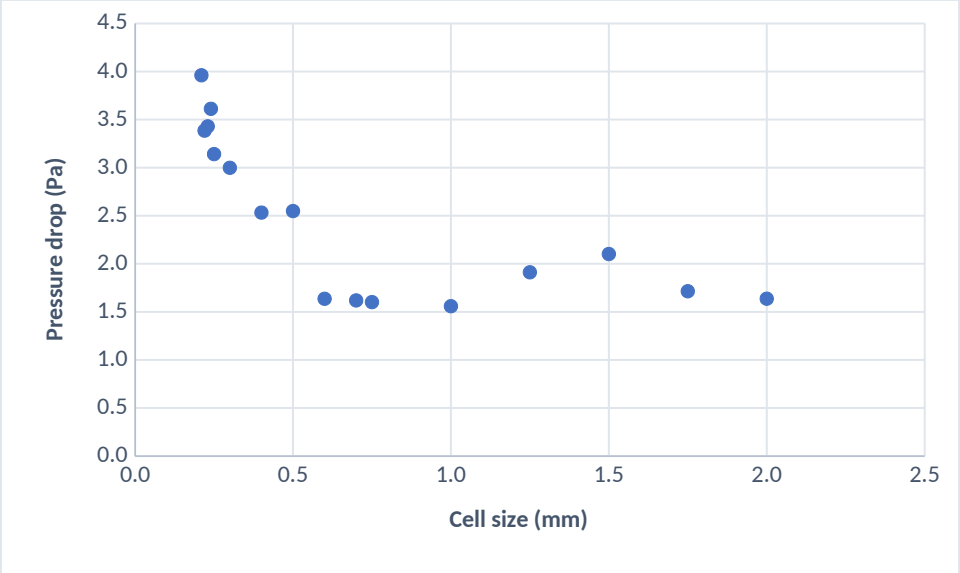


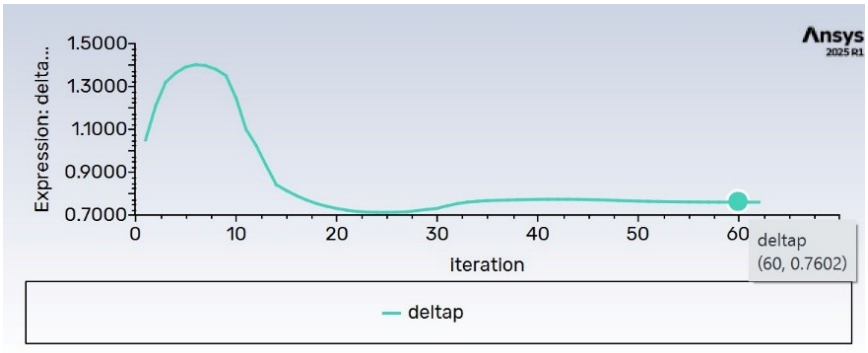

**Figure 2:** Validation of LBM results against Darcy–Weisbach analytical solution for Stage 1

### 3.2. Stage 2 Validation: Water at 300 K

In the second stage, the validation is extended to represent water cooling application. The fluid properties were updated to match water at 300 K, with a density of $\rho = 997.003\ \mathrm{kg/m^3}$ and a kinematic viscosity of $v = 0.857\ mm2/s$. Using the same straight pipe dimensions and velocity (10 mm/s), the pressure drop is analytically determined as 0.68 Pa. The corresponding ANSYS Fluent solution yielded $\Delta P$ = 0.76 Pa as shown in Figure 3b. The LBM simulation results, presented in Figure 3a demonstrated slight overestimation (0.93 Pa), thereby indicating the solver's usability for low-viscosity fluid applications.




**(a)**




**(b)**

**Figure 3:** Validation of LBM and ANSYS Fluent results against Darcy–Weisbach analytical solution for Stage 2 using Water at 300 K

### 3.3. Stage 3: Lattice-Free Branching Baseline

In the third stage, a lattice-free branching structure is simulated to establish a reference hydraulic baseline. This stage evaluates the performance of the bio-inspired channel geometry designed via Murray's Law before the integration of internal TPMS structures.

The results for this baseline are presented in Figure 4. The fluid domain representation given in Figure 4a illustrates the branching network where the coolant flows. Figure 4b presents the pressure distribution contours across the network. The smooth pressure gradients observed in the contours confirm that Murray's Law-based branching effectively distributes the hydraulic load across the plate even without internal architectures.

Furthermore, the stability of the simulation is confirmed via the LBM pressure drop convergence graph shown in Figure 5. This baseline acts as a critical control group; it proves that the main branching architecture is inherently optimized, providing a low-resistance path that serves as the foundation for the final graded lattice design. By establishing this reference, the incremental hydraulic resistance added by the subsequent gyroid lattice can be accurately quantified.

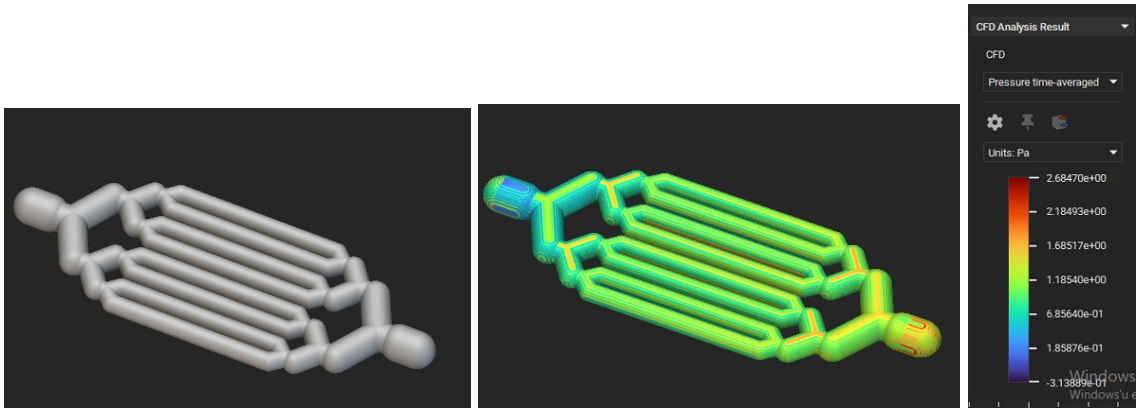



**Figure 4:** Results for the lattice-free branching baseline: (a) Fluid domain/volume representation, (b) Pressure distribution contours showing smooth hydraulic gradients.

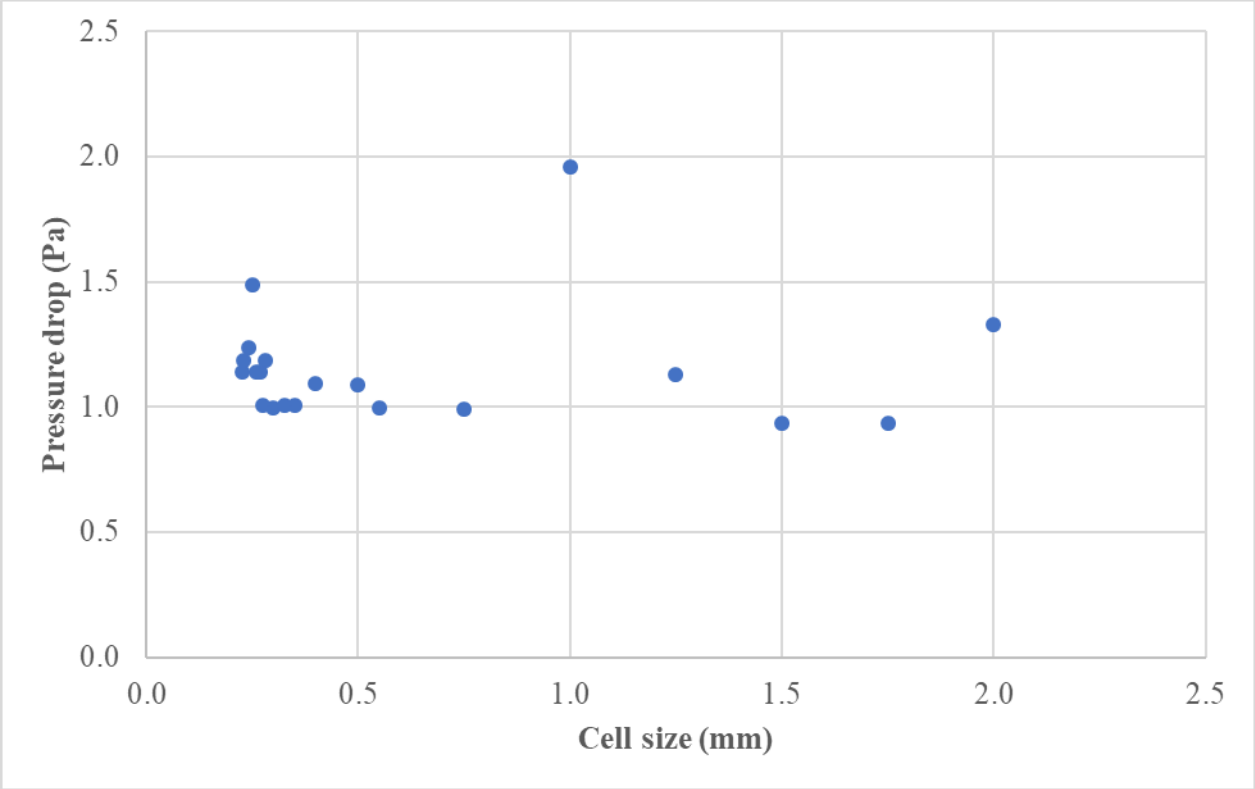



**Figure 5:** LBM pressure drop convergence graph for the Stage 3 baseline.

### 3.4. Optimization Performance and Aliasing Resolution

The final stage of the study involved integrating the graded gyroid lattice into the single SVOLT CM12 module cold plate (Product Code: SVOLT CZ1C6U36A). To achieve the target performance, the optimized configuration is set with a gyroid unit cell size of 10 x 10 x 10 mm as shown in Figure 6. This sizing is strategically selected to maintain structural integrity while ensuring adequate flow paths (Figure 7) at critical junctions of the branching network.

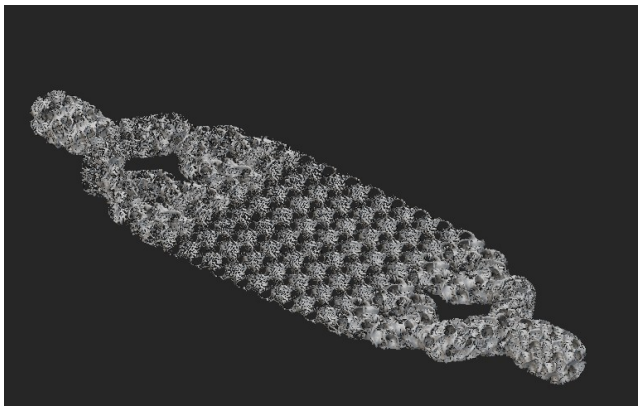


**Figure 6:** Cross-sectional view of the functionally graded gyroid lattice structure integrated within the cold plate

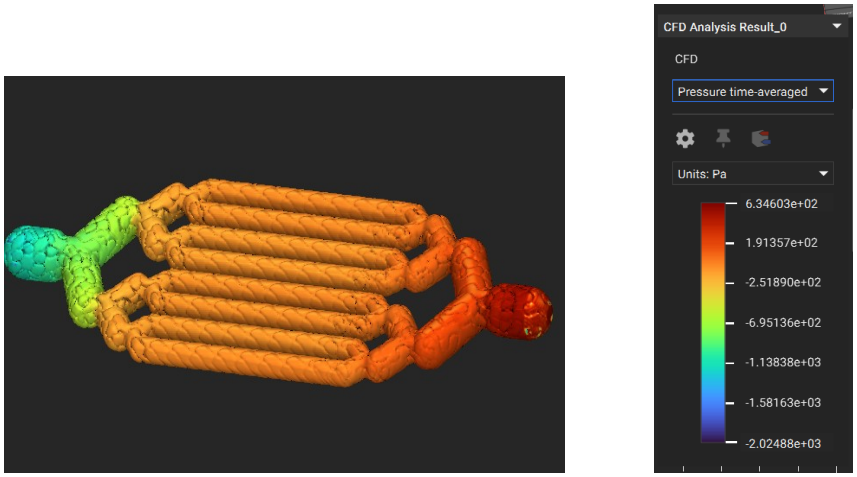



**Figure 7:** Simulated pressure distribution contours across the multi-field graded gyroid cold plate

A critical mesh sensitivity analysis is conducted to resolve non-physical pressure spikes observed during the initial optimization cycles. As illustrated in the convergence study in Figure 8, refining the voxel resolution from 0.55 mm to 0.525 mm is essential to eliminate digital aliasing artifacts. These artifacts occurred when the computational grid failed to accurately resolve the 0.3 mm minimum wall thicknesses, leading to artificial flow blockages and a resultant pressure spike of ~12 kPa.

With the mesh parameters established, the wall thicknesses were algorithmically graded between 0.3 mm and 0.8 mm using a velocity-pressure coupled ramp function. The final design achieved a stable pressure drop of 2.6 kPa per module. This value is within the acceptable operational ranges for electric bus cooling systems, suggesting that the proposed bio-inspired framework is a viable approach for enhancing EV thermal management.

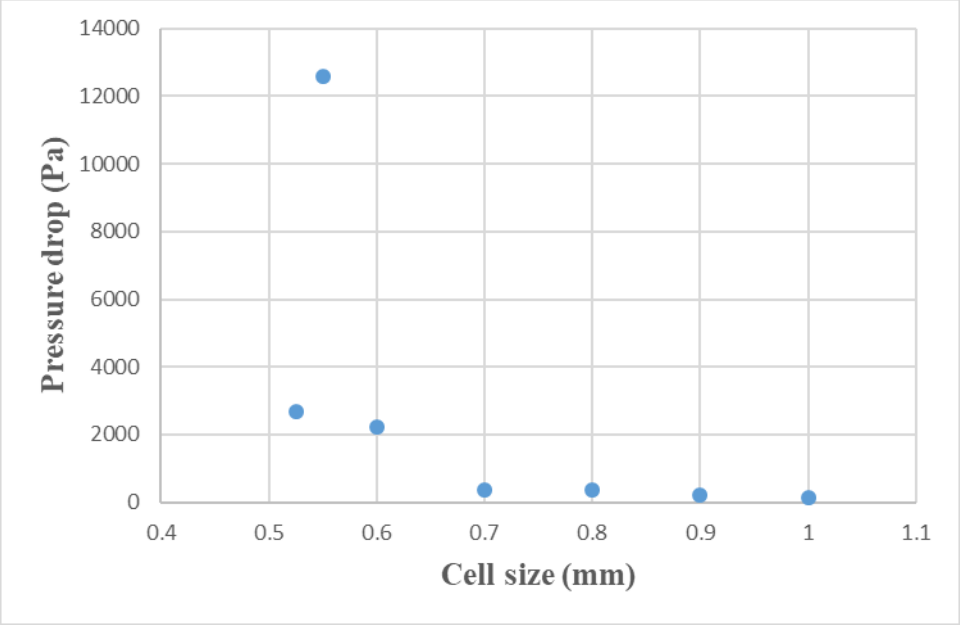



**Figure 8:** Mesh sensitivity analysis demonstrating the resolution of digital aliasing artifacts and pressure drop convergence across different voxel resolutions.

However, it should be noted that these results represent the preliminary iterations of the optimization loop. This work serves as an initial example of the methodology; as the number of iterations increases and the design space is more extensively explored, the solution is expected to converge toward a more global optimum. Future studies involving a higher count of optimization trials will be necessary to fully refine the thermal-hydraulic efficiency of the graded structure.

## 4. CONCLUSION

This study successfully integrates Murray's Law and Field-Driven Design (FDD) for the thermal management of a single SVOLT CM12 battery module. By utilizing velocity-pressure coupled grading in gyroid structures the design effectively minimizes hydraulic resistance while maintaining the complex surface area required for future thermal performance enhancement. Resolving digital aliasing artifacts at a 0.525 mm voxel resolution in the LBM solver yielded a converged pressure drop of 2.6 kPa per module.

While the current results demonstrate the significant potential of bio-inspired grading, they serve as a proof-of-concept for the proposed methodology. Further iterations and a broader range of optimization trials are required to identify the absolute optimum for the heat transfer-to-pressure drop ratio. Nevertheless, the established framework provides a robust and modular foundation for the development of high-performance cooling systems in electric vehicles.

## ACKNOWLEDGEMENTS

This study received funding from the Scientific and Technological Research Council of Türkiye (TÜBİTAK) 1004 ILATERA Platform under Grant Number 22AG018.

## REFERENCES

1. Rao, Z. and Wang, S. (2011), "A Review of Power Battery Thermal Energy Management", *Renewable and Sustainable Energy Reviews*, Vol. 15, No. 9, pp 4554-4571.
2. Kaur, I. and Singh, P. (2021), "State-of-the-Art in Heat Exchanger Based on Triply Periodic Minimal Surfaces", *International Journal of Heat and Mass Transfer*, Vol. 170, 121002.
3. Murray, C.D. (1926), "The Physiological Principle of Minimum Work. I. The Vascular System and the Cost of Blood Volume", *Proceedings of the National Academy of Sciences*, Vol. 12, No. 3, pp 207-214.
4. Maskery, I., et al. (2018), "Effective Design and Simulation of Surface-Based Lattice Structures Featuring Volume Fraction and Cell Size Grading", *Materials & Design*, Vol. 155, pp 220-232.

# PREDICTION OF TENACITY AND ELONGATION IN FILAMENT DRAWING PROCESS USING MOTOR MOMENT BASED MECHANICAL TRANSFORMATION

**Uscan Uskaner**, *uskaner15@itu.edu.tr* Istanbul Technical University, 34437, İstanbul, Turkiye

**Zeynep Parlar**, *parlarze@itu.edu.tr* Istanbul Technical University, 34437, İstanbul, Turkiye

## ABSTRACT

This study relates draw ratio, godet temperature, and an unloaded-moment-compensated effective motor moment ($\tau$) to the final mechanical properties of a 550 dtex / 144 filament POY yarn drawn on the USLAN SpinLab system, using a tenacity gain ratio ($G_\sigma$) and elongation retention ratio ($R_\varepsilon$). $G_\sigma$ increased and $R_\varepsilon$ fell sharply with draw ratio, to about 0.06 at DR 2.25 and above. Temperature governed the processability window: DR 2.50 was sustainable at 80 –90 °C but not at 25 or 100 °C. A preliminary polynomial model relates DR, T and $\tau$ to $G_\sigma$ and $R_\varepsilon$, requiring validation with larger data sets.

**Keywords:** Filament drawing process; Effective motor moment; Mechanical transformation; Tenacity gain ratio; Elongation retention ratio

## 1. INTRODUCTION

Synthetic filament yarn production is a high-volume, process-sensitive area of the textile industry. As production speed increases, tolerance to process variation narrows, so small deviations in temperature, draw ratio, and yarn loading can cause quality variation over long production runs.

Quality control is generally based on post-production laboratory testing of tenacity, elongation, and unevenness. Because this approach is reactive, using in-process machine and process data for quality prediction has become an important research direction in high-speed filament manufacturing.

Meaningful relationships between process parameters and yarn quality have been reported previously: winding speed, cooling-air temperature, and velocity have predicted tenacity, crystallinity, and unevenness in PET-POY production [Yıldırım, 2017]; draw ratio and heater temperature have been linked to yarn properties in PET texturing [Yıldırım, 2015]; and mechanical drive parameters such as screw and pump speed have been associated with fiber tenacity and yarn count [Kuo, 2004].

Draw ratio and temperature are fundamental variables governing the yarn structure–property relationship, affecting molecular orientation, crystallinity, and final mechanical properties [Liu,

2015]. Process-side mechanical responses also matter: tension level and fluctuation have been linked to product uniformity and mechanical performance [Zhang, 2021; Du, 2025; Iwade, 2000]. A quality prediction model should therefore consider both nominal process settings and the mechanical response generated during drawing.

Motor moment is not a direct quality measurement, but it reflects the mechanical load state of the drawing system, combining yarn load, friction, contact geometry, and the unloaded response of the drive itself. Fiber-drawing and capstan-type mechanics link motor moment to the stress/tension state in the drawing zone [Hsiao, 1997], though in multi-contact godet geometries it should not be equated directly with yarn tension. Here, motor moment is therefore treated as a motor-drive-side process response representing mechanical loading during drawing.

In this work, a 550 dtex / 144 filament standard POY yarn was drawn on the USLAN SpinLab filament drawing system. The effects of draw ratio, godet temperature, and G2 motor moment on final tenacity and elongation at break were investigated, using the unloaded-moment-compensated effective motor moment as a process response indicator in an initial-to-final mechanical transformation model.

The schematic yarn path and the real experimental setup of the USLAN SpinLab filament drawing system are shown together in Figure 1.

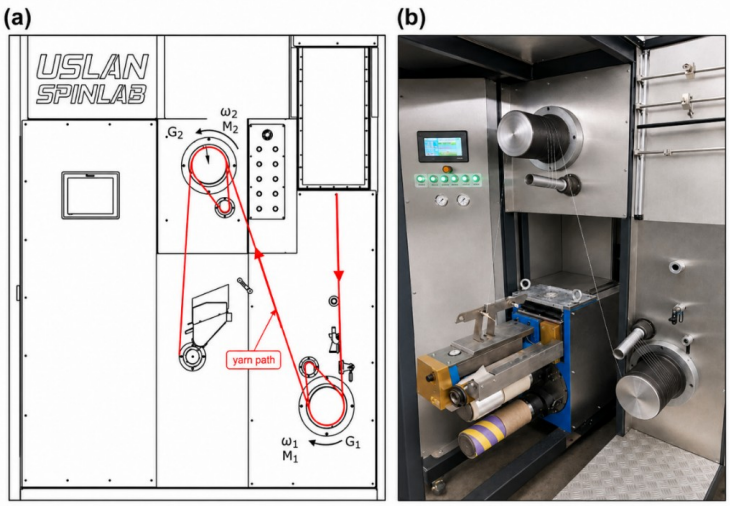



**Figure 1.** USLAN SpinLab filament drawing system: **(a)** schematic representation of the yarn path, godet arrangement, rotational directions $(\omega_2)$, and motor moments $(M_2)$; **(b)** experimental view of the godet region, yarn path, and pre-winder zone used during the drawing experiments.

The main contribution of this study is the use of motor-drive data as an in-process mechanical response indicator for predicting final mechanical properties, without assuming a direct equivalence between motor moment and yarn tension. Instead, the transformation from initial POY to final yarn properties is modeled using dimensionless ratios: tenacity gain ($G_\sigma$) and

elongation retention ($R_\varepsilon$). This work is a preliminary modeling study; with larger data sets it can be extended using regression, Gaussian Process Regression, or artificial neural networks.

## 2. MATERIAL AND METHOD

This study was carried out on the USLAN SpinLab filament drawing system using a 550 dtex / 144 filament standard POY yarn. The system provides independently controlled godets, controlled surface heating, motor-drive-based data acquisition, and the ability to monitor process response under different drawing conditions. The yarn path and experimental setup are shown in Figure 1.

It should be noted that the drawing process and the mechanical property measurements were carried out as two separate stages. First, POY yarn was drawn on the USLAN SpinLab system under each draw ratio–temperature condition, during which the G2 motor moment was recorded. The drawn yarn samples were then removed from the system and tested off-line, after production, on a pneumatic-jaw yarn strength tester (PROWHITE, Vira Color Masterbatches, Gaziantep, Türkiye) in accordance with ASTM D2256, using a 250 mm gauge length and a test speed of 300 mm/min, under standard laboratory atmosphere (21± 1 °C, 65± 2% relative humidity). One specimen was tested per draw ratio–temperature condition; the reported tenacity and elongation values are therefore single measurements rather than replicate averages, a limitation addressed in Section 4.

The main process variables were selected as draw ratio and godet temperature. The draw ratio was obtained by operating the $G_2$ godet at an approximately constant frequency of 104.16 Hz and varying the frequency of the $G_1$ godet. Therefore, the draw ratio was approximately defined as:

$$DR \approx \frac{f_{G2}}{f_{G1}} \tag{1}$$

where $f_{G2}$and $f_{G1}$are the rotational frequencies of the $G_2$ and $G_1$ godets, respectively. In this way, different draw ratio levels were generated through motor-drive frequency settings.

In the experimental data set, the DR = 1.25 and DR = 1.50 conditions were considered transition or phase-forming conditions used to establish the drawing process. Therefore, these conditions were excluded from the main quality analysis. The main analysis range was limited to:

$$DR = 1.75 - 2.50 \tag{2}$$

At some temperature levels, the DR = 2.50 condition could not be sustained in a stable manner. These cases were not treated as missing measurements. Instead, they were considered processability limits under the corresponding thermal conditions.

The $G_2$ motor moment was evaluated as a process-response variable representing mechanical loading on the motor-drive side. Since the $G_2$ godet operated at an approximately constant frequency during the experiments, its moment signal was used to monitor the process response. However, this signal was not interpreted as direct yarn tension because it includes the combined effects of yarn loading, godet contact geometry, wrapping, friction, yarn path, motor-drive characteristics, and the unloaded mechanical response of the system.

To obtain the effective process moment, the $G_2$ godet was first operated under unloaded conditions at 104.16 Hz. The unloaded motor moment was determined as:

$$M_{G2,unloaded} = 7.1\ Nm \tag{3}$$

The effective moment was calculated by subtracting this unloaded value from the measured $G_2$ motor moment during the experiments:

$$M_{G2,eff} = M_{G2,measured} - M_{G2,unloaded} \tag{4}$$

For this study:

$$M_{G2,eff} = M_{G2,measured} - 7.1 \tag{5}$$

The effective moment was denoted as:

$$\tau = M_{G2,eff} \tag{6}$$

This effective moment was treated as a moment-based relative process indicator representing the mechanical loading generated during drawing. It was not used as a direct yarn tension value.

The prediction problem was formulated as an initial-to-final mechanical transformation problem. The initial POY tenacity and elongation at break were taken as reference values:

$$\sigma_0 = 2.06\ \ cN/dtex \tag{7}$$

$$\varepsilon_0 = 132.2\,\% \tag{8}$$

where $\sigma_0$ and $\varepsilon_0$ represent the initial POY tenacity and elongation at break. The final values after drawing were denoted by $\sigma_f$ and $\varepsilon_f$, respectively.

Instead of directly modeling final tenacity and elongation, two dimensionless transformation ratios were defined:

$$G_\sigma = \frac{\sigma_f}{\sigma_0} \tag{9}$$

$$R_\varepsilon = \frac{\varepsilon_f}{\varepsilon_0} \tag{10}$$

Here, $G_\sigma$ represents the tenacity gain ratio and $R_\varepsilon$represents the elongation retention ratio. These ratios describe how the initial POY yarn is transformed into a higher-tenacity and lower-

elongation final yarn. Defining the model outputs as dimensionless ratios also makes the framework more adaptable to different initial POY properties.

The model input vector was defined as:

$$X=[\,DR\,,T\,,\tau\,] \tag{11}$$

where $DR$is the draw ratio, $T$ is the godet temperature, and $\tau$ is the effective motor moment. The model outputs were defined as:

$$\hat{G}_{\sigma}=f\left(DR\,,T\,,\tau\right) \tag{12}$$

$$\hat{R}_{\varepsilon}=g\left(DR\,,T\,,\tau\right) \tag{13}$$

The predicted final tenacity and elongation at break can then be calculated as:

$$\hat{\sigma}_f=\hat{G}_{\sigma}\sigma_0 \tag{14}$$

$$\hat{\varepsilon}_f=\hat{R}_{\varepsilon}\varepsilon_0 \tag{15}$$

In this structure, $\tau$ is used as an auxiliary process variable representing the mechanical response that cannot be fully captured by nominal draw ratio alone. The proposed prediction algorithm is summarized in Figure 2.

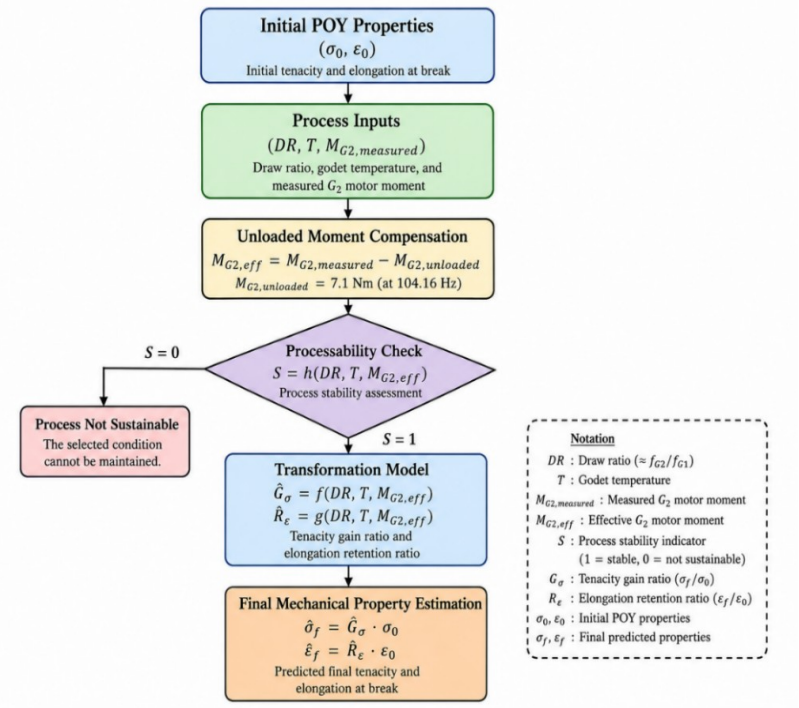



**Figure 2.** Effective-moment-assisted initial-to-final mechanical property prediction algorithm.

The algorithm also includes a processability assessment. A binary process status variable was defined as:

$$S=h\left(DR\,,T\,,\tau\right) \tag{16}$$

where $S=1$ represents a stable process condition and $S=0$ represents a non-sustainable

condition. Thus, the algorithm first evaluates processability and then estimates final mechanical properties only under stable conditions.

The experimental data structure can be summarized as:

$$\left[DR, T, \tau\right] \rightarrow \left[G_{\sigma}, R_{\varepsilon}\right] \tag{17}$$

For each stable condition, the effective moment was calculated first. Then, the measured final tenacity and elongation values were normalized by the initial POY properties to obtain $G_{\sigma}$ and $R_{\varepsilon}$. In this way, the available experimental data were converted into a preliminary training and validation structure for the proposed model architecture.

**Table 1.** Effective moment, mechanical properties, and initial-to-final transformation ratios within the main analysis range.

| Temperature, $T$ (°C) | Draw Ratio, DR (-) | Effective Moment, $\tau$ (Nm) | Final Linear Density, $dT_{exf}$ | Final Tenacity, $\sigma_f$ (cN/dtex) | Final Elongation, $\varepsilon_f$ (%) | Tenacity Gain Ratio, $G_{\sigma}$ (-) | Elongation Retention Ratio, $R_{\varepsilon}$ (-) | Process Status, $S$ |
|---|---|---|---|---|---|---|---|---|
| 25 | 1.75 | 5.0 | 318 | 3.392 | 28.60 | 1.647 | 0.216 | Stable |
| 25 | 2.00 | 7.1 | 278 | 3.919 | 10.13 | 1.902 | 0.077 | Stable |
| 25 | 2.25 | 8.1 | 253 | 5.895 | 8.00 | 2.862 | 0.061 | Stable |
| 25 | 2.50 | — | — | — | — | — | — | Process not sustainable |
| 80 | 1.75 | 4.4 | 341 | 3.205 | 46.68 | 1.556 | 0.353 | Stable |
| 80 | 2.00 | 4.9 | 290 | 4.318 | 22.86 | 2.096 | 0.173 | Stable |
| 80 | 2.25 | 7.1 | 259 | 5.898 | 8.63 | 2.863 | 0.065 | Stable |
| 80 | 2.50 | 12.1 | 240 | 7.077 | 8.07 | 3.435 | 0.061 | Stable |
| 90 | 1.75 | 4.0 | 332 | 3.191 | 45.30 | 1.549 | 0.343 | Stable |
| 90 | 2.00 | 4.6 | 292 | 4.155 | 21.16 | 2.017 | 0.160 | Stable |
| 90 | 2.25 | 7.1 | 261 | 5.434 | 8.57 | 2.638 | 0.065 | Stable |
| 90 | 2.50 | 12.4 | 242 | 7.042 | 8.05 | 3.418 | 0.061 | Stable |
| 100 | 1.75 | 4.4 | 334 | 3.525 | 30.69 | 1.711 | 0.232 | Stable |
| 100 | 2.00 | 6.6 | 292 | 4.811 | 20.62 | 2.335 | 0.156 | Stable |
| 100 | 2.25 | 7.5 | 261 | 5.554 | 8.07 | 2.696 | 0.061 | Stable |
| 100 | 2.50 | — | — | — | — | — | — | Process not sustainable |

Table 1 presents the effective moment, final linear density, final mechanical properties, transformation ratios, and process status within the main analysis range. Since the present data set consists of a limited number of process points, this study should be considered a preliminary modeling study rather than a final and universally valid predictive model.

## 3. RESULTS AND DISCUSSION

### 3.1. Effect of Draw Ratio, Temperature, and Effective Moment on Mechanical

The effective moment, mechanical properties, and transformation ratios calculated within the main analysis range are given in Table 1. The DR 1.25 and DR 1.50 conditions were excluded from the analysis because they were transition conditions. The unstable DR 2.50 cases at 25 °C and 100 °C were evaluated as processability limits.

The results show that final tenacity increased with increasing draw ratio, whereas elongation at break decreased significantly. This agrees with PET filament drawing literature, where draw ratio is reported as the dominant variable increasing molecular orientation, crystallinity,

birefringence, tenacity, and modulus while reducing breaking extension [Rudolf and Smole, 2008; Haji and Rahbar, 2013; Xu, 2005]. Similar trends have also been observed in textured yarns, where draw ratio remains the main variable controlling tenacity, although heater temperature and texturing conditions may also modify the final yarn structure [Yıldırım et al., 2009; Deilamani et al., 2017].

Increasing $G_\sigma$ indicates tenacity improvement relative to the initial POY yarn, while decreasing $R_\varepsilon$ represents loss of initial elongation capacity. As shown in Figure 3, $G_\sigma$ increased and $R_\varepsilon$ decreased sharply with increasing draw ratio.

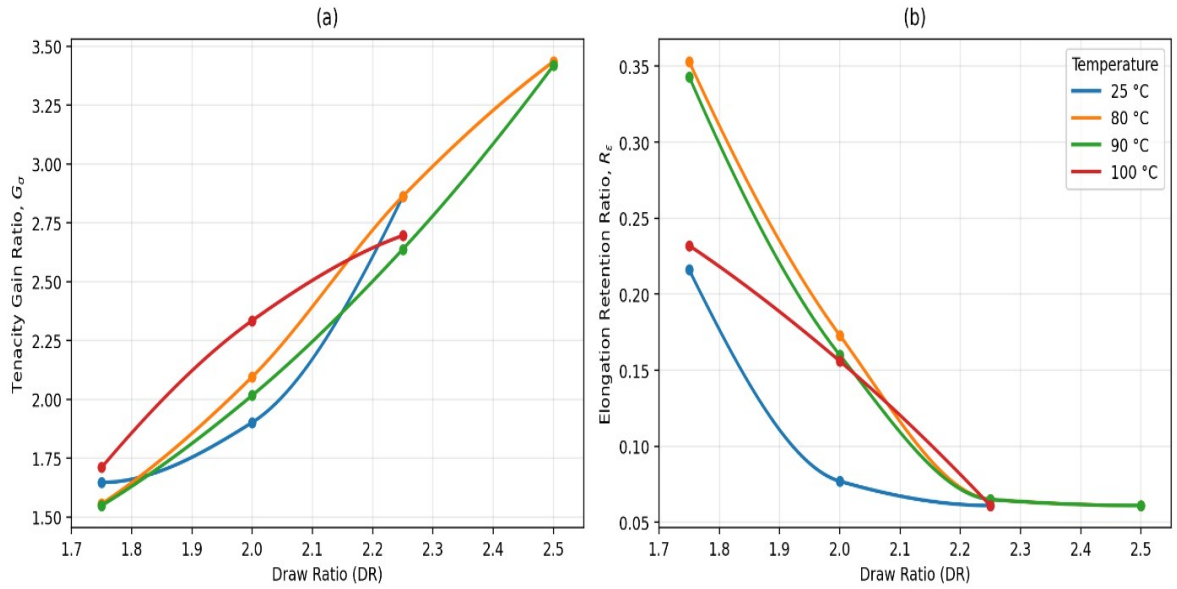



**Figure 3.** Initial-to-final mechanical transformation ratios as a function of draw ratio: (a) tenacity gain ratio $G_\sigma$, and (b) elongation retention ratio $R_\varepsilon$.

At DR 2.25 and above, $R_\varepsilon$ decreased to approximately 0.06. This means that only about 6% of the initial elongation capacity was retained after drawing. At the same time, $G_\sigma$ increased significantly. This behavior indicates a strong transformation from a low-tenacity/high-elongation POY state toward a high-tenacity/low-elongation drawn yarn.

The reduction of $R_\varepsilon$ and increase of $G_\sigma$ indicate a mechanical transformation, though not directly crystallinity, density, or molecular orientation, which would require additional characterization (DSC, WAXD, SAXS, or birefringence). The trend is nonetheless consistent with studies showing that increasing draw ratio increases amorphous orientation and tensile performance in PET yarns [Liu et al., 2015; Haji and Rahbar, 2013].

The effective moment $\tau$ also increased with draw ratio. At 80 °C, $\tau$ increased from 4.4 Nm at DR 1.75 to 12.1 Nm at DR 2.50. At 90 °C, it increased from 4.0 Nm to 12.4 Nm over the same draw ratio range. This behavior is shown in Figure 4 and indicates that higher drawing severity required a stronger mechanical response from the motor-drive system.

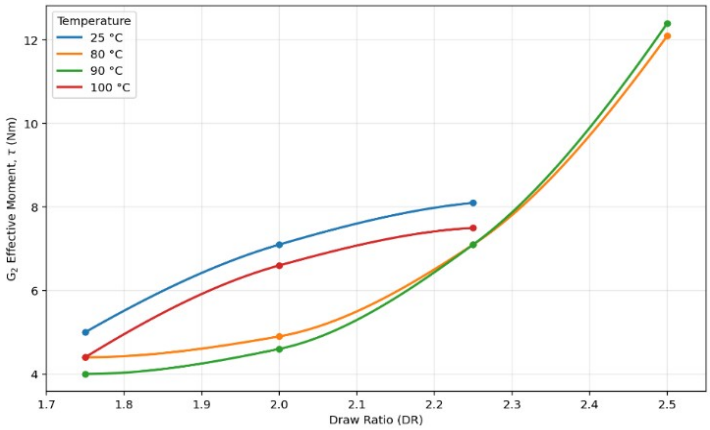



**Figure 4.** Effective motor moment response as a function of draw ratio.

$\tau$ should not be interpreted as the direct physical cause of tenacity improvement; draw ratio remains the primary governing variable. $\tau$ instead provides complementary information on process-side mechanical loading (yarn load, contact geometry, friction, wrapping, motor-drive behavior), consistent with motor moment being physically related to — but not directly equal to — the drawing-zone tension state in a multi-contact godet system [Hsiao, 1997].

### 3.2. Evaluation of the Initial-to-Final Mechanical Transformation Path

Each stable experimental condition was represented by the following transformation relationship:

$$\left[DR, T, \tau\right] \rightarrow \left[G_{\sigma}, R_{\varepsilon}\right] \tag{18}$$

This structure describes the transformation of the initial POY yarn into the final drawn yarn in dimensionless form. Instead of estimating only final tenacity and elongation, the model estimates how much the initial yarn is transformed under a given process condition.

The transformation-path evaluation is presented in Figure 5.

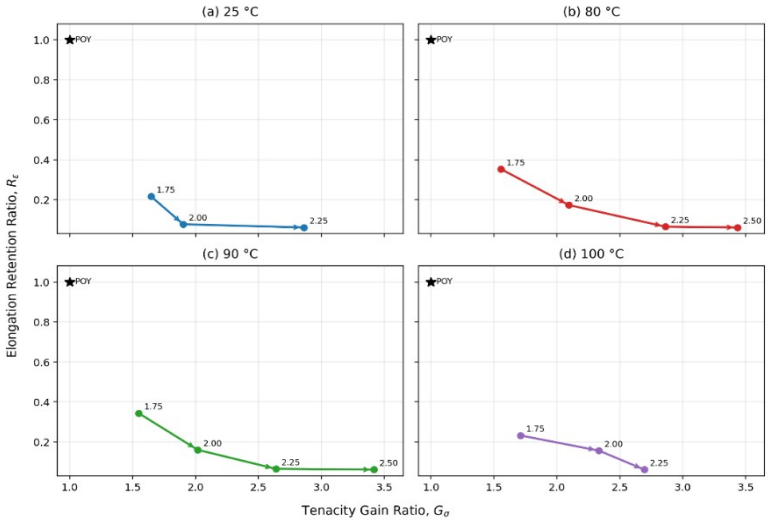


**Figure 5.** Initial-to-final mechanical transformation path at different temperature levels: (a) 25 °C, (b) 80 °C, (c) 90 °C, and (d) 100 °C. The arrows indicate increasing draw ratio.

The results show that increasing draw ratio generally shifted the yarn toward higher $G_\sigma$ and lower $R_\varepsilon$. Movement toward higher $G_\sigma$ represents tenacity gain, while movement toward lower $R_\varepsilon$ represents the consumption of initial elongation capacity. This supports the use of $G_\sigma$ and $R_\varepsilon$ as model outputs because they directly describe the transition from the initial POY mechanical character to the final drawn-yarn character.

The maximum useful draw ratio is not fixed; it depends on polymer structure, initial orientation, drawing temperature, and drawing method [Seguela, 2007; Rudolf and Geršak, 2012; Liu et al., 2015]. This is consistent with the present results, where the transformation path continued to DR 2.50 at 80 °C and 90 °C but could not be sustained at 25 °C and 100 °C.

The very low $R_\varepsilon$ at high draw ratios suggests further tenacity gain may come at the expense of the yarn's elastic reserve. The highest-tenacity condition should therefore not automatically be considered optimal unless elongation reserve and process stability are also taken into account, consistent with reports that drawing beyond a critical point can reduce practical performance through insufficient breaking extension [Rudolf and Geršak, 2012].

### 3.3. Processability and Temperature Effect

Temperature did not act as a simple monotonic factor that improved mechanical properties under all conditions. Instead, it mainly defined the processability window at high draw ratios. In this study, DR 2.50 was stable at 80 °C and 90 °C, but could not be sustained at 25 °C and 100 °C. This processability behavior is summarized in Figure 6.

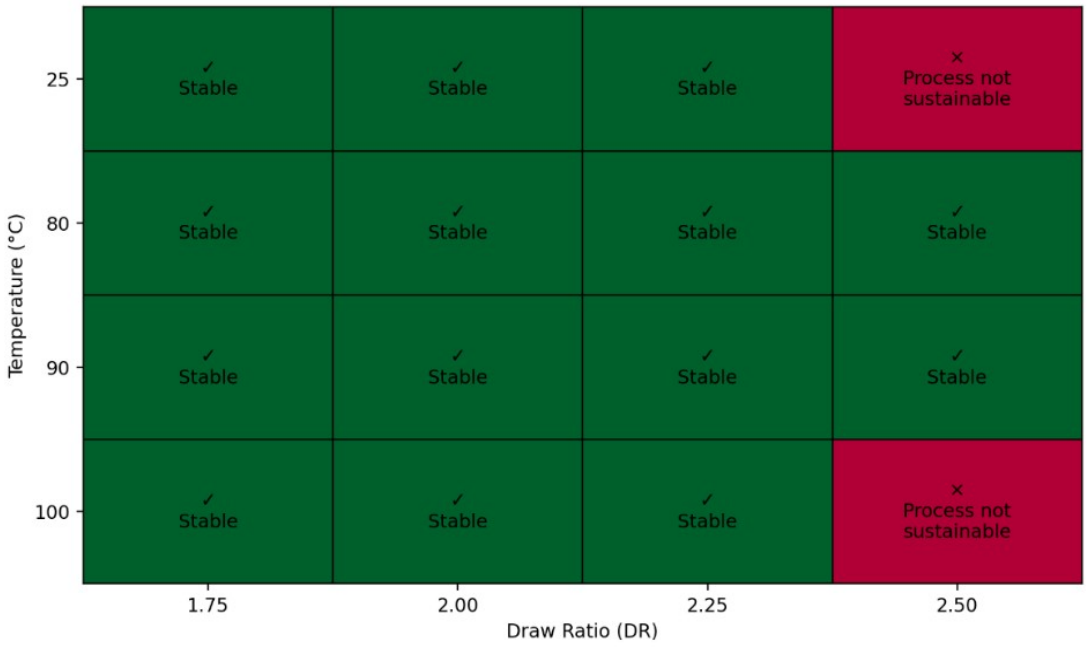


**Figure 6.** Temperature–draw ratio processability map. Green cells represent stable process conditions, while red cells represent non-sustainable conditions.

The 80–90 °C range provides a favorable thermal window for high draw ratios: since the glass transition temperature of PET is near 70 °C, drawing near or above this region increases segmental mobility and drawability, consistent with studies on hot and multistage drawing [Haji and Rahbar, 2013].

However, unstable behavior at 100 °C shows that higher temperature does not always improve processability; relaxation behavior, frictional effects, and drawing-zone instability may become more influential. Temperature should therefore be evaluated in terms of both drawability and process stability.

This supports including the process-status variable S in the proposed algorithm: unstable DR 2.50 cases are meaningful process information rather than data loss, consistent with the concepts of natural and critical draw ratio, where stable drawing is limited by polymer network structure, chain entanglements, and thermal state [Seguela, 2007; Okumura et al., 2002; Ohkoshi et al., 2002].

### 3.4. Polynomial Empirical Representation of the Transformation Model

Based on the model structure defined in Section 2, the relationship between the process inputs and the transformation outputs was represented using a polynomial empirical form, to express the observed trends compactly and provide a preliminary basis for future predictive modeling.

To improve the numerical balance of the regression coefficients, the variables were normalized as:

$$x = DR - 1.75 \tag{19}$$

$$\theta = \frac{T - 80}{20} \tag{20}$$

$$\mu = \frac{\tau - 4.0}{8.4} \tag{21}$$

where $x$ represents the draw-ratio increment within the main analysis range, $\theta$ is the normalized temperature with respect to 80 °C, and $\mu$ is the normalized effective moment response within the experimental range.

Considering the nonlinear increase in tenacity gain with draw ratio and the interaction between draw ratio and effective moment, the following empirical forms were used:

$$\hat{G}_\sigma = a_0 + a_1 x + a_2 x^2 + a_3 \theta + a_4 \mu + a_5 (x\mu) \tag{22}$$

$$\hat{R}_\varepsilon = b_0 + b_1 x + b_2 x^2 + b_3 \theta + b_4 \mu + b_5 (x\mu) \tag{23}$$

The coefficients were obtained from stable experimental data using a least-squares regression

approach. The same normalized input matrix was used for both transformation outputs, while separate coefficient vectors were calculated for $G_\sigma$ and $R_\varepsilon$. This allowed the same process variables to describe two different aspects of the mechanical transformation: tenacity gain and elongation retention.

The preliminary empirical fit for the tenacity gain ratio was:

$$\hat{G}_\sigma = 1.5745 + 1.1109\,x + 2.4861\,x^2 + 0.0263\,\theta + 0.8700\,\mu - 1.6762\,x\mu \quad (24)$$

For the elongation retention ratio:

$$\hat{R}_\varepsilon = 0.3079 - 0.4350\,x + 0.0203\,x^2 + 0.0066\,\theta - 0.4003\,\mu + 0.6280\,x\mu \quad (25)$$

The positive $x$ and $x^2$ coefficients in Eq. (24) indicate that $G_\sigma$ increases nonlinearly with draw ratio. In contrast, the negative $x$ coefficient in Eq. (25) reflects the rapid decrease of $R_\varepsilon$ with increasing draw ratio. These mathematical trends are consistent with the experimental findings presented in Figures 3–6 and with the general PET drawing literature.

The μ and xμ terms represent the contribution of the process-side mechanical response and should not be interpreted as independent physical causes; rather, they complement draw ratio by incorporating effective moment information into the empirical model, giving a compact mathematical representation of the observed transformation behavior.

This empirical model is a preliminary representation of the present, limited experimental range, which does not include repeated measurements or dense intermediate points; the coefficients should therefore not be interpreted as final prediction constants. For a physically stronger model, $\tau$ should be calibrated against measured yarn tension before and after the G2 godet, moving it from a relative indicator toward a physically grounded model input [Zhang, 2021; Du, 2025; Iwade, 2000].

## 4. CONCLUSION AND FUTURE WORK

This study investigated the drawing behavior of a 550 dtex / 144 filament standard POY yarn on the USLAN SpinLab system, using draw ratio, godet temperature, and an unloaded-moment-compensated effective motor moment ($\tau$) as inputs to a preliminary initial-to-final mechanical transformation model.

**Key Findings:**

– Draw ratio was the dominant variable: tenacity gain ($G_\sigma$) increased and elongation retention ( $R_\varepsilon$) decreased sharply as draw ratio increased, falling to about 0.06 at DR 2.25 and above.

– The dimensionless transformation ratios $G_\sigma$ and $R_\varepsilon$ provided a useful framework linking each drawn yarn's mechanical response directly to the initial POY properties, showing that high

tenacity should not be evaluated without also considering remaining elongation capacity and process stability.

– Temperature governed the processability window rather than mechanical properties directly: DR 2.50 was sustainable at 80–90 °C but could not be maintained at 25 °C or 100 °C.

– The effective motor moment $\tau$, used after unloaded-moment compensation, served as a useful process-side mechanical response indicator that complements — but does not replace — draw ratio and nominal process settings.

– The proposed polynomial empirical expressions offer a compact preliminary mathematical description of the observed transformation behavior, though the current coefficients should not yet be treated as final predictive constants given the limited data set.

**Future Work:**

– Expand the experimental data set with repeated trials at the same draw ratio and temperature levels to quantify measurement scatter and process variability.

– Test additional intermediate draw ratios (especially DR 2.25–2.50) and finer temperature intervals around 70–100 °C to better define the stable drawing window.

– Physically calibrate the effective motor moment by measuring yarn tension before and after the G2 godet, moving $\tau$ from a relative indicator toward a physically grounded model input.

– With a larger, calibrated data set, extend the framework using multivariable or ridge regression, Gaussian Process Regression, or artificial neural networks, incorporating additional variables such as final linear density, motor current, and measured yarn tension.

## REFERENCES

1. **Chavan, D. (2017)**. Enhancing tensile properties (yarn strength) of polyester filament

2. **Canoglu, S. (2009)**. Effect of first heater temperature variations on the polyester yarn properties of falsetwist texturing techniques. Fibres & Textiles in Eastern Europe.

3. **Deilamani, M.T., Rashidi, A., Yazdanshenas, M.E., Moghadam, M.B., & Eskandarnejad, S. (2017)**. Effect of major falsetwist texturing parameters on tensile properties and crystallinity of polyester microfilament yarn and optimized by RSM.

4. **Du, [Initials]., et al. (2025)**. Realtime yarn tensionrelated monitoring and its effect on crystallinity and mechanical properties in filament drawing processes.

5. **Haji, A., & Rahbar, R. S. (2013)**. Crystallinity and orientation development upon hot multistage drawing of PET multifilament yarn. The Journal of The Textile Institute. https://doi.org/10.1080/00405000.2012.717377 August 1921, 2026, Istanbul, Türkiye

6. **Hsiao, H. (1997)**. Mechanical behavior and heat transfer in polymer fiber meltspinning August 19-21, 2026, Istanbul, Türkiye and drawing processes.

7. **Iwade, S., et al. (2000)**. Noncontact tension measurement and process monitoring in polyester POY production.

8. **Kuo, C. F. J., et al. (2004)**. Using neural network theory to predict the properties of as spun fibers. Textile Research Journal, 74(9).

9. **Liu, Y., Yin, L., Zhao, H., Song, G., Tang, F. F., Wang, L., Shao, H., & Zhang, Y. (2015)**. Insights into process–structure–property relationships of poly(ethylene terephthalate) industrial yarns by synchrotron radiation WAXD and SAXS. Journal of Applied Polymer Science. https://doi.org/10.1002/app.42512

10. **Mukhopadhyay, A., Misra, A., & Dutta, B. (1990)**. Incremental drawing of polyethylene terephthalate partially oriented yarn (PETPOY). International Polymer Processing. https://doi.org/10.3139/217.900032

11. **Ohkoshi, Y., Watanabe, J., Okumura, W., Gotoh, Y., & Nagura, M. (2002)**. Catastrophic neckflow transition during laserheated drawing of poly(ethylene terephthalate) fiber. Seni Gakkaishi. https://doi.org/10.2115/FIBER.58.182

12. **Okumura, W., Yamaguchi, T., Ohkoshi, Y., Gotoh, Y., & Nagura, M. (2002)**. Direct measurement of fiber temperature in the continuous drawing process of PET fiber heated by $CO_2$ laser radiation. International Polymer Processing. https://doi.org/10.3139/217.1684

13. **Rudolf, A., & Geršak, J. (2012)**. The effect of drawing on PET filament sewing thread performance properties. Textile Research Journal. https://doi.org/10.1177/0040517511420761

14. **Rudolf, A., & Smole, M. S. (2008)**. Structure–properties relations of the drawn poly(ethylene terephthalate) filament sewing thread. Journal of Applied Polymer Science. https://doi.org/10.1002/app.25008

15. **Seguela, R. (2007)**. On the natural draw ratio of semicrystalline polymers: Review of the mechanical, physical and molecular aspects. Macromolecular Materials and Engineering. https://doi.org/10.1002/mame.200600389

16. **Xu, X. J. (2005)**. The research on the physical properties of polyester filament after drawing treatment. Journal of Zhejiang Institute of Science and Technology. August 1921, 2026, Istanbul, Türkiye

17. **Yildirim, Kenan & Cetin, Suna & Ulcay, Y.. (2015)**. A New Regression Based Model for Estimation of the Process Parameters Affect for Texturing of Polyethylene Terephthalate (PET) Yarn. International Journal of Materials, Mechanics and Manufacturing. 3. 174178. 10.7763/IJMMM.2015.V3.190.

18. **Yıldırım, K., Altun, Ş., & Ulcay, Y. (2009)**. Relationship between yarn properties and August 19-21, 2026, Istanbul, Türkiye process parameters in falsetwist textured yarn. Journal of Engineered Fibers and Fabrics. https://doi.org/10.1177/155892500900400205

19. **Yildirim, Kenan & Ogut, Hamdi & Ulcay, Y.. (2017)**. Comparing the Prediction Capabilities of Artificial Neural Network (ANN) and Nonlinear Regression Models in Pet Poy Yarn Characteristics and Optimization of Yarn Production Conditions. Journal of Engineered Fibers and Fabrics. 12. 716. 10.1177/155892501701200302.

20. **Zhang, Dongjian & Tan, Yuan & Ma, Qihua & Liao, He & Lu, Chenhui & Liu, Xiangyu & Fu, Yanan & Wang, Xiangyang & Han, Fuyi & Gan, Xuehui. (2021)**. Real-time tension estimation in the Spinning Process based on the natural frequencies extraction of the Polyester Filament Yarn. Measurement. 188. 110514. 10.1016/j.measurement.2021.110514.

# ONE-WAY FLUID-STRUCTURE INTERACTION (FSI) ANALYSIS OF A GFRP WIND TURBINE BLADE UNDER DIFFERENT WIND VELOCITIES

**Samet AKAR**, *samet.akar@cankaya.edu.tr* Çankaya University, 06930, Ankara, Türkiye

**Ferit SAİT**, *fsait@cankaya.edu.tr* Çankaya University, 06930, Ankara, Türkiye

**İclal Burcu ERCİYAS**, *c2594201@student.cankaya.edu.tr* Çankaya University, 06930, Ankara, Türkiye

## ABSTRACT

In this study, a one-way Fluid–Structure Interaction (FSI) analysis of a wind turbine blade manufactured from Glass Fiber Reinforced Polymer (GFRP) material was investigated. The analyses were performed in the ANSYS Workbench environment by the coupling of the Fluent and Static Structural modules. The blade structure was tested under five different wind speed conditions ranging from 8 m/s to 72 m/s. The effects of fluid-induced surface pressures on deformation, Von Mises stress, and elastic strain distributions on the structural behavior were examined. The analysis results showed that the blade structure operated safely up to a wind speed of 40 m/s, whereas at the extreme wind speed condition of 72 m/s, the stress exceeded the material tensile strength limit of 900 MPa, leading to structural damage.

**Keywords:** Wind Turbine Blade, Fluid-Structure Interaction (FSI), ANSYS, GFRP

## ÖZET

Bu çalışmada, cam elyaf takviyeli polimer (GFRP) malzemeden üretilmiş bir rüzgar türbini kanadının tek yönlü Akışkan-Yapı Etkileşimi (FSI) analizi incelenmiştir. Analizler, ANSYS-Workbench ortamında Fluent ve Static Structural modüllerinin bağlantısı ile gerçekleştirilmiştir. Kanat yapısı, 8m/s ile 72m/s hız değerleri arasında beş farklı rüzgar hız değeri altında test edilmiştir. Akışkan kaynaklı yüzey basınçlarının yapısal davranış üzerindeki deformasyon, Von-Mises gerilmesi ve elastik gerinim dağılımlarına etkileri incelenmiştir. Analizler sonucunda, kanat yapısının 40m/s hıza kadar güvenli çalıştığı, ekstrem koşul hızı olan 72m/s hızda malzemenin çekme dayanım sınırı olan 900 MPa değerini aştığı ve yapısal hasara yol açtığı gözlemlenmiştir.

**Anahtar Kelimeler:** Rüzgar Türbini Kanadı, Akışkan-Yapı Etkileşimi, ANSYS, GFRP

## 1. INTRODUCTION

The rapid depletion of fossil fuels and the increasing global environmental problems caused by greenhouse gas emissions are increasing. Along with this, the transition to sustainable and clean energy sources gained momentum. Among the various renewable energy technologies, wind energy stands out as one of the rapidly growing sectors. Over the past years, global wind energy capacity grown exponentially. This led the wind industry to design larger, more efficient and structurally more robust wind turbines that can operate in different and challenging environmental conditions [Deng et al., 2024].

The blade design of a wind turbine directly affects its efficiency and energy production. To maximize energy gain, the lengths of modern wind turbine blades significantly increased. This naturally increased their structural flexibility and the enormous aerodynamic loads that they experience [Wang et al., 2016]. Therefore, selecting the appropriate structural material is crucial. Glass Fiber Reinforced Polymer (GFRP) composites become a key material in blade production due to their exceptional strength-to-weight ratios, excellent fatigue resistance, low density, and superior resistance to environmental corrosion [Ou et al., 2016]. However, under extreme environmental events such as high-speed storms, these composite blades are subjected to large structural loads that push the material limits to their physical limits.

To accurately predict the structural behavior and safety limits of a wind turbine blade, an understanding of the interaction between the wind flow surrounding the blade and the rigid body is necessary. Traditionally, aerodynamic and structural assessments were performed separately, often leading to oversimplified results. Fluid-Structure Interaction (FSI) analysis matches the two systems by directly transferring the aerodynamic surface pressures obtained from Computational Fluid Dynamics (CFD) analysis to the Finite Element Analysis (FEA) structural model [Roul et al., 2020]. In the literature, some researchers have successfully used FSI techniques to analyze the structural responses of wind turbine blades, such as displacement and regional stress distributions, under different operating conditions [Deng et al., 2024; Roul et al., 2020].

In this study, a one-way FSI analysis of a GFRP wind turbine blade was investigated under five different wind speed scenarios, ranging from a normal operating speed of 8 m/s to an extreme storm condition of 72 m/s. In the analysis performed in the ANSYS Workbench environment, the steady-state aerodynamic flow fields were solved using the advanced Shear Stress Transport (SST) turbulence model in ANSYS Fluent. The obtained surface pressures were transferred to the ANSYS Static Structural module. The material properties of the GFRP composite blade were defined by the user in the ANSYS Workbench Engineering Data module in accordance with standard mechanical parameters [ANSYS, 2024]. The main objective of this study is to reveal the relationship between linear increases in wind speed and the parabolic rise in Von-Mises stresses, elastic strains, and total displacements. Furthermore, the structural safety factor (SF) was calculated against the maximum tensile strength of the material at 900 MPa. Thus, the critical wind speed limit values at which permanent damage and fractures would initiate in the blade were determined.

## 2. GEOMETRY AND MATERIAL PROPERTIES

In analysis studies, geometric model accuracy and material selection are of critical importance in order to obtain realistic and reliable results. In this study, the wind turbine blade geometry was modeled to represent industrial standards and aerodynamic profiles. The outer surface of the blade was designed in a form that allows the aerodynamic pressure loads obtained from the flow field to be transferred to the structural body in a uniform, accurate, and realistic manner. In addition, the geometry was prepared for the finite element mesh to ensure efficient load transfer and reliable numerical analysis results.

As the manufacturing material for the wind turbine blade structure, Glass Fiber Reinforced Polymer (GFRP) was selected because of its advantages in the wind energy industry, such as low weight, high corrosion resistance, and a high strength-to-weight ratio. Although GFRP composite structures naturally exhibit anisotropic behavior, in this study the material was modeled as linear elastic isotropic in order to maintain computational efficiency for the five different operating scenarios. The mechanical properties of the GFRP material used in the structural analysis and defined in the ANSYS Workbench Engineering Data module are presented in Table 1.

Table 1. Mechanical Properties of Glass Fiber Reinforced Polymer (GFRP)

| **Property** | **Value** | **Unit** |
|---|---|---|
| Density | 1900 | $kg/m^3$ |
| Young's Modulus | 35 | GPa |
| Poisson's Ratio | 0.28 | - |
| Ultimate Tensile Strength | 900 | MPa |

During the structural analysis, the tensile strength limit of 900 MPa given in Table 1 was considered as the critical strength limit. The maximum equivalent (Von Mises) stress values occurring on the blade at different wind speeds were compared with this limit. Based on these comparisons, the safe operating limits of the system and the onset of structural damage were determined.

## 3. NUMERICAL METHOD AND ANALYSIS MODEL

The multidisciplinary nature of wind turbine blade structures requires the integration of fluid mechanics and solid mechanics for analysis and evaluation. In this study, a one-way Fluid-Structure Interaction (FSI) analysis was performed in the ANSYS Workbench environment. The flow fields were solved using the ANSYS Fluent module, and the resulting aerodynamic surface pressures were coupled with the ANSYS Static Structural module. Within this framework, an efficient computational platform was established.

### 3.1 Fluid Flow (CFD) Domain and Setup

The fluid domain was modeled as standard atmospheric air with a density of 1.225 kg/m³. The flow simulation was configured as a steady-state flow analysis. The boundaries of the fluid domain were defined to comply with physical constraints and to be of appropriate dimensions for the analysis. The inlet boundary condition was defined as a uniform velocity inlet and was gradually modified for five different operating wind speed scenarios: 8 m/s, 15 m/s, 40 m/s, 60 m/s, and 72 m/s. The outlet boundary condition was defined as a pressure outlet with a gauge pressure of 0 Pa. To accurately represent complex flow behaviors such as high velocity variations and boundary layer separations occurring around the blade, the $k-\omega$ Shear Stress Transport (SST) turbulence model, a robust and reliable model, was used in the analysis solution phase.

### 3.2 Structural Analysis (FEA) Setup

The aerodynamic pressure distributions obtained from the fluid flow solutions were directly transferred to the structural model. For the material properties to be used in the mechanical analysis of the blade, isotropic glass-fiber-reinforced polymer (GFRP) material properties were added to the engineering data module. To realistically simulate the physical connection and the mounting conditions of the blade structure to the wind turbine, a fixed support boundary condition was defined on the blade root face. To investigate the effects of aerodynamic forces transferred from the fluid analysis on the structure, the system was solved linearly. As a result of this analysis, deformation fields, equivalent (von Mises) stresses, and elastic strains were mapped on the solid model.

### 3.3 Mesh Generation

The quality and density of the discretized finite element mesh significantly affect the computational accuracy of both the fluid flow field and the structural deformation. In this study, mesh generation for both fluid and structural fields was performed independently using the ANSYS Meshing module.

For the fluid field, a tetrahedral mesh structure was used to accommodate the complex external aerodynamic curvature of the wind turbine blade. An inflation layer mesh was applied to the blade wall regions to accurately capture the high-velocity gradients, shear stresses, and boundary layer separations around the aerodynamic airfoil profiles. This boundary layer enabled the $k-\omega$ SST turbulence model to operate within mathematically validated limits.

For the solid structural domain, a coherent mechanical mesh was created using higher-order solid elements to ensure high-accuracy mapping of the structural response. Unlike the fluid domain, a single element size was utilized throughout the entire blade structure to maintain structural homogeneity. This homogeneous mesh configuration ensured consistent resolution of aerodynamic pressure distributions transmitted by fluid analysis across the entire blade solid domain. To balance computational cost and convergence stability, a mesh independence study was conducted, and the overall mesh density was kept within mathematically validated limits.

## 4. RESULTS AND DISCUSSION

In this section, the aerodynamic and structural findings obtained from numerical analyses conducted under different wind speed conditions are evaluated as a whole and discussed in terms of blade performance and material strength. Initially, the results of the aerodynamic analysis, which examine the aerodynamic loads and the flow characteristics acting on the blade surface, are presented. Then, the structural responses of these aerodynamic loads on the blade structure and the comparison of these responses with theoretical limits are detailed.

### 4.1 Aerodynamic (CFD) Analysis Results

The numerical results obtained from the steady-state flow analysis for five different wind speed values are presented in Table 2. When the aerodynamic interactions are examined, it can be seen that the aerodynamic drag force and the maximum fluid pressure acting on the blade surface increase in a non-linear manner. In aerodynamic theory, the relationship between the fluid velocity and the dynamic pressure $P_{dyn}$ , it generates is given in Equation1 [Çengel and Cimbala, 2006]:

$$P_{dyn} = \frac{1}{2} \times \rho \times v^2 \quad (1)$$

In Equation 1, $\rho$ represents the fluid density ($\rho$ = 1.225 kg/m³), and $v$ represents the inlet wind speed (m/s). According to the equation, linear increases in wind speed are reflected in force and pressure values proportionally to the square of the speed. This results in a parabolic increase behavior.

When the values in the table are examined, the cases of 8 m/s and 72 m/s can be considered as examples. At a wind speed of 8 m/s, a fluid pressure of 48.25 Pa and an aerodynamic force of -4.35 N were calculated. However, under the extreme condition of 72 m/s wind speed (where the velocity increases by approximately 9 times), the maximum local fluid pressure increases significantly, reaching a value of 3261.00 Pa, in accordance with the square relationship in Equation 1. At the same time, an aerodynamic force of -353.09 N is generated. This dramatic increase in pressure and force is directly related to the rise in maximum local flow velocity, which represents highly accelerated flow paths over the aerodynamic profiles of the blade tip regions. The maximum local flow velocity increases from 11.38 m/s to 110.00 m/s.

Table 2. CFD Results (Force, Pressure and Maximum Local Velocity) Table

| Inlet Wind Velocity | Force | Maximum Fluid Pressure | Maximum Local Flow Velocity |
|---|---|---|---|
| **8 m/s** | -4.35 N | 48.25 Pa | 11.38 m/s |
| **15 m/s** | -15.30 N | 141.50 Pa | 22.67 m/s |
| **40 m/s** | -108.89 N | 1006.00 Pa | 61.47 m/s |
| **60 m/s** | -245.14 N | 2265.00 Pa | 92.58 m/s |
| **72 m/s** | -353.09 N | 3261.00 Pa | 110.00 m/s |

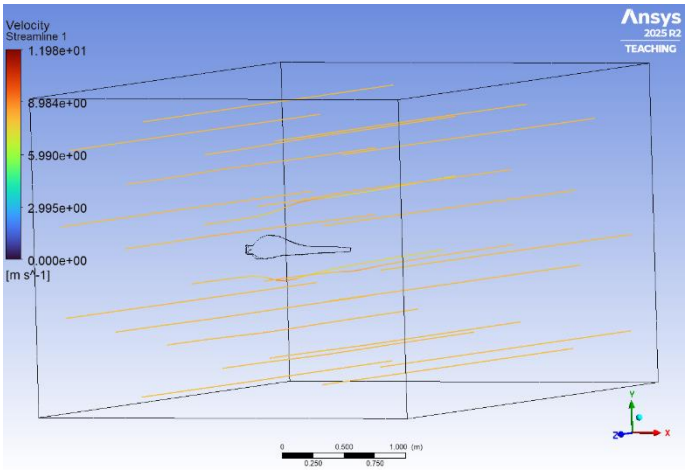



Figure 1. Velocity Streamline of 8m/s

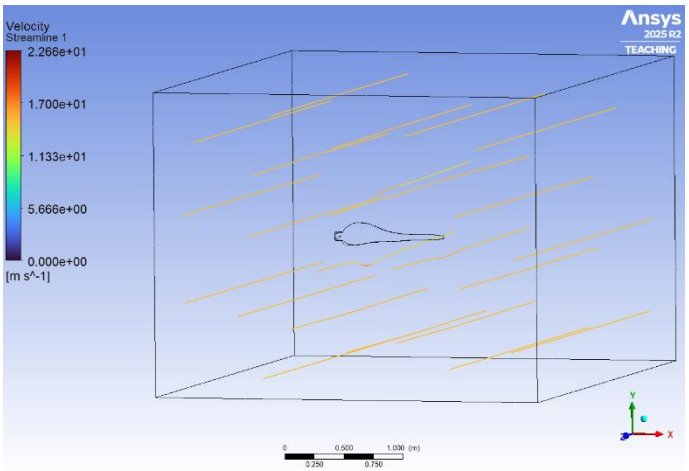



Figure 2. Velocity Streamline of 15m/s

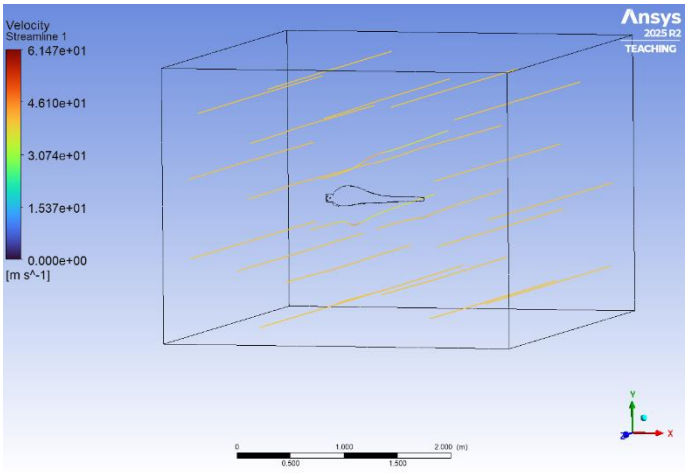



Figure 3. Velocity Streamline of 40m/s

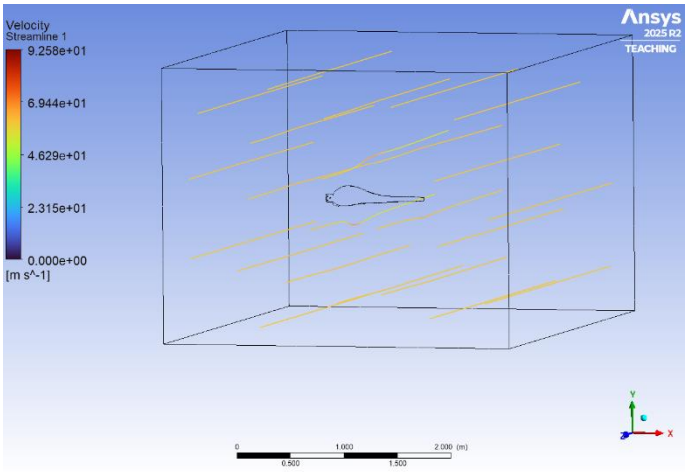



Figure 4. Velocity Streamline of 60m/s

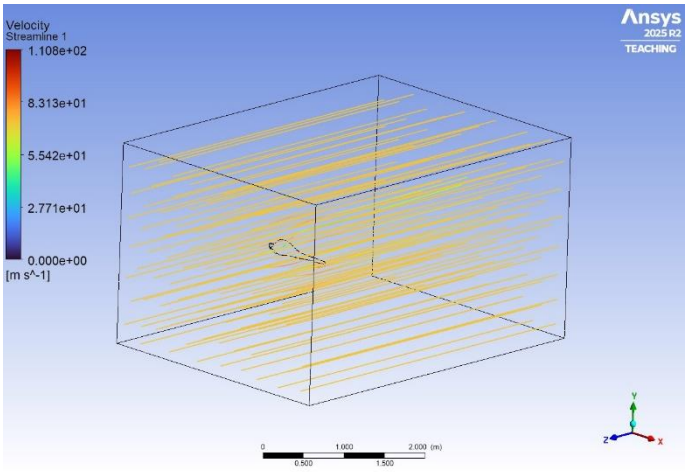



Figure 5. Velocity Streamline of 72m/s

### 4.2 Static Structural Analysis Results and Structural Safety

The structural response of the wind turbine blade under the aerodynamic pressure loads transferred from the flow analysis was evaluated in the Static Structural module. The numerical results obtained are presented in Table 3. The equivalent Von-Mises stress criterion was used for the structural analysis of the multiaxial loading on the blade structure. Accordingly, the equivalent Von-Mises stress, which reduces the three-dimensional stress components to a single scalar value, was calculated using Equation 2 [Budyns and Nisbett, 2008]:

$$\sigma_{vm} = \sqrt{\frac{1}{2} \times [(\sigma_1 - \sigma_2)^2 + (\sigma_2 - \sigma_3)^2 + (\sigma_3 - \sigma_1)^2]} \quad (2)$$

In Equation 2, $\sigma_1$, $\sigma_2$ and $\sigma_3$ represent the principal stresses acting on the solid body. The strength and damage conditions of the blade structure under different operating conditions were determined using the Structural Safety Factor (SF) calculated with Equation3 [Budyns and Nisbett, 2008].

$$SF = \frac{\sigma_{uts}}{\sigma_{vm}} \quad (3)$$

In Equation 3, $\sigma_{uts}$ represents the maximum tensile strength limit (900 MPa) of the GFRP blade structure material, while $\sigma_{vm}$ represents the maximum equivalent Von-Mises stress obtained from the analysis.

The results show that the blade structure maintains adequate strength and stability and operates within safe limits up to a wind speed of 40 m/s. At wind speeds of 8 m/s and 15 m/s, the safety factor is relatively high (SF > 10). At 40 m/s, the safety factor decreases to 3.22. However, the blade is still able to operate safely under all three wind speed conditions.

In contrast, when the wind speed exceeded 40 m/s, a failure point in the structural integrity of the blade was observed. At a wind speed of 60 m/s, the equivalent stress increased to 629.60 MPa. This increase reduced the structural safety factor to 1.43, bringing it close to the yield stage. Under the extreme wind speed condition of 72 m/s, the equivalent stress reached a maximum value of 906.00 MPa, exceeding the material's tensile strength limit $\sigma_{uts}$ of 900 MPa. As a result, the structural safety factor decreased to an unacceptable value of 0.99 (SF < 1.0). This indicates irreversible structural damage and material failure in the regions of the blade subjected to high stress concentrations.

Table 3. Static Structural Analysis Results & Structural Safety Table

| Inlet Wind Velocity | Maximum Total Deformation | Maximum Equivalent Stress | Structural Safety (SF) |
|---|---|---|---|
| **8 m/s** | 21.317 mm | 11.18 MPa | Safe (SF > 10) |
| **15 m/s** | 74.981 mm | 39.32 MPa | Safe (SF > 10) |
| **40 m/s** | 533.00 mm | 279.00 MPa | Safe (SF=3.22) |
| **60 m/s** | 1200.00 mm | 629.60 MPa | Yield (SF = 1.43) |
| **72 m/s** | 1727.00 mm | 906.00 MPa | Failure! (SF = 0.99) |

## 5. CONCLUSIONS

In this study, the aerodynamic and structural behavior of a wind turbine blade manufactured from Glass Fiber Reinforced Polymer (GFRP) under five different wind speeds ranging from 8 m/s to 72 m/s was successfully investigated using a one-way Fluid–Structure Interaction (FSI) methodology. The main findings obtained from the numerical analyses are summarized below:

- It was confirmed that linear increases in the inlet wind speed result in parabolic increases in the maximum local fluid pressure and drag force on the blade surface, in accordance with aerodynamic theory ($P_{dyn} = \frac{1}{2} \times \rho \times v^2$ ).
- The blade exhibited high structural stability under normal operating conditions up to a wind speed of 40 m/s. At this wind speed, the safety factor was calculated as 3.22, indicating that the structure remained within the safe operating region.
- When the wind speed reached 60 m/s, a critical threshold was exceeded in the blade structure. Under this condition, the equivalent Von-Mises stress increased to 629.60 MPa, while the safety factor decreased to 1.43, bringing the material close to its failure limit.
- Under the extreme wind speed condition of 72 m/s, the maximum equivalent stress on the blade reached 906.00 MPa, exceeding the maximum tensile strength limit of the GFRP material (900 MPa). As a result, the safety factor decreased to an unacceptable value of 0.99.
- The obtained results clearly demonstrate that the designed blade structure would experience irreversible structural damage and material failure in high-stress regions under extreme weather conditions such as 72 m/s wind speed.

## 6. REFERENCES

**Deng, Z., Xiao, Q., Huang, Yang., Yang, L. and Liu, Y. (2024),** "A general FSI framework for an effective stress analysis on composite wind turbine blades", Ocean Engineering, Vol. 291, No. 116412, pp 1-20.

**Wang, L., Quant, R. and Kolios, A. (2016),** "Fluid structure interaction modelling of horizontal-axis wind turbine blades based on CFD and FEA", Journal of Wind Engineering and Industrial Aerodynamics, Vol. 158, No. 11-25, pp 11-25.

**Ou, Y., Zhu, D., Zhang, H., Huang, L., Yao, Y., Li, G. and Mobasher, B. (2016),** "Mechanical Characterization of the Tensile Properties of Glass Fiber and Its Reinforced Polymer (GFRP) Composite under Varying Strain Rates and Temperatures", Polymers, Vol. 8, No. 196, pp 1-16.

**Roul, R. and Kumar, A. (2020),** "Fluid-Structure Interaction of Wind Turbine Blade Using Four Different Materials: Numerical Investigation", Symmetry, Vol. 12, No. 1467, pp 1-20.

**ANSYS, (2024),** ANSYS Workbench Engineering Data User's Guide, ANSYS Inc., Canonsburg,Pennsylvania.

**Çengel,Y.A. and Cimbala, J.M., (2006),** "Fluid Mechanics Fundamentals and Applications", McGraw-Hill, 1st edition,New York, p. 189.

**Budyns,R.G. and Nisbett, J.K.,(2008),** "Shigley's Mechanical Engineering Design", McGraw-Hill, 8th edition, New York, p. 214.

# Development of Model Predictive Controlled 12-DoF Bipedal Robot

**Ozan ECEVİT** , oecevit@etu.edu.tr TOBB ETU , 06530 , Ankara, Türkiye

**Giray Cevher ESER** , geser@etu.edu.tr TOBB ETU , 06530 , Ankara, Türkiye

**Bahram LOTFİ ,** **blotfi@etu.edu.tr** TOBB ETU , 06530, Ankara Türkiye

**Hakkı Özgür ÜNVER**, hunver@etu.edu.tr TOBB ETU , 06530 , Ankara, Türkiye

## ABSTRACT

State-of-the-art push recovery algorithms for bipedal robots frequently demand prohibitively expensive and computationally intensive hardware. To address these constraints, this study introduces a two-phase control architecture tailored for low-budget bipedal systems. Grounded in the Linear Inverted Pendulum Model (LIPM), the framework generates nominal walking trajectories offline by employing Zero-Moment Point (ZMP) preview control, a derivative of Model Predictive Control (MPC). For the preservation of balance during walking, real-time push recovery is facilitated by an online Linear Quadratic Regulator (LQR). This approach validates that stability against external perturbations can be effectively achieved utilizing resource-constrained, low-cost microcontrollers.

**Keywords:** Bipedal Robotics, Push Recovery, ZMP Preview Control, Low-Budget Robotic Platforms.

## 1. INTRODUCTION

The control of bipedal robots remains one of the most challenging endeavors in robotics due to their high degrees of freedom and inherently unstable dynamics. To maintain stable walking, researchers have traditionally utilized the Zero-Moment Point (ZMP) criterion [Vukobratovic, 2004] and the Linear Inverted Pendulum Model (LIPM) to simplify complex multibody dynamics into a manageable linear model [Kajita, 2014]. While these fundamental methods provide a robust foundation for nominal gait generation, maintaining stability under external disturbances—commonly referred to as push recovery—requires advanced control strategies capable of reacting to instantaneous deviations.

In recent years, Model Predictive Control (MPC) [Wieber, 2006] has been widely utilized as a successful strategy for dynamic walking and push recovery by optimizing future states over a receding time horizon. However, the continuous real-time execution of MPC requires a massive computational load, necessitating heavy and expensive onboard computers. Such demands impose a severe limitation on low-budget bipedal platforms designed around edge computing devices. Because entry-level microcontrollers, such as the Teensy 4.1, are incapable of solving complex optimization matrices in real time, an alternative approach is required. To overcome these hardware limitations, this paper utilizes a ZMP-based preview control [Kiyotsugu Takaba, 2003] formulation to generate walking trajectories offline. These trajectories are subsequently stored and deployed directly onto the microcontroller.

On the hardware level, an online Linear Quadratic Regulator (LQR) is implemented to maintain dynamic balance while the robot executes the pre-computed walking trajectory. When an external impact occurs, resulting in a physical deviation from the reference path, an Inertial Measurement Unit (IMU) is utilized to continuously record the robot's real-time body acceleration and angular velocity to precisely quantify the disturbance. Instantaneous deviations in the Center of Mass (CoM) position and velocity are then computed based on these sensor readings. To minimize this error and restabilize the system, an offline-computed optimal feedback gain matrix derived from the LQR formulation is multiplied by the state error. This computationally efficient operation allows the microcontroller to swiftly generate the corrective control inputs necessary for robust push recovery.

## 2. MODELLING

Figure 1 illustrates the hardware topology and kinematic chain of the 12-DoF bipedal platform. The block diagram on the left details the parent-child hierarchy from the floating base (torso) to the end-effectors (feet), while the schematic layout on the right shows the physical placement and color-coded clustering of the joints. This bipedal robot is designed with a total of 12 degrees of freedom (DoFs), allocating 6 DoFs per leg to ensure full spatial mobility and stepping ability. The kinematic chain from the hip to the foot is defined in the following sequence:

$$Hip\ Yaw \rightarrow Hip\ Roll \rightarrow Hip\ Pitch \rightarrow Knee\ Pitch \rightarrow Ankle\ Pitch \rightarrow Ankle\ Roll.$$

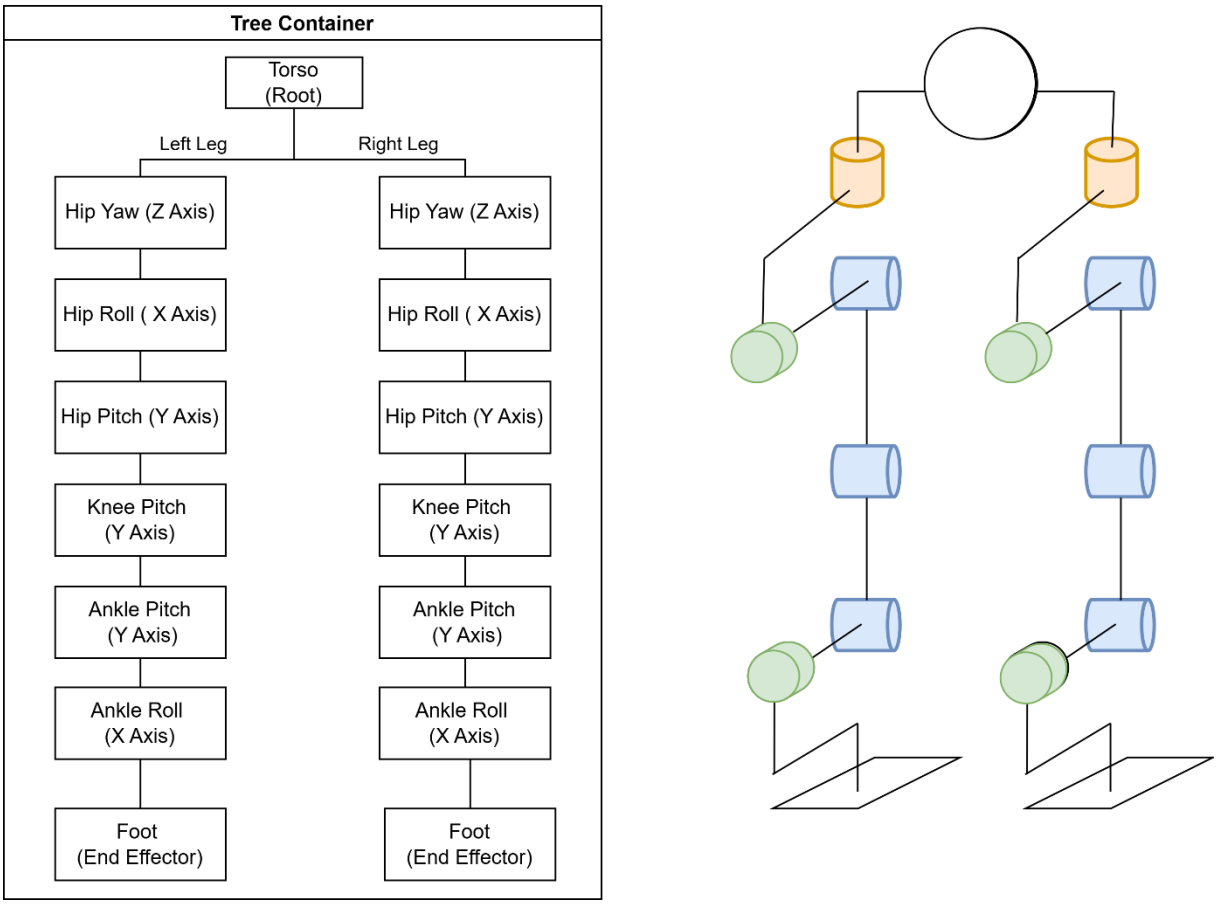



*Figure 1: Kinematic Tree*

The physical prototype incorporates an offset kinematics design. Stacking actuators directly upon each other may lead physical collisions and limits the range of motion. To avoid this, consecutive motors are structurally separated by using custom designed brackets. This configuration could convert decoupling kinematic since motor rotational axes crossing one imaginary point [Sun, 2011]. This mechanical reality is explicitly mapped into the Denavit-Hartenberg (D-H) parameters and the MuJoCo simulation environment to ensure minimize “Sim to Real” gap during inverse kinematics (IK) calculations [Kawaharazuka,2025]. Moreover specific Z offset is preserved between the ankle roll actuator and the flat foot to modelling the natural human ankle height, ensuring realistic torque distribution on the ground contact points.

Following the low cost architecture aim of this study, ST 3025 serial bus servo motors are placed across all joints. In bipedal locomotion, specially during Y-axis push recovery and squatting motions, the highest torque loads occur in the sagittal plane. Consequently, the structural integrity around the Hip Pitch and Knee Pitch joints is maximized. The physical links connecting the actuators are manufactured using CNC machined aluminum to optimize the strength to weight ratio. The leg geometry is symmetrically designed with a thigh length of 0.20 m and a shank length of 0.20 m. During nominal walking, the robot is constrained to keep its Center of Mass (CoM) height constant at 0.32 m. As a result, the low-level microcontroller can rapidly execute Capture Point step reflexes without exceeding the torque limits of the entry-level actuators.

## 3. METHODOLOGY

### 3.1 System Overview

The proposed control architecture is structured into two hierarchical layers to satisfy the real-time constraints imposed by low-cost embedded hardware. The upper layer performs all computationally intensive tasks offline: given a desired footstep sequence, the LIPM-based preview controller generates a Center of Mass (CoM) trajectory that satisfies ZMP stability constraints over a finite preview horizon. The corresponding joint-space trajectories are then computed via analytical Inverse Kinematics (IK) and stored as tables in the microcontroller’s memory to deployment.

The lower layer operates entirely online during locomotion. An MPU6050 Inertial Measurement Unit (IMU) continuously monitors the robot's body orientation and angular velocity. A complementary filter fuses these measurements to estimate the instantaneous CoM state deviation from the nominal trajectory. A pre-computed LQR feedback gain matrix then maps this state error to corrective joint commands, which are superimposed onto the nominal trajectory commands. Since the online computation reduces to a single matrix-vector multiplication, the architecture is fully compatible with the microcontroller operating at 600 MHz. Proposed system presented as overall block diagram [Fig. 2].

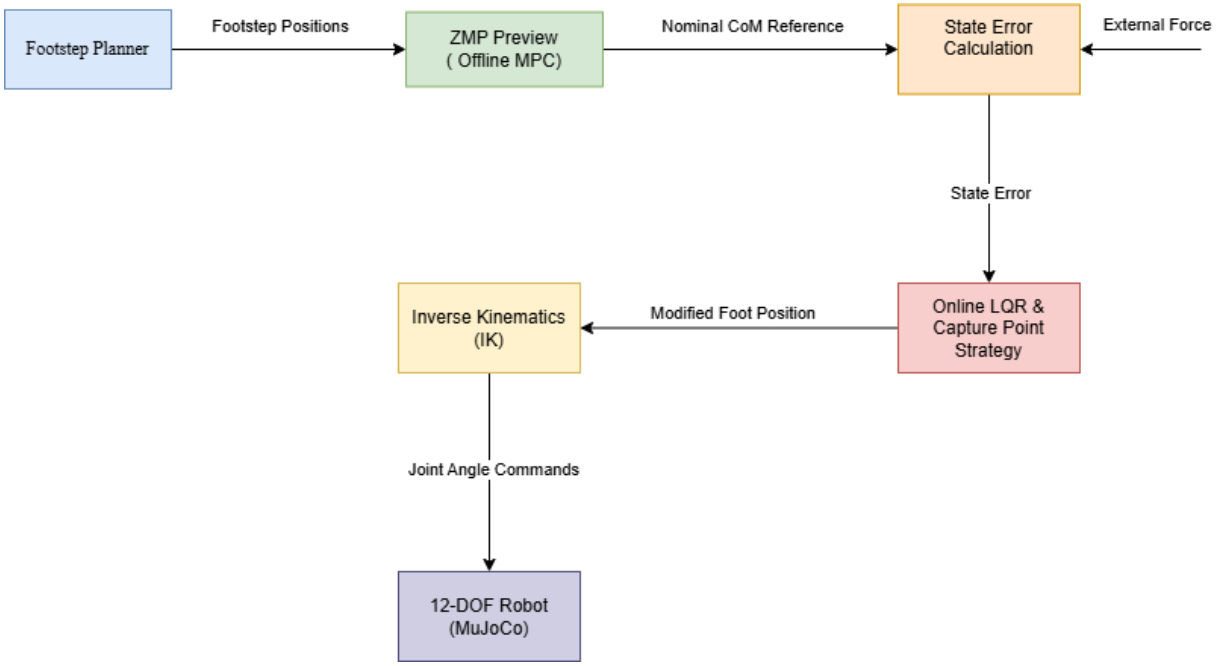



*Figure 2: Overall Control Block Diagram*

### 3.2 Linear Inverted Pendulum Model

The bipedal robot is modeled as a Linear Inverted Pendulum (LIP), in which the total robot mass m is lumped at a single CoM point constrained to move at a constant height ($z_c$) above the ground plane. Neglecting the angular momentum about the CoM, the equation of motion in the sagittal plane is derived from Newton's second law applied at the ZMP:

$$\ddot{x} = \frac{g}{z_c}(x - p_x) \qquad (1)$$

where x is the horizontal CoM position,$p_x$is the ZMP position, and g = 9.81 m/s² is gravitational acceleration. An identical formulation holds for the frontal plane with CoM position y and ZMP position $p_y$The ZMP is defined as the point on the ground plane where the net ground reaction moment about the horizontal axes is zero. For a statically stable configuration, the ZMP must remain within the support polygon at all times [Kajita, 2003].

The key advantage of the LIPM is simplifying complex nonlinear equations into manageable linear forms. Linear equation require less computation load on application of optimal control theory. The constant height constraint $z_c$ is maintained by coordinated ankle and knee joint actuation throughout the gait cycle.

### 3.3 Discrete-Time State-Space Formulation

For digital implementation, equation (1) is discretized with a sampling period T using a zero-order hold. Defining the state vector as:

$$\mathbf{x}_k = \begin{bmatrix} x_k \\ \dot{x}_k \\ \ddot{x}_k \end{bmatrix} \tag{2}$$

and selecting the CoM jerk $u_k$= $x_k$ as the control input, the discrete-time state-space representation becomes:

$$\mathbf{x}_{k+1} = \mathbf{A}\mathbf{x}_k + \mathbf{B}u_k \tag{3}$$

$$p_k = \mathbf{C}\mathbf{x}_k \tag{4}$$

where the system matrices are:

$$\mathbf{A} = \begin{bmatrix} 1 & T & \frac{T^2}{2} \\ 0 & 1 & T \\ 0 & 0 & 1 \end{bmatrix}, \mathbf{B} = \begin{bmatrix} \frac{T^3}{6} \\ \frac{T^2}{2} \\ T \end{bmatrix}, \mathbf{C} = \begin{bmatrix} 1 & 0 & -\frac{z_c}{g} \end{bmatrix} \tag{5}$$

The output represents the predicted ZMP position, which must track the desired ZMP reference throughout the motion.

### 3.4 Offline Trajectory Generation via ZMP Preview Control

The nominal CoM trajectory is generated using the preview control method of Kajita et al. [Kajita, 2003]. The method is formulated as a receding-horizon optimal control problem that minimizes the following quadratic cost function over a preview window of N steps:

$$J = \sum_{k=0}^{\infty}\left[Q_e\tilde{p}_k^2 + \mathbf{x}_k^T\mathbf{Q}_x\mathbf{x}_k + Ru_k^2\right] \quad (6)$$

where $\tilde{p}_k = p_k - p_{ref,k}$ is the ZMP tracking error $Q_e$ is the ZMP error weight $Q_x$ is the state weight matrix and R is the control effort weight [Kajita, 2003].

To incorporate preview information, an augmented error system is constructed by introducing the integrator state:

$$e_{k+1} = e_k + \mathbf{CA}\mathbf{x}_k + \mathbf{CB}u_k - \Delta p_{ref,k+1} \quad (7)$$

The augmented state vector $\tilde{\mathbf{x}}_k = [e_k, \Delta\mathbf{x}_k^T]^T$ leads to the augmented system:

$$\tilde{\mathbf{x}}_{k+1} = \widetilde{\mathbf{A}}\tilde{\mathbf{x}}_k + \widetilde{\mathbf{B}}\Delta u_k - \widetilde{\mathbf{G}}\Delta p_{ref,k+1} \quad (8)$$

The optimal control law that minimizes equation (6) is then:

$$\Delta u_k = -K_e e_k - \mathbf{K}_x\Delta\mathbf{x}_k + \sum_{j=0}^{N-1} f_j\,\Delta p_{ref,k+1+j} \quad (9)$$

where $K_e$ and $K_x$ are the optimal feedback gains obtained by solving the discrete-time Algebraic Riccati Equation (DARE) [Kayatama,1995] , and $f_j$ are the preview gains that weight future ZMP references over the horizon N. The complete gain sequences are computed once offline. This anticipatory structure allows the CoM to smoothly shift in advance of each footstep, producing natural and dynamically consistent gait trajectories. The resulting CoM position, velocity, and ZMP sequences are stored as discrete arrays in the microcontroller memory.

### 3.5 Inverse Kinematics and Joint Trajectory Generation

The offline-computed CoM trajectories are converted into the joint-space using an analytical geometric solver. The bipedal platform has 6 degrees of freedom per leg (hip roll, hip pitch, hip yaw, knee pitch, ankle pitch, ankle roll), System has 12-DOF total.

Given the planned CoM position and the according to foot positions from the footstep planner, the relative position of each foot with respect to the torso is computed. The knee joint angle $\theta_{knee}$ is obtained using the law of cosines applied to the upper and lower leg link lengths $L_1$ and $L_2$ :

$$\theta_{knee} = \pi - \cos^{-1}\left(\frac{L_1^2+L_2^2-d^2}{2L_1L_2}\right) \quad (10)$$

where d is the Euclidean distance from hip to ankle. The remaining hip and ankle angles are resolved using atan2-based geometric decomposition in the sagittal and frontal planes [Sun,2011]. The resulting joint angle sequences $\theta_k$ for all 12 joints are pre-computed, and stored on the microcontroller as tables indexed by gait phase.

### 3.6 Online Push Recovery via LQR

During gait cycle external disturbances (force impact) leads the actual CoM state to deviate from the offline trajectory. The state error vector is defined as:

$$\mathbf{e}_k = \mathbf{x}_{actual,k} - \mathbf{x}_{nominal,k} = \begin{bmatrix}\Delta x_k \\ \Delta \dot{x}_k\end{bmatrix} \quad (11)$$

An LQR controller is designed for the reduced second-order LIPM model around the nominal trajectory. The optimal gain matrix K is obtained by solving the DARE:

$$\mathbf{P} = \mathbf{A}^T\mathbf{P}\mathbf{A} - \mathbf{A}^T\mathbf{P}\mathbf{B}(\mathbf{B}^T\mathbf{P}\mathbf{B} + R)^{-1}\mathbf{B}^T\mathbf{P}\mathbf{A} + \mathbf{Q} \quad (12)$$

$$\mathbf{K} = (R + \mathbf{B}^T\mathbf{P}\mathbf{B})^{-1}\mathbf{B}^T\mathbf{P}\mathbf{A} \quad (13)$$

where Q and R are the state and input weighting matrices chosen to balance recovery speed against joint effort. The resulting weight matrices used in this study are:

$$\mathbf{Q} = \begin{bmatrix}q_1 & 0 \\ 0 & q_2\end{bmatrix}, R = r \quad (14)$$

The online corrective input is then computed as:

$$u_{corr,k} = -\mathrm{K}e_k \tag{15}$$

This corrective jerk command is integrated nominal joint commands retrieved from the lookup table. Since the operation in equation (15) is a $1 \times 2$ matrix-vector multiplication, the computational cost is negligible, enabling control loop execution at 500 Hz on the microcontroller.

### 3.7 State Estimation via Complementary Filter

The CoM state error in equation (11) is not directly measurable. It must be estimated by reading IMU data. The MPU6050 provides raw 3 axis accelerometer (a) and gyroscope (ω) measurements at 1 kHz. A discrete time complementary filter is implemented to fuse both signals and estimate the tilt angle θ:

$$\hat{\theta}_k = \alpha\left(\hat{\theta}_{k-1} + \omega_k T\right) + (1-\alpha)\theta_{acc,k} \tag{16}$$

where $\theta_{acc_k}$= atan2($a_y$, $a_z$) is the accelerometer derived tilt estimate. T is the sampling time period, and α ∈ (0,1) is the filter coefficient which is determines frequency. The angular velocity estimated by gyroscope after compensation. The CoM position and velocity deviations are then approximated from the tilt angle and angular velocity through the LIPM kinematic relationship:

$$\Delta x \approx z_c \cdot \hat{\theta}, \Delta\dot{x} \approx z_c \cdot \hat{\omega} \tag{17}$$

These estimates form the state error vector fed into the LQR controller at each control cycle.

### 3.8 Hardware Implementation

Our architecture is deployed on a custom built bipedal platform based on the Limo chassis, actuated by 12 servo motors. All onboard computation is performed by a microcontroller (ARM Cortex-M7, 600 MHz, 1 MB RAM). The communication between the microcontroller and servos is handled via a serial PWM interface at 50 Hz. The IMU data reading and complementary filter run at 500 Hz, while the LQR correction loop operates at the same rate. On the parameter table key hardware and software parameters of the platform demonstrated in Table 1 .

| Parameter Description | Symbol | Value | Unit |
|---|---|---|---|
| Total Degrees of Freedom | $DoF$ | 12 | - |
| Nominal Center of Mass (CoM) Height | $z_c$ | 0.32 | m |
| Thigh Link Length | $A_{\{leg\}}$ | 0.20 | m |
| Shank Link Length | $B_{\{leg\}}$ | 0.20 | m |
| Hip Lateral Offset | $D_{\{right\}}/D_{\{left\}}$ | 0.05 | m |
| Step Length (Forward) | $d_x$ | 0.08 | m |
| Foot Step Height | $H_{step}$ | 0.04 | m |
| Step Duration | $T_{step}$ | 0.55 | s |
| MPC Sampling Time Period | $\Delta t_{mpc}$ | 0.01 | s |
| ZMP Preview Window Horizon | $N_{preview}$ | 400 | steps |
| Applied External Disturbance (Torso Push) | $F_{push}$ | 30.0 | N |
| Disturbance Duration | $\Delta t_{push}$ | 0.10 | s |

*Table 1. Hardware & Software Parameter Table*

## 4 Electromechanical System Architecture

### 4.1 Mechanical Structure

The developed platform is a 12-DoF bipedal robot consisting of two identical 6-DoF legs. Each leg includes Hip Yaw, Hip Roll, Hip Pitch, Knee Pitch, Ankle Pitch, and Ankle Roll joints. The foot geometry defines the support polygon used during single- and double-support phases and provides the physical basis for ZMP-based locomotion. The structural components are designed to provide sufficient rigidity while maintaining low overall mass, reducing actuator loading and improving dynamic performance.

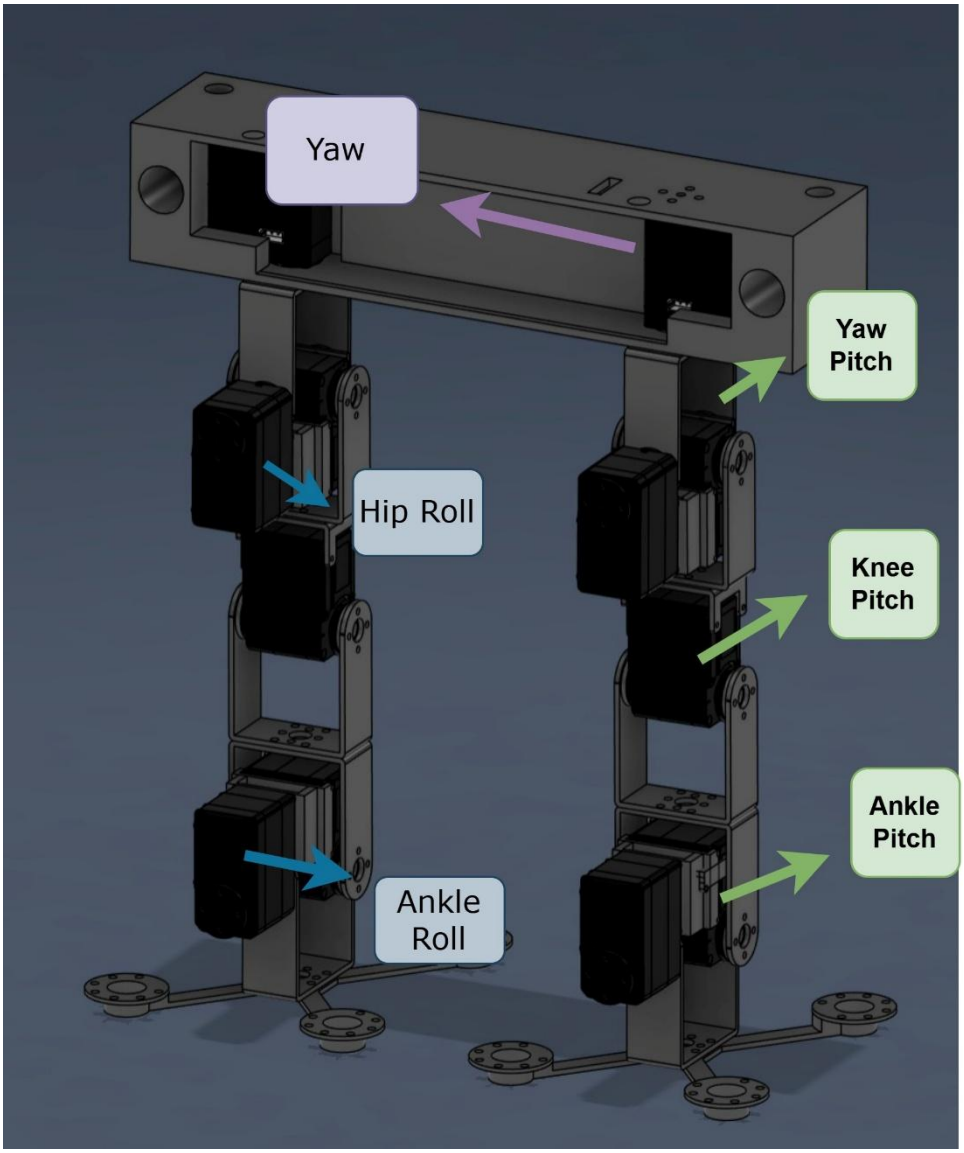



*Figure 3 : The physical layout and kinematic chain hierarchy of the leg assembly, demonstrating the sequence of the Yaw, Roll, and Pitch joints from the pelvis to the foot*

The proposed bipedal robot features a 12-DOF lower-body structure, with 6 DOFs allocated to each leg to ensure full spatial mobility. As illustrated in Figure 3, the kinematic chain of each leg is designed hierarchically from the pelvis (base) to the foot (end-effector) in the following sequence: Hip Yaw, Hip Roll, Hip Pitch, Knee Pitch, Ankle Pitch, and Ankle Roll.

Specifically, the Hip Yaw joint connects the torso to the leg assembly, allowing rotational movement around the vertical Z-axis. This is immediately followed by the Hip Roll (X-axis) and Hip Pitch (Y-axis) joints. The knee acts as a single-axis hinge joint driven by the Knee Pitch motor. Finally, the ankle joint combines an Ankle Pitch and an Ankle Roll motor, which is crucial for maintaining maximum foot contact with the ground and regulating the Zero-Moment Point (ZMP) during lateral disturbances.

### 4.2 Actuation System

All joints are actuated by serial bus servomotors controlled directly by microcontroller through a UART communication interface. Higher-torque actuators are assigned to the Knee Pitch and Hip Pitch joints, where the largest gravitational and dynamic loads occur during locomotion. The remaining joints utilize standard-torque servos sufficient for balance control and foot placement.

Each actuator provides integrated position feedback through an internal magnetic encoder, enabling CL (closed-loop) position control at the servo level. The use of serial bus communication reduces wiring complexity and allows simultaneously transmission of joint commands during gait execution.

### 4.3 Sensing and State Estimation Hardware

Robot state estimation is performed using an MPU6050 inertial measurement unit mounted near the torso region. The sensor provides three-axis accelerometer and gyroscope measurements that are sampled at high frequency by the microcontroller.

A complementary filter combines the short-term accuracy of gyroscope measurements with the long-term stability of accelerometer measurements to estimate body orientation. These orientation estimates are subsequently used to approximate the CoM state deviations required by the LQR push-recovery controller.

To monitor foot-ground interaction, force-sensitive resistor (FSR) sensors are embedded within both feet. The sensor measurements are used to estimate the center of pressure (CoP) and to experimentally verify the ZMP behavior predicted by the controller. This information is primarily utilized for system evaluation and stability analysis.

### 4.4 Embedded Control Hardware

All real-time computations are executed on a microcontroller featuring a 600 MHz ARM Cortex-M7 processor. The nominal walking trajectories generated offline by the preview controller are stored in onboard memory as lookup tables and retrieved during locomotion according to the gait phase.

The online control layer executes complementary filter, state estimation, and LQR feedback calculations. Since the push-recovery algorithm requires only matrix-vector operations using pre-computed gains, the computational demand remains well within the processing capability of the embedded platform.

### 4.5 Power Distribution System

The robot is powered by a rechargeable 3-cell lithium-polymer battery pack. Separate power rails are employed for the actuators and low-voltage control electronics to reduce the influence of motor-induced electrical noise on sensor measurements and microcontroller operations, as illustrated in the power distribution network layout in Figure 4.

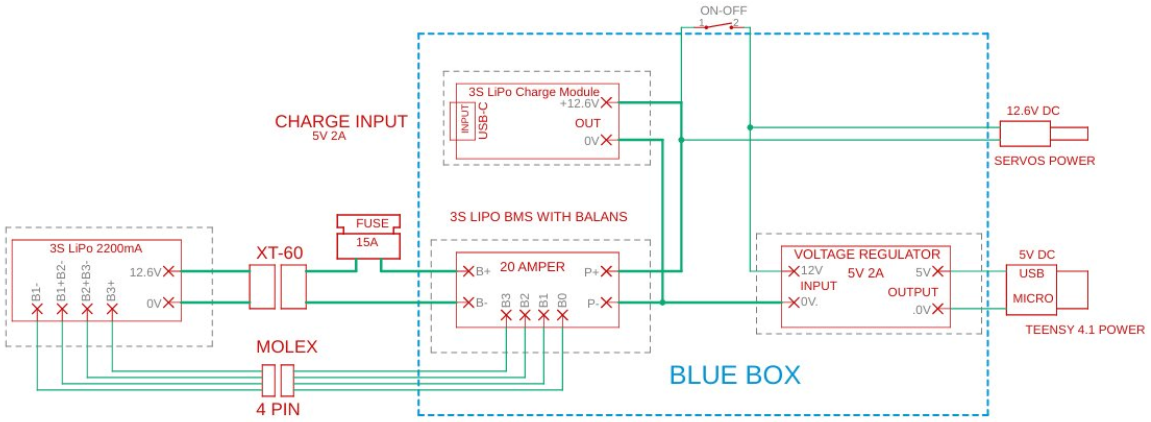



*Figure 4: Power Distribution Network: 3S LiPo battery, BMS, charge module, voltage regulator, and servo power bus.*

A voltage regulation stage supplies the required logic voltage for the microcontroller and sensing hardware, while the actuator bus is powered directly from the battery source [Fig 4]. Protection circuitry is incorporated to prevent over-current, over-discharge, and short-circuit conditions during operation

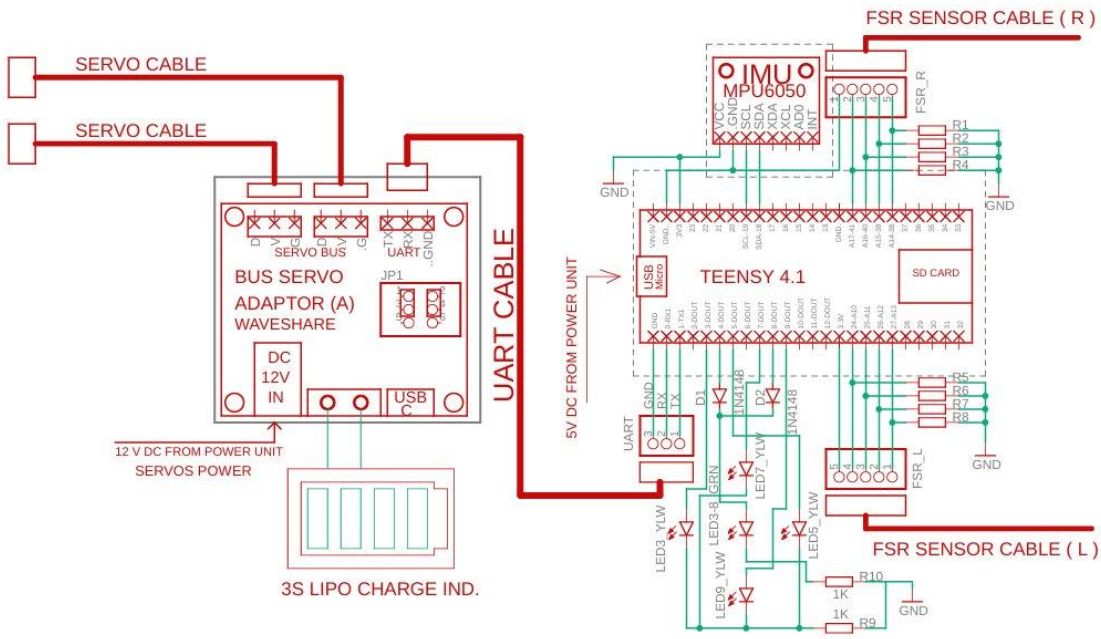



*Figure 5: Control Electronics Schematic: Teensy 4.1, MPU-6050 IMU, Bus Servo Adaptor (Waveshare), FSR sensor arrays, and UART communication interface*

## 5. SIMULATION RESULTS

The performance of the proposed low-cost control architecture was tested using a 12-DOF bipedal robot model in the MuJoCo physics engine. To test the stability of the algorithm, two different scenarios were analyzed using only Inverse Kinematics (IK)-based joint position control: ‘Figure 6’ nominal walking without external disturbances and ‘Figure 7’ push recovery using a capture point strategy under a lateral impact.

### 5.1. Scenario A: Nominal Walking Without External Disturbances

In the first scenario the robot was commanded to walk on a flat surface with no external forces. The nominal Center of Mass (CoM) trajectory, generated offline by the MPC algorithm, was tracked in real-time using state-space equations. However MuJoCo accurately calculate heel-strike impacts and included the mass  of the robot’s legs unlike the simplified LIPM assumption (which the leg masses are neglected). As a result, the simulated dynamics exhibited more realistic transient behaviors during foot-ground contact and swing-leg motion.

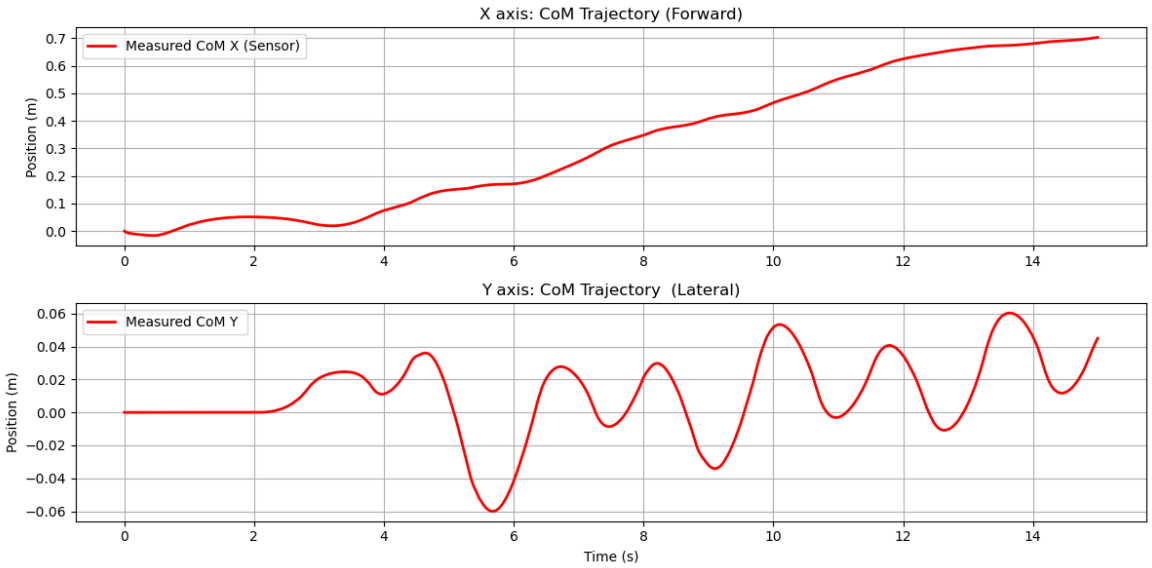



*Figure 6: CoM Trajectory without Force Impact*

As shown in Figure 6, the measured CoM position follows footsteps certain precision. The target joint angles computed via analytical IK were directly fed to MuJoCo's internal PD controllers. Due to the standard LIPM assumptions and the absence of an upper body to provide a compensatory inverse moment for the lower body moment, the ideal CoM trajectory deviated from the Z axis . The results demonstrate that this position-based approach is sufficient to achieve human like natural smooth walking, despite the mass distribution simplifications inherent in Linear Inverted Pendulum Model (LIPM).

### 5.2. Scenario B: Push Recovery via Capture Point Strategy

The second scenario tests the robustness of the system against external disturbances. During the walking cycle, a lateral impact of 30 Newtons was applied to the robot's torso for 0.1 seconds (between t = 6.0 and t = 6.1). Figure 7 illustrates the lateral CoM trajectory response during the impact. At the moment the force is applied (indicated by the vertical dotted line), the actual CoM rapidly deviates from yaw axis of the planned trajectory and accelerates. At this critical point, rather than commanding extra balancing torque to the ankle motors (ankle strategy), the system triggers a capture point reflex. The dynamic step planner instantly detects this drift through the state error and expands the target landing foot position of the swing leg toward the direction of the fall [Englsberger, 2011; Wahrmann, 2018]. As clearly seen in the graph, robot takes a wider step to prevent falling. Within a few seconds after the impact, the CoM error dissipates, and the robots returns to its nominal walking trajectory.

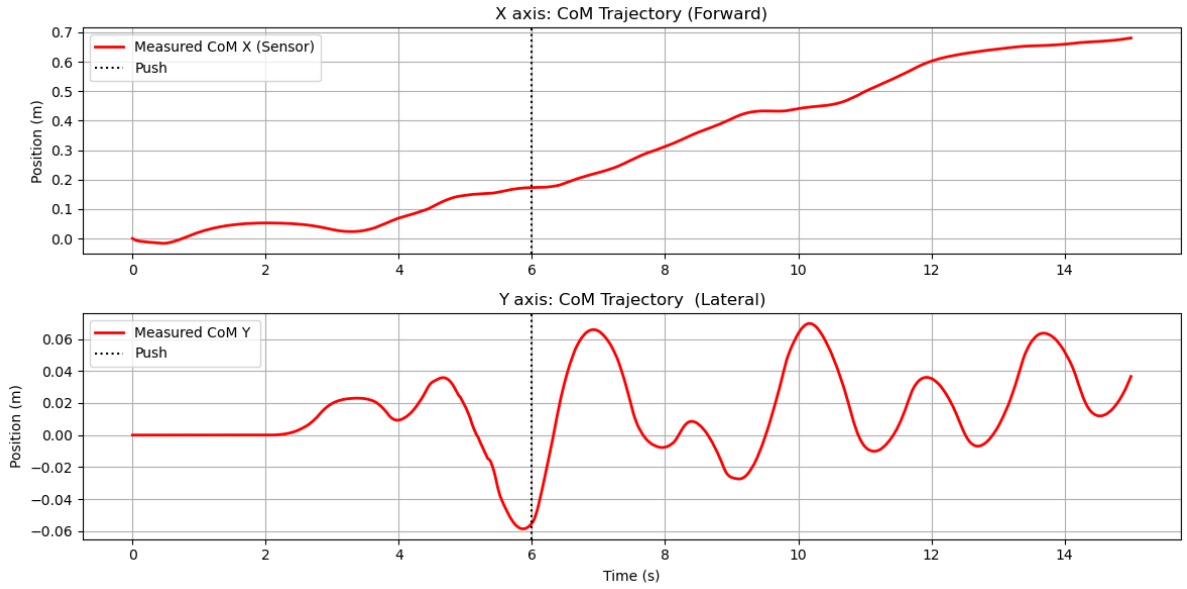



*Figure 7: CoM Trajectory with Force Impact*

### 5.3. Discussion

These findings indicate that push recovery operations in bipedal robots do not strictly require computationally expensive algorithms like Nonlinear MPC or online torque optimization by calculated by minicomputer unlike entry level microcontroller.

In the proposed architecture, heavy trajectory planning is solved offline, while instantaneous balance reactions are handled simply by updating the kinematic target points (capture point). The joint actuators only follow position references. This strategic division of tasks drastically reduces the overall computational cost of the system. Consequently, it provides a practical and industrial framework that can easily run on low-budget microcontroller, for edge computing applications.

## 6. CONCLUSION AND FUTURE WORK

In this study, a computationally efficient and low-cost control architecture for 12-DOF bipedal robots was proposed and successfully validated in the MuJoCo physics engine. Unlike traditional methods that heavily rely on real-time nonlinear torque optimization requiring expensive hardware, the proposed framework utilizes an offline Model Predictive Control (MPC) for nominal trajectory generation. For dynamic balance, an online capture point strategy combined with Inverse Kinematics (IK) position control was implemented to achieve robust push recovery. The simulation results demonstrated that the robot could maintain stable walking and successfully recover from a 30 N lateral impact by dynamically adjusting its swing leg's landing position without demanding extra joint torque limits.

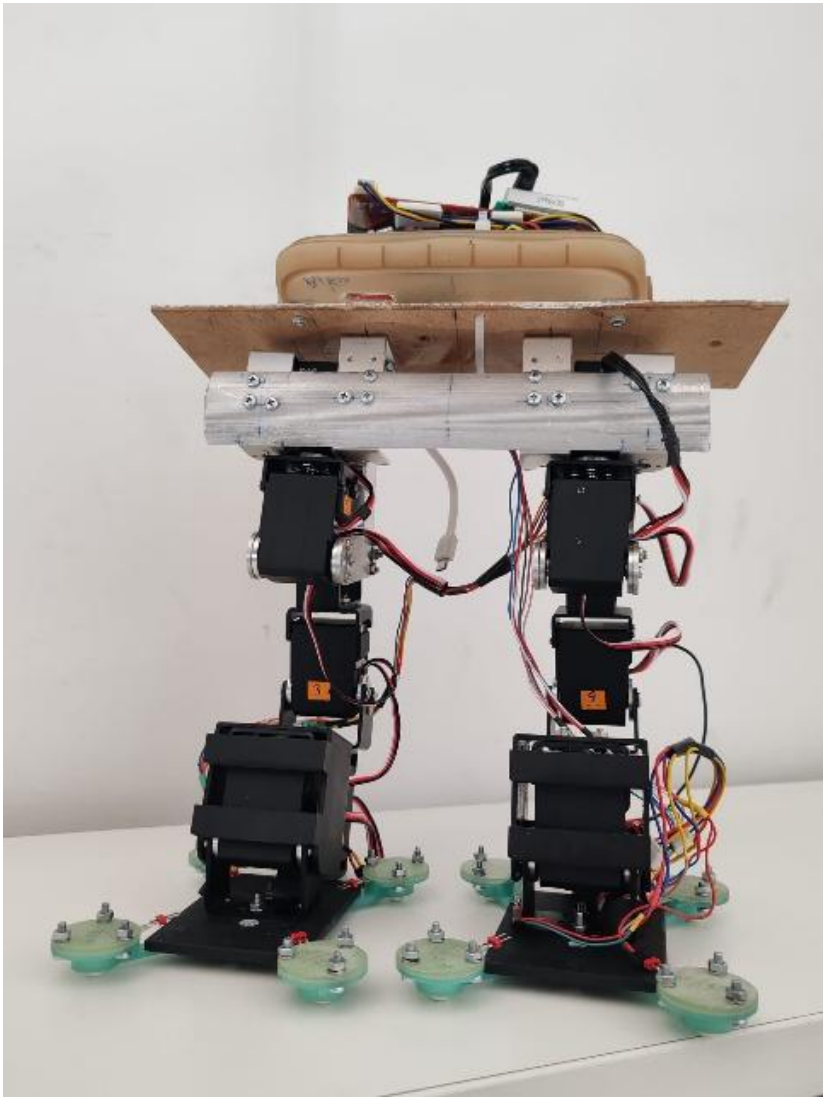


*Figure 8: First Prototype of Robot (Early Phase)*

Furthermore, the mechanical assembly and initial electronic wiring of the physical 12-DOF bipedal robot platform have been completed, as shown in Figure 8. The strategic division of trajectory planning and instantaneous balance reflexes drastically reduces the computational cost, making it highly suitable for edge computing. As future work, the control algorithms validated in this simulation environment will be deployed onto a low-budget microcontroller. Subsequent research will primarily focus on bridging the Sim-to-Real gap, addressing real-world hardware constraints such as sensor noise and backlash, to achieve autonomous physical locomotion.

## REFERENCES

1. **Kajita, S., et al. (2014)**, Introduction to Humanoid Robotics, Springer Tracts in Advanced Robotics.

2. **Wieber, P.B. (2006)**, "Trajectory Free Linear Model Predictive Control for Biped Walking", IEEERAS International Conference on Humanoid Robots.

3. **Kawaharazuka, K. (2025)**, "MEVITA OpenSource Bipedal Robot Assembled from E Commerce Components via Sheet Metal Welding".

4. **Kim, S. (2017)**, "Design of Dynamic Legged Robots", Foundations and Trends in Robotics.

5. **Wisse, M. (2004)**, "Essentials of dynamic walking; Analysis and design of twolegged robots", PhD thesis, TU Delft.

6. **Wahrmann, D. (2018)**, "Timevariable, eventbased walking control for biped robots", International Journal of Advanced Robotic Systems.

7. **Kajita, S. (2003)**, "Biped Walking Pattern Generation by using Preview Control of Zero Moment Point", IEEE International Conference on Robotics and Automation.

8. **Vukobratovic, M. (2004)**, "ZEROMOMENT POINT — THIRTY FIVE YEARS OF ITS LIFE", International Journal of Humanoid Robotics, Vol. 1, No. 1.

9. **Englsberger, J., Ott, C. and AlbuSchäffer, A. (2011)**, "Threedimensional bipedal walking control using Divergent Component of Motion", IEEE/RSJ International Conference on Intelligent Robots and Systems.

10. **Sun, F. (2011)**, "A New 12DoF Biped Robot's Mechanical Design and Kinematic Analysis", International Conference on Electronic and Mechanical Engineering and Information Technology.

11. **Katayama, T. (1985)**, "Design of an optimal controller for a discretetime system subject to previewable demand", International Journal of Control.

12. **Takaba, K. (2003)**, "A tutorial on preview control systems", SICE Annual Conference.

13. **Takaba, K. (1995)**, "Discretetime preview control systems", Proceedings of the IEEE Conference on Decision and Control. August 1921, 2026, Istanbul, Türkiye August 19-21, 2026, Istanbul, Türkiye

# FRICTION TORQUE LOSS IN RELATION TO FLEX THICKNESS ON ROTARY SHAFT SEALS

**Beliğ Tarık OTSAY** *beligtarik@gmail.com* Bursa Uludağ University, 16110, Bursa, Türkiye
**Prof.Dr.M.Cemal ÇAKIR** *cemal@uludag.edu.tr* Bursa Uludağ University,16059,Bursa,Türkiye

## ABSTRACT

In all types of machinery and mobility, friction losses from rotary shaft seals are contributing to significant energy consumption and putting thermal strain on rotating members. This study experimentally investigates the main relationship between flex thickness of rotary shaft seal and its effect on friction torque. In this study tests are conducted in controlled shaft speed and lubrication conditions while using seals with different flex thickness. Friction torque measured constantly and used to cross examine other results. Results show clear correlation between flex thickness, radial force and friction torque.
**Keywords:** Friction loss, Torque loss, Radial Force, Flex Thickness,

## 1. INTRODUCTION

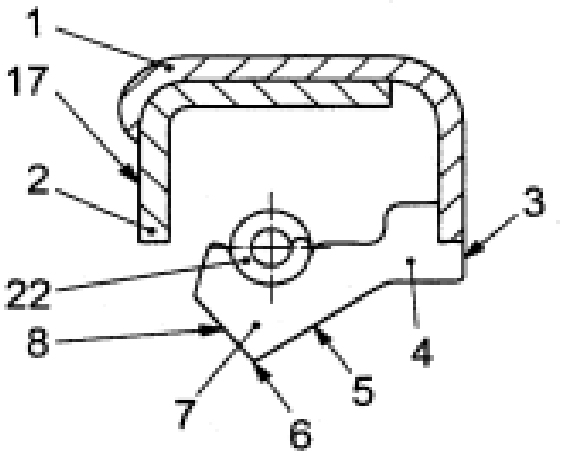
Rotary shaft seals are used in all types of mechanical and mobility systems which retain some form of rotation. Main function of such dynamic sealing is to prevent leakage of lubricants used in construction or prevent outside contaminants to enter into rotating machinery space. Performance of sealing directly effects system efficiency and durability of machinery and maybe more importantly operational reliability of mobility systems. The mechanical efficiency of sealing systems is always a subject of discussion and study. With the new electric mobility systems, renewed focus on efficiency (Hart, 2025) is resulting in expectation of improvement at all systems (IEA report, 2025).

One of the most important performance characteristics of rotary shaft seal is friction caused by the shaft and seal interference. This can result in considerable power losses and unexpected heat generation. In turn elevated temperatures can result in elastomer aging and changing lip mechanics and create a loop of more contact and heat and more aging of elastomer until failure (Frölich et al., 2013). While studies and observations show maintaining friction torque is one of the best indicators of seal lifetime (Frölich et al., 2013)., choosing solutions with minimal friction loss and heat generation is important for optimized seal design (Plath et al., 2005)

Friction torque in rotary shafts are well studied area and known to directly influenced by a combination of material properties, lubrication, shaft surface, seal geometry. For determining contact pressure and contact width on shaft surface, sealing lip geometry is in defining role (Tok et al., 2018).

In this context seal lip flexibility which is characterized by flex thickness of seal lip is directly effecting contact compliance. Variations of flex thickness can therefore greatly influence friction losses , heat generation and subsequently wear behavior. Despite its big effect on construction efficiency, flex thickness frequently selected empirically, and friction loss is optimized only by interference between seal lip and the shaft. (Jia et al., 2013). Rather than assigning a single predetermined flex thickness value for crankshaft applications and another one for axle applications, the design of flex section should also account for friction torque loss optimization as well.

The objective of this study is to experimentally investigate the relationship between friction torque and the flex thickness in rotary shaft seals. By using standardized ISO seal geometry and fixed test parameters, influence of flex thickness is evaluated.




| No | Designation |
|---|---|
| 1 | Case |
| 2 | Inner case |
| 3 | Heel |
| 4 | Flex section |
| 5 | Air side lip face |
| 6 | Sealing edge |
| 7 | Head section |
| 8 | Fluid side lip face |
| 17 | Fluid side face |
| 22 | Garter Spring |

Figure 1. ISO 6194-2 Rotary shaft lip-type seals incorporating elastomeric sealing elements and designations.

## 2. SETUP FOR EXPERIMENT

The experiments were conducted using dedicated test rig designed for high rotation speeds and in order to evaluate test results, this rig also measures friction torque generated by rotary shaft seals while in operation.

Test rig consists of electric drive unit, a horizontally aligned test shaft, rigid housing with motorized axial movement, inline torque reader, and computer for data collection. Friction torque generated at seal lip and shaft interference is transmitted through the shaft and

measured by torque sensor. Shaft is rotating at constant rotational speed while radial shaft seal is mounted concentrically in the housing to ensure repeatability of alignment and other conditions. All measurement data is digitally recorded in synchronized form for evaluation.

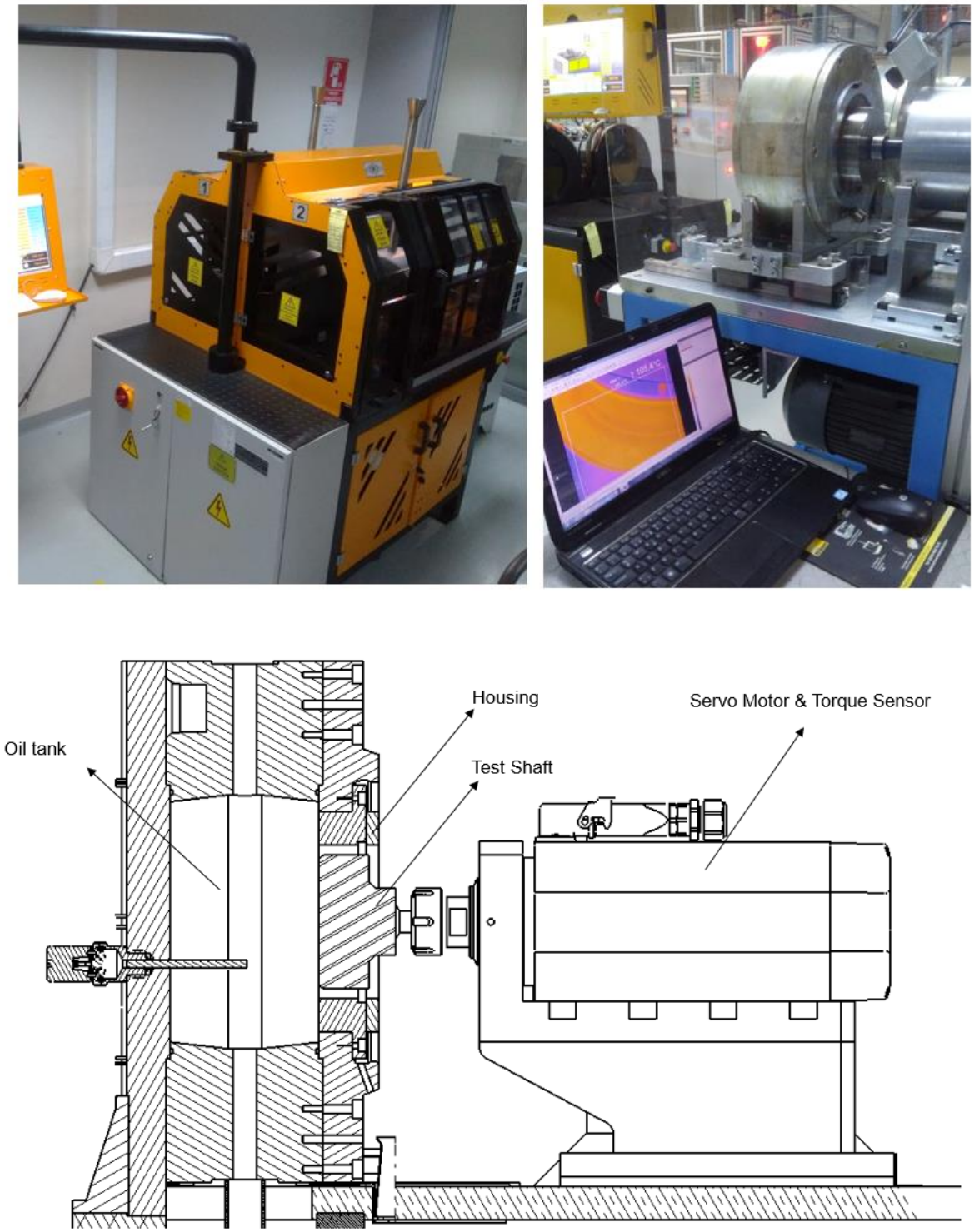



Figure 2. Top Left- High rpm test rig with torque measurement sensor. Top Right- Temperature sensor and measurement method. Bottom- Test rig section

## 3. TEST METHODOLOGY

Friction torque is measured continuously through each test with torque sensor to detect variations on torque between related seal geometry changes. The measurement includes both initial run-in phase and steady operating phase for different rotation speeds to acquire data about different operating conditions.

All seals are measured before testing in order to record and compare any possible differences which can effect results. Other than flex thickness, no changes made in compared profiles. Flex thickness is defined as effective elastomer thickness of the sealing lip and main parameter for elastic bending while seal is in contact with shaft. Three flex thickness values are investigated in this study. Before testing measurements showed that without altering Lip diameter, increase in flex thickness profiles results in increased radial force.

Table 1: Before Testing Measurements

| | *Seal 1* | *Seal 2* | *Seal 3* |
|---|---|---|---|
| Material | FKM | FKM | FKM |
| Flex Thickness (mm) | 1,40 | 1,15 | 0,90 |
| Radial Force (N) | 56,2 | 36,2 | 30,7 |
| Lip Diameter With Spring(mm) | 123,95 | 124,01 | 123,88 |

*Note: All material refers to same compound.*

Flex thickness values on table is determined by cross sectional cuts of seal lip from representative samples. These sections are perpendicular to shaft axis and thickness measurements are taken from a defined location on ISO seal profile at Figure 1 (4-Flex section).

Each seal was tested using an identical parameters. Test are started with rotational speed of 100 rpm and maintained this speed for predefined duration. Following this step rotation speed is increased in increments of 100 rpm and each speed level held for same duration until a maximum speed of 500 rpm was reached. For better inspection of higher speeds, last two step duration is selected longer than first steps. After concluding tests, last 5 minutes of 500 rpm period is compared with other seals tested for direct comparison.

All seals are pre lubricated with same amount of grease before mounting to ensure the dry friction or slip stick does not effect the results. After tests started no additional lubrication was

applied. Shaft surface condition and mounting procedure were kept identical for all three tests and measurements were carried out for each test to ensure that rig alignment and concentricity is repeatable.

## 4. RESULTS AND DISCUSSION

Friction torque recorded through all test steps for each seal. All three seals showed expected start off torque peak which at the very start of the test torque values started high and after small period settled into stable operating values. This pattern repeated for each step of rpm increase as short torque spike but for shorter time period. This is expected in context of redistributing lubrication film at the seal lip contact zone for sudden change of speed.
Figure 3. shows the Torque/Time graph profiles for all three seals across the test duration. As mentioned, step increase in speed are clearly visible in torque graph and the settling behavior after first start of each step.

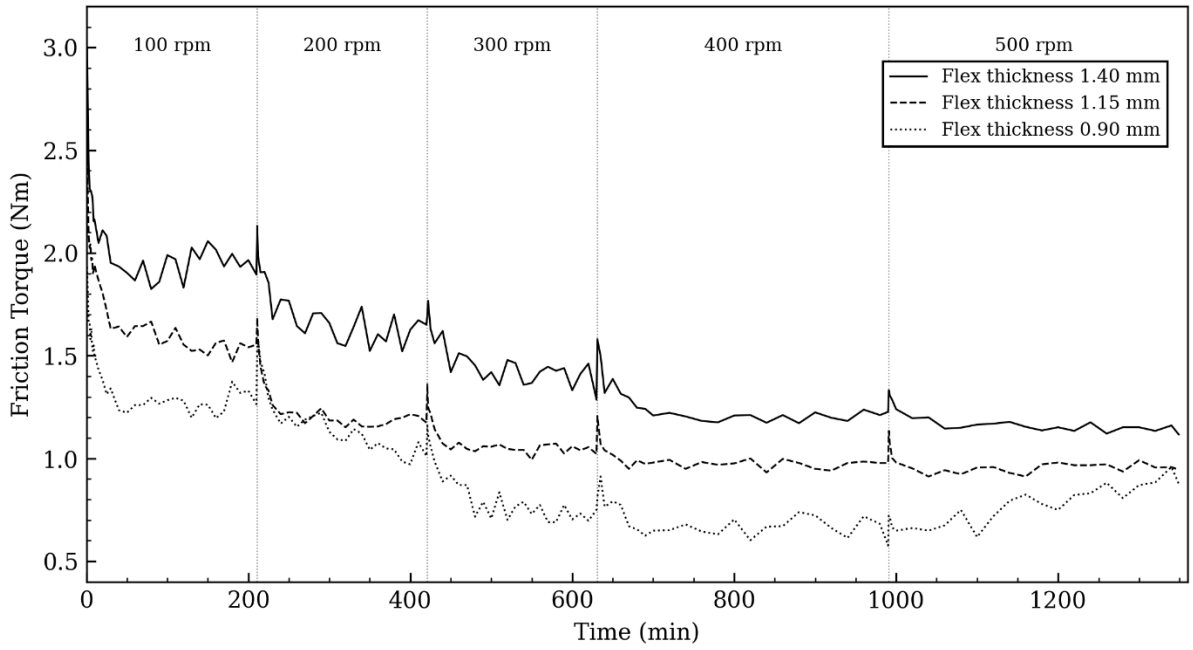



Figure 3. Torque / Time graph

Across all speed steps, Seal  with highest flex thickness is consistently observed to have highest friction torque when Seal with lowest flex thickness is has lowest. For the direct comparison between seals, the mean friction torque measured during the last 5 minutes of the 500 rpm step was taken as representing value for seals. Results are summarized in Table 2.

Table 2: Test Results

| | Seal 1 | Seal 2 | Seal 3 |
|---|---|---|---|
| Flex Thickness (mm) | 1,40 | 1,15 | 0,90 |
| Radial Force (N) | 56,2 | 36,2 | 30,7 |
| Mean Friction Torque (Nm)* | 1,168 | 0,969 | 0,771 |
| Torque Change % | - | -17,0% | -33,9% |

*Note 1: * Mean of last 5 minute of 500 rpm step,*

*Note 2: For torque change % calculation, Seal 1 is used as reference.*

Results of study clearly demonstrate that flex thickness of rotary shaft seal lip is an important and predictable parameter which effects friction torque behavior of seal. Across all tests friction torque and flex thickness correlation is consistent, thicker flex sections resulted in increased friction torque across all speeds. This consistency confirms that flex thickness influence on friction is repeatable and in tested range, not a function of speed.

Interesting point from results is the relationship between radial force and friction force correlation for all three tested seal versions. Measurements before testing showed radial force does not correlate linearly with flex thickness. Gap between Seal 1and Seal 2 is much bigger than gap between Seal 2 and Seal 3 despite flex thickness increments are fairly more even. Despite all this friction torque steady state follows more linear correlation with flex thickness. This difference is suggesting that flex thickness effects friction torque through not only radial force, but other mechanisms related to lip geometry as well. Mainly changes lip compliance to shaft contact and lip contact section force distribution likely plays role to create nonlinear effect mechanism to differentiates two measurement.

The Run in or takeoff torque phenomena is observed on all tests and worth noting. Each test started with elevated torque reading and after short time gradually settled into stable operating levels. Also worth mentioning, this effect repeated at the start of each speed step. Main possible explanation for repeated torque peak accompanied with steps all across tests can be redistribution of lubricant film under seal lip. These peaks stayed at expected values and did not produce any interference in result graph.

## 5. CONCLUSION

This study aims to provide experimental evidence that flex thickness is primary and controllable design parameter for optimizing friction torque in rotary shaft seals. Rather than selected empirically for working area of seal, flex thickness should be treated as design value with

predictable outcomes to friction loss. The results support its effect on optimizing sealing along with interference and radial force parameters.

As limitations of methodology, this study designed as step by step increase up to 500 rpm with fixed durations. Different duty cycles and higher speeds can produce different results and with higher speed this effect can decrease. Further testing with different protocols can extend these findings. Additionally, only same FKM elastomer is used on this study in order to stay out of temperature effects on elastomer aging range as possible. Different elastomers can show different correlations with similar test procedure. In order to understand effect of elastomer difference, a new study with same geometry will follow this one in near future.

## REFERENCES

**Hart,F., (2025)**. “New Seals Reduce Friction for electric Vehicle Adoption”, Trelleborg Sealing Solutions Technical Article, Machine Design, February 2025.

**International Energy Agency (IEA), (2025)**, "Energy Efficiency 2025", IEA Publications, Paris, France.

**Frölich,D., Magyar, B., Sauer, B., (2014)**. A Comprehensive Model of Wear, Friction and Contact Temperature in Radial Shaft Seals. Wear. 311.

**Plath, S., Meyer, S., Wollesen, V.M., (2005)**, "Friction Torque of a Rotary Shaft Lip Type Seal – A Comparison Between Test Results and Finite Element Simulation", Mechanika, Vol. 4, No. 54, pp. 55–59.

**Tok, G., Parlar, Z. and Temiz, V., (2018)**, "Numerical Investigation of the Effect of Radial Lip Seal Geometry on Sealing Performance", IOP Conference Series: Materials Science and Engineering, Vol. 295, No. 1, Article No. 012003.

**Jia, X., Guo, F.,Huang,L., Salant,R.F, Wang Y.,(2013)** Parameter analysis of the radial lip seal by orthogonal array method ,Tribology International,Volume 64,Pages 96102,

**ISO 6194**2:2009 (2009). Rotary shaft liptype seals incorporating elastomeric sealing elements Part 2: Vocabulary.

# INVERSE POSITION ANALYSIS OF A 4-RPR PLANAR PARALLEL ROBOT WITH CONFIGURABLE QUADRILATERAL PLATFORM

**İrem Beyza EKİCİ**, *beyza.ekici@marmara.edu.tr* Marmara University, Faculty of Engineering, Department of Mechanical Engineering, Recep Tayyip Erdoğan Campus, 34854 Maltepe, İstanbul, Türkiye, ORCID iD: https://orcid.org/0000-0002-4208-384X

**Mustafa ÖZDEMİR**, *mustafa.ozdemir@marmara.edu.tr* Marmara University, Faculty of Engineering, Department of Mechanical Engineering, Recep Tayyip Erdoğan Campus, 34854 Maltepe, İstanbul, Türkiye, ORCID iD: https://orcid.org/0000-0002-4981-9573

## ABSTRACT

Parallel robots with configurable platforms constitute a new class of parallel robots that can perform multi-tasking through the simultaneous operation of multiple end-effectors. This paper presents an inverse position analysis of one such robot, namely a 4-RPR planar parallel robot with a configurable quadrilateral platform. This four-degree-of-freedom robot has two end-effectors, each possessing two degrees of freedom. An analytical solution is obtained for the inverse position kinematics of this robot. A numerical example is also provided to illustrate the solution procedure. The study contributes to the analytical developments in the emerging area of configurable-platform parallel robots.

**Keywords:** Parallel robot, Configurable platform, Inverse kinematics, Analytical solution

## 1. INTRODUCTION

Parallel robots have an important role in industrial and medical applications due to their high accuracy, load capacity, and stiffness [Zhang et al., 2009]. These advantages result from the load being distributed among the robot's legs [Tian and Zhang, 2025].

A conventional parallel robot has a rigid moving platform. In contrast, a parallel robot with a configurable platform has an extra closed-loop kinematic chain instead of a rigid platform [Lambert and Herder, 2016]. The configurable platform offers several advantages due to its internal degrees of freedom. For instance, the platform can be configured to grasp objects. It can also accommodate two or more end-effectors. Although the platform's configurability provides significant advantages, it increases the complexity of kinematic analysis [Marchi et al., 2021].

The kinematic analysis of parallel robots is divided into two types: direct and inverse kinematics. Direct kinematics deals with determining the end-effector variables given the input joint variables. Inverse kinematics determines the required input joint variables for a given set of end-effector variables [Ratiu and Anton, 2020]. In general, numerical techniques are used to solve the direct kinematic problem of parallel manipulators [Staicu, 2019]. However, their

inverse kinematics is generally more straightforward and hence is solvable analytically. Williams II and Shelley [1997] obtained the inverse position and velocity kinematic solutions for three-degree-of-freedom planar parallel robots with a rigid triangular platform.

Various studies in the literature have examined different aspects of parallel robots with configurable platforms. Several design concepts were discussed in the works of Mohamed and Gosselin [2005] and Lambert and Herder [2016]. Based on these, numerous spatial [Hoevenaars et al., 2017; Xu et al., 2020; Yue et al., 2024] and planar [Gallardo-Alvarado and Tinajero-Campos, 2019; Marchi et al., 2021] architectures have been introduced. This paper studies the solution to the inverse position kinematics of a 4-RPR planar parallel robot with configurable quadrilateral platform and two end-effectors. An analytical solution is obtained in this regard. A numerical example is also provided.

## 2. INVERSE POSITION ANALYSIS

Figure 1 shows a 4-RPR planar parallel robot with configurable quadrilateral platform where R and P denote revolute and prismatic joints. The locations of the base revolute joints are represented in the fixed coordinate system $Oxy$ as $A_0(x_1, y_1)$, $B_0(x_2, y_2)$, $C_0(x_3, y_3)$ and $D_0(x_4, y_4)$. Each base revolute joint is driven by a motor. The actuated joint variables are $\theta_1$, $\theta_2$, $\theta_3$ and $\theta_4$. The lengths of the links that constitute the configurable platform are labeled as $AB = a_1$, $BC = a_2$, $CD = a_3$ and $DA = a_4$.The link variables of the configurable platform are $\phi_1$, $\phi_2$, $\phi_3$ and $\phi_4$. The prismatic joint variables are defined as $s_1 = A_0A$, $s_2 = B_0B$, $s_3 = C_0C$ and $s_4 = D_0D$.

Since the mechanism has four degrees of freedom, two end-effectors, each with two degrees of freedom, can be mounted on the configurable platform. The end-effectors are selected as points $A$ and $C$.

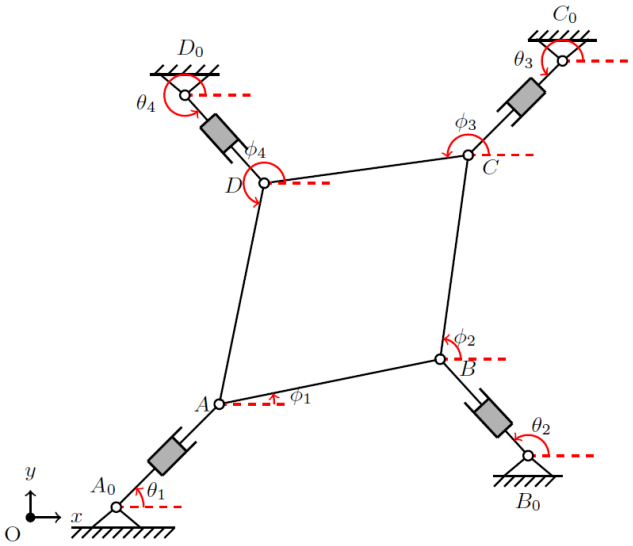



Figure 1. A 4-RPR Planar Parallel Robot with Configurable Quadrilateral Platform.

The loop-closure equations of the mechanism can be written in terms of complex numbers as follows:

$$s_1 e^{i\theta_1} + a_1 e^{i\phi_1} = x_{A_0B_0} + i\, y_{A_0B_0} + s_2 e^{i\theta_2} \quad (1)$$

$$s_2 e^{i\theta_2} + a_2 e^{i\phi_2} = x_{B_0C_0} + i\, y_{B_0C_0} + s_3 e^{i\theta_3} \quad (2)$$

$$s_3 e^{i\theta_3} + a_3 e^{i\phi_3} = x_{C_0D_0} + i\, y_{C_0D_0} + s_4 e^{i\theta_4} \quad (3)$$

$$s_4 e^{i\theta_4} + a_4 e^{i\phi_4} = x_{D_0A_0} + i\, y_{D_0A_0} + s_1 e^{i\theta_1} \quad (4)$$

where $i$ is the unit imaginary number. Here and in the rest of the paper, we use the notation $x_{MN} = x_N - x_M$ and $y_{MN} = y_N - y_M$ for the two points $M(x_M, y_M)$ and $N(x_N, y_N)$.

Given the location of point $A$, we can write

$$s_1 e^{i\theta_1} = x_{A_0A} + i\, y_{A_0A} \quad (5)$$

Equation (5) can be solved for $\theta_1$ and $s_1$ as follows:

$$\theta_1 = \operatorname{atan2}(y_{A_0A}, x_{A_0A}) \quad (6)$$

$$s_1 = \sqrt{x_{A_0A}^2 + y_{A_0A}^2} \quad (7)$$

where $\operatorname{atan2}(y, x)$ is the four-quadrant arctangent function. Our $\operatorname{atan2}$ notation is as follows: $\theta = \operatorname{atan2}(\sin(\theta), \cos(\theta))$.

Similarly, the following equation can be written for a given position of point $C$:

$$s_3 e^{i\theta_3} = x_{C_0C} + i\, y_{C_0C} \quad (8)$$

Solving equation (8) for $\theta_3$ and $s_3$ gives

$$\theta_3 = \operatorname{atan2}(y_{C_0C}, x_{C_0C}) \quad (9)$$

$$s_3 = \sqrt{x_{C_0C}^2 + y_{C_0C}^2} \quad (10)$$

Summing equations (1) and (2) side-by-side and simplifying the resulting equation using equations (5) and (8) gives

$$a_1 e^{i\phi_1} + a_2 e^{i\phi_2} = x_{AC} + i\, y_{AC} \quad (11)$$

Equation (11) has two unknowns, which are $\phi_1$and $\phi_2$. In order to eliminate $\phi_2$, the $a_2 e^{i\phi_2}$ term needs to be left alone on one side of the equation.

$$a_2 e^{i\phi_2} = x_{AC} + i\, y_{AC} - a_1 e^{i\phi_1} \quad (12)$$

The complex conjugate of equation (12) can be written as

$$a_2 e^{-i\phi_2} = x_{AC} - i\, y_{AC} - a_1 e^{-i\phi_1} \quad (13)$$

Multiplying equations (12) and (13) side-by-side, then simplifying and rearranging the resulting equation, gives

$$-2\, x_{AC} a_1 \cos(\phi_1) - 2\, y_{AC} a_1 \sin(\phi_1) + x_{AC}^2 + y_{AC}^2 + a_1^2 - a_2^2 = 0 \quad (14)$$

Equation (14) can be rearranged to a more compact form as

$$\kappa_1 \cos(\phi_1) + \lambda_1 \sin(\phi_1) = \mu_1 \quad (15)$$

where

$$\kappa_1 = 2\,x_{AC}\,a_1 \tag{16}$$
$$\lambda_1 = 2\,y_{AC}\,a_1 \tag{17}$$
$$\mu_1 = x_{AC}^2 + y_{AC}^2 + a_1^2 - a_2^2 \tag{18}$$

Equation (15) can be solved for $\phi_1$ using the tangent half-angle formulas. Let

$$\tau_1 = \tan\left(\frac{\phi_1}{2}\right) \tag{19}$$

Then $\cos(\phi_1)$ and $\sin(\phi_1)$ can be written as

$$\cos(\phi_1) = \frac{1-\tau_1^2}{1+\tau_1^2} \tag{20}$$
$$\sin(\phi_1) = \frac{2\tau_1}{1+\tau_1^2} \tag{21}$$

Substituting equations (20) and (21) into equation (15), followed by rearranging and simplifying, yields the following:

$$\alpha_1\tau_1^2 + \beta_1\tau_1 + \gamma_1 = 0 \tag{22}$$

where

$$\alpha_1 = \kappa_1 + \mu_1 \tag{23}$$
$$\beta_1 = -2\,\lambda_1 \tag{24}$$
$$\gamma_1 = -\kappa_1 + \mu_1 \tag{25}$$

Solving the quadratic equation (22) yields

$$\tau_1 = \frac{-\beta_1 + \sigma_1\sqrt{\beta_1^2 - 4\,\alpha_1\gamma_1}}{2\,\alpha_1} \tag{26}$$

where $\sigma_1 = \pm 1$ gives two different configurations of the mechanism. Recalling the definition of $\tau_1$, the angle $\phi_1$ is found as follows:

$$\phi_1 = 2\tan^{-1}(\tau_1) \tag{27}$$

The $\phi_2$ angle can then be determined by using the real and imaginary components of equation (12) as

$$\phi_2 = \operatorname{atan2}\left(y_{AC} - a_1\sin(\phi_1),\, x_{AC} - a_1\cos(\phi_1)\right) \tag{28}$$

Substituting equation (5) into equation (1) and rearranging gives

$$s_2 e^{i\theta_2} = x_{B_0A} + i\,y_{B_0A} + a_1 e^{i\phi_1} \tag{29}$$

Equation (29) can be solved for $\theta_2$ and $s_2$ as

$$\theta_2 = \operatorname{atan2}\left(y_{B_0A} + a_1\sin(\phi_1),\, x_{B_0A} + a_1\cos(\phi_1)\right) \tag{30}$$
$$s_2 = \sqrt{\left(x_{B_0A} + a_1\cos(\phi_1)\right)^2 + \left(y_{B_0A} + a_1\sin(\phi_1)\right)^2} \tag{31}$$

Summing equations (3) and (4) side-by-side and simplifying the resulting equation using equations (5) and (8) yields

$$a_3 e^{i\phi_3} + a_4 e^{i\phi_4} = x_{CA} + i\, y_{CA} \tag{32}$$

Equation (32) has two unknowns, namely, $\phi_3$ and $\phi_4$. In order to eliminate $\phi_4$, the $a_4 e^{i\phi_4}$ term needs to be left alone on one side of the equation.

$$a_4 e^{i\phi_4} = x_{CA} + i\, y_{CA} - a_3 e^{i\phi_3} \tag{33}$$

The complex conjugate of equation (33) can be written as

$$a_4 e^{-i\phi_4} = x_{CA} - i\, y_{CA} - a_3 e^{-i\phi_3} \tag{34}$$

Multiply equations (33) and (34) side-by-side, then simplify and rearrange the resulting equation to get

$$-2\, x_{CA}\, a_3 \cos(\phi_3) - 2\, y_{CA}\, a_3 \sin(\phi_3) + x_{CA}^2 + y_{CA}^2 + a_3^2 - a_4^2 = 0 \tag{35}$$

Equation (35) can be rewritten as follows:

$$\kappa_3 \cos(\phi_3) + \lambda_3 \sin(\phi_3) = \mu_3 \tag{36}$$

where

$$\kappa_3 = 2\, x_{CA}\, a_3 \tag{37}$$

$$\lambda_3 = 2\, y_{CA}\, a_3 \tag{38}$$

$$\mu_3 = x_{CA}^2 + y_{CA}^2 + a_3^2 - a_4^2 \tag{39}$$

We now define

$$\tau_3 = \tan\left(\frac{\phi_3}{2}\right) \tag{40}$$

and write

$$\cos(\phi_3) = \frac{1 - \tau_3^2}{1 + \tau_3^2} \tag{41}$$

$$\sin(\phi_3) = \frac{2\tau_3}{1 + \tau_3^2} \tag{42}$$

Substituting equations (41) and (42) into equation (36), followed by rearranging and simplifying, yields the following:

$$\alpha_3 \tau_3^2 + \beta_3 \tau_3 + \gamma_3 = 0 \tag{43}$$

where

$$\alpha_3 = \kappa_3 + \mu_3 \tag{44}$$

$$\beta_3 = -2\, \lambda_3 \tag{45}$$

$$\gamma_3 = -\kappa_3 + \mu_3 \tag{46}$$

Solving the quadratic equation (43) gives

$$\tau_3 = \frac{-\beta_3 + \sigma_3 \sqrt{\beta_3^2 - 4\alpha_3\gamma_3}}{2\alpha_3} \tag{47}$$

where $\sigma_3 = \pm 1$ gives two more different configurations of the mechanism. Recalling the definition of $\tau_3$, the angle $\phi_3$ is found as follows:

$$\phi_3 = 2\tan^{-1}(\tau_3) \tag{48}$$

The $\phi_4$ angle can then be determined by using the real and imaginary components of equation (33) as

$$\phi_4 = \text{atan2}\left(y_{CA} - a_3\sin(\phi_3), x_{CA} - a_3\cos(\phi_3)\right) \tag{49}$$

Substituting equation (8) into equation (3) and rearranging gives

$$s_4 e^{i\theta_4} = x_{D_0C} + i\, y_{D_0C} + a_3 e^{i\phi_3} \tag{50}$$

Equation (50) can be solved for $\theta_4$ and $s_4$ as

$$\theta_4 = \text{atan2}\left(y_{D_0C} + a_3\sin(\phi_3), x_{D_0C} + a_3\cos(\phi_3)\right) \tag{51}$$

$$s_4 = \sqrt{\left(x_{D_0C} + a_3\cos(\phi_3)\right)^2 + \left(y_{D_0C} + a_3\sin(\phi_3)\right)^2} \tag{52}$$

That completes the solution to the inverse position kinematics of the robot. All the joint variables ($\theta_1$, $\theta_2$, $\theta_3$, $\theta_4$, $s_1$, $s_2$, $s_3$, $s_4$, $\phi_1$, $\phi_2$, $\phi_3$ and $\phi_4$) are determined for the given positions of the end-effectors $A$ and $C$.

## 3. NUMERICAL EXAMPLE

Table 1 presents the numerical values that are assigned to the robot parameters. Let end-effector $A$ be at $x_A = 0.105$ m and $y_A = 0.09$ m, and let end-effector $C$ be at $x_C = 0.36$ m and $y_C = 0.46$ m. Table 2 shows the numerical values of the joint variables for these end-effector positions with $\sigma_1 = -1$ and $\sigma_3 = -1$. Figure 2 shows a sketch of the robot with these found values.

Table 1. Numerical Values of the Robot Parameters.

| Parameter | Value (m) |
|---|---|
| $x_1$ | 0 |
| $y_1$ | 0 |
| $x_2$ | 0.5 |
| $y_2$ | 0 |
| $x_3$ | 0.5 |
| $y_3$ | 0.5 |
| $x_4$ | 0 |
| $y_4$ | 0.5 |
| $a_1$ | 0.3 |
| $a_2$ | 0.3 |
| $a_3$ | 0.3 |

| | |
|---|---|
| $a_4$ | 0.3 |

Table 2. The Numerical Values of the Joint Variables Found.

| Variable | Value | Unit |
|---|---|---|
| $\theta_1$ | 0.7086 | rad |
| $\theta_2$ | 2.1402 | rad |
| $\theta_3$ | -2.8633 | rad |
| $\theta_4$ | -1.0206 | rad |
| $s_1$ | 0.1383 | m |
| $s_2$ | 0.1926 | m |
| $s_3$ | 0.1456 | m |
| $s_4$ | 0.1316 | m |
| $\phi_1$ | 0.2430 | rad |
| $\phi_2$ | 1.6917 | rad |
| $\phi_3$ | -2.8986 | rad |
| $\phi_4$ | -1.4499 | rad |

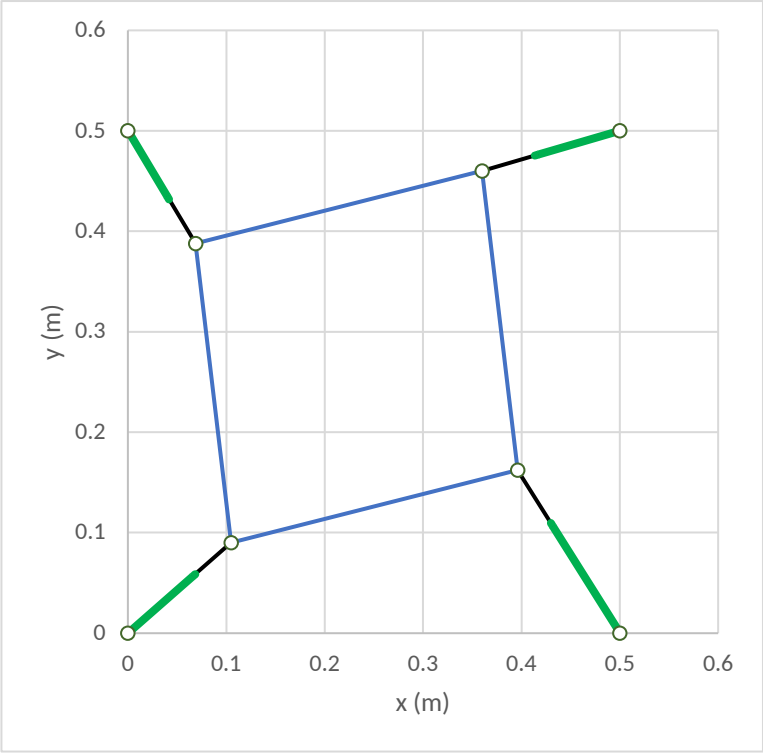



Figure 2. Sketch of the Robot Showing the Obtained Numerical Solution.

## 4. CONCLUSIONS

This paper presents an inverse position analysis of a 4-RPR planar parallel robot with a configurable quadrilateral platform. This is a four-degree-of-freedom robot with two end-effectors. Each end-effector has two degrees of freedom. Using the derived expressions, all the joint variables of the robot can be determined analytically for a given set of positions of its

end-effectors. A numerical example is provided for a configuration of the robot where end-effector $A$ is located at $x_A = 0.105$ m and $y_A = 0.09$ m, and end-effector $C$ is at $x_C = 0.36$ m and $y_C = 0.46$ m. Using these end-effector positions, both actuated and unactuated joint variables are obtained numerically for a selected working mode of the robot. For visualization purposes, the robot is also sketched using these results. Since inverse position analysis constitutes a fundamental step towards workspace analysis, the derived analytical expressions enable future workspace evaluations of this 4-RPR configurable-platform planar parallel robot.

## ACKNOWLEDGEMENTS

This paper is based on a part of the Master of Science Thesis being prepared by the first author (Research Assistant İrem Beyza EKİCİ) in the Department of Mechanical Engineering (English) at Marmara University Institute of Pure and Applied Sciences under the supervision of the second author (Prof. Dr. Mustafa ÖZDEMİR).

## REFERENCES

**1. Zhang, Y., Liu, H. and Wu, X.**, **(2009)**, "Kinematics analysis of a novel parallel manipulator", Mechanism and Machine Theory, Vol.44, No.9, pp 1648–1657.

**2. Tian, C. and Zhang, D.**, **(2025)**, "A Review on Kinematically Redundant Parallel Mechanisms With Configurable Platforms", SmartBot, Vol.1, No.4, e70014.

**3. Lambert, P. and Herder, J.L.**, **(2016)**, "Parallel robots with configurable platforms: Fundamental aspects of a new class of robotic architectures", Proceedings of the Institution of Mechanical Engineers, Part C: Journal of Mechanical Engineering Science, Vol.230, No.3, pp 463–472.

**4. Marchi, T., Mottola, G., Porta, J.M., Thomas, F. and Carricato, M.**, **(2021)**, "Position and Singularity Analysis of a Class of Planar Parallel Manipulators with a Reconfigurable End-Effector", Machines, Vol.9, No.1, 7.

**5. Ratiu, M. and Anton, D.M.**, **(2020)**, "A brief overview of parallel robots and parallel kinematic machines", IOP Conference Series: Materials Science and Engineering, Vol.898, 012007.

**6. Staicu, S.**, **(2019)**, Dynamics of Parallel Robots, Springer, Cham.

**7. Williams, R.L., II and Shelley, B.H.**, **(1997)**, "Inverse Kinematics for Planar Parallel Manipulators", Proceedings of the ASME 1997 Design Engineering Technical Conferences. Volume 2: 23rd Design Automation Conference. Sacramento, California, USA. September 14 –17, 1997. V002T29A007. ASME.

**8. Mohamed, M.G. and Gosselin, C.M.**, **(2005)**, "Design and analysis of kinematically redundant parallel manipulators with configurable platforms", IEEE Transactions on Robotics, Vol.21, No.3, pp 277–287.

**9. Hoevenaars, A.G.L., Gosselin, C., Lambert, P. and Herder, J.L.**, **(2017)**, "A Systematic Approach for the Jacobian Analysis of Parallel Manipulators with Two End-Effectors", Mechanism and Machine Theory, Vol.109, pp 171–194.

**10. Xu, Y., Liang, Z. and Liu, J.**, **(2020)**, "A New Metamorphic Parallel Leg Mechanism with Reconfigurable Moving Platform", Mathematical Problems in Engineering, Vol.2020, 3234969.

**11. Yue, J., Lin, C., Jiang, S., Li, W., Gao, F. and Chen, W.**, **(2024)**, "Design, analysis and optimization of a novel redundant (6+1)-degree-of-freedom parallel mechanism with configurable platform", Mechanism and Machine Theory, Vol.192, 105550.

**12. Gallardo-Alvarado, J. and Tinajero-Campos, J.H.**, **(2019)**, "A Parallel Manipulator with Planar Configurable Platform and Three End-Effectors", Mathematical Problems in Engineering, Vol.2019, 7972837.

# EXPLORATORY MILLING OF MUONIONALUSTA IRON METEORITE USING CrN-, AlTiN-, AND TiAlN-COATED SOLID-CARBIDE END MILLS: PRELIMINARY CUTTING-FORCE ANALYSIS

**Nevzat Bircan BUĞDAYCI**, *bugdayci@msu.edu* Michigan State University, East Lansing, MI, USA

**Hasan Sinan BANK**, *sinan.bank@colostate.edu* Colorado State University, Fort Collins, USA

## ABSTRACT

This paper presents the results of an exploratory milling study conducted on Muonionalusta iron meteorite samples at Michigan State University in collaboration with EMUGE-Franken. Three cutter families—Aero 5 (CrN), TiNoxNF (AlTiN), and Topcut (TiAlN)—were evaluated at multiple feed conditions using cutting force signals. The signals show a clear monotonic rise of signal RMS with feed for every tool family, and one condition (the 6-flute cutter at the highest feed) exhibits a force spike 5–10$\times$ larger than all other tests, consistent with a tool-failure event observed during the experiment. The dataset provides a systematic basis for comparing tool performance on a compositionally heterogeneous extraterrestrial workpiece and supports ongoing research into advanced manufacturing processes relevant to in-space resource utilization.

**Keywords:** meteorite machining, end milling, cutting forces, EMUGE-Franken, machinability, heterogeneous materials

## 1. INTRODUCTION

Manufacturing science has traditionally focused on engineering alloys whose composition and microstructure are tightly controlled. Iron meteorites represent a fundamentally different class of workpiece: their composition and phase distribution reflect billions of years of natural processing in space, resulting in Widmanstätten iron–nickel banding, silicate inclusions, and localized carbide or sulfide phases that can produce abrupt changes in hardness at the cutting edge [Buchwald, 1975]. These features make meteorite machining an extreme case study in heterogeneous material removal.

Beyond fundamental scientific interest, the ability to manufacture asteroidal or meteoritic material is relevant to long-term in-space manufacturing and resource utilization concepts [Meurisse et al., 2018]. Understanding how commercial cutting tools respond to these materials is a necessary first step toward developing process guidelines for future In-Situ Resource Utilization (ISRU) scenarios. The immediate contribution of the present work is to characterize the terrestrial machinability of a highly heterogeneous Fe–Ni workpiece; ISRU relevance is a longer-term motivation, since ISRU feedstock would ultimately be asteroidal metal or regolith rather than a curated terrestrial specimen.

The Muonionalusta meteorite, an IVA iron meteorite recovered in northern Sweden, was selected as the test material because it is metallurgically well-characterized and available in laboratory-scale quantities. The collaboration between Michigan State University (MSU) and EMUGE-Franken was established to leverage industrial tooling expertise and to rapidly screen multiple

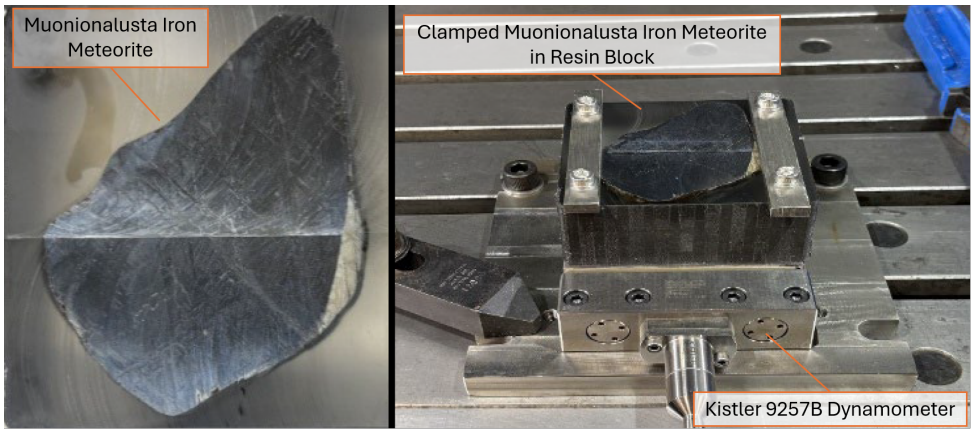



Figure 1. Experimental Setup.

cutter designs in a realistic machining setup. This paper reports the experimental design, data acquisition approach, and preliminary observations from the study.

## 2. BACKGROUND

Iron meteorites of the IVA classification, such as Muonionalusta, are composed predominantly of kamacite (body-centered cubic Fe–Ni, ∼6 wt% Ni) and taenite (face-centered cubic Fe–Ni, ∼30–50 wt% Ni) arranged in the characteristic Widmanstätten pattern. This banded microstructure creates periodic hardness variation at the sub-millimeter scale (kamacite band width ∼0.3 mm; Muonionalusta is a fine octahedrite [Buchwald, 1975]), which directly influences the cutting force signals experienced by a milling tool [Krot et al., 2014].

Previous work on machining of high-nickel iron alloys suggests that tool wear, cutting force stability, and surface finish are highly sensitive to both tool geometry and cutting parameters [Ezugwu & Wang, 1997]. Although meteoritic iron has long been worked into artisanal products such as jewellery and knives [Aerolite Meteorites, n.d.; Oppenheimer, n.d.], no systematic, instrumented (force-measured) study of end milling applied specifically to iron meteorite material using modern coated carbide tools has been reported in the open literature. This study is designed to begin to address that gap at a preliminary level and to generate a dataset that supports future systematic experiments.

EMUGE-Franken tooling was selected because of the company's established expertise in aerospace-grade milling applications, particularly in difficult-to-cut materials such as titanium and nickel-based superalloys. The Aero 5, TiNoxNF, and Topcut cutter families represent distinct geometrical and coating strategies that can be expected to respond differently to the hard, heterogeneous meteorite matrix.

## 3. EXPERIMENTAL SETUP

*Workpiece Material.* The workpiece material was a block of Muonionalusta meteorite (IVA iron, ∼7.8 wt% Ni, Widmanstätten structure with kamacite bandwidth ∼0.3 mm (fine octahedrite)). The sample was prepared with a flat milled reference surface prior to the experiment to ensure consistent initial conditions as seen in Figure 1

*Cutting Tools.* Three families of solid carbide end mills supplied by EMUGE-Franken were




Figure 2. Representative EMUGE-Franken Topcut solid-carbide end mill.

evaluated:

- Aero 5 (5-flute, designed for aerospace aluminum and titanium alloys; CrN coating)
- TiNoxNF (4-flute, optimized for titanium and nickel-based alloys with AlTiN-based coating)
- Topcut (4-flute and 6-flute configurations, general-purpose high-performance end mill; TiAlN coating)

All tools had a nominal diameter of 1/4 in. A representative cutter is shown in Figure 2.

*Machine Tool and Conditions.* Experiments were carried out at the MSU Engineering Research Center on a HAAS VF4 vertical CNC machining center. All cutting was performed under end-milling conditions with down-milling orientation and in dry milling conditions.

*Force Measurement and Data Acquisition.* Cutting forces were measured using a Kistler 9257B table-type dynamometer. Four measurement channels (Fx, Fy, Fz, and moment— were recorded simultaneously in LabVIEW at a sampling rate of 6,000 samples/s per channel (6 kHz; $\Delta t = 0.000167$ s).

## 4. TEST MATRIX

A total of 21 milling conditions were tested across the three cutter families. The test matrix was designed to capture the effect of feed rate within each tool family and to explore two larger step-over conditions with TiNoxNF and Topcut tools. Table 1 summarizes all tested conditions.

Table 1. Experimental Test Matrix—EMUGE-Franken Tools on Muonionalusta Meteorite

| Tool Family | Flutes | Spindle Speed | Ax. Depth | Feed rate [mm/min] | Notes |
|---|---|---|---|---|---|
| Aero 5 | 5 | S688 | 1 mm | F61 / F122 / F244 | 3 feed levels |
| TiNoxNF | 4 | S688 | 1 mm | F50 / F100 / F200 | 3 feed levels |
| TiNoxNF | 4 | S917 | 3 mm | F280 | 40% step-over |
| TiNoxNF | 4 | S917 | 6 mm | F280 | 20% step-over |
| Topcut | 4 | S688 | 1 mm | F50 / F100 / F200 | 3 feed levels |
| Topcut | 4 | S917 | 1 mm | F100 | 2 repeat runs |
| Topcut | 4 | S917 | 1.2 mm | F100 | Extended depth |
| Topcut | 4 | S917 | 6 mm | F280 | 20% step-over |
| Topcut | 6 | S688 | 1 mm | F74 / F148 / F200 / F296 | 4 feed levels |

Table 2. Data Acquisition Parameters

| Parameter | Value / Notes |
|---|---|
| Force measurement | Kistler 9257B table-type dynamometer |
| Data acquisition software | LabVIEW (National Instruments) |
| Number of channels | 4 (Fx, Fy, Fz, and moment) |
| Sampling rate | 6 kHz |
| Sampling interval | 0.000167 s |
| Signal units | Newton |
| File format | Tab-delimited, LabVIEW .lvm format |

## 5. DATA STRUCTURE AND QUALITY

Each test was saved as a tab-delimited LabVIEW Measurement file (.lvm) containing four synchronized voltage channels. The acquisition parameters are summarized in Table 2.

An initial review of the dataset revealed that all files have a consistent structure that enables automated batch processing. Cutting forces vary visibly across feed conditions in preliminary inspections, suggesting a detectable force–feed relationship even before calibration. One record, however, is not a steady-state cut—the 6-flute Topcut at the highest feed (Topcut6fl-S688-1mm-F296) shows amplitudes 5–10$\times$ larger than every other test, with the failure onset near 24–25 s consistent with a tool-failure event observed during the experiment (Section 7; Figure 5). This record should be treated as a failure signature rather than a process measurement. Entry and exit transients are present in the time-domain records and should be windowed out before steady-state metrics are computed. A representative steady-state record (Aero 5, F61) is shown in Figure 3.

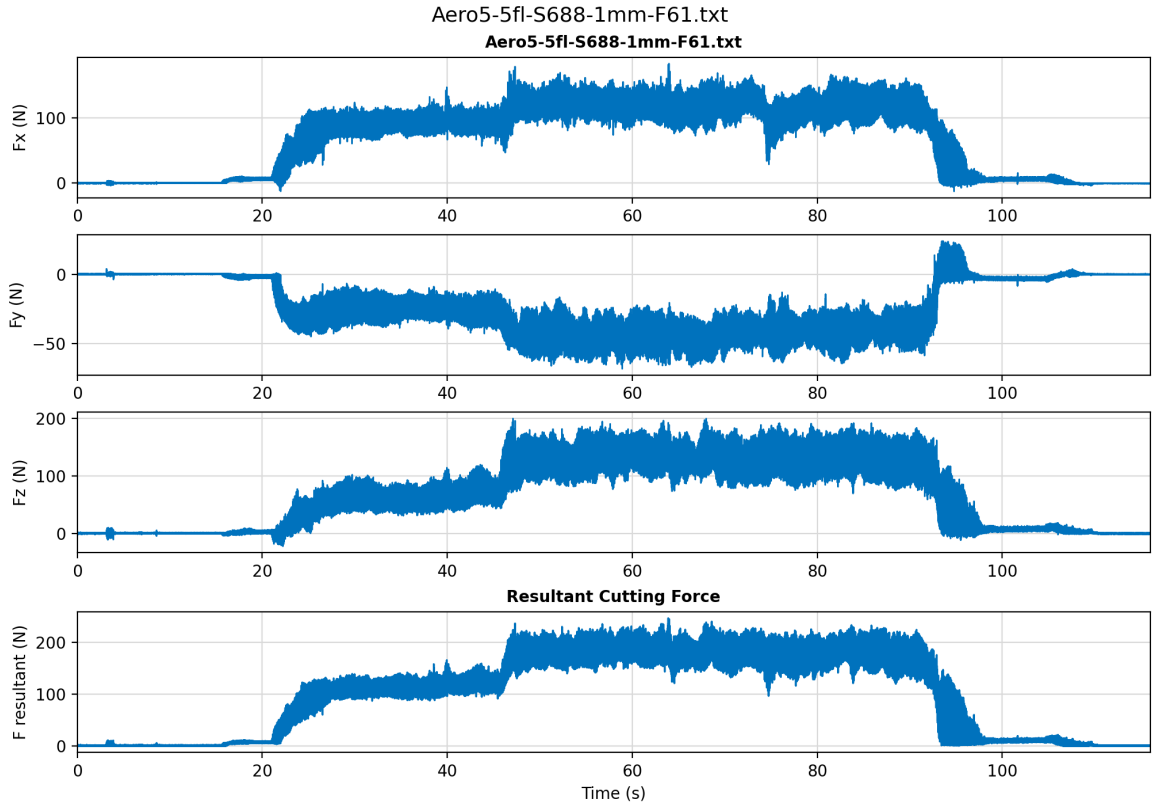



Figure 3. Representative cutting-force record (Aero 5, 5-flute, S688, 1 mm, F61).

Table 3. RMS resultant cutting force, $F_R = \sqrt{F_x^2 + F_y^2 + F_z^2}$, versus feed-per-tooth level (speed code S688, 1 mm axial depth).

| **Tool (flutes)** | **Low** $f_z$ | **Med** $f_z$ | **High** $f_z$ |
|---|---|---|---|
| Aero 5 (5) | 125 N (F61) | 171 N (F122) | 220 N (F244) |
| TiNoxNF (4) | 56 N (F50) | 85 N (F100) | 122 N (F200) |
| Topcut (4) | 59 N (F50) | 82 N (F100) | 114 N (F200) |
| Topcut (6) | 93 N (F74) | 111 N (F148) | 731 N† (F296) |

†Contaminated by the tool-failure event (Section 7); not a valid steady-state point.

*Preliminary Force–Feed Trend.* The cutting force signals show a clear, monotonic increase with feed for every tool family (Table 3). When the feed codes are grouped by approximately constant feed per tooth (feed code divided by flute count), the families fall in a relatively narrow band at matched feed per tooth, with Aero 5 consistently highest.

Figure 4 overlays all records on a common time axis: the F296 record (tool failure) is the clear outlier, which otherwise share a common envelope.

## 6. ANALYSIS METHODOLOGY

The following step-by-step workflow is proposed for processing the complete dataset:

1. Import all files automatically; parse metadata (tool family, flute count, speed code, feed value, step-over) from file names.
2. Plot raw channel voltages for each test; visually inspect for anomalies, entry/exit transients, and signal saturation.
3. Window the steady-state cutting region, excluding ramp-in and ramp-out segments.
4. Compute descriptive metrics per channel: mean, RMS, standard deviation, and peak-to-peak

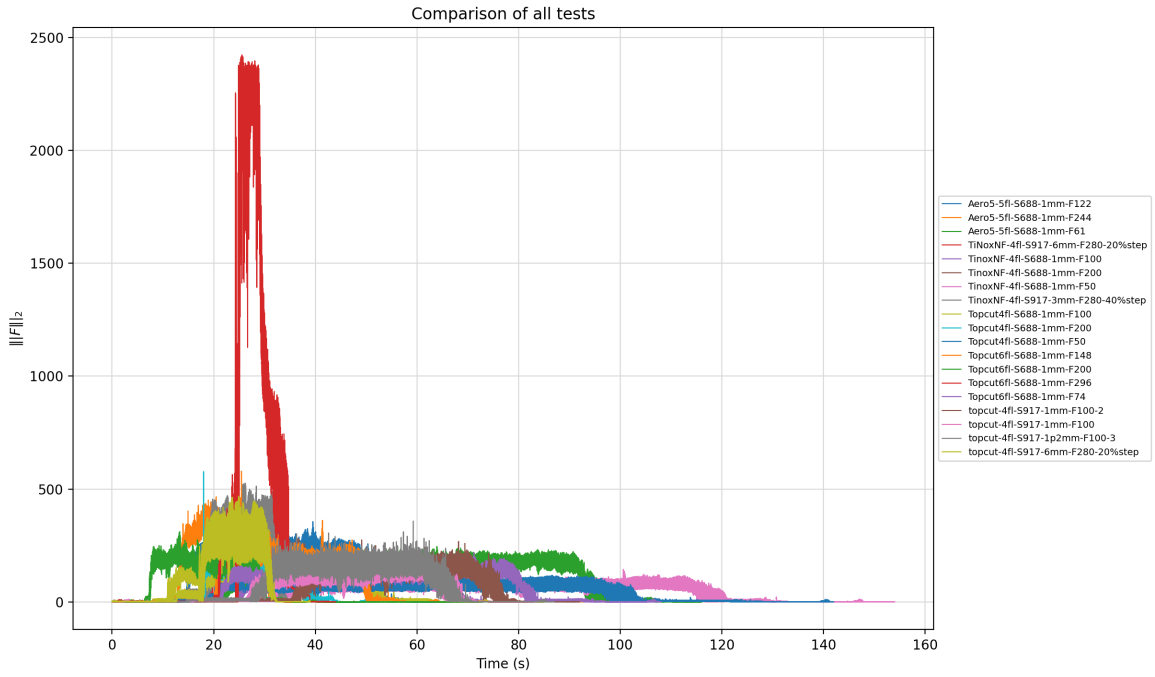



Figure 4. Combined magnitudes for all test records on a common time axis.

amplitude.

5. Apply the dynamometer calibration matrix to convert voltages to force components (Fx, Fy, Fz, and moment if applicable).
6. Compare average cutting force and force oscillation content across tool families and feed levels.
7. Perform frequency-domain analysis (FFT/PSD) to identify potential chatter frequencies or harmonic excitation related to tooth-pass frequency.
8. Identify which tool produced the most stable cutting response and which conditions generated large transients or instability signatures.
9. Correlate force behavior with observed surface quality, chip morphology, tool wear, and operator notes from the test day.

## 7. DISCUSSION

This study represents an important first step toward understanding how modern commercial milling tools behave when cutting meteorite material. The Muonionalusta meteorite's Widmanstätten microstructure with kamacite and taenite bands creates a periodically varying cutting resistance that has no direct analogue in conventional aerospace alloy machining. Because the band width is sub-millimeter, the cutting edge traverses several bands per revolution at the feeds used here, so any band-induced force modulation may be partly averaged out. This heterogeneity is expected to produce force oscillations that are not synchronized with the tooth-pass frequency, making frequency-domain analysis particularly informative for identifying instability.

The three tool families tested represent distinct design philosophies. The Aero 5 (5-flute) is optimized for high material removal rates in lighter aerospace alloys and offers high stiffness through its flute count. The TiNoxNF is designed for difficult-to-cut materials with high chemical affinity for the tool, suggesting that its coating may perform differently against the iron-nickel matrix of the meteorite than against conventional titanium workpieces. The Topcut in 6-flute configuration is expected to distribute cutting forces more evenly, potentially offering an advantage in terms of surface finish on the heterogeneous material.

The feed sweep within each tool family (three to four feed levels) will allow fitting of a force-feed relationship of the form $F_c = C \cdot f_z^k$, where $F_c$ is the resultant cutting force, $f_z$ is the feed per tooth, and $k$ is an empirically determined exponent. Comparison of the exponent $k$ across tool families may reveal differences in the force-generation mechanism related to tool geometry and coating.

The collaboration with Evan Duncanson from EMUGE-Franken contributed significant practical value: real-time qualitative assessment of chip color, morphology, cutting sound, and surface appearance during the experiments cannot be captured in force data alone. These observations, once formally recorded and incorporated into the dataset, will be essential for a complete interpretation of the force signals.

The larger step-over conditions (3 mm and 6 mm axial depth with 20–40% radial step-over) tested with TiNoxNF and Topcut tools offer a first look at force levels under more aggressive

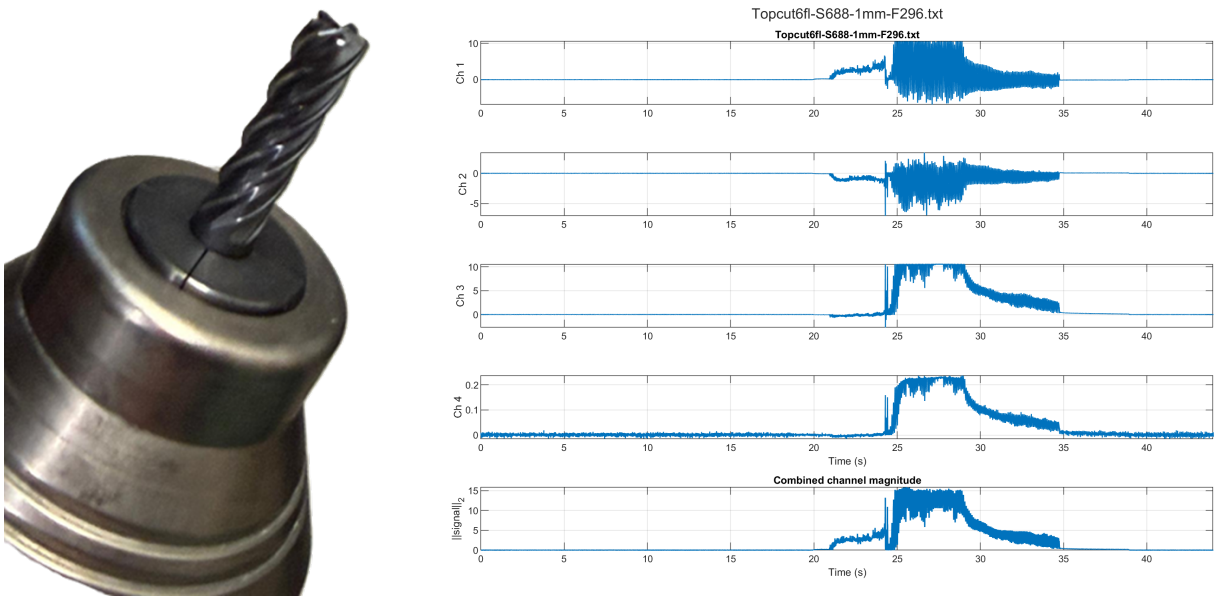



Figure 5. Tool-failure event (Topcut, 6-flute, S688, 1 mm, F296): (left) fractured end-mill tip; (right) the corresponding force record.

material removal scenarios. These conditions are particularly relevant for evaluating whether the tools can sustain stable cutting when the effective engagement area increases and the probability of encountering phase boundaries per unit time rises.

Several design limitations bound the strength of any cross-tool conclusion. (i) The matrix is exploratory rather than balanced: spindle speed changes with axial depth (S688 at 1 mm, S917 at 3/6 mm), and the 3 mm/40% and 6 mm/20% cases differ in both depth and step-over, so these effects are confounded. (ii) The aggressive (large step-over) conditions were run only with TiNoxNF and Topcut, so Aero 5 cannot be compared at those conditions. (iii) All cuts were taken on a single block in one session, so tool wear and cut location are confounded with tool family, and with essentially one run per condition (a single repeated point) repeatability is not yet quantified. (iv) The tool-failure record (Figure 5) indicates that the most aggressive 6-flute condition exceeded a process limit. These points motivate a balanced, replicated follow-up campaign that includes a reference workpiece (e.g. a conventional steel or Ti alloy) to place the meteorite forces in context.

## 8. CONCLUSIONS

A collaborative milling experiment was successfully completed on Muonionalusta iron meteorite material at Michigan State University with EMUGE-Franken support. The following conclusions are drawn from the preliminary analysis:

- A total of 21 milling conditions covering three cutter families (Aero 5, TiNoxNF, Topcut), multiple flute counts (4, 5, 6), and feed rates spanning F50 to F296 mm/min were successfully completed and recorded.
- Cutting force data acquired at 6 kHz via a Kistler dynamometer have a clean, consistent structure suitable for automated batch processing and both time-domain and frequency-domain analysis.

- Cutting force signals rise monotonically with feed for every tool family (Table 3), and at matched feed per tooth the families differ only modestly (Aero 5 highest).
- The 6-flute Topcut at the highest feed (F296) produced a force signature 5–10× larger than all other tests, consistent with a tool-failure event recorded during the experiment—a concrete machinability limit for the most aggressive condition tested.
- The one-day screening format was effective in generating a broad comparative dataset; targeted follow-up experiments can now be designed around the most promising tool–condition combinations identified from this data.
- These results lay the groundwork for a systematic machinability study of extraterrestrial materials and may contribute to process development for in-space manufacturing applications.

## ACKNOWLEDGEMENT

The authors gratefully acknowledge EMUGE-Franken for providing the cutting tools used in this study and for their valuable technical support and process engineering expertise. The authors also thank Jianxin Zhao for assistance with the CNC machining and data acquisition systems. The meteorite material used in this work was obtained from Aerolite Meteorites, whose support in facilitating material acquisition is sincerely appreciated. Access to machining and instrumentation facilities was provided by the MSU Engineering Research Center. This work was supported in part by the National Aeronautics and Space Administration (NASA) under Award No. 80NSSC25M7087 through the Michigan Space Grant Consortium (MSGC).

## REFERENCES

1. **Buchwald, V.F. (1975)**, Handbook of Iron Meteorites, University of California Press, Berkeley.

2. **Ezugwu, E.O. and Wang, Z.M. (1997)**, “Titanium alloys and their machinability—a review”, Journal of Materials Processing Technology, Vol. 68, No. 3, pp. 262–274.

3. **Krot, A.N., Keil, K., Scott, E.R.D., Goodrich, C.A. and Weisberg, M.K. (2014)**, “Classifica tion of meteorites and their genetic relationships”, in Treatise on Geochemistry, 2nd ed., Vol. 1, Elsevier, pp. 1–63.

4. **Meurisse, A., Makaya, A., Willsch, C. and Sperl, M. (2018)**, “Solar 3D printing of lunar regolith”, Acta Astronautica, Vol. 152, pp. 800–810.

5. **EMUGEFranken (2025)**, Aerospace Milling Tool Catalog—Aero 5, TiNoxNF, Topcut Series, EMUGEFranken GmbH & Co. KG, Lauf a.d. Pegnitz, Germany.

6. **Altintas, Y. (2012)**, Manufacturing Automation: Metal Cutting Mechanics, Machine Tool Vibrations, and CNC Design, 2nd ed., Cambridge University Press, Cambridge, UK.

7. **Kienzle, O. (1952)**, “Die Bestimmung von Kräften und Leistungen an spanenden Werkzeugen und Werkzeugmaschinen”, VDIZ, Vol. 94, pp. 299–305. August 19–21,

2026, Istanbul, Türkiye

8. **Scott, E.R.D. and Wasson, J.T. (1975)**, “Classification and properties of iron meteorites”, Reviews of Geophysics, Vol. 13, No. 4, pp. 527–546. August 19–21, 2026, Istanbul, Türkiye

9. **Aerolite Meteorites, Inc. (n.d.)**, Authentic meteorites and meteorite jewellery [commercial supplier], Benson, AZ, USA, https://aerolite.org/ (accessed 25 May 2026).

10. **Oppenheimer, T. (n.d.)**, “What do you do with a meteorite? Make a knife,” Craftsmanship Magazine, https://craftsmanship.net/sidebar/whatdoyoudowitha meteorite-m akeaknife/ (accessed 25 May 2026).

# DEVELOPMENT OF A PROCESS-CONTROLLED CALENDERING MACHINE

**M. Çağrı ÖZKADER**, *mustafacagriozkader@hitit.edu.tr* Hitit University, 19030, Çorum, Türkiye

**Barış ÇETİN,** *cetin.baris@fnss.com.tr* FNSS Savunma Sistemleri AŞ, Ankara, Türkiye

**Öncü AKYILDIZ**, *oncuakyildiz@hitit.edu.tr* Hitit University, 19030, Çorum, Türkiye

## ABSTRACT

In this study, a precision-controlled prototype calendering machine was developed to enhance the fabrication quality of lithium-ion battery electrodes. The system integrates a robust control infrastructure engineered to provide precise, real-time regulation over interconnected process parameters: roller speeds up to 5 m/min, operating temperatures up to 150 ℃, and micro-adjustable compression forces reaching 20 kN. This control infrastructure was specifically designed to balance between densification and resistive losses, ensuring consistent electrode properties. Preliminary functional validation of the physical prototype demonstrates significant improvements in compaction density across coatings.

**Keywords:** Lithium ion battery, Calendering, Process control

## 1. INTRODUCTION

The manufacturing of high-performance lithium-ion batteries relies heavily on electrode film processing, which begins with the deposition of an active material slurry onto a metallic current collector, followed by drying. The subsequent calendering process - where the electrode film is compressed between rotating rollers - is a critical step for reducing porosity and achieving the target energy density (1). The effectiveness of the calendering process is highly sensitive to fluctuations in mechanical and thermal settings (2).

Currently, commercial calendering machinery often lacks the high-fidelity, real-time monitoring and multi-parameter control required for advanced materials research. Many existing systems fail to provide integrated, synchronous regulation of roller speed, temperature, and compression force, leading to inconsistencies in electrode microstructure and performance. Furthermore, there is a clear academic and practical necessity for laboratory-scale systems that bridge the gap between bench-top experiments and industrial-scale production. Addressing this research gap, this study presents the design and development of a precision-controlled calendering prototype. The system features a sophisticated, computer-based architecture capable of accurately monitoring and recording critical process parameters -specifically roller speed, electrode gap thickness, thermal load, and compression force- thereby establishing a robust foundation for repeatable, high-consistency electrode fabrication.

## 2. MATERIALS AND METHODS

The calendaring device was built using CNC-machined aluminum components and Ø100 × 200 mm induction hardened chrome plated stainless steel bars selected for their wear resistance and surface finish quality under compressive loads. The system enables adjustable roller gap control through a stepper-motor-driven linear motion mechanism, controlled heating via resistive heaters connected to the main control board, roller rotation driven by a geared DC motor, and force measurement using load cells. All these parameters are monitored via a computer software connected to a microcontroller on main control board.

A structured parametric experimental matrix was designed to evaluate the performance of the prototype. Three primary operational factors were investigated across two distinct engineering levels: calendering force compaction force (100 N vs. 400 N), operating temperature (25 ℃ vs. 75 ℃), and roller speed (0.1 m/min vs. 2 m/min) (3). The combination of these variables was executed across four distinct experimental trials to observe their coupled effects on the physical properties of layered oxide lithium ion battery electrodes, using an un-calendered sample as a baseline control. Following the trials, the physical metrics of the processed electrodes were quantitatively determined. The structural evolution was characterized by tracking the electrode thicknesses before and after calendering $\delta_o$ and $\delta$), and the electrode mass per unit area (m), the post-calendering compact density ($\rho$), and the porosity ($\phi$) of the active material layer.

## 3. RESULTS AND DISCUSSION

The developed calendering platform (Figure 1) is engineered as a high-precision, process-controlled system specifically designed to optimize the density of battery electrodes through modulation of mechanical and thermal parameters. The apparatus' compact and modular design is specifically tailored for seamless integration into inert glovebox environments, facilitating material screening without compromising the electrochemical integrity of sensitive active materials. By offering a wide range of rolling speeds, the system allows for the effective management of the trade-off between reduced charge transfer resistance and increased ionic resistance, providing a robust hardware foundation for advanced battery research.

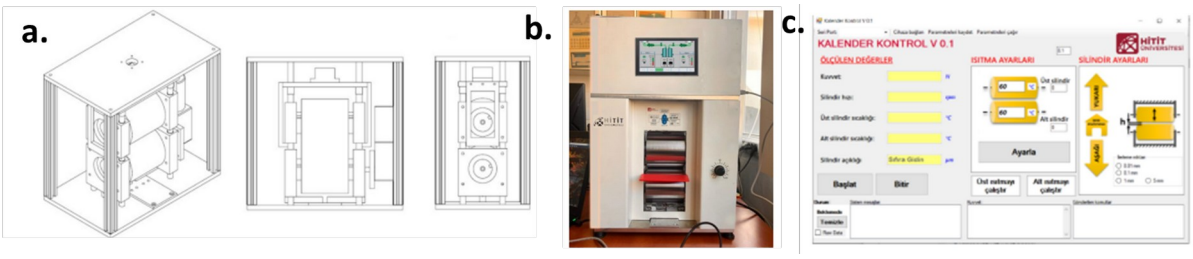


Figure 1. a. Technical schema b. Manufactured system c. PC software

To evaluate the performance of the developed prototype calendering machine, physical compaction trials were conducted under a structured multi-variable parameter matrix.

Table 1. Electrode thicknesses before and after calendering ($\delta_o$ and $\delta$), electrode mass per unit area (m), densities (ρ), and porosity ($\phi$) at different temperature (T), forces (F) and speeds (v).

| | T (℃) | F(N) | v(m/min) | $\delta_o$ (μm) | $\delta$ (μm) | m (mg/cm$^2$) | ρ (g/cm$^3$) | $\phi$ (%) |
|---|---|---|---|---|---|---|---|---|
| Test 0 | - | - | - | 30.63 | 30.63 | 5.80 | 1.67 | 70.52 |
| Test 1 | 25 | 100 | 0.1 | 40.15 | 31.90 | 6.45 | 1.79 | 68.52 |
| Test 2 | 25 | 400 | 2.0 | 35.90 | 28.20 | 6.10 | 1.91 | 66.53 |
| Test 3 | 75 | 100 | 2.0 | 38.15 | 30.40 | 6.85 | 1.99 | 64.92 |
| Test 4 | 75 | 400 | 0.1 | 35.57 | 28.95 | 6.60 | 2.02 | 64.51 |

The experimental data detailed in Table 1 demonstrates a highly systematic and predictable response to the machine's micro-adjustable compression profiles. While the un-calendered baseline (Test 0) exhibited a lower density of 1.67 g/cm$^3$ and a high porosity of 70.52%, the application of the synchronized process parameters in Tests 1–4 yielded a steady, controlled reduction in electrode thickness (δ). The combination of elevated compression forces (F up to 400 N), thermal assistance (T up to 75 ℃) and longer application times (v down to 0.1 m/min) directly enhanced the plastic deformation behavior of the composite matrix, driving the final electrode compaction density incrementally up to a peak of 2.02 g/cm$^3$ in Test 4. This mechanical densification directly corresponds to a linear, controlled reduction in electrode porosity ($\phi$), which successfully dropped from the initial 70.52 % baseline down to 64.51 %. In lithium-ion battery manufacturing, the ability to fine-tune porosity within these strict margins is paramount; sufficient compaction is mandatory to lower charge transfer resistance and prevent active material delamination, while avoiding over-compaction that restricts electrolyte wetting (4). The highly predictable, step-wise scaling of density and porosity across the multi-parameter matrix confirms the excellent repeatability, high load-bearing fidelity, and robust process-control capabilities of the laboratory-scale prototype under dynamic manufacturing conditions.

## 4. CONCLUSION

In conclusion, this process-controlled calendering system provides a high-precision capability for optimizing the energy density of lithium-ion battery electrodes. By enabling exact control over speed and compaction force with a compact design, the device maintains the ideal balance between ionic resistance and charge transfer, ensuring enhanced performance. Preliminary functional testing of the physical prototype demonstrates that this integrated control architecture achieves the mechanical stability and geometric repeatability necessary for consistent electrode fabrication. Future work will leverage this system to establish

comprehensive, quantitative correlation maps between dynamic calendering parameters and long-term electrochemical cell performance.

## 5. REFERENCES

1. **Reynolds, C. D., Slater, P. R., Hare, S. D., Simmons, M. J. H., & Kendrick, E. (2021).** A review of metrology in lithium-ion electrode coating processes. Materials and Design, 209, 109971.

2. **Ge, R., Cumming, D. J., & Smith, R. M. (2022).** Discrete element method (DEM) analysis of lithium ion battery electrode structures from X-ray tomography-the effect of calendering conditions. Powder Technology, 403, 117366.

3. **Nikpour, M., Liu, B., Minson, P., Hillman, Z., Mazzeo, B. A., & Wheeler, D. R. (2022).** Li-ion Electrode Microstructure Evolution during Drying and Calendering. Batteries, 8(9).

4. **Luglio, A., Fink, K., Usseglio-Viretta, F., Colclasure, A., Walker, P., Mangum, J. S., & Brow, R. (2025).** Maximizing calendering effects through the mechanical pulverization of Co-free nickel-rich cathodes in lithium-ion cells. MRS Bulletin, 50(9), 1013–1022.

## 6. ACKNOWLEDGEMENT

This work was supported by the Hitit University, research Grant No: MUHMİTEK19001.24.001.

# TÜRKÇE BİLDİRİLER

## TURKISH PAPERS

# YÜKSEK GÜVENİLİRLİK GEREKTİREN SAVUNMA SANAYİİ İMALAT SÜREÇLERİNDE YAPAY ZEKÂ DESTEKLİ ÜRETİM VE KALİTE GÜVENCE YAKLAŞIMI

***Mehmet Can BAYTEKİN**, can.baytekin@roketsan.com.tr, ROKETSAN, 06780, Ankara, Türkiye*

***Beyzanur ZEYBEK**, beyzanur.zeybek@roketsan.com.tr, ROKETSAN, 06780, Ankara, Türkiye*

## ÖZET

Bu çalışma, yüksek güvenilirlik gerektiren savunma sanayii imalat süreçlerinde üretim ve kalite güvence faaliyetlerini destekleyen endüstriyel yapay zekâ uygulamalarını sunmaktadır. Bilgisayarlı görü, görsel-dil modelleri, video analitiği ve doğal dil işleme yaklaşımları; hata tespiti, bileşen muayenesi, teknik resim incelemesi ve kalite kayıtları analizi için bütünleşik bir çerçevede ele alınmıştır. Ön pilot değerlendirmelerde, bazı manuel görsel kontrol adımlarının yapay zekâ desteğiyle yaklaşık 1,5 kat daha hızlı tamamlanabildiği ve görsel hata tespitinde yaklaşık %85 F1 skoruna ulaşıldığı gözlemlenmiştir.

**Anahtar Kelimeler:** Yapay zekâ, kalite güvence, üretim izleme, bilgisayarlı görü, görsel-dil modelleri, savunma sanayii imalatı

## ABSTRACT

This paper presents industrial artificial intelligence applications supporting production and quality assurance in high-reliability defense manufacturing. Computer vision, vision-language models, video analytics, and natural language processing are addressed within an integrated framework for defect detection, component inspection, technical drawing review, and quality record analysis. Preliminary pilot evaluations indicate that selected manual visual inspection steps can be completed approximately 1.5 times faster with AI support, while visual defect detection achieved an F1 score of approximately 85%. The proposed approach positions AI as a human-supervised decision-support capability rather than an autonomous inspection authority.

**Keywords:** Artificial intelligence, quality assurance, production monitoring, computer vision, vision-language models, defense manufacturing

## 1. GİRİŞ

Modern savunma sistemleri, tüm yaşam döngüsü boyunca yüksek güvenilirlik, sıkı kalite güvence ve sürekli izlenebilirlik gerektirmektedir. Üretim ve kalite güvence faaliyetleri yalnızca nihai muayene ile sınırlı olmayıp; sistem entegrasyonu, test başarımı, bakım planlaması ve

uzun dönem operasyonel güvenilirlik üzerinde doğrudan etkiye sahiptir. Bu nedenle üretim ve kaliteyle ilişkili sapmaların erken aşamalarda tespit edilmesi, yorumlanması ve izlenebilir şekilde kayıt altına alınması kritik önemdedir.

Savunma sanayii üretim süreçleri; görsel muayene, teknik dokümantasyon kontrolü, kontrol listesi temelli incelemeler, süreç izleme ve kalite kayıtları gibi uzman odaklı iş akışlarına dayanmaktadır. Ancak artan ürün karmaşıklığı, çok aşamalı muayene gereksinimleri, büyüyen veri hacmi ve tutarlı karar verme ihtiyacı, manuel inceleme süreçlerini zorlaştırmaktadır. Bu nedenle uzmanları destekleyen, tekrarlayan iş yükünü azaltan ve karar standardizasyonunu artıran yapay zekâ tabanlı sistemlere ihtiyaç duyulmaktadır.

Yapay zekâ ve veri odaklı yöntemler, modern imalat ortamlarında akıllı üretim, kestirimci kalite ve süreç odaklı karar destek uygulamaları için önemli araçlar hâline gelmiştir [Zhong, 2017; Tercan, 2022]. Bilgisayarlı görü yöntemleri görsel hata tespiti ve konumlandırma için kullanılabilirken [Redmon, 2016; He, 2017], endüstriyel anomali tespiti çalışmaları sınırlı hata örnekleri, hata çeşitliliği ve değişken muayene koşullarının dikkate alınması gerektiğini göstermektedir [Bergmann, 2019; Liu, 2024]. Görsel-dil modelleri bileşen muayenesinde görsel kanıtların metinsel kriterlerle ilişkilendirilmesini desteklemekte [Radford, 2021]; doğal dil işleme yöntemleri kalite kayıtlarının analizinde [Vaswani, 2017; Devlin, 2019], video analitiği ise süreç ve test kayıtlarında olağan dışı örüntülerin belirlenmesinde kullanılabilmektedir [Chandola, 2009; Liu, 2024].

Bu çalışma, yüksek güvenilirlik gerektiren savunma sanayii imalat ortamlarında üretim ve kalite güvence süreçlerini destekleyen endüstriyel yapay zekâ uygulamalarını bütünleşik bir yol haritası kapsamında ele almaktadır. Kullanım senaryoları; bilgisayarlı görü tabanlı görsel hata tespiti, görsel-dil modeli destekli bileşen muayenesi, kontrol listesi temelli teknik resim incelemesi, video tabanlı süreç anomalisi tespiti ve doğal dil işleme tabanlı kalite kayıtları analizinden oluşmaktadır.

Çalışmanın özgün katkısı, bu yöntemleri yalnızca ayrı uygulamalar olarak değil; güvenli kurum içi çalıştırma, insan denetimli doğrulama, izlenebilirlik, model yaşam döngüsü yönetimi ve mevcut üretim iş akışlarıyla entegrasyon gereksinimleriyle birlikte ele alan bütünleşik bir uygulama çerçevesi sunmasıdır. Bu yönüyle çalışma, yapay zekâ destekli üretim ve kalite güvence uygulamalarını model başarımının ötesinde; yaşam döngüsü, karar standardizasyonu, süreç izlenebilirliği ve operasyonel iyileştirme perspektifiyle değerlendirmektedir.

## 2. ENDÜSTRİYEL MOTİVASYON VE YAŞAM DÖNGÜSÜ PERSPEKTİFİ

Modern bir savunma sisteminin yaşam döngüsü; tasarım, imalat, kalite güvence, entegrasyon, test, operasyon, bakım ve geri bildirim aşamalarını içermektedir. Bu aşamalardan birinde alınan kararlar veya gözlemlenen sapmalar, sonraki aşamaları doğrudan etkileyebilmektedir. Bu nedenle yaşam döngüsü odaklı kalite yönetimi, farklı süreç aşamalarından gelen bilgilerin toplanmasını, analiz edilmesini ve anlamlı şekilde yorumlanmasını gerektirmektedir.

Yüksek güvenilirlik gerektiren imalat ortamlarında üretim ve kalite güvence süreçleri; parça görüntüleri, muayene raporları, teknik resimler, süreç/test videoları, uygunsuzluk kayıtları, ölçüm sonuçları ve uzman yorumları gibi heterojen veri kaynakları üretmektedir. Bu kaynakların birlikte analiz edilmesi, tekrar eden kalite problemlerinin, süreç değişkenliklerinin ve iyileştirme fırsatlarının daha bütüncül şekilde anlaşılmasını sağlayabilir. Yapay zekâ yöntemleri, bu verilerin mühendisler, kalite personeli ve karar vericiler için uygulanabilir bilgiye dönüştürülmesini desteklemekte; bu yaklaşım akıllı imalat ve kestirimci kalite çalışmalarıyla da uyum göstermektedir [Zhong, 2017; Tercan, 2022].

Bu çalışmada ele alınan uygulamaların temel motivasyonu, yapay zekânın üretim ve kalite güvence iş akışlarında yardımcı bir kabiliyet olarak kullanılmasıdır. Amaç, uzman karar mekanizmasını ortadan kaldırmak veya nihai kalite kararlarını tamamen otomatikleştirmek değil; görünürlüğü artırmak, tekrarlayan inceleme yükünü azaltmak, karar standardizasyonunu güçlendirmek ve potansiyel problemlerin daha erken fark edilmesini sağlamaktır. Bu nedenle önerilen yaklaşım insan denetimli bir yapı üzerine kuruludur; yapay zekâ çıktıları karar destek girdileri olarak kullanılmakta, nihai değerlendirme ve onay alan uzmanlarında kalmaktadır.

Endüstriyel yapay zekâ yol haritası üç temel hedefe odaklanmaktadır. Birincisi, bilgisayarlı görü, görsel-dil modelleri ve video analitiğiyle muayene kabiliyetini iyileştirmektir. İkincisi, kalite kayıtları, muayene notları ve teknik dokümantasyondan yapılandırılmış bilgi çıkararak süreç izlenebilirliğini artırmaktır. Üçüncüsü ise yapay zekâ destekli analiz kabiliyetini kestirimci bakım, gerçek zamanlı izleme, otomatik kök neden analizi ve üretim-kalite geri bildirim döngüleri gibi yaşam döngüsü seviyesinde karar destek uygulamalarına genişletmektir. Bu yönelim, üretim ve süreç verilerinin risk tahmini, geri bildirim üretimi ve yaşam döngüsü seviyesinde karar destek amacıyla kullanılmasını ele alan çalışmalarla uyumludur [Tercan, 2022; Xu, 2021].

Yaşam döngüsü perspektifinden bakıldığında, teknik resim uygunluk incelemesi tasarım ve mühendislik dokümantasyonu aşamasını; görsel hata tespiti ve bileşen muayenesi imalat ve kalite güvence aşamalarını; video tabanlı anomali tespiti entegrasyon, süreç izleme ve test faaliyetlerini; kalite kayıtlarının analizi ise geri bildirim, düzeltici faaliyet planlama ve sürekli iyileştirme süreçlerini desteklemektedir. Kestirimci bakım ve bütünleşik karar destek sistemleri

ise operasyon ve idame aşamalarına yönelik planlanan genişletmeler olarak değerlendirilmektedir.

## 3. BÜTÜNLEŞİK ENDÜSTRİYEL YAPAY ZEKÂ YOL HARİTASI

Bu çalışmada sunulan endüstriyel yapay zekâ uygulamaları, bağımsız kavramsal doğrulama çalışmaları yerine bütünleşik bir yol haritası kapsamında ele alınmaktadır. Bu yol haritası; uygun üretim ve kalite güvence problemlerinin belirlenmesi, ilgili yapay zekâ yöntemlerinin seçilmesi, süreç etkisinin değerlendirilmesi ve başarılı uygulamaların yaşam döngüsü seviyesinde karar destek kabiliyetlerine genişletilmesi için yapılandırılmış bir yaklaşım sunmaktadır.

Yol haritası; veri edinimi, ön işleme ve yapılandırma, yapay zekâ tabanlı analiz, insan denetimli doğrulama ve süreç entegrasyonu olmak üzere beş temel katmandan oluşmaktadır. Veri edinimi katmanı; parça görüntüleri, süreç/test videoları, teknik resimler, kontrol listeleri, kalite kayıtları, ölçüm sonuçları ve uzman yorumlarını kapsamaktadır. Bu veriler, analiz öncesinde görüntü iyileştirme, ilgi bölgesi seçimi, kare çıkarımı, optik karakter tanıma, metin temizleme, etiketleme ve yapılandırma gibi ön işleme adımlarından geçirilmektedir.

Yapay zekâ tabanlı analiz katmanında, süreç ihtiyacına göre farklı yöntemler kullanılmaktadır. Görsel hata tespiti için nesne tespiti ve segmentasyon yöntemleri [Redmon, 2016; He, 2017], endüstriyel anomali problemleri için sınırlı hata örneği ve hata çeşitliliğini dikkate alan yaklaşımlar [Bergmann, 2019; Liu, 2024], bileşen muayenesi için görsel-dil modelleri [Radford, 2021], teknik dokümantasyon için doküman anlama yöntemleri [Xu, 2020], kalite kayıtları için doğal dil işleme yöntemleri [Vaswani, 2017; Devlin, 2019] ve süreç/test kayıtları için video analitiği ile anomali tespiti yöntemleri kullanılmaktadır [Chandola, 2009; Liu, 2024]. Gelecek genişletmelerde ise zaman serisi analizi ve kestirimci modelleme yaklaşımlarının kestirimci bakım ve yaşam döngüsü seviyesinde risk değerlendirme amacıyla kullanılması planlanmaktadır [Serradilla, 2022].

Yüksek güvenilirlik gerektiren imalat ortamlarında yapay zekâ çıktıları, uzman incelemesi olmaksızın nihai karar olarak ele alınmamalıdır. Bu nedenle hata bölgeleri, anomali aralıkları, kontrol listesi bulguları ve kalite kayıt özetleri gibi çıktılar karar destek bilgisi olarak kullanılmalı ve resmi kararlar öncesinde alan uzmanları tarafından doğrulanmalıdır. Bu yaklaşım, açıklanabilirlik ve otomasyona uygun düzeyde güven duyulması gereklilikleriyle uyumludur [Arrieta, 2020; Lee, 2004].

Son katman olan süreç entegrasyonu, yapay zekâ uygulamalarının mevcut üretim, kalite güvence, dokümantasyon ve raporlama iş akışlarıyla ilişkilendirilmesini kapsamaktadır. Beklenen çıktı yalnızca model başarımı değil; muayene süresinin azaltılması, hata tespit

kabiliyetinin iyileştirilmesi, izlenebilirliğin artırılması ve uzman kararlarının standartlaştırılması gibi ölçülebilir süreç etkileridir [Zhong, 2017; Tercan, 2022].

Tablo 1'de temel yapay zekâ uygulama alanları, veri kaynakları, kullanılan yaklaşımlar, çıktılar ve beklenen süreç etkileri özetlenmektedir.

Tablo 1 Yapay zekâ destekli üretim ve kalite güvence kullanım senaryolarının özeti.

| Uygulama Alanı | Veri Kaynağı | Yapay Zekâ Yaklaşımı | Çıktı | Beklenen Süreç Etkisi |
|---|---|---|---|---|
| Görsel hata tespiti | Parça görüntüleri | Bilgisayarlı görü, nesne tespiti, segmentasyon | Hata konumu, uygunluk değerlendirme desteği | Daha hızlı ve daha standart muayene |
| Bileşen muayenesi | Bileşen görüntüleri ve muayene notları | Görsel-dil modelleri | Hata açıklaması, kalite karar desteği | Manuel inceleme yükünün azaltılması ve tutarlılığın artırılması |
| Teknik resim incelemesi | Teknik resimler ve kontrol listeleri | OCR, görsel-dil modelleri, kural tabanlı kontroller | Kontrol listesi temelli uygunluk bulguları | Dokümantasyon problemlerinin daha erken tespit edilmesi |
| Video tabanlı anomali tespiti | Süreç ve test videoları | Video analitiği, anomali tespiti | Anomali aralıkları ve olay seviyesinde bulgular | Uzun kayıtların daha hızlı incelenmesi |
| Kalite kayıtları analizi | Kalite formları, uygunsuzluk kayıtları ve notlar | Doğal dil işleme, metin sınıflandırma, kümeleme | Problem grupları, özetler, eğilimler | İzlenebilirliğin artırılması ve kök neden analizi desteği |

## 4. UYGULANAN YAPAY ZEKÂ UYGULAMALARI

Bu bölümde, endüstriyel yapay zekâ yol haritası kapsamında ele alınan uygulamalar sunulmaktadır. Uygulamalar; üretim ve kalite güvence iş akışlarıyla ilişkileri, süreç verisinin erişilebilirliği, ölçülebilir iyileştirme potansiyeli ve güvenli kurum içi devreye alma yapısına uygunlukları dikkate alınarak seçilmiştir.

### 4.1. Bilgisayarlı Görü Tabanlı Görsel Hata Tespiti

Bilgisayarlı görü tabanlı görsel hata tespiti, imal edilen parçaların muayene süreçlerini desteklemek amacıyla kullanılmaktadır. İşlem hattı; görüntü edinimi, ön işleme, ilgi bölgesi seçimi ve yapay zekâ tabanlı analiz adımlarından oluşmaktadır. Hata tipine ve veri erişilebilirliğine bağlı olarak nesne tespiti, sınıflandırma veya segmentasyon yöntemleri kullanılabilmektedir. Nesne tespiti ve örnek segmentasyonu, hem sınıf hem de konum bilgisi sağladığı için görsel hata tespiti açısından önemlidir [Redmon, 2016; He, 2017].

Bu uygulamanın temel süreç etkisi; manuel muayene yükünün azaltılması, hataların daha erken tespit edilmesi, kararların standartlaştırılması ve görsel izlenebilirliğin artırılmasıdır. Sistem, nihai kalite kararını tek başına veren bir yapı olarak değil, uzman incelemesi için potansiyel problemli bölgeleri öne çıkaran ikinci kontrol mekanizması olarak

konumlandırılmaktadır. Ön pilot değerlendirmelerde, seçili görsel kontrol adımlarının yapay zekâ destekli işlem hattı ile manuel gözle kontrole kıyasla yaklaşık 1,5 kat daha hızlı tamamlanabildiği ve sınırlı pilot veri üzerinde yaklaşık %85 F1 skoru elde edildiği gözlemlenmiştir. Temel zorluklar ise aydınlatma değişkenliği, kamera açısı, yüzey yansımaları, sınırlı hata örneği, parça çeşitliliği ve yanlış alarm yönetimidir [Bergmann, 2019; Liu, 2024].

### 4.2. Görsel-Dil Modeli Destekli Bileşen Muayenesi

Bazı muayene görevleri, görsel kanıtların metinsel kriterlerle birlikte yorumlanmasını gerektirmektedir. Bu kullanım senaryosunda bileşen görüntüleri; muayene talimatları, uzman notları veya önceden tanımlanmış değerlendirme kriterleriyle birlikte analiz edilmektedir. Görsel-dil modelleri; gözlenen hata tipi, etkilenen bölge, olası önem derecesi ve dikkat edilmesi gereken muayene noktaları gibi yapılandırılmış çıktılar üretebilmektedir [Radford, 2021].

Bu uygulamanın temel katkısı, muayene açıklamalarının standartlaştırılması, tekrarlayan raporlama yükünün azaltılması ve bileşen seviyesindeki değerlendirmelerde tutarlılığın artırılmasıdır. Bununla birlikte görsel-dil modelleri, küçük veya belirsiz görsel detaylarda hatalı ya da gereğinden emin yorumlar üretebilir. Bu nedenle model çıktıları, doğrudan kalite kararı olarak değil, alan uzmanı tarafından doğrulanan karar destek girdileri olarak kullanılmalıdır [Arrieta, 2020; Lee, 2004].

### 4.3. Kontrol Listesi Temelli Teknik Resim İncelemesi

Teknik resimler; imalat, muayene, montaj ve kalite gereksinimlerini tanımlayan kritik dokümanlardır. Eksik bilgiler, tutarsız notlar veya kontrol listesi maddeleriyle uyumsuzluklar, üretim ve kalite güvence süreçlerinde problemlere yol açabilmektedir. Bu nedenle teknik resimlerin kontrol listeleriyle manuel olarak incelenmesi etkili olmakla birlikte, karmaşık dokümanlarda yüksek zaman ve uzman dikkati gerektirebilmektedir.

Bu kullanım senaryosunda yapay zekâ destekli teknik resim incelemesi; doküman ayrıştırma, optik karakter tanıma, yerleşim analizi, sembol/not çıkarımı ve kural tabanlı doğrulama adımlarını içerebilmektedir. Metin ve yerleşim bilgisini birlikte modelleyen doküman anlama yöntemleri, teknik belgelerden yapılandırılmış bilgi çıkarımı için uygun bir temel sunmaktadır [Xu, 2020]. Sistem çıktısı; uygun, uygun değil, eksik bilgi veya uzman incelemesi gerekli gibi madde seviyesinde bulgular şeklinde yapılandırılmaktadır.

Bu uygulama, tekrarlayan manuel inceleme yükünü azaltmayı ve kontrol listesi uygulamasını standartlaştırmayı hedeflemektedir. Uzman, tüm teknik resim elemanlarını baştan incelemek yerine sistem tarafından işaretlenen maddelere ve riskli bölgelere odaklanabilir. Temel

zorluklar; teknik resim karmaşıklığı, düşük kaliteli taranmış dokümanlar, farklı çizim standartları, sembol çeşitliliği, tablo çıkarım hataları ve alana özgü kurallara duyulan ihtiyaçtır.

### 4.4. Video Tabanlı Süreç Anomalisi Tespiti

Üretim, entegrasyon ve test faaliyetleri; süreç davranışı, hareket örüntüleri, ekipman durumu veya olağan dışı olaylar hakkında bilgi içeren uzun video kayıtları üretebilmektedir. Bu kayıtların manuel olarak incelenmesi zaman alıcıdır. Video tabanlı yapay zekâ yöntemleri, ilgili zaman aralıklarının belirlenmesine ve uzmanların kritik olaylara daha hızlı odaklanmasına yardımcı olabilir.

Bu kullanım senaryosunda süreç veya test kayıtlarına video analitiği ve anomali tespiti yöntemleri uygulanmaktadır. Genel işlem hattı; kare çıkarımı, ilgi bölgesi seçimi, hareket analizi, zamansal öznitelik çıkarımı ve olay seviyesinde sınıflandırma adımlarından oluşmaktadır. Sistem; olağan dışı hareketleri, ani görsel değişimleri, beklenmeyen durumları veya beklenen zamansal davranıştan sapmaları tespit ederek anomali zaman damgaları, şüpheli aralıklar ve özet raporlar üretebilir [Chandola, 2009].

Bu uygulamanın temel süreç etkisi, uzun videoların daha hızlı incelenmesi ve süreç/test olaylarına ilişkin izlenebilirliğin artırılmasıdır. Ancak kamera hareketi, örtüşme, aydınlatma değişkenliği, arka plan değişimleri, sürece bağlı normal davranışın farklılaşması ve sınırlı etiketli anomali örnekleri önemli zorluklardır. Aşırı yanlış alarm kullanıcı güvenini azaltabileceği için sistem, nihai karar üretmek yerine şüpheli aralıklar sunan karar destek aracı olarak konumlandırılmaktadır [Bergmann, 2019; Liu, 2024; Xu, 2021].

### 4.5. Kalite Kayıtlarının Doğal Dil İşleme Tabanlı Analizi

Kalite güvence süreçleri; muayene notları, uygunsuzluk açıklamaları, düzeltici faaliyet kayıtları, süreç yorumları ve uzman değerlendirmeleri gibi yapılandırılmış ve yapılandırılmamış metinsel veriler üretmektedir. Bu kayıtlar tekrar eden problemler, süreç zayıflıkları ve iyileştirme fırsatları hakkında değerli bilgi içerse de büyük hacimli metinlerin manuel olarak analiz edilmesi zordur.

Bu kullanım senaryosunda kalite kayıtlarının analiz edilmesi için metin temizleme, normalizasyon, anahtar kelime çıkarımı, sınıflandırma, kümeleme ve özetleme adımlarından oluşan doğal dil işleme yöntemleri kullanılmaktadır. Bu adımlar, transformer tabanlı dil modelleriyle desteklenebilmektedir [Vaswani, 2017; Devlin, 2019]. Amaç, yapılandırılmamış notları eğilim analizi ve kök neden incelemesini destekleyecek yapılandırılmış bilgiye dönüştürmektir.

Bu uygulamanın beklenen süreç etkisi; izlenebilirliğin artırılması, geçmiş bilgiye daha hızlı erişim sağlanması ve düzeltici/önleyici faaliyet planlamasının desteklenmesidir. Temel

zorluklar ise terminoloji farklılıkları, kısaltmalar, eksik kayıtlar, alana özgü ifadeler ve gizlilik gereksinimleridir. Bu nedenle modellerin kurum içi terminolojiye uyarlanması, güvenli ortamda devreye alınması ve üretilen özet, küme veya kök neden önerilerinin uzman tarafından doğrulanması gerekmektedir.

## 5. SÜREÇ ETKİSİ VE DEĞERLENDİRME GÖSTERGELERİ

Bu çalışmada sunulan yapay zekâ uygulamaları yalnızca model başarımı açısından değil, üretim ve kalite güvence iş akışlarına sağladıkları katkı açısından da değerlendirilmektedir. Endüstriyel ortamlarda teknik doğruluğu yüksek bir model, manuel iş yükünü azaltmıyor, izlenebilirliği iyileştirmiyor, uzman kararlarını desteklemiyor veya ölçülebilir süreç iyileştirmesi oluşturmuyorsa sınırlı pratik değer sağlayabilir. Bu nedenle benimsenen değerlendirme yaklaşımı hem teknik göstergeleri hem de süreç odaklı göstergeleri dikkate almaktadır. Bu bakış açısı, makine öğrenmesi sistemlerinin değerinin yalnızca model doğruluğu ile değil, süreç iyileştirme ve kaliteyle ilişkili karar verme faaliyetlerini destekleme kabiliyetiyle de ölçülmesi gerektiğini vurgulayan kestirimci kalite çalışmalarıyla uyumludur [Tercan, 2022].

Görsel hata tespiti için temel teknik göstergeler hata tespit başarımı, konumlandırma kabiliyeti, yanlış alarm oranı ve farklı muayene koşulları altında tahmin tutarlılığıdır. Görsel-dil modeli destekli bileşen muayenesinde uzman kararıyla uyum, açıklama doğruluğu ve terminoloji tutarlılığı dikkate alınmaktadır. Teknik resim incelemesinde değerlendirme, yapay zekâ tarafından üretilen bulguların uzman tarafından gözden geçirilmiş kontrol listesi sonuçlarıyla karşılaştırılması yoluyla madde seviyesinde yapılmaktadır. Video tabanlı süreç anomalisi tespitinde anormal aralıkların belirlenmesi, zaman damgası doğruluğu ve yanlış alarm sıklığı; kalite kayıtlarının doğal dil işleme tabanlı analizinde ise sınıflandırma doğruluğu, kümeleme kalitesi ve özetlerin faydalılığı öne çıkan göstergelerdir.

Ön pilot değerlendirmeler, yapay zekâ destekli uygulamaların özellikle manuel görsel kontrol ve inceleme süreçlerinde ölçülebilir operasyonel iyileştirme potansiyeli sunduğunu göstermektedir. Seçili görsel kontrol adımlarında yapay zekâ destekli işlem hattı, manuel gözle kontrole kıyasla yaklaşık 1,5 kat daha hızlı sonuç üretmiştir. Bu durum, ilgili adımlarda yaklaşık %30–35 seviyesinde manuel inceleme süresi azalımına karşılık gelmektedir. Görsel hata tespiti senaryolarında sınırlı pilot veri üzerinde yaklaşık %85 F1 skoru elde edilmiş, yanlış alarm oranı ise uygulama koşullarına bağlı olarak yaklaşık %10–15 bandında gözlemlenmiştir. Bu değerler nihai sistem doğrulaması olarak değil, yöntemin üretim ve kalite güvence süreçlerinde karar destek potansiyelini gösteren ön pilot bulgular olarak değerlendirilmelidir.

Tablo 2'de her uygulama alanı için dikkate alınan temel teknik göstergeler, süreç odaklı göstergeler ve ön pilot bulgular özetlenmektedir.

Tablo 2 Uygulanan yapay zekâ uygulamaları için değerlendirme göstergeleri ve ön pilot bulgular.

| Uygulama Alanı | Teknik Göstergeler | Süreç Odaklı Göstergeler | Ön Pilot Bulgular |
|---|---|---|---|
| Görsel hata tespiti | Hata tespit başarımı, konumlandırma kabiliyeti, yanlış alarm oranı | Muayene yükünün azaltılması, erken hata tespiti, izlenebilirliğin artırılması | Yaklaşık %85 F1 skoru, %10–15 yanlış alarm oranı |
| Bileşen muayenesi | Uzman kararıyla uyum, açıklama doğruluğu, terminoloji tutarlılığı | Raporlama yükünün azaltılması, muayene notlarının standartlaştırılması | Uzman incelemesini yönlendiren karar destek çıktıları |
| Teknik resim incelemesi | Kontrol listesi maddesi doğruluğu, bilgi çıkarım kalitesi, kural kontrol başarımı | Manuel inceleme süresinin azaltılması, dokümantasyon problemlerinin erken tespiti | Seçili kontrol adımlarında yaklaşık 1,5 kat hızlanma |
| Video tabanlı anomali tespiti | Olay tespit başarımı, anomali zaman damgası konumlandırması, yanlış alarm sıklığı | Video inceleme süresinin azaltılması, süreç olay izlenebilirliğinin artırılması | Şüpheli aralıkların önceliklendirilmesi |
| Kalite kayıtları analizi | Sınıflandırma doğruluğu, kümeleme kalitesi, özet ilgililiği | Geçmiş kayıtlara daha hızlı erişim, kök neden analizi desteği | Benzer kayıtların gruplanması ve özetlenmesi |

Değerlendirme sonuçları hem teknik iyileştirme hem de operasyonel devreye alma kararlarını yönlendirmek amacıyla kullanılmaktadır. Model başarımı yüksek olmasına rağmen iş akışına katkısı sınırlı kalan uygulamalar için kullanıcı arayüzünün, raporlama yapısının veya entegrasyon mekanizmasının yeniden tasarlanması gerekebilir. Benzer şekilde, teknik başarımı orta seviyede olan bazı uygulamalar; tekrarlayan işleri azaltıyor, görünürlüğü artırıyor veya uzman önceliklendirmesini destekliyorsa pratik değer sağlayabilir. Bu sürekli geri bildirim mekanizması, açıklanabilir ve güvenilir yapay zekâ benimsenmesini desteklemekte; uzman doğrulaması ise yapay zekâ destekli önerilere uygun düzeyde güven duyulmasını sağlamaktadır [Arrieta, 2020; Lee, 2004].

## 6. SAVUNMA SANAYİİ İMALATINDA DEVREYE ALMA HUSUSLARI

Savunma sanayii imalat ortamlarında yapay zekâ uygulamalarının devreye alınması, model geliştirme adımlarının ötesinde güvenlik, izlenebilirlik, operasyonel risk ve iş akışı entegrasyonu gibi ek değerlendirmeler gerektirmektedir. Üretim ve kalite güvence verileri; bileşenler, süreçler, test koşulları, teknik dokümantasyon ve kurum içi kalite kayıtlarıyla ilişkili hassas bilgiler içerebilir. Bu nedenle uygulamalar; veri depolama, model çalıştırma ve sonuç raporlama süreçlerinin kurum içi güvenlik gereksinimlerine uygun şekilde kontrol edilebildiği güvenli kurum içi ortamlarda değerlendirilmelidir [Xu, 2021; ISO 9001, 2015; ISO/IEC 27001, 2022].

Önerilen devreye alma yaklaşımı; kalite yönetimi, bilgi güvenliği, endüstriyel sistem güvenliği ve yapay zekâ risk yönetimi açısından ilgili standartlarla ilişkilendirilebilir. ISO 9001 süreç izlenebilirliği ve kalite yönetimi, ISO/IEC 27001 bilgi güvenliği yönetimi, IEC 62443 endüstriyel otomasyon ve kontrol sistemleri güvenliği, ISO/IEC 23894 yapay zekâ risk yönetimi, ISO/IEC 42001 ise yapay zekâ yönetim sistemi ve kurumsal yönetişim gereksinimleri için temel referanslar olarak değerlendirilebilir [ISO 9001, 2015; ISO/IEC 27001, 2022; IEC 62443, 2024; ISO/IEC 23894, 2023; ISO/IEC 42001, 2023].

Devreye alma sürecindeki temel ilke, yapay zekâ uygulamalarının uzman karar mekanizmasını ikame etmek yerine desteklemesidir. Yapay zekâ çıktıları; şüpheli bölgelerin işaretlenmesi, kontrol listesi bulgularının önerilmesi, kalite kayıtlarının özetlenmesi veya anormal video aralıklarının belirlenmesi gibi karar destek amaçlı kullanılmalı; resmi üretim ve kalite kararları öncesinde alan uzmanları tarafından incelenip onaylanmalıdır. Bu yaklaşım, açıklanabilir yapay zekâ ve otomasyona uygun güven literatürüyle uyumludur [Arrieta, 2020; Lee, 2004].

İzlenebilirlik ve iş akışı entegrasyonu sürdürülebilir kullanım için kritik önemdedir. Yapay zekâ tarafından üretilen her bulgu; girdi verisi, işleme adımları, model sürümü ve uzman doğrulama sonucu ile ilişkilendirilmelidir. Çıktılar ayrıca mevcut muayene, dokümantasyon, raporlama ve düzeltici faaliyet süreçleriyle uyumlu raporlar, inceleme arayüzleri veya panolar üzerinden sunulmalıdır.

Bir diğer önemli konu veri ve model yaşam döngüsü yönetimidir. Endüstriyel veri; yeni bileşen tipleri, güncellenen muayene kriterleri, süreç değişiklikleri, kamera değişimleri veya dokümantasyon standartlarındaki değişimler nedeniyle zaman içinde farklılaşabilir. Bu nedenle model başarımı periyodik olarak izlenmeli, uzman geri bildirimleriyle veri setleri ve karar eşikleri güncellenmeli, yanlış pozitif ve yanlış negatif davranışı süreç riskine göre kontrol edilmelidir. Bu nedenle önerilen yaklaşım, kara kutu otomasyon yerine şeffaf, izlenebilir ve uzman tarafından doğrulanabilir karar destek çıktılarının kullanılmasını önceliklendirmektedir [Arrieta, 2020; Lee, 2004; Xu, 2021].

## 7. PLANLANAN GENİŞLETMELER

Uygulanan yapay zekâ uygulamaları, daha geniş kapsamlı bir yaşam döngüsü zekâsı yaklaşımının üretim ve kalite güvence temelini oluşturmaktadır. Gelecek çalışmalarda endüstriyel yapay zekâ yol haritasının kestirimci bakım, gerçek zamanlı süreç izleme, otomatik kök neden analizi ve bütünleşik karar destek sistemleri yönünde genişletilmesi planlanmaktadır. Bu genişletmelerin amacı; üretim, kalite güvence, test, bakım, iş sağlığı ve güvenliği ile mühendislik geri bildirim süreçlerinin daha etkin şekilde ilişkilendirilmesidir.

### 7.1. Kestirimci Bakım

Kestirimci bakım, yol haritasının planlanan genişletme alanlarından biridir. Bu alandaki temel amaç; geçmiş üretim verileri, test sonuçları, bakım kayıtları, kalite bulguları, sensör ölçümleri ve süreç göstergelerinden yararlanarak olası ekipman yıpranması, bileşen seviyesinde risk veya bakım ihtiyacının arıza oluşmadan önce tahmin edilmesidir. Bu tür sistemler; risk skorları, erken uyarı göstergeleri, bakım önceliği önerileri ve geçmiş benzerlik analizleri üretebilir. Derin öğrenme tabanlı kestirimci bakım çalışmaları, anomali tespiti, zaman serisi modelleme ve kalan faydalı ömür tahminini aynı bakım zekâsı çerçevesi içinde ilişkili problemler olarak ele almaktadır [Serradilla, 2022].

### 7.2. Gerçek Zamanlı Süreç İzleme

Bir diğer planlanan genişletme alanı, video, sensör ve üretim verileri kullanılarak gerçek zamanlı süreç izleme yapılmasıdır. Uygulanan video tabanlı anomali tespiti yaklaşımı ağırlıklı olarak kayıtlı verilerin analizine odaklanırken, gerçek zamanlı süreç izleme operasyon sırasında anormal süreç davranışlarının tespit edilmesini amaçlamaktadır. Olası çıktılar arasında canlı anomali uyarıları, süreç kararlılığı göstergeleri, görsel olay işaretleyicileri ve anormal aralıkların otomatik raporlanması yer almaktadır. Endüstriyel devreye alma açısından gecikme süresi, güvenilirlik, yanlış alarm kontrolü ve mevcut izleme altyapısıyla entegrasyon temel gereksinimlerdir.

### 7.3. Otomatik Kök Neden Analizi

Kalite problemleri çoğu zaman muayene kayıtları, üretim parametreleri, teknik dokümantasyon, test sonuçları ve uzman yorumları gibi birden fazla veri kaynağı üzerinden inceleme yapılmasını gerektirmektedir. Otomatik kök neden analizi kapsamında doğal dil işleme, veri madenciliği, istatistiksel analiz ve alan kurallarının birlikte kullanılarak mühendislerin tekrar eden problemlerin olası nedenlerini belirlemesinin desteklenmesi planlanmaktadır. Buradaki amaç, nihai kök nedeni tamamen otomatik olarak belirlemek değil; benzer vakaları gruplamak, tekrar eden örüntüleri tespit etmek, ilişkili kayıtları birbirine bağlamak ve olası katkı sağlayan faktörleri önererek inceleme yükünü azaltmaktır. Bu genişletme, anomali tespiti, kök neden analizi ve kalan faydalı ömür tahmininin endüstriyel bakım iş akışları içinde ilişkili görevler olarak ele alındığı kestirimci bakım literatürüyle de bağlantılıdır [Serradilla, 2022].

### 7.4. Bütünleşik Karar Destek Sistemleri

Yol haritasının uzun vadeli hedefi, üretim ve kalite yönetimi için bütünleşik karar destek sistemleri oluşturmaktır. Bu tür sistemler; görsel muayene, bileşen muayenesi, teknik resim

incelemesi, video tabanlı anomali tespiti, kalite kayıtları analizi, kestirimci bakım ve süreç izleme uygulamalarından gelen çıktıları bir araya getirebilir. Panolar, risk göstergeleri, eğilim analizleri, geçmiş vaka erişimi, problem önceliklendirme ve yaşam döngüsü geri bildirim mekanizmaları; mühendislerin ve yöneticilerin üretim ve kalite durumunu daha bütüncül şekilde değerlendirmesine olanak sağlayabilir. Bu bütünleşik bakış açısı; üretim, kalite, güvenilirlik ve geri bildirim verilerinin yaşam döngüsü seviyesinde karar vermeyi desteklemek için ilişkilendirildiği akıllı imalat ve kestirimci kalite araştırmalarıyla uyumludur [Zhong, 2017; Tercan, 2022; Xu, 2021].

## 8. SONUÇ

Bu çalışmada, yüksek güvenilirlik gerektiren savunma sanayii imalat süreçlerinde üretim ve kalite güvence faaliyetlerini iyileştirmeye yönelik endüstriyel yapay zekâ uygulamaları sunulmuştur. Çalışma kapsamında, bütünleşik bir endüstriyel yapay zekâ yol haritası içinde hem uygulanmış kullanım senaryoları hem de planlanan genişletmeler ele alınmıştır. Uygulanan kullanım senaryoları; bilgisayarlı görü tabanlı görsel hata tespiti, görsel-dil modeli destekli bileşen muayenesi, kontrol listesi temelli teknik resim incelemesi, video tabanlı süreç anomalisi tespiti ve doğal dil işleme tabanlı kalite kayıtları analizi olarak değerlendirilmiştir.

Uygulamalar hem teknik hem de süreç odaklı göstergeler açısından incelenmiştir. Teknik göstergeler arasında hata tespit başarımı, konumlandırma kabiliyeti, kontrol listesi maddesi doğruluğu, olay tespit başarımı, uzman kararıyla uyum ve metin analizi kalitesi yer almaktadır. Süreç odaklı göstergeler ise muayene yükünün azaltılması, hataların daha erken tespit edilmesi, izlenebilirliğin artırılması, uzman kararlarının standartlaştırılması, uzun video kayıtlarının daha hızlı incelenmesi, raporlama tutarlılığının iyileştirilmesi ve iş sağlığı/güvenliği süreçlerinin desteklenmesi olarak ele alınmıştır. Ön pilot bulgular, seçili manuel görsel kontrol adımlarında yaklaşık 1,5 kat hızlanma sağlanabildiğini ve görsel hata tespiti senaryolarında sınırlı pilot veri üzerinde yaklaşık %85 F1 skoru seviyesine ulaşılabildiğini göstermektedir. Bu bulgular, yapay zekâ destekli uygulamaların yalnızca model başarımı açısından değil, pratik iş akışı katkısı açısından da değerlendirilmesi gerektiğini ortaya koymaktadır.

Çalışmada ayrıca savunma sanayii imalat ortamlarına özgü devreye alma hususları vurgulanmıştır. Güvenli kurum içi devreye alma, insan denetimli doğrulama, izlenebilirlik, mevcut iş akışlarıyla entegrasyon, model yaşam döngüsü yönetimi, yanlış alarm kontrolü, açıklanabilirlik ve kullanıcı kabulü, yüksek güvenilirlik gerektiren ortamlarda yapay zekâ sistemlerinin sürdürülebilir kullanımı için temel gereksinimlerdir. Bu bağlamda yapay zekâ sistemleri, otonom karar verici yapılar olarak değil, uzman kararlarını destekleyen, izlenebilir ve doğrulanabilir karar destek bileşenleri olarak konumlandırılmalıdır.

Gelecek çalışmalarda yol haritasının kestirimci bakım, gerçek zamanlı süreç izleme, otomatik kök neden analizi ve bütünleşik karar destek sistemleri yönünde genişletilmesi planlanmaktadır. Bu genişletmelerin, üretim, kalite güvence, test, bakım, iş sağlığı ve güvenliği ile mühendislik geri bildirim süreçlerini modern savunma sistemleri için daha kapsamlı bir yaşam döngüsü zekâsı perspektifi içinde ilişkilendirmesi hedeflenmektedir.

## TEŞEKKÜR

Yazarlar, bu çalışmada sunulan endüstriyel yapay zekâ uygulamalarının yürütülmesine sağladığı destek için Roketsan'a teşekkür eder.

## KAYNAKÇA

1. **Zhong, R.Y., Xu, X., Klotz, E. and Newman, S.T., (2017)**, "Intelligent Manufacturing in the Context of Industry 4.0: A Review", Engineering, Vol. 3, No. 5, pp. 616630.

2. **Tercan, H. and Meisen, T., (2022)**, "Machine Learning and Deep Learning Based Predictive Quality in Manufacturing: A Systematic Review", Journal of Intelligent Manufacturing, Vol. 33, No. 7, pp. 18791905.

3. **Redmon, J., Divvala, S., Girshick, R. and Farhadi, A., (2016)**, "You Only Look Once: Unified, RealTime Object Detection", Proceedings of the IEEE Conference on Computer Vision and Pattern Recognition, pp. 779788.

4. **He, K., Gkioxari, G., Dollár, P. and Girshick, R., (2017)**, "Mask RCNN", Proceedings of the IEEE International Conference on Computer Vision, pp. 29612969.

5. **Bergmann, P., Fauser, M., Sattlegger, D. and Steger, C., (2019)**, "MVTec AD — A Comprehensive RealWorld Dataset for Unsupervised Anomaly Detection", Proceedings of the IEEE/CVF Conference on Computer Vision and Pattern Recognition, pp. 9584-9592.

6. **Liu, J., Xie, G., Wang, J., Li, S., Wang, C., Zheng, F. and Jin, Y., (2024)**, "Deep Industrial Image Anomaly Detection: A Survey", Machine Intelligence Research, Vol. 21, No. 1, pp. 104 135.

7. **Chandola, V., Banerjee, A. and Kumar, V., (2009)**, "Anomaly Detection: A Survey", ACM Computing Surveys, Vol. 41, No. 3, Article No. 15.

8. **Radford, A., Kim, J.W., Hallacy, C., Ramesh, A., Goh, G., Agarwal, S., Sastry, G., Askell, A., Mishkin, P., Clark, J., Krueger, G. and Sutskever, I., (2021)**, "Learning Transferable Visual Models from Natural Language Supervision", Proceedings of the 38th International Conference on Machine Learning, Vol. 139, pp. 87488763.

9. **Xu, Y., Li, M., Cui, L., Huang, S., Wei, F. and Zhou, M., (2020)**, "LayoutLM: Pre-training of Text and Layout for Document Image Understanding", Proceedings of the 26th

ACM SIGKDD International Conference on Knowledge Discovery and Data Mining, pp. 11921200.

10. **Vaswani, A., Shazeer, N., Parmar, N., Uszkoreit, J., Jones, L., Gomez, A.N., Kaiser, L. and Polosukhin, I., (2017)**, "Attention Is All You Need", Advances in Neural Information Processing Systems, Vol. 30.

11. **Devlin, J., Chang, M.W., Lee, K. and Toutanova, K., (2019)**, "BERT: Pretraining of Deep Bidirectional Transformers for Language Understanding", Proceedings of NAACL HLT, pp. 41714186.

12. **Barredo Arrieta, A., DíazRodríguez, N., Del Ser, J., Bennetot, A., Tabik, S., Barbado, A., García, S., GilLópez, S., Molina, D., Benjamins, R., Chatila, R. and Herrera, F., (2020)**, "Explainable Artificial Intelligence (XAI): Concepts, Taxonomies, Opportunities and Challenges toward Responsible AI", Information Fusion, Vol. 58, pp. 82115.

13. **Lee, J.D. and See, K.A., (2004)**, "Trust in Automation: Designing for Appropriate Reliance", Human Factors, Vol. 46, No. 1, pp. 5080.

14. **Xu, Z. and Saleh, J.H., (2021)**, "Machine Learning for Reliability Engineering and Safety Applications: Review of Current Status and Future Opportunities", Reliability Engineering and System Safety, Vol. 211, Article No. 107530.

15. **Serradilla, O., Zugasti, E., Rodriguez, J. and Zurutuza, U., (2022)**, "Deep Learning Models for Predictive Maintenance: A Survey, Comparison, Challenges and Prospects", Applied Intelligence, Vol. 52, pp. 1093410964.

16. **ISO 9001**, (2015), "Quality Management Systems — Requirements", International Organization for Standardization, Geneva, Switzerland.

17. **ISO/IEC 27001, (2022)**, "Information Security, Cybersecurity and Privacy Protection — Information Security Management Systems — Requirements", International Organization for Standardization, Geneva, Switzerland.

18. **IEC 62443, (2024)**, "Security for Industrial Automation and Control Systems", International Electrotechnical Commission, Geneva, Switzerland.

19. **ISO/IEC 23894, (2023)**, "Information Technology — Artificial Intelligence — Guidance on Risk Management", International Organization for Standardization, Geneva, Switzerland.

20. **ISO/IEC 42001, (2023)**, "Information Technology — Artificial Intelligence — Management System", International Organization for Standardization, Geneva, Switzerland.

# KODLANMIŞ METAYÜZEY YÖNTEMİYLE RADAR KESİT ALANI (RKA) AZALTMA VE ANALİZİ

**Khangul ABDULLAYEVA**, *xangulabdullayeva8@gmail.com* İstanbul Gedik Üniversitesi, İstanbul, Türkiye

**Yavuz KAYIHAN**, *yavuzkayihan@itu.edu.tr* İstanbul Teknik Üniversitesi, 34467, İstanbul, Türkiye

**Mete KAYIHAN,** *kayihanm@itu.edu.tr* İstanbul Teknik Üniversitesi, 34467, İstanbul, Türkiye

## ÖZET

Bu çalışmanın temel amacı, askeri sezinleme sistemlerinde yaygın olarak kullanılan X-bandı (8-12 GHz) frekans aralığında yüksek performans gösteren, ultra ince ve optimize edilmiş bir "Kodlanmış Metayüzey" tasarımı gerçekleştirerek bu kısıtlamaları aşmaktır. Önerilen metayüzey tasarımı, mikrodalga frekanslarında tam yansıtma ve faz kontrolü sağlamak amacıyla üç katmanlı bir sandviç model mimarisine dayanmaktadır. Sonlu Elemanlar Yöntemi (FEA) tabanlı simülasyon sonuçlarına göre, tasarlanan metayüzey X-bandının tamamında askeri standartlarca kabul gören -10 dB eşik değerinin altında bir performans sergilemiştir. Yapılan yüzey akımı analizleri, yapının elektriksel ve manyetik rezonans mekanizmaları sayesinde elektromanyetik enerjiyi yüksek bir verimlilikle ısı enerjisine dönüştürdüğünü ve endüstriyel üretim dayanıklılığına sahip olduğu doğrulanmıştır.

**Anahtar Kelimeler:** Sonlu Elemanlar Yöntemi, Askeri sezinleme, X-bandı, kodlanmış metayüzey, sandviç model, elektromanyetik yüzey

## ABSTRACT

The primary aim of study is overcoming limitations developing an ultra-thin, optimized “encoded metasurface” design delivers high performance in the X-band (8–12 GHz) frequency range widely used in military sensing. The metasurface design is based on a three-layer sandwich model architecture providing full reflection and phase control at microwave frequencies. According to Finite Element Analysis (FEA)-based simulation results, the designed metasurface demonstrated performance below the -10 dB threshold value accepted by military standards. Surface current analyses confirmed the structure efficiently converts electromagnetic energy into thermal energy through its

electrical/magnetic resonance mechanisms and possesses the durability required for industrial production.

**Keywords:** Finite Element Method, Military surveillance, X-band, encoded metasurface, sandwich model, electromagnetic surface

## 1. GİRİŞ

Modern askeri doktrinlerde ve savunma teknolojilerinde, bir savunma platformunun (hava, deniz veya kara unsurları) görevini başarıyla tamamlaması ve operasyonel ömrünü sürdürebilmesi büyük ölçüde "Beka" (Survivability) kabiliyetine bağlıdır [1-3]. Savunma platformlarının bekası; platformun tehdit tarafından tespit edilmesini engelleyen duyarlılık (susceptibility) ve bir isabet durumunda platformun aldığı hasara karşı koyabilme yeteneği olan savunmasızlık (vulnerability) bileşenlerinin optimize edilmesiyle sağlanır [4-6]. Gelişen radar ve sezinleme teknolojileri, platformların tespit edilme riskini artırmış; bu durum karşı tedbir olarak "Düşük Görünürlük" (Stealth) teknolojilerinin geliştirilmesini zorunlu kılmıştır [7-10].

Tehdit radar sistemlerinin bir hedefi tespit etme, izleme ve angaje olma sürecini ifade eden "Tehdit Zinciri" (Kill Chain) mekanizmasının ilk ve en kritik halkası sezinlemedir. Bu zincirin erken aşamada kırılması, platformun elektromanyetik spektrumdaki izinin minimize edilmesiyle mümkündür [11]. Bir platformun radar sistemleri tarafından ne büyüklükte algılandığının temel göstergesi ise Radar Kesit Alanı (RKA / RCS - Radar Cross Section) değeridir [12-15]. RKA değerinin düşürülmesi, düşman radar menzilini daraltarak platforma taktiksel bir üstünlük ve erken uyarı avantajı kazandırmaktadır [16].

Geleneksel RKA azaltma yöntemleri temel olarak iki ana yaklaşıma dayanmaktadır: Geometrik şekillendirme ve Radar Soğurucu Malzeme (RAM - Radar Absorbing Material) kaplamaları. Ancak bu geleneksel yöntemlerin yapısal ve operasyonel sınırları bulunmaktadır. Geometrik şekillendirme, aerodinamik ve hidrodinamik performans kriterleri nedeniyle her platformda serbestçe uygulanamamaktadır [17]. Geleneksel RAM kaplamalar ise genellikle yüksek kalınlık, ağır yapısal yük, dar çalışma bant genişliği ve çevresel koşullara (nem, sıcaklık değişimi, korozyon) karşı dayanıksızlık gibi dezavantajlara sahiptir. Özellikle savunma platformlarında hacim, ağırlık ve güç (SWaP - Size, Weight, and Power) optimizasyonunun hayati önem taşıdığı göz önüne alındığında, daha hafif, ince ve geniş bantta etkili alternatif yapıların geliştirilmesi bir zorunluluk haline gelmiştir [18-20].

Son yıllarda elektromanyetik malzeme bilimindeki gelişmeler, yapay olarak üretilen ve doğal malzemelerde bulunmayan dalga yönlendirme özelliklerine sahip metamalzemeleri ve bunların iki boyutlu türevleri olan "Metayüzeyleri" ön plana çıkarmıştır [21]. Özellikle "Kodlanmış Metayüzeyler" (Coding Metasurfaces), geleneksel pasif soğurma mantığının

ötesine geçerek, yüzeye gelen elektromanyetik dalgaların fazını manipüle etme ve bu dalgaları tek bir yöne yansıtmak yerine farklı açılara dağıtarak (bistatik saçılma) monostatik RKA'yı kritik seviyede düşürme yeteneğine sahiptir [22,23]. Bu durum, hafiflik ve yüksek performans arayışındaki modern savunma sanayii projeleri için güçlü bir motivasyon kaynağı oluşturmaktadır [24].

Bu çalışmanın temel amacı, savunma platformlarının RKA değerlerini düşürmek amacıyla askeri sezinleme ve radar sistemlerinde yaygın olarak kullanılan X-bandı (8-12 GHz) frekans aralığında yüksek performans gösteren, ultra ince ve optimize edilmiş bir kodlanmış metayüzey tasarımı gerçekleştirmek ve simüle etmektir.

Bu genel amaç doğrultusunda şu alt hedeflere odaklanılmıştır:

1. X-bandı askeri radarlarına karşı etkili dalga manipülasyonu sağlayabilecek özgün birim hücre (unit cell) geometrilerinin geliştirilmesi,

2. Seçilen dielektrik katmanların (FR4/Rogers vb.) kalınlık ve kayıp tanjantı parametrelerinin elektromanyetik performans üzerindeki etkilerinin incelenerek gerekçelendirilmesi,

3. Tasarlanan yüzeyin yansıma katsayısı (S-parametreleri) ve rezonans frekanslarındaki yüzey akımı (surface currents) dağılımlarının sayısal modelleme yöntemleriyle analiz edilmesi,

4. Tasarımın farklı geliş açılarında (monostatik ve bistatik) ve farklı polarizasyon durumlarında (TE ve TM dalgaları) serbest uzay ortamındaki performans kararlılığının ölçülmesi.

## 2. YÖNTEM

Savunma platformlarının beka kabiliyetini artırmak amacıyla yürütülen bu çalışmada, askeri sezinleme ve radar sistemlerinde yoğun olarak kullanılan X-bandı (8-12 GHz) frekans aralığında yüksek performans gösteren, polarizasyondan bağımsız bir kodlanmış metayüzey tasarımı gerçekleştirilmiştir. Tasarım ve analiz süreçlerinde elektromanyetik dalga teorisi, radar menzil denklemleri, platform beka analizi modelleri ve sayısal analiz yöntemleri bir bütün olarak ele alınmıştır.

Projenin matematiksel ve teorik altyapısı, Maxwell denklemlerine ve mikrodalga sistemlerinin temelini oluşturan radar menzil formülasyonlarına dayanmaktadır. Bir savunma platformunun düşman radar sistemleri tarafından tespit edilme mesafesini belirleyen temel maksimum tespit menzili Denklem 1'de ifade edilmektedir:

$$R_{max} = \sqrt[4]{((P_t \cdot G^2 \cdot \lambda^2 \cdot \sigma)/((4\pi)^3 \cdot P_m in))} \quad (1)$$

Bu denklemde yer alan $R_{max}$ maksimum tespit menzilini, $P_t$ radar verici gücünü, G anten kazancını, λ çalışma dalga boyunu ve $P_{min}$ radar alıcısının algılayabileceği minimum sinyal gücünü temsil etmektedir. Formülde açıkça görüldüğü üzere, radar sistemine ait parametreler sabit tutulduğunda, platformun tespit edilme menzilini kısaltarak görünmezlik sağlamanın tek yolu hedef platformun öz niteliği olan "σ " yani Radar Kesit Alanı (RKA) değerinin düşürülmesidir [6, 4, 22]. Hedef yüzeylerden yansıyan dalgaların uzak alandaki RKA karşılığı ise gelen elektrik alan ($E_i$) ve saçılan elektrik alan ($E_s$) bileşenleri cinsinden Denklem 2'deki matematiksel limit fonksiyonu ile hesaplanmaktadır:

$$\sigma = \lim_{R\to\infty} 4\pi R^2 \frac{|E_s|^2}{|E_i|^2} \quad (2)$$

Önerilen kodlanmış metayüzey yaklaşımında, yüzeye dik veya eğik açıyla gelen elektromanyetik dalgaların doğrudan radar alıcısına geri dönmesini engellemek adına faz manipülasyonu yöntemi uygulanmıştır. Yüzeyden saçılan toplam uzak alan faktörü, periyodik dizilimde yer alan birim hücrelerin yansıma katsayıları ve aralarındaki faz farkları dikkate alınarak süperpozisyon ilkesi uyarınca hesaplanmaktadır.

Askeri unsurların operasyon sahasındaki sağ kalma olasılığı, platform bekası teorisi kapsamında matematiksel olarak modellenmiştir. Bir platformun vurulma olasılığı ($P_H$), düşman sezinleme sistemlerinin "Tehdit Zinciri" mekanizmasını oluşturan tespit edilme ($P_{detect}$), izlenme ($P_{track}$), fırlatma $P_{launch}$ ve önleme $P_{intercept}$ olasılıklarının bir çarpımı olarak tanımlanmaktadır:

$$P_H = P_{detect} \cdot P_{track} \cdot P_{launch} \cdot P_{intercept} \quad (3)$$

Platformun nihai sağ kalma veya başka bir deyişle beka olasılığı ($P_S$) ise, vurulma olasılığı ile vurulan platformun aldığı hasar sonucu imha olma olasılığının $\left(P_{\left(\frac{K}{H}\right)}\right)$ fonksiyonu olarak Denklem 4'te formüle edilmektedir:

$$P_S = 1 - P_H \cdot P_{\left(\frac{K}{H}\right)} \quad (4)$$

Tasarlanan metayüzey yapısı, tehdit zincirinin henüz ilk ve en kritik halkası olan $P_{detect}$ değerini hedef almaktadır. Platformun RKA değeri elektromanyetik manipülasyonla düşürülerek düşman radarının tespit olasılığı sıfıra yaklaştırılmakta, böylece toplam vurulma olasılığı minimize edilerek platformun toplam beka olasılığı teorik olarak maksimum seviyeye çıkarılmaktadır.

Geleneksel ağır ve dar bantlı radar yutucu malzeme kaplamalarının operasyonel sınırlarını aşmak adına, tasarlanan düşük profilli metayüzey yapısında Empedans Uyumu teorisi esas alınmıştır. Yüzeyin giriş empedansının ($Z_{in}$), serbest uzay empedansına "($Z_0$≈377 Ω)" eşitlenmesi sağlanarak dalganın yüzey sınırından geri yansıması

engellenmekte ve elektromanyetik enerji dielektrik katman içerisinde hapsedilmektedir. Yansıma katsayısı $S_{11}$ ile giriş empedansı arasındaki bu ilişki Denklem 5'te gösterilmektedir [15, 18, 19, 21, 23]:

$$\gamma = S_{11} = (Z_{in} - Z_0)/(Z_{in} + Z_0) \quad (5)$$

Yansıtıcı yüzey elemanlarının mantıksal "0" ve "1" bitleri olarak kodlandığı bu metayüzey tasarımında, elemanlar arasındaki faz farkının (ΔΦ), X-bandı merkez frekansı olan 10 GHz seviyesinde ideal olarak şu koşulu sağlaması hedeflenmiştir:

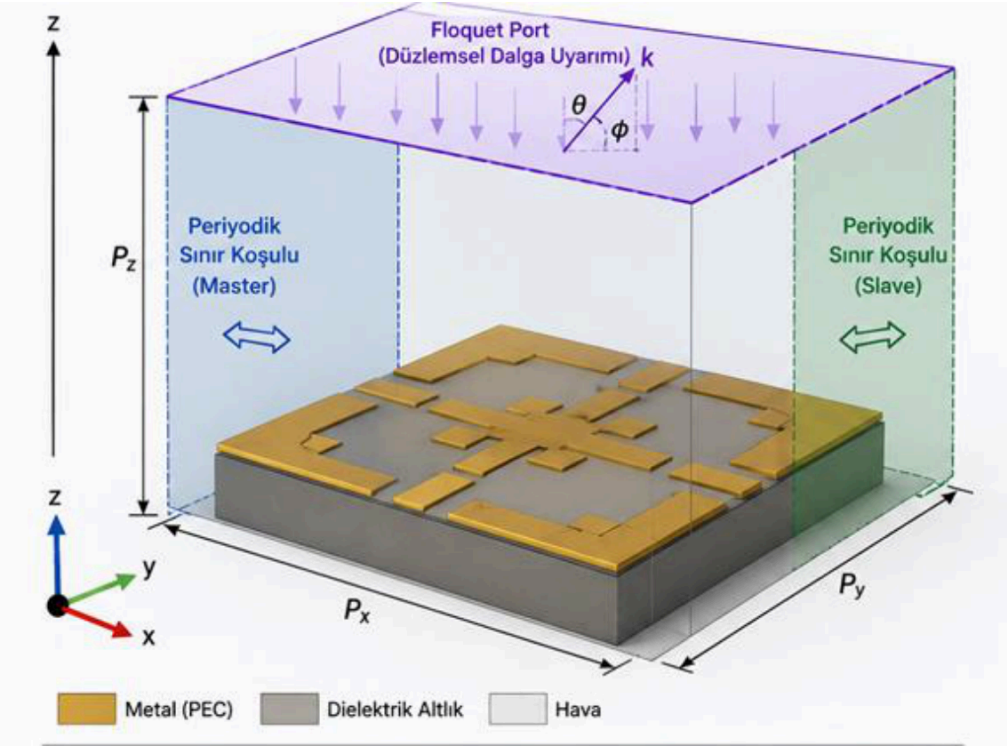
$$\Delta\Phi = |\Phi_0 - \Phi_1| \approx 180^\circ \pm 30^\circ$$

Bu faz koşulunun tam olarak karşılandığı rezonans durumlarında, yüzeyden monostatik olarak geri yansıması beklenen dalgalar yıkıcı girişim üreterek birbirini sönümlemekte veya enerjiyi ana eksenin dışındaki çok farklı açılara bistatik olarak dağıtarak RKA değerinde kritik bir azalma meydana getirmektedir.

Metayüzey birim hücresinin geometrik tasarımı, optimizasyon süreçleri ve üç boyutlu elektromanyetik analizleri COMSOL Multiphysics Sonlu Elemanlar Yöntemi (FEA) tabanlı yüksek frekans simülasyon yazılımları kullanılarak gerçekleştirilmiştir. Birim hücrenin fiziksel hafiflik, yapısal dayanım ve endüstriyel standartlara uygunluk kriterlerini sağlaması adına, savunma elektroniğinde sıklıkla tercih edilen ve efektif dielektrik sabiti $\epsilon_{eff}$=4.4, kayıp tanjantı tanδ=0.02 olan FR4 malzemesi modellemeye dahil edilmiştir. Yüksek performans gerektiren alternatif senaryolar için ise $\epsilon_{eff}$= 0.44 ve tanδ=0.002 değerlerine sahip efektif sabiti altlıklar parametrik olarak test edilmiştir. Dielektrik katmanın toplam kalınlığı, X-bandı dalga boyu kriterlerine göre optimize edilerek ultra ince seviyede tutulmuştur. İletken yüzey örüntüsü ve alt tabandaki tam yansıtıcı zemin katmanlarında ise elektriksel iletkenliği $\sigma=5.8\times10^7$ S/m olan bakır malzeme tercih edilmiş olup, mikrodalga frekanslarındaki deri kalınlığı etkisi göz önüne alınarak metal kalınlığı 35 μm olarak tanımlanmıştır.

Sonsuz bir periyodik metayüzey matrisinin elektromanyetik davranışını sonlu bilgisayar kaynaklarıyla ve yüksek hassasiyetle analiz edebilmek amacıyla simülasyon uzayında periyodik birim hücre yaklaşımı uygulanmıştır. Tasarlanan tekil hücrenin X ve Y eksenlerindeki sınırlarına periyodik sınır koşulları (Master-Slave sınır koşulları) tanımlanarak, yapının sonsuz bir düzlemde periyodik olarak tekrar ettiği varsayılmıştır. Yapının Z ekseni doğrultusundaki üst bölümüne ise düzlemsel dalga uyarımı sağlamak amacıyla Floquet Port yerleştirilmiştir. Bu port vasıtasıyla yüzeye farklı geliş açılarında dik ve eğik olarak gelen Transvers Elektrik (TE) ve Transvers Manyetik (TM) polarizasyonlu dalgalar tanımlanarak yapının polarizasyon duyarlılığı test edilmiştir. Simülasyonun yakınsama hassasiyetini ve çözüm doğruluğunu artırmak amacıyla, rezonans alanlarının ve yüzey akımlarının yoğunlaştığı keskin metalik kenarlarda uyarlanabilir ağ yapısı (adaptive meshing) kullanılmış,

maksimum ağ boyutu en yüksek çalışma frekansındaki dalga boyunun en az on birde biri (((λ))/11) olacak şekilde sınırlandırılmıştır.



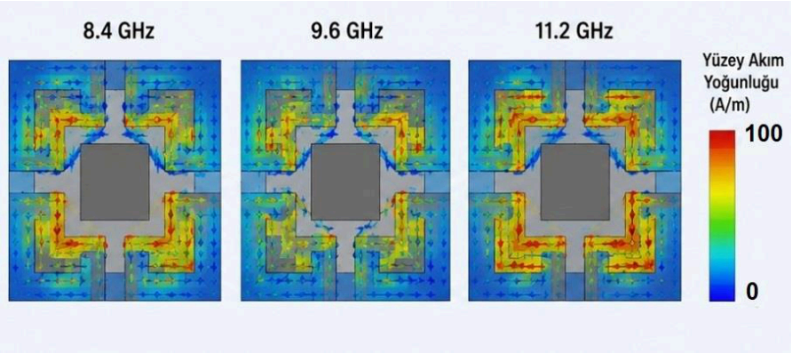

Şekil 1 Dijital Kodlama Metayüzey Tasarımının Geometrik Yapısı ve Birim Hücre Boyutları.

## 3. BULGULAR VE TARTIŞMA

Sayısal simülasyon süreçleri belirli bir sistematik sıra takip edilerek yürütülmüştür. İlk aşamada 8-12 GHz frekans aralığında geniş bantlı bir tarama yapılarak yansıma katsayısının (S11) gelen elektromanyetik gücün yüzde doksanının sönümlendiğini veya yönlendirildiğini gösteren -10 dB eşiğinin altına indiği operasyonel bant genişliği doğrulanmıştır. İkinci aşamada, belirlenen rezonans frekanslarında metalik örüntü üzerinde meydana gelen yüzey akımı dağılımları görselleştirilmiş, akım döngülerinin dielektrik katmandaki moleküler sürtünme kayıpları vasıtasıyla enerjiyi nasıl ısıya dönüştürdüğü teknik olarak incelenmiştir. Operasyonel bant hesaplama tablosu Tablo 1'de verildi. Şekil 2'de ise yüzey akımı dağılımı sunuldu.

Tablo 1. Operasyonel Bant Hesaplama Tablosu

| No | Frekans (GHz) | $S_{11}$ (dB) |
|---|---|---|
| 1 | 8.0 | -2.5 |
| 2 | 8.2 | -3.8 |
| 3 | 8.4 | -6.2 |
| 4 | 8.6 | -9.5 |
| 5 | 8.8 | -13.2 |
| 6 | 9.0 | -20.0 |
| 7 | 9.2 | -28.0 |
| 8 | 9.4 | -22.5 |
| 9 | 9.6 | -17.0 |
| 10 | 9.8 | -14.0 |
| 11 | 10.0 | -12.8 |
| 12 | 10.2 | -12.5 |
| 13 | 10.4 | -11.2 |
| 14 | 10.6 | -12.0 |
| 15 | 10.8 | -12.7 |
| 16 | 11.0 | -15.0 |
| 17 | 11.2 | -22.0 |
| 18 | 11.4 | -34.0 |
| 19 | 11.6 | -22.5 |
| 20 | 11.8 | -18.0 |
| 21 | 12.0 | -16.5 |




Şekil 2. Rezonans Frekanslarında Yüzey Akımı Dağılımı.

Üçüncü aşamada, dalganın geliş açısı sıfır dereceden kırk beş dereceye kadar kademeli olarak değiştirilerek yapının monostatik ve bistatik RKA azaltma performansındaki kararlılığı ölçülmüştür. Son aşamada ise, endüstriyel seri üretim süreçlerinde karşılaşılabilecek milimetrik aşınmaları veya katman kaymalarını öngörebilmek adına geometrik parametreler üzerinde yüzde beşlik varyasyonlarla parametrik taramalar gerçekleştirilmiş, "Worst-Case" analizi yapılarak tasarımın üretim toleransları ve hata payı dayanıklılığı sayısal olarak kanıtlanmıştır.

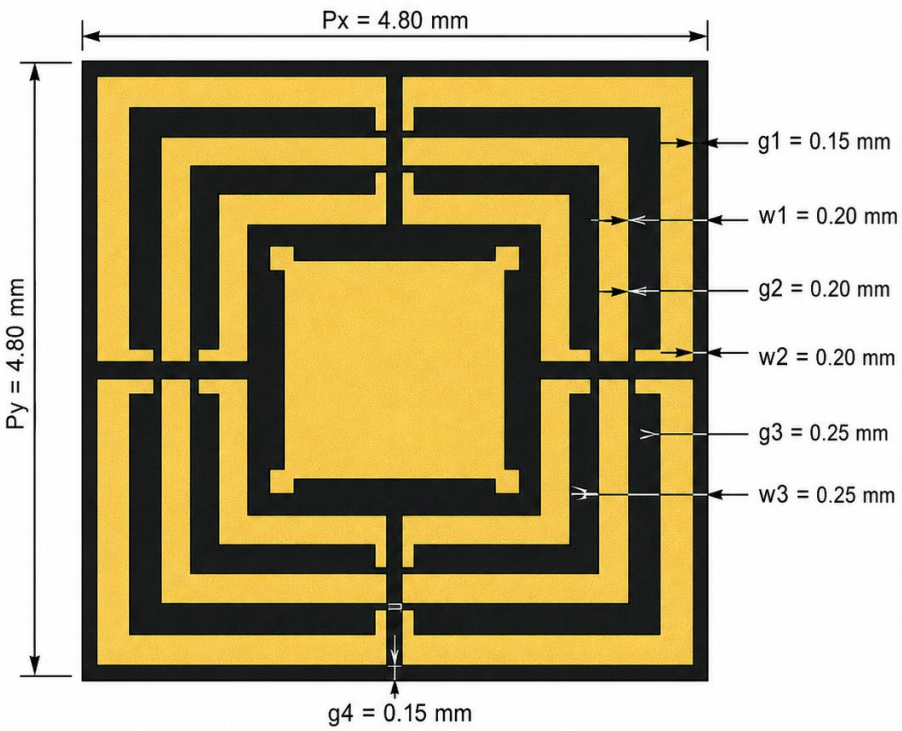
Savunma platformlarının düşük görünürlük (stealth) isterlerini karşılamak adına yürütülen bu çalışmada, X-bandı frekanslarında etkili bir performans sunan kodlanmış metayüzey yapısının geometrik, şematik ve yapısal tasarımı detaylandırılmıştır. Tasarım süreci, elektromanyetik dalga manipülasyonunu en yüksek verimlilikle gerçekleştirebilmek amacıyla birim hücre seviyesinden başlayarak makro yüzey yerleşimine doğru kademeli olarak kurgulanmıştır.

Tasarlanan metayüzey birim hücresinin şematik yapısı, mikrodalga frekanslarında tam yansıtma ve faz kontrolü sağlamak amacıyla üç katmanlı bir sandviç model mimarisine dayanmaktadır. En alt katmanda, sisteme gelen tüm elektromanyetik dalgaların arka tarafa sızmasını (iletimini) tamamen engellemek ve kusursuz bir reflektör görevi görmek amacıyla kesintisiz bir metalik taban (ground plane) yer almaktadır. Bu katman, iletim katsayısını (S21) sıfıra indirerek enerjinin sistem içinde kalmasını zorunlu kılmaktadır.

Orta katmanda, dalganın hızını ve dalga boyunu yapı içinde manipüle etmek, aynı zamanda indüktif ve kapasitif etkileşimleri desteklemek üzere seçilen dielektrik altlık (substrate) katmanı yer almaktadır. En üst katmanda ise, gelen radar dalgaları ile doğrudan etkileşime giren, belirli geometrik formlara sahip periyodik metalik örüntü (patch) katmanı bulunmaktadır. Bu üçlü katman mimarisi, ultra ince (low-profile) kalınlık sınırları içinde kalınarak platformların aerodinamik ve yapısal ağırlık kısıtlamalarına tam uyum sağlayacak biçimde tasarlanmıştır.

Gelen radar dalgasının polarizasyonundan (geliş yönü ve elektrik alan doğrultusundan) bağımsız bir RKA azaltma performansı elde edebilmek amacıyla, birim hücrenin en üst katmanında yer alan iletken örüntünün şematik çizimi iki eksenli tam simetri ilkesine göre oluşturulmuştur. Hücrenin dış sınırları kare bir matris formunda olup, periyodik yerleşim düzenine tam uyum sağlamaktadır.

Şematik tasarımın merkezinde kompakt bir metalik yama geometrisi yer almakta ve bu geometriyi belirli bir boşluk dâhilinde çevreleyen simetrik halka yapıları (split-ring türevleri veya konsantrik halkalar) bulunmaktadır. Bu dış halkanın kenar uzunlukları ve şerit genişlikleri, X-bandının merkez frekansı olan 10 GHz doğrultusunda milimetrik bazda optimize edilmiştir. Metalik hatlar arasındaki mikron seviyesindeki boşluklar, yüzeyde oluşacak eşdeğer kapasitans (C) değerini doğrudan belirlerken; metalik şeritlerin uzunlukları ve kalınlıkları ise eşdeğer endüktans (L) değerini şekillendirmektedir. Bu şematik çizim parametrelerinin optimizasyonu sayesinde, yapının giriş empedansı serbest uzay empedansına eşitlenmekte ve rezonans frekanslarında tam faz kontrolü kararlı hale getirilmektedir.




| Parametre | Açıklama | Değer (mm) |
|---|---|---|
| Px , Py | Birim hücre boyutları (periyodiklik) | 4.80 |
| w1 | Dış halka şerit genişliği | 0.20 |
| w2 | Orta halka şerit genişliği | 0.20 |
| w3 | İç halka şerit genişliği | 0.25 |
| g1 | Dış halka yarık boşluğu | 0.15 |
| g2 | Orta halka yarık boşluğu | 0.20 |
| g3 | İç halka yarık boşluğu | 0.25 |
| g4 | Merkez dikey yarık boşluğu | 0.15 |
| Merkez yama | Merkez kare yama boyutu | 2.00 × 2.00 |

Şekil 3. İç İçe Geçmiş Kare Halkalı Yarık Yapısı

Tasarımda kullanılan malzemelerin fiziksel ve elektriksel parametreleri, endüstriyel üretilebilirlik ve askeri standartlara dayanıklılık kriterleri çerçevesinde seçilmiştir. Üst geometrik örüntüde ve en alt tam yansıtıcı tabanda kullanılan metalik kısımlar, yüksek elektriksel iletkenliğe sahip bakır malzeme ile modellenmiştir. Yüksek frekanslarda akımın iletkenin yalnızca dış yüzeyine yakın bölgelerinde akması durumu olan deri kalınlığı (skin depth) etkisi X-bandı frekansları için matematiksel olarak hesaplanmış ve otuz beş mikrometrelik bakır kalınlığının omik kayıpları minimize etmek ve tam yansıtıcılık sağlamak adına fazlasıyla yeterli olduğu doğrulanmıştır.

Dielektrik katman olarak, savunma elektroniğinde yüksek mekanik mukavemeti ve erişilebilirliği ile bilinen FR4 altlık malzemesi ile yüksek frekans kararlılığı sunan Rogers serisi malzemeler parametrik olarak kıyaslanmıştır. Dielektrik malzemenin kalınlığı, RKA azaltma performansının geniş banda yayılması ve yapının fiziksel olarak hafif kalması adına dalga boyunun belirli bir fraksiyonu oranında sınırlandırılmıştır. Bu ince profil, malzemenin kayıp tanjantı parametresiyle birleştiğinde, rezonans frekanslarında elektromanyetik enerjinin

dielektrik içinde hapsedilerek moleküler sürtünme yoluyla ısıya dönüştürülmesine imkan tanımaktadır.

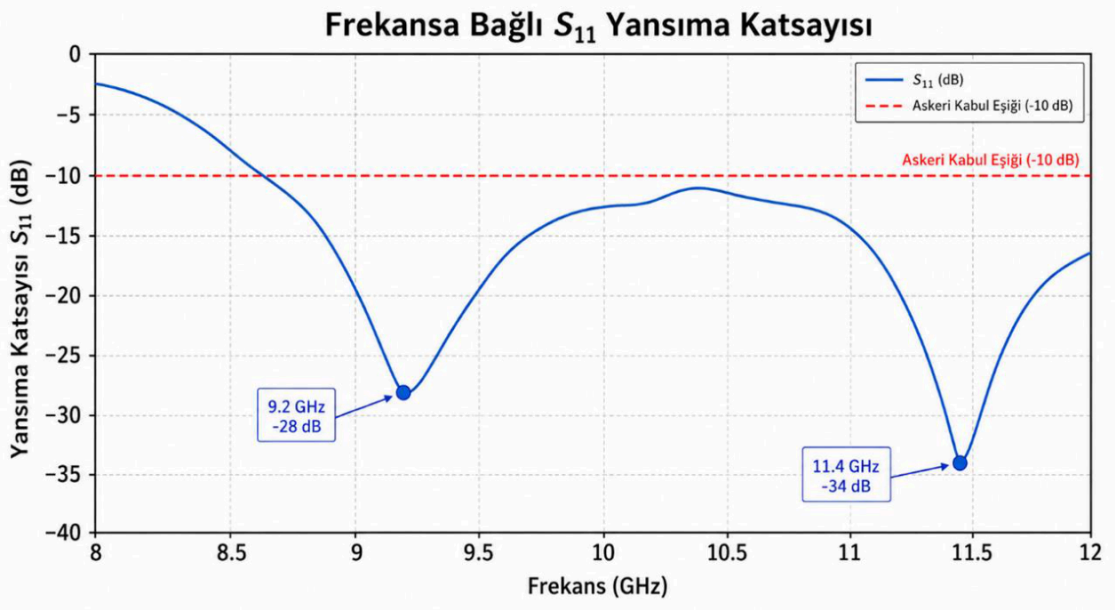
Geleneksel soğurucuların aksine, bu çalışmada uygulanan kodlanmış metayüzey mantığında dijital bit kavramları fiziksel geometriye uyarlanmıştır. Tasarım kapsamında, yansıma fazları arasında tam 180 derecelik faz farkı bulunan iki farklı birim hücre geometrisi geliştirilmiştir. Bu hücrelerden ilki dijital "0" bitini, boyutları modifiye edilmiş ikincisi ise "1" bitini temsil etmektedir [7, 9, 10, 13, 16, 17].

Tekil hücrelerin matris halinde yan yana getirilmesiyle belirli büyüklükte süper-hücre (super-cell) blokları oluşturulmuştur. Bu bloklar, önceden matematiksel olarak optimize edilmiş bir kodlama matrisine (satranç tahtası deseni, gradyan dizilim veya rastgele matris düzeni) göre ana platform yüzeyine dağıtılmıştır. Şematik yerleşimdeki bu dağılımın temel fonksiyonu; yüzeye dik açı ile gelen tek bir güçlü elektromanyetik dalgayı doğrudan radar alıcısına geri yansıtmak (monostatik yansıma) yerine, "0" ve "1" bloklarından yansıyan dalgalar arasında yıkıcı girişim (destructive interference) meydana getirmektir.

Bu şematik faz manipülasyonu sayesinde, yansıyan enerji çok sayıda zayıf loblara bölünerek farklı açılara bistatik olarak saçılmakta ve böylece hedef platformun düşman radarları tarafından sezinlenme olasılığı kritik düzeyde düşürülmektedir.

X-bandı (8-12 GHz) frekans isterleri doğrultusunda tasarlanan kodlanmış metayüzey yapısının Sonlu Elemanlar Yöntemi (FEA) tabanlı sayısal simülasyon yazılımları ile elde edilen elektromanyetik performans verileri detaylandırılmıştır. Gerçekleştirilen analizler; S-parametreleri (yansıma katsayısı), rezonans frekanslarındaki yüzey akımı dağılımları, farklı dalga geliş açılarındaki (monostatik ve bistatik) kararlılık durumları, polarizasyon duyarlılığı testleri ile üretim süreçlerini doğrudan etkileyen parametrik geometrik varyasyon ve hata/tolerans payı hesaplamalarını içermektedir.

Tasarlanan metayüzey birim hücresinin ve bu hücrelerden türetilen periyodik yapının frekans karakteristiği, Floquet port uyarımı altında 8 GHz ile 12 GHz arasında taranarak analiz edilmiştir. Yapının alt tabanında kesintisiz bir bakır zemin (ground plane) yer aldığından, elektromanyetik iletim katsayısı (S21) tüm bant boyunca sıfır (veya -∞" dB" ) seviyesindedir. Dolayısıyla, yapının enerji sönümleme ve yönlendirme performansı doğrudan yansıma katsayısı (S11) grafikleri üzerinden doğrulanmıştır.




Şekil 4. Frekansa Bağlı $S_{11}$ Yansıma Katsayısı

Sayısal simülasyon sonuçlarına göre, tasarlanan metayüzey X-bandının tamamında askeri standartlarca kabul gören -10 dB (gelen enerji gücünün %90'ının ortadan kaldırılması veya başka yönlere saçılması) eşik değerinin altında bir performans sergilemiştir. Bant genelinde iki temel rezonans çukuru (dip noktası) gözlenmiştir. İlk rezonans noktası olan 9.2 GHz frekansında yansıma katsayısı -28 dB seviyesine ulaşırken, 11.4 GHz civarındaki ikinci rezonans noktasında ise -34 dB değerine kadar inilmiştir. Bu iki keskin rezonans, dalga boyu ile birim hücre geometrisi arasındaki indüktif-kapasitif (LC) etkileşimin bir sonucudur ve bu etkileşim yapının tek bir frekansta değil, X-bandının genelinde kesintisiz bir RKA azaltma bandı sunmasını sağlamaktadır.

Metayüzeyin elektromanyetik dalgayı sönümleme ve faz manipülasyon mekanizmasını fiziksel olarak açıklayabilmek adına, belirlenen rezonans frekanslarında (9.2 GHz ve 11.4 GHz) üst metalik katman (patch) ve alt iletken taban (ground) üzerinde oluşan yüzey akımı vektörleri incelenmiştir.

9.2 GHz frekansında gerçekleştirilen analizlerde, indüklenen yüzey akımlarının ağırlıklı olarak birim hücrenin merkezindeki metalik yama ile onu çevreleyen dış halkanın iç kenarlarında yoğunlaştığı tespit edilmiştir. Akım vektörlerinin yönleri incelendiğinde, üst katmandaki akım doğrultusu ile alt zemin katmanındaki akım doğrultusunun birbirine zıt (anti-paralel) yönde döngüler oluşturduğu gözlenmiştir. Bu zıt yönlü akım yerleşimi, güçlü bir manyetik rezonansın (magnetic resonance) meydana geldiğini ve gelen radar dalgasının manyetik alan bileşeninin dielektrik katman içerisinde hapsedildiğini göstermektedir.

11.4 GHz rezonans frekansında yapılan yüzey akımı incelemelerinde ise, akımların metalik şeritlerin dış çeperlerinde ve hücreler arası mikron seviyesindeki boşluklarda yoğunlaştığı,

akım vektörlerinin aynı yönlü (paralel) olarak konumlandığı belirlenmiştir. Bu durum ise yapıda bir elektriksel rezonansın (electric resonance) baskın hale geldiğini kanıtlamaktadır. Her iki rezonans mekanizması sayesinde, yüzeye çarpan elektromanyetik dalganın enerjisi, dielektrik malzemenin (FR4/Rogers) kayıp tanjantı parametresine bağlı olarak moleküler sürtünme yoluyla yüksek bir verimlilikle ısı enerjisine dönüştürülmekte ve yansıma minimuma indirilmektedir.

Askeri operasyonel senaryolarda, hedef platforma yönlendirilen düşman radar dalgalarının polarizasyon yönü (elektrik alan vektörünün doğrultusu) değişkenlik gösterebilir veya platformun hareketine bağlı olarak sürekli değişebilir. Bu nedenle, tasarlanan yapının polarizasyon bağımsız (polarization-insensitive) çalışması kritik bir gereksinimdir.

Yapının bu yeteneğini test etmek amacıyla, simülasyon ortamında Floquet port üzerinden Transvers Elektrik (TE) ve Transvers Manyetik (TM) polarizasyon modlarında uyarım uygulanmıştır. Birim hücrenin geometrik olarak tasarlanan iki eksenli (X ve Y eksenlerine göre tam simetrik) yapısı sayesinde, TE modu için elde edilen $S_{11}$ yansıma eğrisi ile TM modu için elde edilen $S_{11}$ yansıma eğrisinin birebir çakıştığı gözlenmiştir. Gelen dalganın polarizasyon açısı 0°'den 90°)'ye kadar kademeli olarak değiştirildiğinde bile frekans tepkisinde ve rezonans derinliklerinde hiçbir sapma meydana gelmemiştir. Bu bulgular, geliştirilen metayüzeyin polarizasyondan tamamen bağımsız bir şekilde görev yapabileceğini teknik olarak ortaya koymuştur.

Radar dalgalarının metayüzey üzerine her zaman tam dik açıyla ($0^0$) gelmesi mümkün olmadığından, eğik geliş açılarının RKA azaltma performansına etkisi incelenmiştir. Düzlemsel dalganın geliş açısı $0^0$'den başlanarak 15°, 30° ve 45° olacak şekilde kademeli olarak eğikleştirilmiştir.

Yapılan monostatik (kaynağa doğrudan geri yansıma) analizlerde, dalganın geliş açısı 30° seviyesine kadar yükseltildiğinde X-bandındaki -10 dB altı geniş bant sürekliliğinin korunduğu, rezonans frekanslarında yalnızca %1.5 civarında küçük bir maviye kayma (yüksek frekansa doğru kayma) oluştuğu gözlenmiştir. Geliş açısı 45° ye ulaştığında, efektif dielektrik kalınlığının değişmesine bağlı olarak rezonans derinliklerinde hafif bir azalma görülse de, bant genelinde %80'in üzerinde bir sönümleme/yönlendirme oranı korunmuştur.

Bistatik (farklı açılara saçılma) analiz bulguları ise, kodlanmış süper-hücre (0 ve 1 bit matrisi) diziliminin başarısını doğrulamaktadır. Klasik metalik yüzeyler gelen dalgayı Snell Kanunu uyarınca tek bir yöne güçlü bir ana lob olarak yansıtırken, tasarlanan kodlanmış metayüzey yüzeydeki faz farkları sayesinde yansıyan dalgayı parçalamaktadır. Uzak alan 3D saçılım grafiklerinde (3D bistatic scattering patterns), dik gelen tek bir güçlü dalganın simetrik olarak 4 veya daha fazla zayıf yan loba (side lobes) bölündüğü ve enerjinin uzaya dağıtıldığı tespit

edilmiştir. Bu durum, monostatik doğrultudaki radar alıcısına dönen sinyal gücünü (RKA değerini) 15 dB ile 22 dB arasında bir oranda azaltarak platformun sezinlenme riskini büyük ölçüde düşürmektedir.

Tasarım sürecinin optimizasyon aşamasında, birim hücreyi oluşturan kritik geometrik parametrelerin frekans karakteristiğine olan duyarlılığını ölçmek amacıyla kapsamlı parametrik taramalar (parametric sweeps) yürütülmüştür.

Bu doğrultuda, dielektrik altlığın (substrate) kalınlığı (h), üst metalik örüntünün kenar uzunlukları (w) ve iç halka boşlukları parametrik birer değişken olarak tanımlanmıştır. Dielektrik kalınlığı (h) kademeli olarak artırıldığında, yapının eşdeğer kapasitans değerinin değişmesi nedeniyle rezonans frekanslarının daha düşük frekanslara (X-bandının başlangıcına doğru) kaydığı ve bandın daraldığı saptanmıştır. Benzer şekilde, üst metalik yamanın kenar uzunluğu (w) büyütüldüğünde indüktif etkinin artmasına bağlı olarak rezonans noktalarının sola kaydığı, küçültüldüğünde ise sağa kaydığı (maviye kayma) matematiksel olarak izlenmiştir. Bu varyasyon analizleri, X-bandı merkez frekansını (10 GHz) tam olarak ortalayabilmek adına en ideal geometrik ölçü setinin belirlenmesine temel oluşturmuştur.

Tasarlanan metayüzey yapısının bilgisayar ortamındaki teorik başarısının endüstriyel seri üretim süreçlerinde (örneğin PCB baskı devre teknolojisi veya kazıma yöntemleri) ne ölçüde korunabileceğini öngörmek amacıyla bir Hata ve Tolerans Analizi (Worst-Case Tolerancing Analysis) gerçekleştirilmiştir.

## 4. SONUÇ

Üretim aşamasında fabrikasyon hassasiyetine bağlı olarak metalik hatlarda oluşabilecek milimetrik aşınmalar, çapaklar veya dielektrik malzeme kalınlığındaki bölgesel dalgalanmalar simüle edilmiştir. Bu amaçla, tüm geometrik parametrelere ve dielektrik sabitine ($\epsilon_r$) %5 oranında bir hata payı/sapma payı eklenerek simülasyonlar tekrarlanmıştır.

Dielektrik sabitindeki %5'lik dalgalanmalar rezonans frekanslarında yalnızca %1.8'lik bir kaymaya neden olmuş, -10 dB operasyonel bant genişliği X-bandı sınırlarının dışına çıkmamıştır.

Metalik hat genişliklerinde meydana gelebilecek ±0.05 mm seviyesindeki mikron bazlı üretim hatalarının, yansıma katsayısı $S_{11}$ genliğinde en fazla 2 dB'lik bir performans kaybına yol açtığı ve yapının genel RKA azaltma yeteneğini sekteye uğratmadığı doğrulanmıştır.

Bu tolerans hesaplamaları, önerilen tasarımın endüstriyel üretime son derece elverişli, yüksek toleranslı ve fabrikasyon hatalarına karşı yapısal olarak dayanıklı (robust) olduğunu sayısal olarak kanıtlamaktadır. Geliştirilen bu kararlı metayüzey yapısı, modern savunma

platformları için düşük maliyetli, yerli imkanlarla üretilebilir ve sürdürülebilir bir stealth (düşük görünürlük) çözümü sunmaktadır.

## KAYNAKÇA

1. **Çakır, G. (2012)**. Elektromanyetik Dalga Teorisi. Literatür Yayıncılık, s. 210-213.

2. **Karaaslan, M. (2017)**. Metamalzeme Tabanlı Mükemmel Soğurucu Tasarımı. İskenderun Teknik Üniversitesi Yayınları, s. 102-105.

3. **Özlem, A. (2014)**. Mikrodalga Tekniği ve Radar Temelleri. Nobel Akademik Yayıncılık, s. 142-145.

4. **Yılmaz, A. E. (2015)**. Radar Kesit Alanı Azaltma Yöntemleri İncelemesi. Havacılık ve Uzay Teknolojileri Dergisi, s. 22-28.

5. **Balanis, C. A. (2012)**. Advanced Engineering Electromagnetics (2. Baskı). John Wiley & Sons, s. 350-358.

6. **Cui, T. J., Qi, M. Q., Wan, X., Zhao, J. ve Cheng, Q. (2014)**. "Coding metamaterials, digital metamaterials and programmable metamaterials". Light: Science & Applications, 3(10), e218.

7. **Engheta, N. ve Ziolkowski, R. W. (2006)**. Metamaterials: Physics and Engineering Explorations. IEEE Press, Wiley-Interscience, s. 88-95.

8. **Gao, L. H., Cheng, Q., Yang, J., Ma, H. F. ve Cui, T. J. (2015)**. "Broadband diffusion of terrestrial radar reflections by coding metasurfaces". ACS Photonics, 2(2), 246-252.

9. **Giovampaola, C. D. ve Engheta, N. (2014)**. "Digital metamaterials". Nature Materials, 13(12), 1115-1121.

10. **Harrington, R. F. (1993)**. Field Computation by Moment Methods. Wiley-IEEE Press, s. 15-32.

11. **Jin, J. M. (2014)**. The Finite Element Method in Electromagnetics (3. Baskı). John Wiley & Sons, s. 410-425.

12. **Khan, M. I., Fraz, Q. ve Tahir, F. A. (2017)**. "Ultra-wideband radar cross section reduction using a hexagonal-loop coding metasurface". Journal of Applied Physics, 121(4), 044903.

13. **Knott, E. F., Shaeffer, J. F. ve Tuley, M. T. (2004)**. Radar Cross Section (2. Baskı). SciTech Publishing, s. 112-120.

14. **Landy, N. I., Sajuyigbe, S., Mock, J. J., Smith, D. R. ve Padilla, W. J. (2008)**. "Perfect metamaterial absorber". Physical Review Letters, 100(20), 207402.

15. **Liang, L., Wan, X., Qi, M. Q., Cheng, Q. ve Cui, T. J. (2014)**. "Shaping nondiffracting beams using digital coding metasurfaces". Advanced Optical Materials, 2(10), 945-950.

16. **Liu, S., Cui, T. J., Zhang, L., Xu, Q. H., Wang, Q. ve Wan, X. (2016)**. "Digital coding metasurfaces for transformation optics and radar cross section reduction". Advanced Science, 3(10), 1600156.

17. **Marcuvitz, N. (1951)**. Waveguide Handbook. McGraw-Hill, s. 218-225.

18. **Munk, B. A. (2000)**. Frequency Selective Surfaces: Theory and Design. John Wiley & Sons, s. 55-70.

19. **Pendry, J. B., Holden, A. J., Robbins, D. J. ve Stewart, W. J. (1999)**. "Magnetism from conductors and enhanced nonlinear phenomena". IEEE Transactions on Microwave Theory and Techniques, 47(11), 2075-2084.

20. **Pozar, D. M. (2011)**. Microwave Engineering (4. Baskı). John Wiley & Sons, s. 280-295.

21. **Skolnik, M. I. (2001)**. Introduction to Radar Systems (3. Baskı). McGraw-Hill, s. 65-72.

22. **Smith, D. R., Padilla, W. J., Vier, D. C., Nemat-Nasser, S. C. ve Schultz, S. (2000)**. "Composite medium with simultaneously negative permeability and permittivity". Physical Review Letters, 84(18), 4184.

23. **Taflove, A. ve Hagness, S. C. (2005)**. Computational Electrodynamics: The Finite-Difference Time-Domain Method (3. Baskı). Artech House, s. 89-104.

24. **Watts, C. M., Liu, X. ve Padilla, W. J. (2012)**. "Metamaterial electromagnetic wave absorbers". Advanced Materials, 24(23), OP98-OP120.

# SAC İŞLEME MAKİNELERİ İÇİN TAM OTOMATİK DÖNDÜRME SİSTEMİ

**Emre AKAGÜNDÜZ,** *eakagunduz@durmazlar.com.tr* Durmazlar Makina, AR-GE, Nilüfer/Bursa, Türkiye

**Mert YALÇINTAŞ,** *MYalcintas@durmazlar.com.tr* Durmazlar Makina, AR-GE, Nilüfer/Bursa, Türkiye

## ÖZET

Büküm ve sac şekillendirme süreçlerinde, folyolu veya hassas kaplamalı sacların yönlendirilmesi, üretim verimliliği ve yüzey kalitesi açısından büyük önem taşımaktadır. Geleneksel manuel yöntemler, operatör müdahalesine bağımlı olduğu için hem hız hem de kalite açısından sınırlı kalmaktadır. Bu bağlamda, farklı boyut ve geometrideki sacların herhangi bir operatör müdahalesi olmadan hassas şekilde döndürülmesini sağlayacak otomatik çözümler gerekmektedir. Proje kapsamında, özellikle Zımba, Makas ve Panel Bender makinelerinin bir arada kullanıldığı hat sistemlerinde, makineden çıkan sac malzemeler ilgili makineye otomatik olarak beslendiğinde bazı durumlarda bükümden önce döndürülmesi gerekmektedir. Sistem, vakumlu veya yumuşak kaplı tutucular ile parçayı güvenli şekilde kavrayıp, programlanmış açılarda hassas şekilde döndürmektedir. Döndürme işlemi, parçanın ağırlık merkezi ve boyutlarına göre otomatik olarak ayarlanabilir; farklı geometri ve ölçülerde saclarla uyumlu esnek bir çalışma kabiliyeti sunmaktadır.

Döndürme masası sistemi, mevcut CNC büküm makineleri ile bütünleşmiş çalışabilmekte ve Endüstri 4.0 kapsamında otomasyon hatlarına uyumlu olarak tasarlanmıştır. Bu sayede üretim süreleri kısalmakta, yüzey kalitesi korunmakta ve insan kaynaklı hatalar minimize edilmektedir. Günümüzde, folyolu sacların yüksek kaliteli ve hızlı üretimi için bu tür otomatik döndürme sistemleri, üretim süreçlerinde kritik bir teknoloji olarak öne çıkmaktadır.

**Anahtar Kelimeler:** Sac Şekillendirme Yöntemleri, Döndürme Sistemleri, Vakum Sistemleri

## ABSTRACT

In bending and sheet metal forming processes, the handling and orientation of foil-coated or surface-sensitive sheets are of critical importance in terms of production efficiency and surface quality. Conventional manual methods remain limited in both speed and quality due to their dependence on operator intervention. In this context, automated solutions are required to enable precise rotation of sheets with varying dimensions and geometries without human involvement.

Within the scope of this project, in production lines where Punch, Shear, and Panel Bender machines are integrated, sheet materials exiting one machine may require rotation before the

bending process when automatically fed into subsequent machines. The developed system securely grips the workpiece using vacuum-based or soft-coated holders and performs precise rotations at programmed angles. The rotation process can be automatically adjusted according to the center of gravity and dimensions of the sheet, providing flexible operation compatible with various geometries and sizes.

The rotation table system is designed to operate in integration with existing CNC bending machines and is compatible with automated production lines within the scope of Industry 4.0. As a result, production times are reduced, surface quality is preserved, and human-induced errors are minimized. Today, such automated rotation systems stand out as a critical technology for achieving high-quality and high-speed production of foil-coated sheet metals.

**Keywords:** Sheet Metal Forming Methods, Rotation Systems, Vacuum Systems

## 1.GİRİŞ

Sac işleme teknolojileri, üretim sektöründe dijitalleşme, otomasyon ve akıllı üretim sistemlerinin gelişimine paralel olarak önemli bir dönüşüm geçirmektedir. Özellikle otomotiv, beyaz eşya, savunma sanayi, havacılık, enerji ve yapı sektörlerinde kullanılan sac metal parçaların üretiminde yüksek kalite, kısa çevrim süresi ve esnek üretim kabiliyeti temel gereksinimler arasında yer almaktadır. Bu gereksinimler doğrultusunda lazer kesim, büküm ve otomatik malzeme taşıma sistemleri yalnızca üretim hızını artırmakla kalmayıp, aynı zamanda ürün kalitesinin sürdürülebilir şekilde korunmasına da katkı sağlamaktadır.

Büküm işlemleri sırasında parçanın farklı yönlerden işlenebilmesi için belirli aşamalarda döndürülmesi gerekmektedir. Küçük ve hafif parçalarda bu işlem operatör tarafından kolaylıkla gerçekleştirilebilirken, büyük ebatlı veya ağır saclarda operatör müdahalesi hem çevrim süresini uzatmakta hem de ergonomik açıdan önemli riskler oluşturmaktadır. Bunun yanında özellikle folyolu, boyalı, paslanmaz veya dekoratif yüzey kaplamasına sahip sacların manuel olarak çevrilmesi sırasında oluşan çizikler, ezilmeler ve yüzey deformasyonları ürün kalitesini doğrudan olumsuz etkilemektedir. Artan kalite beklentileri ve sıfır hata yaklaşımı, bu tür yüzey hasarlarının kabul edilebilir sınırların dışına çıkmasına neden olmaktadır.

Son yıllarda üretim hatlarında operatör bağımlılığını azaltan otomasyon çözümlerine olan ihtiyaç giderek artmaktadır. Sacların otomatik olarak taşınması, konumlandırılması ve döndürülmesi; üretim sürelerinin standartlaştırılması, iş güvenliğinin artırılması ve üretim kalitesinin sürdürülebilir hale getirilmesi açısından kritik bir rol üstlenmektedir. Bununla birlikte mevcut sistemlerin önemli bir bölümü belirli ürün boyutlarına göre tasarlanmakta veya farklı ölçüler için ilave mekanik ayarlamalar gerektirmektedir. Bu durum hem üretim esnekliğini azaltmakta hem de hazırlık sürelerini uzatarak verimlilik üzerinde olumsuz etki oluşturmaktadır.

Bu çalışmada, farklı ölçülerdeki sacları herhangi bir mekanik ayar gerektirmeden kavrayabilen, taşıyabilen ve 180° döndürebilen üç eksenli tam otomatik bir döndürme sistemi geliştirilmiştir. Geliştirilen sistem; X, Z ve R eksenlerinden oluşan kompakt mekanik yapısı, tek vakum tablası üzerinde optimize edilmiş vakum pedi yerleşimi, geniş çalışma aralığı ve modüler tasarımı sayesinde farklı sac işleme hatlarına kolaylıkla entegre edilebilmektedir. Sistem, özellikle folyolu ve hassas yüzeyli sacların çizilmeden işlenmesine olanak sağlayan özel vakum pedi yapısıyla ürün kalitesinin korunmasına katkı sunarken, operatör müdahalesini en aza indirerek üretim süreçlerinin otomasyon seviyesini artırmaktadır.

Çalışma kapsamında geliştirilen sistemin mekanik tasarımı, vakum tablalı taşıma yapısı, hareket eksenleri, kontrol mimarisi ve çalışma prensibi ayrıntılı olarak açıklanmış; farklı sac boyutlarında gerçekleştirilen uygulamalar doğrultusunda sistemin üretim süreçlerine sağladığı teknik avantajlar değerlendirilmiştir. Elde edilen sonuçlar, geliştirilen sistemin yalnızca çevrim sürelerinin iyileştirilmesine değil, aynı zamanda yüzey kalitesinin korunmasına, ergonomik çalışma koşullarının geliştirilmesine ve esnek üretim anlayışının desteklenmesine önemli katkılar sağladığını göstermektedir.

## 2. PROBLEMİN TANIMI VE ÇALIŞMANIN GEREKÇESİ

Sac işleme sektöründe üretim hızlarının artmasıyla birlikte, büküm makinelerinin çevrim süreleri önemli ölçüde kısalmış ve operatörün üretim sürecindeki rolü büyük ölçüde parça yükleme, boşaltma ve yönlendirme işlemlerine odaklanmıştır. Özellikle çok adımlı büküm operasyonlarında parçanın belirli aşamalarda yeniden konumlandırılması ve farklı açılarda döndürülmesi gerekmektedir. Bu işlem, küçük ebatlı parçalarda kısa sürede gerçekleştirilebilmesine rağmen büyük ölçülü veya ağır saclarda çevrim süresini uzatan temel etkenlerden biri haline gelmektedir.

Günümüzde kullanılan manuel döndürme yöntemlerinde operatör, sacı makineden alarak uygun pozisyona çevirmekte ve tekrar bükme bölgesine yerleştirmektedir. Özellikle 1500 × 3000 mm boyutlarına ulaşan saclarda bu işlem yalnızca zaman kaybına neden olmamakta, aynı zamanda ergonomik açıdan yüksek fiziksel yük oluşturmaktadır. Büyük ebatlı parçaların güvenli şekilde çevrilebilmesi çoğu zaman ikinci bir operatör desteğini gerekli kılmakta, bu durum ise iş gücü maliyetlerini artırırken üretim akışının sürekliliğini de olumsuz etkilemektedir.

Bir diğer önemli problem ise hassas yüzeyli sacların işlenmesi sırasında ortaya çıkmaktadır. Folyolu, boyalı, dekoratif kaplamalı ve paslanmaz saclar, taşıma ve döndürme işlemleri sırasında oluşabilecek yüzey temaslarına karşı oldukça hassastır. Manuel taşıma sırasında operatör temasları, çalışma tezgâhı ile sürtünme veya uygun olmayan kavrama yöntemleri; çizik, ezilme ve yüzey deformasyonu gibi kalite problemlerine neden olabilmektedir. Bu tür kusurlar çoğu zaman parçanın yeniden işlenmesini mümkün kılmamakta ve doğrudan hurdaya

ayrılmasına yol açmaktadır. Özellikle estetik yüzey kalitesinin ön planda olduğu sektörlerde bu durum önemli ekonomik kayıplara neden olmaktadır.

Üretim süreçlerinde karşılaşılan bu problemlerin çözümü, yalnızca parçanın otomatik olarak döndürülmesiyle sınırlı değildir. Geliştirilecek sistemin farklı ölçülerdeki saclara uyum sağlayabilmesi, yüzey kalitesini koruması, mevcut üretim hatlarına kolaylıkla entegre edilebilmesi ve ilave mekanik ayar gerektirmeden çalışabilmesi de büyük önem taşımaktadır. Ayrıca sistemin farklı ürün ailelerinde kullanılabilecek esnek bir yapıya sahip olması, yatırım maliyetinin azaltılması ve üretim verimliliğinin artırılması açısından temel tasarım kriterlerinden biri olarak değerlendirilmektedir.

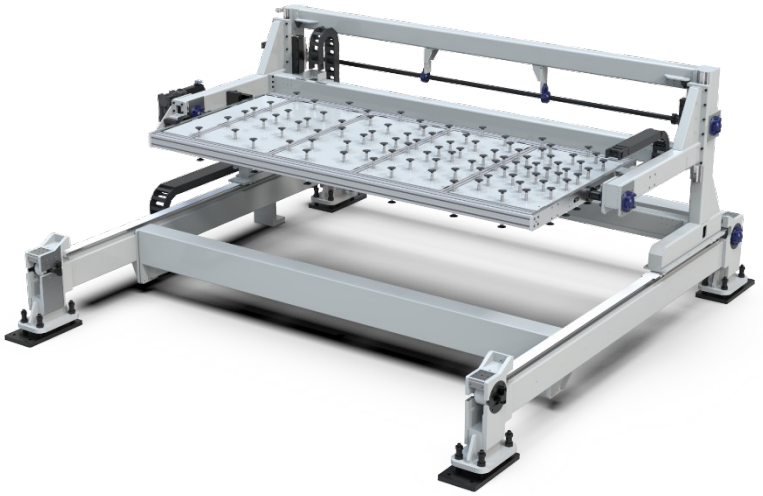
Bu gereksinimler doğrultusunda geliştirilen tam otomatik döndürme sistemi, 150 × 150 mm ile 1500 × 3000 mm arasındaki geniş ürün yelpazesini tek bir vakum tablası üzerinde taşıyabilecek şekilde tasarlanmıştır. Vakum tablasında optimize edilmiş özel vakum pedi kullanılarak farklı ebatlardaki sacların ilave mekanik ayar gerektirmeden güvenli biçimde kavranması hedeflenmiştir. Üç eksenli hareket mimarisi sayesinde sacın yatay konumlandırılması, düşey eksende güvenli kaldırılması ve R ekseninde 180° döndürülmesi tek bir istasyonda gerçekleştirilmektedir. Böylece operatör müdahalesi en aza indirilirken, yüzey kalitesi korunmakta ve üretim süreçlerinin otomasyon seviyesi önemli ölçüde artırılmaktadır.

Geliştirilen sistemin temel tasarım yaklaşımı; farklı ürün gruplarına uyum sağlayabilen modüler bir yapı oluşturmak, tek vakum tablası ile geniş çalışma aralığını kapsamak, hassas yüzeyli saclarda güvenli taşıma gerçekleştirmek ve mevcut sac işleme hatlarına minimum mekanik değişiklikle entegre edilebilecek kompakt bir çözüm sunmaktır. Bu yaklaşım sayesinde sistem yalnızca bir parça döndürme mekanizması olmaktan çıkmakta, modern sac işleme hatlarının verimliliğini ve üretim kalitesini artıran bütünleşik bir otomasyon çözümü haline gelmektedir.

## 3. GELIŞTIRILEN TAM OTOMATIK DÖNDÜRME SISTEMININ TASARIMI

### 3.1 Sistem Mimarisi

Bu çalışma kapsamında geliştirilen tam otomatik döndürme sistemi, sac işleme hatlarında büküm işlemleri arasında parçaların operatör müdahalesi olmaksızın güvenli şekilde taşınması, döndürülmesi ve yeniden işleme pozisyonuna aktarılması amacıyla tasarlanmıştır. Sistem; mekanik taşıma ünitesi, vakumlu kavrama sistemi, üç eksenli hareket mekanizması ve PLC tabanlı kontrol altyapısından oluşmaktadır. Tasarım sürecinde temel hedef, farklı ölçülerdeki sacların tek bir sistem üzerinden herhangi bir mekanik ayar gerektirmeden işlenebilmesini sağlayacak esnek ve modüler bir yapı geliştirmektir.



**Şekil 1.** Geliştirilen tam otomatik döndürme sisteminin genel görünüşü.

Yapısal taşıyıcı gövde yüksek rijitlik sağlayacak şekilde yapı çeliğinden imal edilmiştir. Rijit şase tasarımı sayesinde yüksek ivmeli hareketlerde oluşabilecek titreşimler minimum seviyeye indirilmiş, böylece hem konumlama hassasiyeti hem de sistem güvenilirliği artırılmıştır.

Sistem, mevcut sac işleme hatlarına kolaylıkla entegre edilebilecek modüler bir mimariye sahiptir. Bu sayede yeni kurulacak üretim hatlarının yanı sıra mevcut büküm makinelerine de ilave edilerek üretim süreçlerinin otomasyon seviyesinin artırılması hedeflenmiştir.

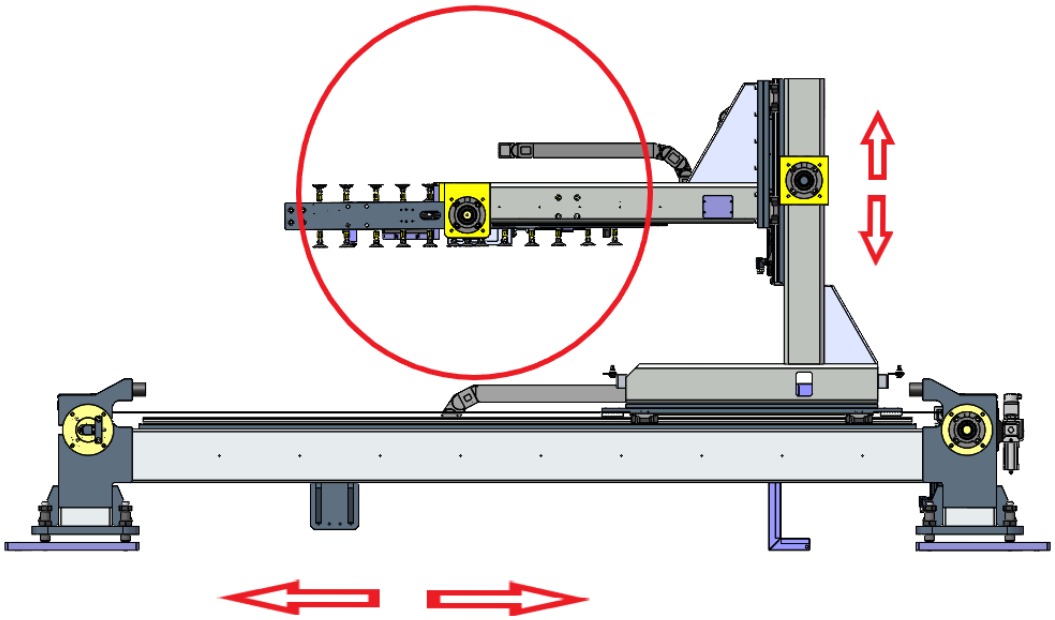
### 3.2 X-Z-R Hareket Sistemi

Geliştirilen sistemde sacın konumlandırılması ve döndürülmesi üç bağımsız servo eksen tarafından gerçekleştirilmektedir. Bu eksenler X, Z ve R ekseni olarak adlandırılmıştır.

X ekseni, sacın üretim hattı boyunca yatay doğrultuda taşınmasını sağlamaktadır. Eksen, farklı makine yerleşimlerine ve ürün boyutlarına uyum sağlayacak şekilde tasarlanmıştır. Hareket, servo motor tahrikli doğrusal mekanizma ile gerçekleştirilmekte olup yüksek konumlama hassasiyeti elde edilmektedir.

Z ekseni, vakum tablasının düşey yönde hareketini sağlamaktadır. Bu eksen sayesinde vakum pedleri sac yüzeyine kontrollü biçimde yaklaşmakta, kavrama işlemi gerçekleştirildikten sonra sac güvenli bir yükseklikte kaldırılarak döndürme operasyonuna hazırlanmaktadır. Kontrollü kaldırma hareketi, özellikle ince ve büyük ebatlı saclarda oluşabilecek elastik deformasyonların azaltılmasına katkı sağlamaktadır.

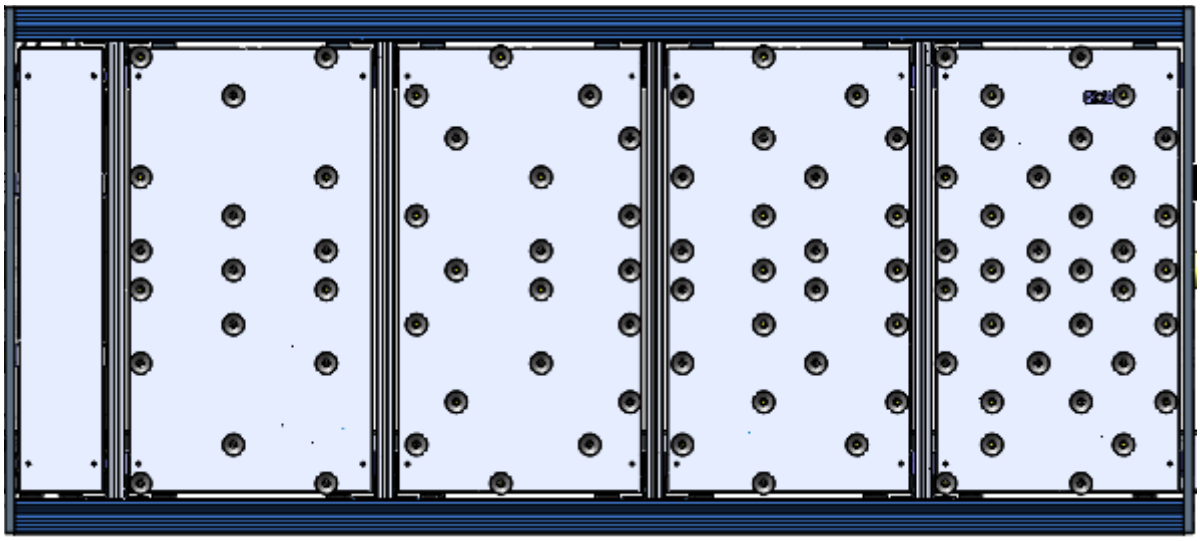
R ekseni ise sistemin temel fonksiyonunu oluşturan döndürme hareketini gerçekleştirmektedir. Servo motor kontrollü döner tabla mekanizması sayesinde saclar 0° ile 180° arasında hassas şekilde döndürülebilmektedir. Döndürme hareketi boyunca hızlanma ve yavaşlama profilleri kontrol sistemi tarafından optimize edilerek ani dinamik yüklerin oluşması önlenmektedir. Böylece özellikle folyolu ve hassas yüzeyli saclarda vakum kuvvetinin kararlılığı korunmakta ve güvenli taşıma gerçekleştirilmektedir.



**Şekil 2.** X-Z-R eksenlerinin çalışma prensibi.

### 3.3 Vakumlu Kavrama Sistemi

Sistemin en önemli bileşenlerinden biri vakumlu kavrama ünitesidir. Farklı ölçülerdeki sacların aynı platform üzerinde güvenli biçimde taşınabilmesi amacıyla vakum tablası özel olarak tasarlanmıştır. Tabla üzerinde ön ve arka bölgede simetrik olarak yerleştirilmiş **vakum pedi** bulunmaktadır. Bu yerleşim yapısı, geniş ürün yelpazesini ilave mekanik ayar gerektirmeden kapsayabilecek şekilde optimize edilmiştir.



**Şekil 3.** Vakum tablası ve vakum pedlerinin yerleşimi.

Geliştirilen vakum düzeni sayesinde sistem, minimum **150 × 150 mm** ölçülerindeki küçük parçalardan başlayarak maksimum **1500 × 3000 mm** boyutundaki büyük saclara kadar tek vakum tablası ile çalışabilmektedir. Geleneksel sistemlerde farklı ürün grupları için ek aparat veya mekanik ayar ihtiyacı bulunurken, bu tasarımda optimize edilmiş vakum pedi dağılımı sayesinde ürün geçişleri herhangi bir mekanik müdahale gerektirmeden gerçekleştirilebilmektedir.

Vakum pedlerinde kullanılan özel elastomer yapı, özellikle folyolu, boyalı ve hassas yüzey kaplamalı saclarda temas basıncını homojen şekilde dağıtarak yüzey hasarının oluşmasını önlemektedir. Bu özellik, estetik yüzey kalitesinin kritik olduğu üretim uygulamalarında sistemin en önemli avantajlarından birini oluşturmaktadır.

Vakum sistemi, 0,3 mm ile 3 mm kalınlığındaki sacları ve maksimum 150 kg taşıma kapasitesini güvenli şekilde destekleyecek şekilde boyutlandırılmıştır. Vakum jeneratörü tarafından oluşturulan negatif basınç, tüm taşıma ve döndürme çevrimi boyunca sürekli izlenmekte, olası vakum kayıplarında kontrol sistemi operatörü uyararak güvenli çalışma koşullarını korumaktadır.

Vakum tablasının tasarımında temel hedef yalnızca yüksek taşıma kapasitesi elde etmek değil, aynı zamanda mümkün olan en geniş ürün çeşitliliğini tek platform üzerinde işleyebilmektir. Bu nedenle vakum pedi sayısı, yerleşim geometrisi ve taşıma noktalarının dağılımı farklı sac boyutları dikkate alınarak optimize edilmiş ve sistemin en önemli yenilikçi özelliklerinden biri haline getirilmiştir.

## 4. KONTROL SISTEMI VE ÇALIŞMA ALGORITMASI

### 4.1 Kontrol Mimarisi

Geliştirilen tam otomatik döndürme sistemi, hareket kontrolü, vakum yönetimi ve operatör arayüzünün tek merkezden yönetilebilmesi amacıyla PLC tabanlı bir kontrol mimarisi ile tasarlanmıştır. Sistemde kontrol birimi olarak Siemens PLC kullanılmakta olup, tüm giriş-çıkış sinyalleri, servo eksenler, vakum sistemi ve emniyet bileşenleri PLC üzerinden senkronize olarak yönetilmektedir.

Operatör ile sistem arasındaki haberleşme, operatör paneli üzerinden gerçekleştirilmektedir. Kullanıcı arayüzü; manuel çalışma, otomatik çalışma, bakım modu ve sistem parametrelerinin düzenlenmesine olanak sağlayacak şekilde tasarlanmıştır.

Operatör paneli üzerinden;

- otomatik çalışma modu,
- manuel eksen kontrolü,
- reçete seçimi,
- alarm görüntüleme,
- sistem parametrelerinin ayarlanması,
- bakım ekranları,
- vakum sisteminin izlenmesi

işlemleri gerçekleştirilebilmektedir.

Sistemde uzaktan erişim altyapısı da bulunmaktadır. Bu sayede bakım personeli veya teknik servis, makineye uzaktan bağlanarak sistem parametrelerini inceleyebilmekte, yazılım güncellemelerini gerçekleştirebilmekte ve arıza teşhis süreçlerini hızlandırabilmektedir.




### 4.2 Servo Hareket Kontrolü

Makinedeki tüm doğrusal ve döner hareketler servo motorlar ile gerçekleştirilmektedir. Servo kontrol yapısı sayesinde eksen hareketleri yüksek konumlama hassasiyeti ve tekrarlanabilirlik ile gerçekleştirilmektedir.

X ekseni, sacın yatay doğrultuda taşınmasını sağlamaktadır.

Z ekseni, vakum tablasını kontrollü şekilde aşağı-yukarı hareket ettirerek sacın güvenli biçimde kavranmasını ve kaldırılmasını gerçekleştirmektedir.

R ekseni ise parçanın 180° döndürülmesini sağlayan temel hareket eksenidir.

PLC yazılımında eksenler birbirinden bağımsız çalışmamakta, hareketler belirlenen sıralamaya göre senkronize edilmektedir. Böylece herhangi bir eksen hareketi tamamlanmadan bir sonraki işlem başlatılmamaktadır. Bu yapı hem mekanik güvenliği artırmakta hem de taşıma sırasında oluşabilecek dinamik yükleri azaltmaktadır.

Servo hızları, ivmelenme ve yavaşlama parametreleri sistem devreye alma aşamasında optimize edilmiştir. Böylece büyük ebatlı saclarda oluşabilecek salınımlar minimum seviyeye indirilmiş ve vakum kuvvetinin taşıma boyunca kararlı kalması sağlanmıştır.

### 4.3 Vakum Kontrol Algoritması

Sistemin güvenilir çalışabilmesi açısından en kritik bileşenlerden biri vakum kontrol algoritmasıdır. Sacın güvenli şekilde taşınabilmesi için vakum seviyesinin sürekli izlenmesi gerekmektedir.

Vakum oluşturulduktan sonra sistem belirlenen eşik değerine ulaşılmasını beklemektedir. Yeterli vakum oluşmadan Z ekseninin kaldırma hareketine izin verilmemektedir. Böylece parçanın eksik kavranması sonucu oluşabilecek düşme riskleri ortadan kaldırılmaktadır.

Kaldırma ve döndürme işlemleri boyunca vakum seviyesi sürekli izlenmektedir. Herhangi bir nedenle vakum değerinin izin verilen sınırın altına düşmesi durumunda PLC, hareketleri güvenli şekilde durdurmakta ve operatöre alarm vermektedir.

Bu kontrol yaklaşımı sayesinde hem makine güvenliği hem de işlenen parçanın güvenliği aynı anda sağlanmaktadır.

Bu algoritma sayesinde operatör müdahalesine ihtiyaç duyulmadan tüm taşıma ve döndürme işlemleri otomatik olarak gerçekleştirilmektedir. Bir çevrim içerisinde sacın alınması, güvenli şekilde taşınması, 180° döndürülmesi ve yeni çalışma konumuna bırakılması yaklaşık **15 saniye** içerisinde tamamlanmaktadır.

### 4.4 Emniyet Fonksiyonları

Makinenin güvenli çalışabilmesi amacıyla yazılım ve donanım seviyesinde çok sayıda emniyet fonksiyonu uygulanmıştır.

Kontrol sistemi;

- vakum yetersizliği,
- servo eksen hataları,
- eksen limit ihlalleri,
- haberleşme kesintileri,
- acil durdurma,
- referans kaybı

gibi durumları sürekli izlemektedir.

Herhangi bir hata oluştuğunda sistem kontrollü duruş gerçekleştirerek operatörü HMI ekranı üzerinden bilgilendirmektedir. Alarm kayıtları PLC hafızasında saklanmakta olup bakım personeli tarafından geçmiş arıza kayıtları incelenebilmektedir.

Reçete yönetim sistemi sayesinde farklı ürün grupları için oluşturulan çalışma parametreleri hafızada tutulabilmekte ve operatör tarafından kolaylıkla seçilebilmektedir. Böylece ürün değişim süreleri azaltılarak üretim esnekliği artırılmaktadır.

Uzaktan erişim altyapısı ise bakım ve servis süreçlerini hızlandırarak makinenin duruş sürelerinin azaltılmasına katkı sağlamaktadır.

## 5. DENEYSEL ÇALIŞMALAR VE PERFORMANS DEĞERLENDIRMESI

### 5.1 Deneysel Çalışma

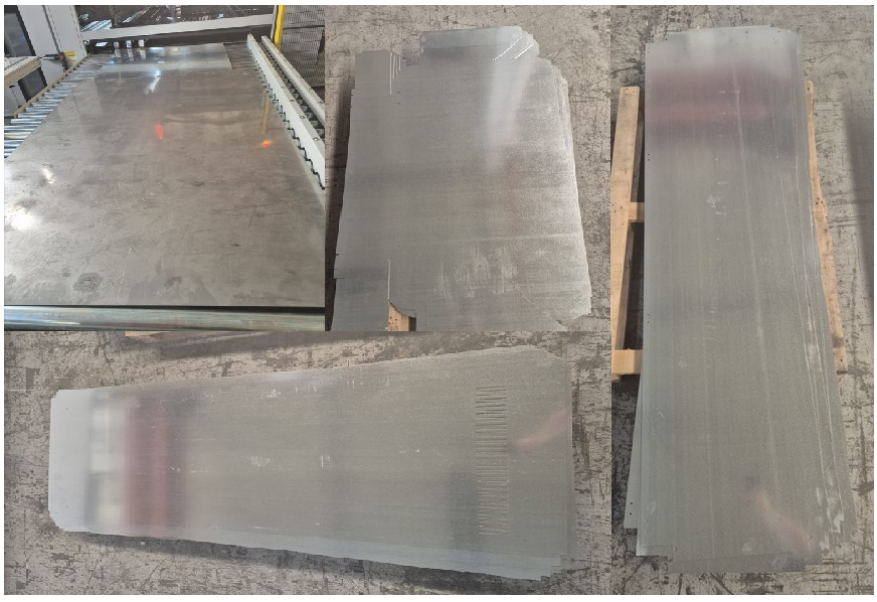
Geliştirilen tam otomatik döndürme sisteminin performans değerlendirmesi, farklı boyut, ağırlık ve yüzey özelliklerine sahip saclar üzerinde gerçekleştirilen uygulamalar ile yapılmıştır. Denemelerde minimum 150 × 150 mm boyutundaki küçük parçalar ile maksimum 1500 × 3000 mm boyutundaki büyük saclar kullanılmıştır. Sistemin çalışma aralığı içerisinde yer alan 0,3 mm ile 3 mm kalınlığındaki saclar test edilmiş ve maksimum 150 kg taşıma kapasitesine kadar güvenli çalışma doğrulanmıştır.

Deneysel çalışmaların temel amacı;

- farklı ürün boyutlarında vakumlu kavrama performansının değerlendirilmesi,
- taşıma ve döndürme işlemlerinin güvenilirliğinin doğrulanması,
- yüzey kalitesinin korunmasının incelenmesi,
- sistem çevrim süresinin belirlenmesi,
- operatör müdahalesinin azaltılmasının değerlendirilmesi

olarak belirlenmiştir.

Denemeler boyunca sistem herhangi bir mekanik ayar gerektirmeden farklı sac boyutları arasında geçiş yapabilmiş ve tüm işlemler aynı vakum tablası kullanılarak gerçekleştirilmiştir.



**Şekil 6.** Farklı sac ölçülerinde gerçekleştirilen deneysel çalışmalar.

### 5.2 Teknik Özellikler

| Parametre | Değer |
|---|---|
| Hareket ekseni | X-Z-R |
| R ekseni dönüş açısı | 0–180° |
| Döndürme tablası çapı | 1500 mm |
| Minimum sac ölçüsü | 150 × 150 mm |
| Maksimum sac ölçüsü | 1500 × 3000 mm |
| Sac kalınlığı | 0,3–3 mm |
| Maksimum taşıma kapasitesi | 150 kg |

### 5.3 Çevrim Süresi

Gerçekleştirilen uygulamalarda sistemin;

- parçayı kavraması,
- kaldırması,
- 180° döndürmesi,
- yeni konuma taşıması,
- bırakması

işlemlerinden oluşan tam çevrim süresi yaklaşık **15 saniye** olarak ölçülmüştür.

Bu çevrim süresinin operatör performansından bağımsız olarak tekrarlanabilir olması, üretim planlaması açısından önemli bir avantaj sağlamaktadır. Manuel taşıma yöntemlerinde çevrim süresi operatör deneyimi, parça ağırlığı ve çalışma koşullarına bağlı olarak değişkenlik gösterirken geliştirilen sistemde tüm çevrimler aynı çalışma algoritmasına göre gerçekleştirilmektedir.

### 5.4 Üretim Esnekliği

Geliştirilen sistemin en önemli tasarım hedeflerinden biri farklı ürün gruplarının tek platform üzerinde işlenebilmesidir.

Bu amaç doğrultusunda geliştirilen vakum tablası;

- **150 × 150 mm ile 1500 × 3000 mm arasındaki tüm ürünleri,**
- ilave aparat gerektirmeden,
- mekanik ayar yapmadan,
- aynı vakum tablası ile

taşıyabilecek şekilde tasarlanmıştır.

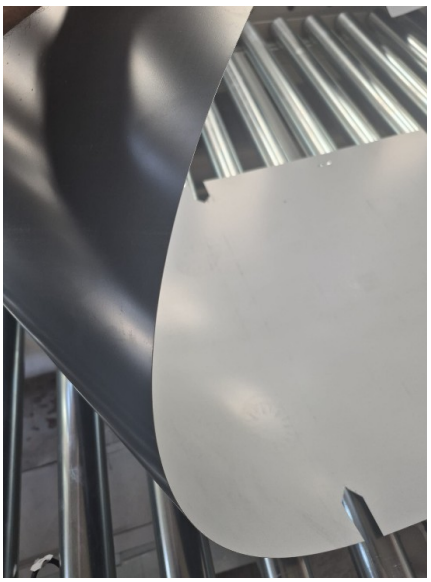
Bu özellik özellikle yüksek ürün çeşitliliğine sahip üretim tesislerinde hazırlık sürelerinin azaltılmasına katkı sağlamaktadır.

### 5.5 Yüzey Kalitesi

Folyolu ve hassas yüzey kaplamalı sacların üretiminde taşıma sistemi yalnızca çevrim süresini değil ürün kalitesini de doğrudan etkilemektedir.

Geliştirilen sistemde kullanılan özel vakum pedleri sayesinde taşıma kuvveti sac yüzeyine homojen biçimde dağıtılmaktadır. Böylece taşıma ve döndürme işlemleri sırasında oluşabilecek noktasal yükler azaltılarak yüzey deformasyonlarının önüne geçilmektedir.

Yapılan uygulamalarda özellikle folyolu saclarda manuel taşıma sırasında karşılaşılan çizik ve sürtünme kaynaklı yüzey kusurlarının oluşmadığı gözlemlenmiştir.



**Şekil 8.** Folyolu sac üzerinde gerçekleştirilen uygulama.

### 5.6 Ergonomi ve İş Güvenliği

Büyük ebatlı sacların manuel olarak döndürülmesi operatör açısından yüksek fiziksel yük oluşturmaktadır.

Geliştirilen sistem sayesinde;

- operatörün sacı kaldırmasına gerek kalmamakta,
- büyük parçalar tek kişi tarafından yönetilebilmekte,
- ikinci operatör ihtiyacı ortadan kaldırılabilmekte,
- operatörün tekrarlı kaldırma ve döndürme hareketleri azaltılmaktadır.

Bu durum yalnızca üretim verimliliğine değil iş sağlığı ve güvenliği açısından daha ergonomik çalışma koşullarının oluşturulmasına da katkı sağlamaktadır.

### 5.7 Sistemin Öne Çıkan Özellikleri

Geliştirilen tam otomatik döndürme sistemi aşağıdaki mühendislik özellikleri ile öne çıkmaktadır.

- Tek vakum tablası üzerinde konumlandırılmış **vakum pedi** ile geniş ürün çeşitliliğinin desteklenmesi.
- **150 × 150 mm ile 1500 × 3000 mm arasındaki farklı sac ölçülerinin herhangi bir mekanik ayar gerektirmeden işlenebilmesi.**
- 0,3 mm ile 3 mm kalınlığındaki sacların güvenli şekilde taşınabilmesi.
- Maksimum 150 kg taşıma kapasitesi.
- Üç eksenli (X-Z-R) kompakt mekanik yapı.
- Aynı istasyonda taşıma, kaldırma ve 180° döndürme işlemlerinin gerçekleştirilebilmesi.
- Hassas yüzeyli ve folyolu saclarda yüzey kalitesini koruyan özel vakum pedi yapısı.
- Modüler tasarımı sayesinde farklı sac işleme hatlarına entegre edilebilmesi.
- PLC tabanlı kontrol sistemi ile reçete yönetimi, alarm yönetimi ve uzaktan erişim özelliklerinin desteklenmesi.
- Operatör bağımlılığını azaltarak üretim süreçlerinde standardizasyon sağlaması.

Bu özellikler değerlendirildiğinde geliştirilen sistemin yalnızca bir taşıma mekanizması olmadığı, farklı ürün çeşitliliğine sahip modern sac işleme hatlarında üretim verimliliğini, yüzey kalitesini ve proses güvenilirliğini artırmaya yönelik bütünleşik bir otomasyon çözümü olduğu görülmektedir.

## 6. SONUÇ VE DEĞERLENDIRME

Bu çalışmada, sac işleme hatlarında büküm işlemleri arasında parçaların operatör müdahalesi olmadan güvenli bir şekilde taşınması ve 180° döndürülmesini sağlayan üç eksenli tam

otomatik bir döndürme sistemi geliştirilmiştir. Geliştirilen sistem, farklı ölçü ve yüzey özelliklerine sahip sacların tek bir platform üzerinde herhangi bir mekanik ayar gerektirmeden işlenebilmesini hedefleyen modüler bir tasarım yaklaşımıyla oluşturulmuştur.

Sistemin mekanik yapısı; X ekseninde yatay taşıma, Z ekseninde düşey konumlandırma ve R ekseninde döndürme hareketlerini gerçekleştirecek şekilde tasarlanmıştır. Servo kontrollü hareket sistemi ile vakumlu kavrama mekanizmasının senkron çalışması sayesinde sacın güvenli şekilde kavranması, taşınması ve döndürülmesi tek bir çevrim içerisinde gerçekleştirilmektedir. PLC tabanlı kontrol altyapısı, reçete yönetimi, alarm yönetimi ve uzaktan erişim fonksiyonları ile sistemin farklı üretim senaryolarına kolaylıkla uyarlanabilmesine olanak sağlamaktadır.

Geliştirilen sistemin en önemli tasarım özelliklerinden biri, tek vakum tablası üzerinde optimize edilmiş vakum pedinin kullanılmasıdır. Vakum pedlerinin yerleşim geometrisi, minimum 150 × 150 mm boyutundaki parçalardan maksimum 1500 × 3000 mm boyutundaki saclara kadar geniş bir çalışma aralığını destekleyecek şekilde optimize edilmiştir. Böylece farklı ürün grupları arasında geçiş yapılırken ilave aparat kullanımına veya mekanik ayarlara ihtiyaç duyulmamaktadır. Bu özellik, üretim esnekliğini artırırken hazırlık sürelerinin azaltılmasına da katkı sağlamaktadır.

Sistemde kullanılan özel vakum pedleri sayesinde özellikle folyolu, boyalı ve hassas yüzey kaplamalı saclarda taşıma ve döndürme işlemleri sırasında oluşabilecek çizik, sürtünme ve yüzey deformasyonlarının önüne geçilmiştir. Bu durum yalnızca ürün kalitesini artırmakla kalmayıp, yeniden işleme ve hurda oluşumunun azaltılması açısından da önemli bir avantaj sağlamaktadır.

Gerçekleştirilen uygulamalarda sistemin maksimum 150 kg taşıma kapasitesine sahip olduğu, 0,3 mm ile 3 mm kalınlığındaki sacları güvenli şekilde taşıyabildiği ve 150 × 150 mm ile 1500 × 3000 mm arasındaki farklı ürün boyutlarında herhangi bir mekanik ayar gerektirmeden çalışabildiği doğrulanmıştır. Yaklaşık 15 saniyelik çevrim süresi ile taşıma ve döndürme işlemlerinin operatörden bağımsız, tekrarlanabilir ve standart bir şekilde gerçekleştirilebildiği gözlemlenmiştir.

Operatörün büyük ebatlı sacları manuel olarak kaldırması ve döndürmesi gerekliliğinin ortadan kaldırılması, ergonomik çalışma koşullarının iyileştirilmesine ve iş güvenliğinin artırılmasına katkı sağlamaktadır. Ayrıca sistemin modüler yapısı sayesinde mevcut sac işleme ve büküm hatlarına kolaylıkla entegre edilebilmesi, yeni yatırım gereksinimini azaltarak farklı üretim tesislerinde uygulanabilirliğini artırmaktadır.

Sonuç olarak geliştirilen tam otomatik döndürme sistemi; geniş ürün yelpazesini destekleyen vakumlu kavrama yapısı, üç eksenli kompakt mekanik tasarımı, hassas yüzeyleri koruyan

taşıma yaklaşımı ve otomasyon sistemleri ile uyumlu kontrol altyapısı sayesinde modern sac işleme teknolojileri için etkin bir çözüm sunmaktadır. Özellikle yüksek ürün çeşitliliğine sahip üretim tesislerinde üretim sürekliliğinin sağlanması, operatör bağımlılığının azaltılması, ürün kalitesinin korunması ve dijital üretim süreçlerinin desteklenmesi açısından önemli bir katkı sağlamaktadır.

İlerleyen çalışmalarda sistemin görüntü işleme tabanlı parça tanıma algoritmaları ile desteklenmesi, vakum bölgelerinin otomatik olarak yönetilmesi, farklı döndürme açılarını destekleyen akıllı hareket planlama algoritmalarının geliştirilmesi ve üretim yönetim sistemleri ile gerçek zamanlı veri paylaşımının sağlanması hedeflenmektedir. Bu geliştirmelerin, sistemin esnek üretim kabiliyetini ve akıllı fabrika uygulamalarındaki kullanım potansiyelini daha da artıracağı öngörülmektedir.

# SCARA ROBOT TABANLI FREZELEME SİSTEMİNİN TASARIMI VE GELİŞTİRİLMESİ

**Sıla Betül KİRZUK,** *202213702058@ogr.balikesir.edu.tr* Balıkesir Üniversitesi, 10145, Balıkesir, Türkiye

**Furkan DURMAZ**, *202213702038@ogr.balikesir.edu.tr* Balıkesir Üniversitesi, 10145, Balıkesir, Türkiye

**Osman ATSAN**, *202313707567@ogr.balikesir.edu.tr* Balıkesir Üniversitesi, 10145, Balıkesir, Türkiye

**Kerem Yağız KARAKAŞ**, *202213709064@ogr.balikesir.edu.tr* Balıkesir Üniversitesi, 10145, Balıkesir, Türkiye

**Yunus Emre NEHRİ,** *yunusnehri@balikesir.edu.tr* Balıkesir Üniversitesi, 10145, Balıkesir, Türkiye

**Ali ORAL,** *a.oral@balikesir.edu.tr* Balıkesir Üniversitesi, 10145, Balıkesir, Türkiye

## ÖZET

Bu çalışmada, düşük kesme kuvvetli talaşlı imalat uygulamaları için kompakt, düşük maliyetli ve enerji verimli bir SCARA robot tabanlı frezeleme prototipi geliştirilmiştir. Sistem, 2B CAD çizimlerini DXF formatında işleyerek Python tabanlı yazılım ve ters kinematik denklemler aracılığıyla robot eklem açılarına dönüştürmektedir. Arduino Mega 2560 kontrollü step motorlar ve DC spindle ile 2,5 eksende otomatik talaş kaldırma sağlanmıştır. Çalışma, G-koda ihtiyaç duymayan yazılım mimarisi ve taşınabilir robotik işleme yaklaşımıyla prototipleme, eğitim ve küçük ölçekli üretim uygulamalarına katkı sunmaktadır.

**Anahtar kelimeler:** SCARA robot, robotik frezeleme, talaşlı imalat, ters kinematic analiz

## ABSTRACT

In this study, a compact, low-cost, and energy-efficient SCARA robot-based milling prototype was developed for machining applications involving low cutting forces. The system processes 2D CAD drawings in DXF format and converts them into robot joint angles through Python-based software and inverse kinematics equations. Automatic material removal in 2.5 axes was achieved using stepper motors controlled by an Arduino Mega 2560 and a DC spindle. By employing software architecture that does not require G-code and a portable robotic machining approach, the study contributes to prototyping, education, and small-scale manufacturing applications.

**Keywords:** SCARA robot, robotic milling, machining, inverse kinematics analysis

## 1.GİRİŞ

Endüstriyel otomasyon ve imalat teknolojilerindeki hızlı gelişmeler, üretici firmaları daha yüksek kalitede, daha kısa zamanda ve daha ekonomik metotlarla üretim yapmaya zorlamaktadır. Bu rekabet ortamı, geleneksel CNC tezgahlarına alternatif sistemlerin geliştirilmesini kritik hale getirmiştir [Arseven, 2013].

Robotik sistemlerin endüstriyel işlemede kullanımının yaygınlaşmasına rağmen, rijitlik kısıtlamaları önemli bir sorun teşkil etmektedir [Aktan, 2012]. Endüstriyel robotlar, sundukları esneklik, geniş çalışma hacmi ve düşük yatırım maliyeti gibi avantajlara rağmen, talaş kaldırma işlemlerinde düşük rijitlik nedeniyle titreşim problemleri oluşmaktadır. Oluşan titreşimler takım aşınmasını hızlandırmakta, işleme hassasiyetini ve nihai yüzey kalitesini olumsuz etkilemekte, takım kırılması gibi ciddi sorunlara yol açabilmektedir [Hou_Lei_Ding, 2025]. Bu kapsamda, titreşimi minimize etmek ve proses stabilitesini sağlamak için çeşitli optimizasyon stratejileri geliştirilmiştir. Hız, ivme ve sarsıntı limitlerini dikkate alan değişken ilerleme hızı optimizasyonu ile işleme verimliliğinin artırılabileceği gösterilmiştir [Hou_Lei_Ding, 2025].

SCARA robotlar ise yatay düzlemde yüksek hız ve hassasiyet sunmaları sebebiyle öne çıkmaktadır. Literatürde geliştirilen düşük maliyetli SCARA robot prototiplerinin, özellikle delme, alma-yerleştirme ve montaj işlemleri için uygun maliyetli çözümler sunduğu görülmektedir [Misra_Sharma_Singh_Kumar_Rastogi, 2020].

Geleneksel programlama yöntemlerine alternatif olarak, bilgisayarlı görü ve görüntü işleme teknikleri de giderek önem kazanmaktadır. El Naser tarafından yapılan çalışmada, çapak temizleme uygulamalarında kameradan alınan görüntülerin işlenmesiyle parça sınırlarının belirlenebildiği ve robot yörüngesinin hassas bir şekilde oluşturulabildiği gösterilmiştir [El Naser, 2018].

Bu çalışmada mevcut bir SCARA robot platformu yeniden yapılandırılarak düşük maliyetli bir robotik frezeleme sistemi geliştirilmiştir. Sistemde doğrusal hareket sağlayan bir Z ekseni mekanizması eklenmiş, kontrol elektroniği yeniden tasarlanmış ve Python tabanlı özgün bir kontrol yazılımı geliştirilmiştir. Geliştirilen yazılım sayesinde DXF formatındaki teknik çizimler doğrudan okunabilmekte, takım yolları oluşturulabilmekte ve ters kinematik hesaplamaları kullanılarak robot hareketlerine dönüştürülebilmektedir. Böylece geleneksel G-kod üretim sürecine ihtiyaç duyulmadan doğrudan CAD çizimlerinden üretim gerçekleştirilebilmektedir.

Çalışmanın amacı, küçük ölçekli üretim, hızlı prototipleme, eğitim ve bakım-onarım uygulamalarında kullanılabilecek düşük maliyetli ve modüler bir robotik işleme sistemi geliştirmek ve mevcut SCARA platformlarının frezeleme uygulamalarındaki kullanılabilirliğini araştırmaktır.

## 2. SİSTEM TASARIMI VE GELİŞTİRİLMESİ

### Mekanik Sistem Tasarımı

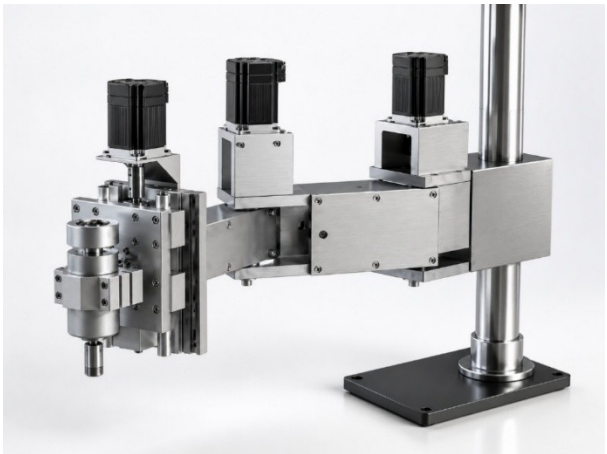
Bu çalışmada temel platform olarak mevcut bir SCARA robot konstrüksiyonu kullanılmıştır. Hızlı sıralama uygulamalarında kullanılan sistem, frezeleme operasyonlarına uygun hale getirilebilmesi amacıyla yeniden tasarlanmış ve talaşlı imalat yapmaya uygun hale getirilmiştir. Bu amaçla robot üzerine doğrusal hareket sağlayan bir Z ekseni mekanizması, spindle taşıyıcı sistemi, motor bağlantı elemanları ve güç aktarım bileşenleri entegre edilmiştir.

Z ekseninde lineer yataklar, doğrusal miller ve vidalı mil mekanizması kullanılarak rijit ve hassas bir düşey hareket yapısı oluşturulmuştur. Bu mekanizma sayesinde spindle motorun kontrollü şekilde konumlandırılması ve işleme derinliğinin hassas olarak ayarlanması sağlanmıştır. Geliştirilen Z ekseni mekanizması Şekil 1’de verilmiştir.

Frezeleme işlemleri sırasında oluşabilecek kesme kuvvetlerinin güvenli şekilde karşılanabilmesi amacıyla mekanik bağlantılar güçlendirilmiş, taşıyıcı elemanlar yeniden düzenlenmiş ve sistemin yapısal kararlılığı artırılmıştır. Tasarım sürecinde rijitlik, titreşim davranışı, üretilebilirlik ve montaj kolaylığı temel tasarım kriterleri olarak dikkate alınmıştır. Geliştirilen SCARA robot tabanlı frezeleme sisteminin mekanik yapısı Şekil 2’de gösterilmektedir.

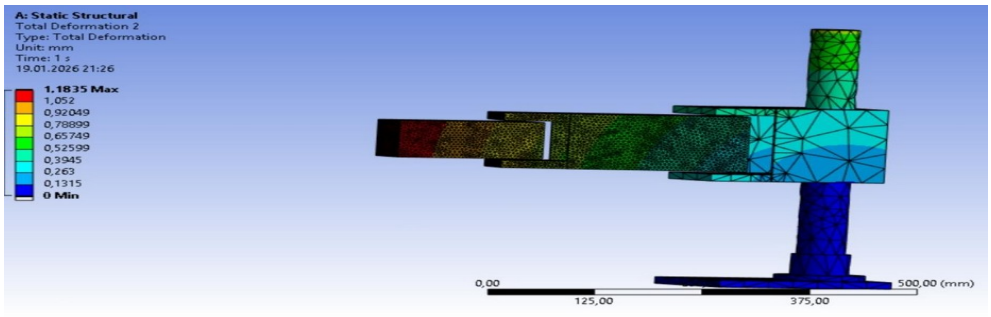


*Şekil 1. Sisteme entegre edilen Z ekseni ve spindle taşıyıcı mekanizması*



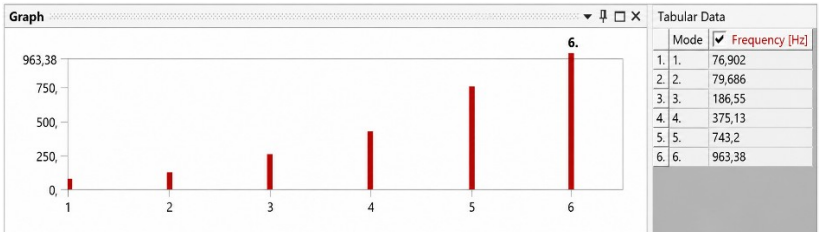
*Şekil 2. SCARA robot sisteminin frezeleme uygulamalarına yönelik dönüştürülmüş mekanik yapısı*

Geliştirilen sistemin frezeleme işlemleri sırasında maruz kalacağı yükler altındaki davranışını değerlendirmek amacıyla ANSYS Workbench ortamında statik ve modal analizler gerçekleştirilmiştir. Analizler robot gövdesi ve taşıyıcı elemanlar çalışma koşullarını temsil edecek şekilde sınır şartları altında gerçekleştirilmiştir. Statik analiz kapsamında sistemde oluşan toplam deformasyon değerleri incelenmiştir. Elde edilen sonuçlar, mekanik yapının düşük kesme kuvvetli işleme uygulamaları için yeterli rijitlik davranışı sergilediğini ve özellikle Z ekseni ile takım taşıyıcı bölgesindeki elastik deformasyonların kabul edilebilir seviyelerde kaldığını göstermektedir. Toplam deformasyon analiz sonucu Şekil 3'te verilmiştir.

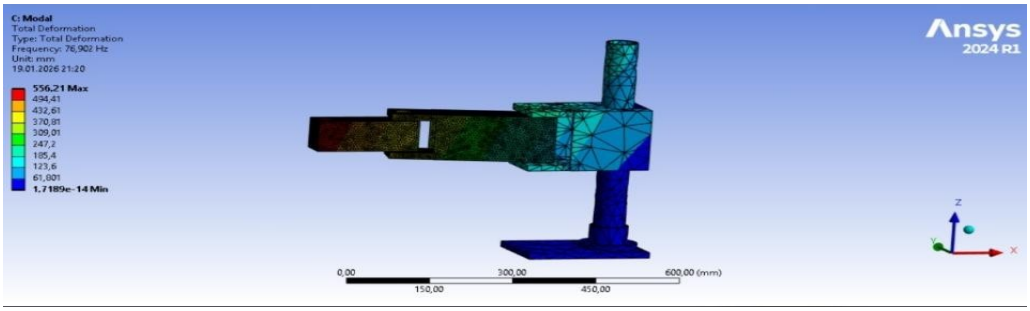



*Şekil 3. SCARA robot gövdesi toplam deformasyon (statik) analizi sonucu*

Sistemin dinamik davranışını değerlendirmek amacıyla modal analiz gerçekleştirilmiştir. Elde edilen doğal frekans değerleri, olası rezonans bölgelerinin belirlenmesi açısından incelenmiştir. Modal analiz sonucunda ilk doğal frekans 76,902 Hz olarak elde edilmiş ve mod şekilleri üzerinden sistemin titreşim davranışı değerlendirilmiştir. Sonuçlar, geliştirilen robotun kesme şartları altında titreşim kaynaklı kararsızlık riskinin sınırlı seviyede kalabileceğini göstermektedir. Modal analiz sonuçları Şekil 4 ve Şekil 5'te verilmiştir.




*Şekil 4. İlk altı moda ait doğal frekans değerlerinin grafiksel ve tablosal gösterimi*



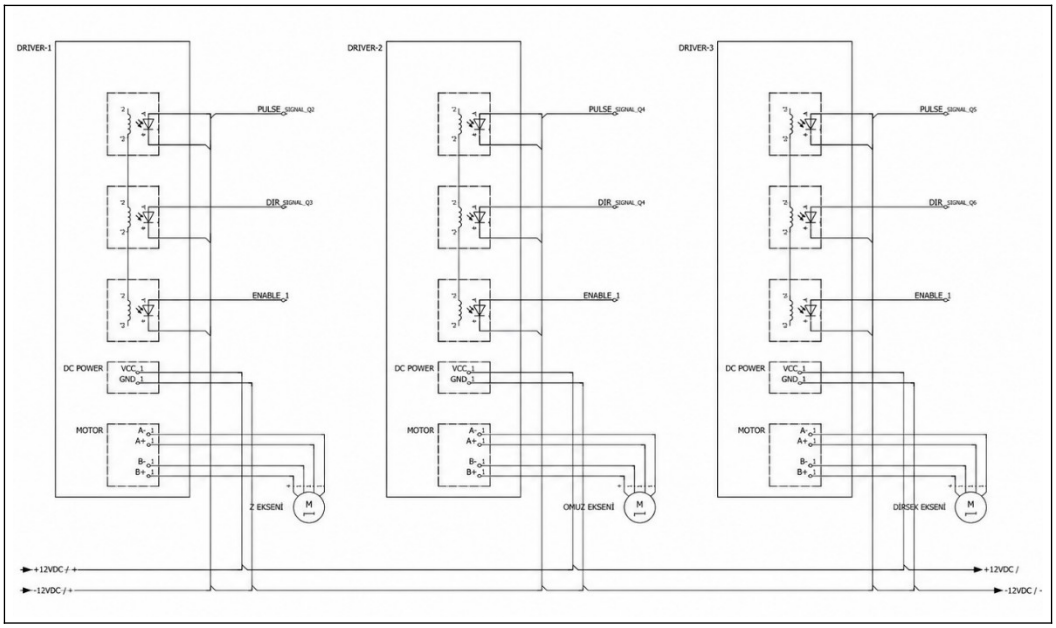
*Şekil 5. Mod 1 (76.902 Hz) için sistemin deformasyon karakteristiği*

Sistemde kullanılan iş milinin çalışma aralığı ve güç kapasitesi dikkate alınarak yapılan dinamik değerlendirmede, modal analiz sonuçları ile çalışma koşulları birlikte ele alınmış, yapının belirli bir doğal frekans bölgesinde rezonans riskinden kaçınacak şekilde çalışmasının sağlanması hedeflenmiş ve elde edilen statik ve modal analiz sonuçları, geliştirilen SCARA robot tabanlı frezeleme prototipinin mevcut çalışma şartları altında yeterli yapısal kararlılık ve uygun dinamik performans sergileyebileceğini ortaya koyduğu görülmüştür.

### Elektronik Kontrol Sistemi

Robotun hareket kontrolü Arduino Mega 2560 R3 mikrodenetleyicisi kullanılarak gerçekleştirilmiştir. Hareket eksenlerinde 2,2 Nm tork değerine sahip NEMA23 step motorlar tercih edilmiş ve motorların sürülmesinde JSS556 dijital step motor sürücüleri kullanılmıştır.

Sistemde omuz, dirsek ve Z ekseni hareketleri bağımsız olarak kontrol edilmektedir. Frezeleme işlemi için kullanılan spindle motor ayrı bir güç hattı üzerinden beslenmiş, kontrol elektroniği ile güç elektroniği birbirinden ayrılarak elektromanyetik girişimlerin azaltılması amaçlanmıştır. Sistem güvenliğinin artırılması amacıyla limit anahtarları, acil durdurma mekanizması ve yazılımsal güvenlik sınırları uygulanmıştır. Böylece eksenlerin mekanik sınırların dışına çıkması engellenmiş ve olası kontrol hatalarına karşı koruma sağlanmıştır.




*Şekil 6. SCARA robot sistemine ait genel elektriksel kontrol mimarisi*

## 3. KİNEMATİK MODELLEME VE YAZILIM ALTYAPISI

### SCARA Robot Kinematik Modeli

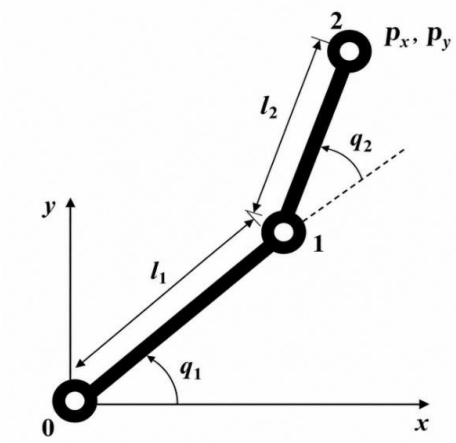
SCARA robot iki dönel eksen ve bir doğrusal eksenden oluşmaktadır. Robot Z eksenine bağlanan kesici takımın konumunun belirlenebilmesi ve takım yolu oluşturulabilmesi amacıyla

ileri ve ters kinematik hesaplamaları kullanılmıştır. İleri kinematik hesaplamalarında eklem açıları kullanılarak uç efektörün Kartezyen koordinatları elde edilmektedir [Eşitlik (1)-(2)].

$$x = L_1\cos(\theta_1) + L_2\cos(\theta_1 + \theta_2) \quad (1)$$

$$y = L_1\sin(\theta_1) + L_2\sin(\theta_1 + \theta_2) \quad (2)$$

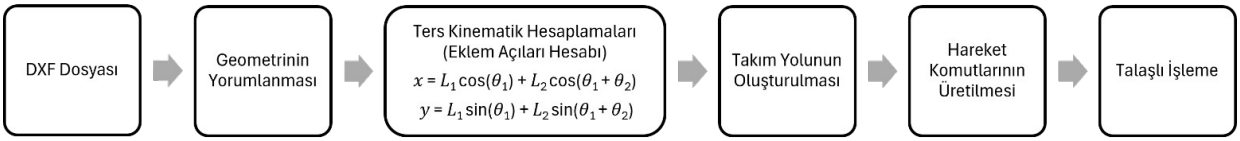
Ters kinematik çözümünde ise hedef koordinatlar kullanılarak eklem açıları hesaplanmaktadır. Böylece DXF dosyalarından elde edilen takım yolu noktaları robot hareketlerine dönüştürülebilmektedir.




*Şekil 7. İki serbestlik dereceli SCARA robotunun geometrik modeli ve eklem açıları. [Oral_Erzincanlı, 2004]*

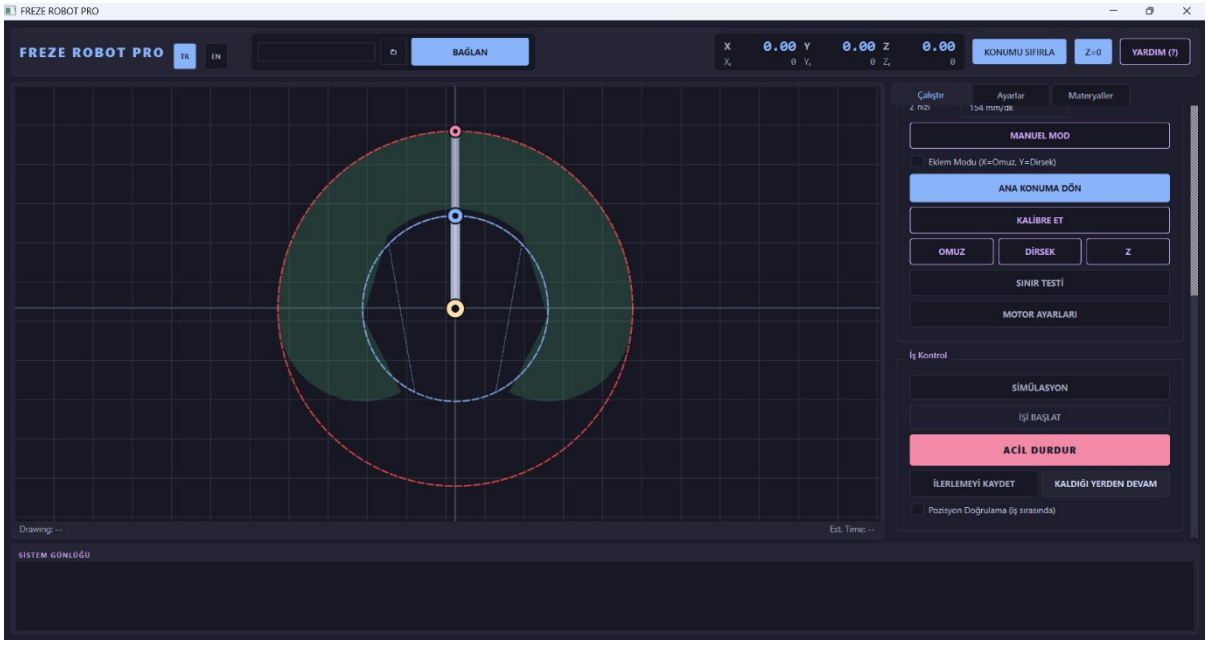
**DXF Tabanlı Takım Yolu Oluşturma**

Geliştirilen kontrol yazılımı Python programlama dili kullanılarak hazırlanmıştır. Yazılımın temel görevi, DXF formatındaki teknik çizimleri okuyarak robot tarafından takip edilebilecek takım yollarına dönüştürmektir. DXF dosyasından talaşlı işleme sürecine kadar izlenen genel yazılım akışı Şekil 8'de verilmiştir.




*Şekil 8. DXF dosyasından talaşlı işleme sürecine kadar izlenen yazılım iş akışı*

DXF dosyasında bulunan çizgi, yay ve eğrisel geometriler ayrıştırılarak işlenebilir koordinat dizilerine dönüştürülmektedir. Eğrisel yapılar belirli toleranslar altında doğrusal segmentlere bölünmekte ve takım yolu sürekliliği sağlanmaktadır. Ayrıca takımın boşta hareket sürelerini azaltmak amacıyla en yakın komşu yaklaşımına dayalı bir sıralama algoritması uygulanmaktadır. İşlenen koordinatlar ters kinematik çözümü yardımıyla eklem açılarına dönüştürülmekte ve seri haberleşme aracılığıyla mikrodenetleyiciye gönderilmektedir. Mikrodenetleyici tarafında ivmeli hareket profilleri kullanılarak eksen hareketleri gerçekleştirilmektedir. Geliştirilen PyQt tabanlı kullanıcı arayüzü üzerinden robot kol pozisyonu, çalışma alanı, manuel kontrol komutları ve sistem durumu görsel olarak takip edilebilmektedir. Geliştirilen yazılımda, DXF yükleme ve çevrimdışı simülasyon modu Şekil 9'da gösterilmektedir.




*Şekil 9. DXF yükleme ve çevrimdışı simülasyon modu ekran görünümü*

## 4. DENEYSEL SONUÇLAR

### Takım Yolu Doğrulama Ve Frezeleme Testleri

Geliştirilen kontrol yazılımının doğrulanması amacıyla çeşitli DXF tabanlı takım yolu testleri gerçekleştirilmiştir. Bu kapsamda ilk olarak Şekil 10'da verilen imza geometrisi DXF dosyası üzerinden yazılım ortamına aktarılmış ve elde edilen geometri arayüz üzerinde görüntülenmiştir.



*Şekil 10. DXF dosyasından elde edilen imza geometrisinin arayüz üzerinde gösterimi*

İlk aşamada oluşturulan takım yolları yazılım ortamında simüle edilerek robot hareketleri doğrulanmıştır. Simülasyonlar sırasında ters kinematik çözümlerinin doğruluğu, takım yolu sürekliliği ve hareket planlama algoritmasının performansı değerlendirilmiştir. İmza geometrisine ait takım yolu simülasyonu ve SCARA robot çalışma alanı içerisindeki konumu Şekil 11'de gösterilmektedir.

Gerçekleştirilen testler sonucunda sistemin düşük yoğunluklu köpük malzemeler üzerinde frezeleme ve çizim işlemlerini başarıyla gerçekleştirebildiği görülmüştür. DXF tabanlı takım yolu oluşturma, ters kinematik çözümü, hareket planlama ve mikrodenetleyici kontrol katmanları birlikte değerlendirildiğinde sistemin tasarım hedeflerini karşıladığı belirlenmiştir.

İmza geometrisinin köpük malzeme üzerine işlenmesi sonucunda elde edilen fiziksel çıktı Şekil 12'te verilmiştir.

*Şekil 11. İmza geometrisine ait takım yolu simülasyonu ve SCARA robot çalışma alanı içerisindeki görünümü*






*Şekil 12. 2D CAD verisinin köpük malzeme üzerine işlenmesi sonucunda elde edilen fiziksel çıktı*

Yapılan deneyler sırasında referanslama mekanizmasının kararlı çalıştığı, takım yollarının başarıyla takip edildiği ve kullanıcı arayüzü ile mikrodenetleyici arasındaki haberleşmenin güvenilir şekilde sürdürüldüğü gözlemlenmiştir. Ayrıca uygulanan backlash (boşluk) telafisi ve filtreleme algoritmalarının sistem doğruluğunu olumlu yönde etkilediği belirlenmiştir.

## 5. SONUÇLAR VE ÖNERİLER

Bu çalışmada, düşük maliyetli, kompakt ve eğitim amaçlı kullanıma uygun bir SCARA robot tabanlı frezeleme sistemi tasarlanmış ve prototip olarak gerçekleştirilmiştir. Mekanik yapı, elektronik kontrol altyapısı ve yazılım bileşenleri bütünleşik bir sistem yaklaşımıyla geliştirilmiştir. Geliştirilen sistemde, DXF formatındaki geometriler Python tabanlı arayüz üzerinden işlenerek takım yollarına dönüştürülmüş, ters kinematik hesaplamaları ile robot eklem açıları elde edilmiştir. Mikrodenetleyici tabanlı kontrol altyapısı sayesinde hareket komutları eksenlere aktarılmış ve 2,5 eksenli frezeleme işlemi yapılmıştır. Yapılan deneysel

çalışmalarda, sistemin referanslama işlemini kararlı biçimde gerçekleştirdiği, oluşturulan takım yollarını takip edebildiği ve 2,5 eksen frezeleme işlemlerini yapabildiği görülmüştür.

Gelecek çalışmalarda daha yüksek güçlü iş mili motoru, yüksek torklu step veya servo motorlar ve daha rijit bir mekanik yapı kullanılarak sistemin işleme kapasitesi artırılabilir. Ayrıca görüntü işleme destekli otomatik hizalama, gelişmiş takım yolu optimizasyonu ve manyetik mengene entegrasyonu ile sistemin taşınabilir işleme ve yerinde bakım-onarım uygulamalarına uygunluğu geliştirilebilir.

**KAYNAKÇA**

1. **Aktan, M. E. (2012),** "Çok Amaçlı 3 Eksen Kartezyen Robot Sisteminin Tasarımı ve İmalatı", Yüksek Lisans Tezi, Marmara Üniversitesi, Fen Bilimleri Enstitüsü, Mekatronik Anabilim Dalı, İstanbul, Türkiye.

2. **El Naser, Y. H. (2018),** "Endüstriyel Amaçlı Robot Kol Tasarımı ve Üretimi", Yüksek Lisans Tezi, Sakarya Üniversitesi, Fen Bilimleri Enstitüsü, Mekatronik Mühendisliği Anabilim Dalı, Sakarya, Türkiye**.**

3. **Hou, T., Lei, Y. and Ding, Y. (2025),** "Chatter-Free Process Parameter Optimization for Robotic Machining of Pockets with the Spiral Tool Path", Journal of Manufacturing Processes, Vol. 150, pp. 1241-1259.

4. **Misra, A., Sharma, A., Singh, G., Kumar, A. and Rastogi, V. (2020),** "Design and Development of a Low-Cost CNC Alternative SCARA Robotic Arm", Procedia Computer Science, Vol. 171, pp. 2459-2468.

**5. ORAL, A. AND ERZINCANLI, F. (2004), "COMPUTER-ASSISTED ROBOTIC TILING OF MOSAICS", ROBOTICA, VOL. 22, PP. 235-239.**

6. **Sezen Arseven, Z. (2013),** "Görüntü İşleme Metodu ile Robotik Beslemeli Çok Amaçlı Multieksen CNC Tezgah Tasarımı ve Uygulaması", Yüksek Lisans Tezi, Marmara Üniversitesi, Fen Bilimleri Enstitüsü, Mekatronik Anabilim Dalı, İstanbul, Türkiye.

# AUTHOR INDEX

# AUTHOR INDEX


| LAST NAME | NAME | PAPER NO. (PAGE) |
|---|---|---|
| Abdullayeva | Khangul | 73(284) |
| Acar | Erdem | 45(54) |
| Akagündüz | Emre | 3(300) |
| Akar | Samet | 69(202) |
| Akyıldız | Öncü | 16(264) |
| Atsan | Osman | 115(316) |
| Bakkal | Mustafa | 49(154) |
| Bank | Hasan Sinan | 83(254) |
| Baykut | Alp | 49(154) |
| Baytekin | Mehmet Can | 106(270) |
| Beköz | Fatih Furkan | 74(178) |
| Birk | Max-Heiner | 15(38) |
| Buğdaycı | Nevzat Bircan | 83(254) |
| Çakır | Hasan | 49(154) |
| Çakır | Mustafa Cemal | 18(236) |
| Çelik | Sare | 60(172) |
| Çetin | Barış | 16(264) |
| Durmaz | Furkan | 115(316) |
| Ecevit | Ozan | 110(216) |
| Ekici | İrem Beyza | 26(244) |
| Engler | Michael | 15(38) |
| Erciyas | İclal Burcu | 69(202) |
| Eser | Giray Cevher | 110(216) |
| Ertürk | Yusuf Ata | 74(178) |
| Gaus | Andreas | 15(38) |
| Hirao | Akinari | 25(130), 54(144) |
| İçten | N. Berk | 45(54) |
| İlbeyli | Mert | 60(172) |
| Inokuma | Hiroko | 39(120) |
| Karakaş | Kerem Yağız | 115(316) |
| Kayıhan | Mete | 73(284) |
| Kayıhan | Yavuz | 73(284) |
| Khummongkol | Rojanee | 24(90) |
| Kida | Yuki | 39(120) |
| Kirzuk | Sıla Betül | 115(316) |
| Lotfi | Bahram | 110(216) |
| Miyachi | Hideo | 14(80) |
| Murakami | Tamotsu | Keynote(22) |
| Nazlıgül | Semih | 49(154) |
| Nehri | Yunus Emre | 115(316) |
| Nguyen | Minh Tien | 25(130) |
| Ogi | Tetsuro | 39(120) |
| Okutucu-Özyurt | Tuba | 74(178) |
| Oral | Ali | 115(316) |
| Otsay | Beliğ Tarık | 18(236) |
| Özdemir | Mustafa | 26(244) |
| Özkader | M. Çağrı | 16(264) |
| Parlar | Zeynep | 65(188) |
| Reich | Christoph | 15(38) |
| Sait | Ferit | 69(202) |
| Sakurai | Towa | 34(104) |
| Suzuki | Kai | 54(144) |
| Türkoğlu | Türker | 60(172) |
| Ünver | Hakkı Özgür | 110(216) |
| Uskaner | Uscan | 65(188) |
| Yakoh | Takahiro | 34(104), 39(120) |
| Yalçıntaş | Mert | 3(300) |
| Yokota | Masao | 24(90) |
| Zeybek | Beyzanur | 106(270) |